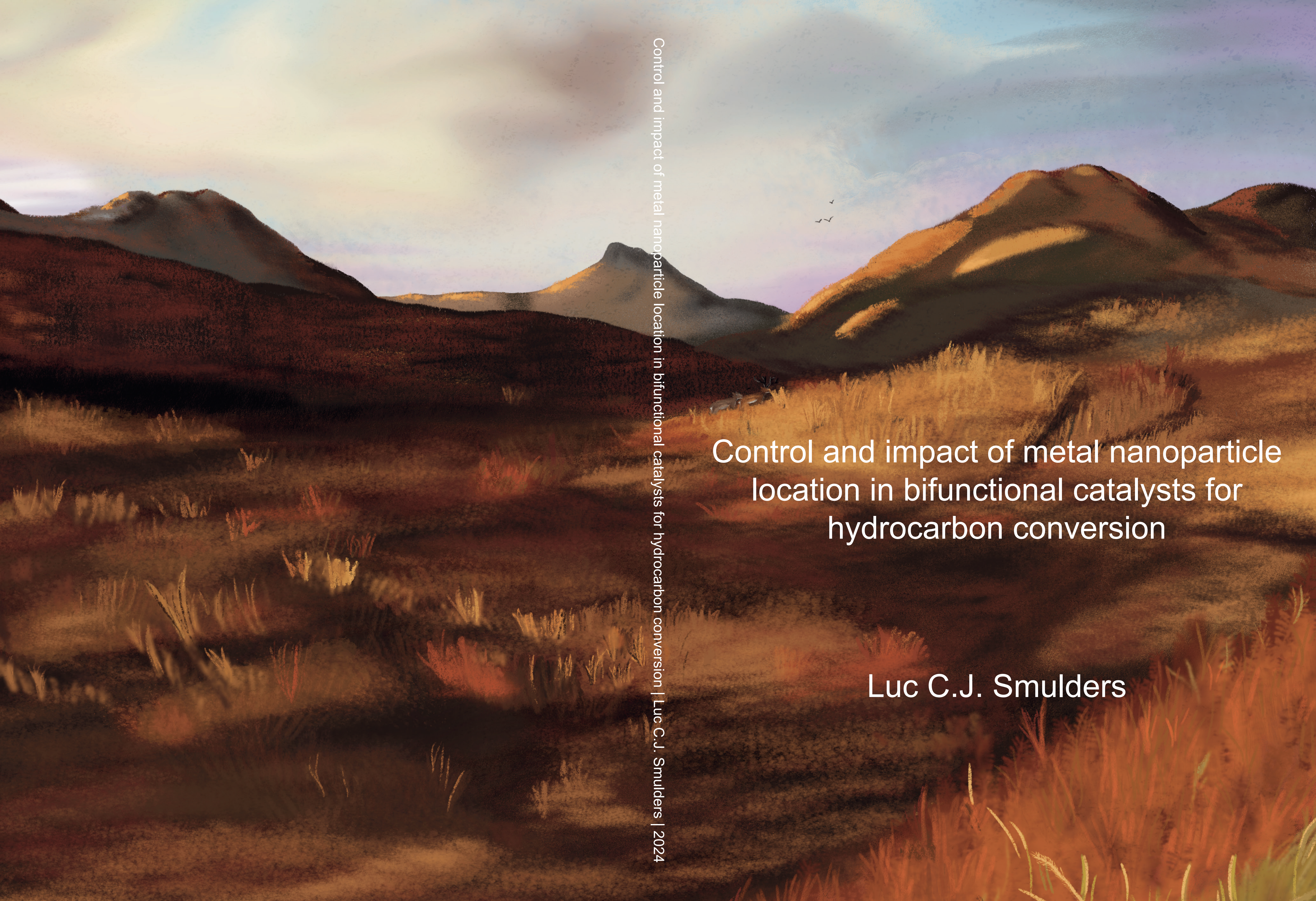

Control and impact of metal nanoparticle location in bifunctional catalysts for hydrocarbon conversion | Luc C.J. Smulders | 2024

Control and impact of metal nanoparticle location in bifunctional catalysts for hydrocarbon conversion

Luc C.J. Smulders

Control and impact of metal nanoparticle location in bifunctional catalysts for hydrocarbon conversion

Luc C.J. Smulders

Author: Luc Cornelis Jacobus Smulders
Title: Control and impact of metal nanoparticle location in bifunctional catalysts
for hydrocarbon conversion
ISBN: 978-94-6483-917-3
DOI: 10.33540/2251
Cover art: Elena Maria Höppener
Printed by: Ridderprint | www.ridderprint.nl

Control and impact of metal nanoparticle location in bifunctional catalysts for hydrocarbon conversion

Controle over en invloed van de locatie van metaalnanodeeltjes in bifunctionele katalysatoren voor koolwaterstofomzetting

(met een samenvatting in het Nederlands)

Proefschrift

ter verkrijging van de graad doctor aan de
Universiteit Utrecht
op gezag van de rector magnificus, prof. dr. H.R.B.M. Kummeling,
ingevolge het besluit van het college voor promoties
in het openbaar te verdedigen op

woensdag 1 mei 2024 des ochtends te 10.15 uur

door

Luc Cornelis Jacobus Smulders

geboren op 30 december 1993
te Eindhoven

Promotoren:
Prof. dr. ir. K.P. de Jong
Prof. dr. P.E. de Jongh

Beoordelingscommissie:
Prof. dr. P.C.A. Bruijnincx
Prof. dr. F.M.F. de Groot
Prof. dr. D.Y. Murzin
Dr. S.T. Roberts
Prof. dr. E.T.C. Vogt

This PhD thesis was financially supported by BP plc.

Table of contents

Chapter 1 Introduction 7

Chapter 2 Steering the metal precursor location in bifunctional catalysts 31

Chapter 3 Maximizing noble metal utilization in bifunctional catalysts by control of nanoparticle location 59

Chapter 4 Silica as support and binder in bifunctional catalysts with ultralow Pt loadings 87

Chapter 5 Location effects in Ni based bifunctional catalysts 115

Chapter 6a Summary, concluding remarks & outlook 139

Chapter 6b Nederlandse samenvatting voor een breder publiek 147

List of abbreviations 158

List of publications and presentations 160

Acknowledgements | Dankwoord 162

About the author 167

Chapter 1

Introduction

1.1. Energy and Fuel Production

Energy is required for many different purposes, such as heating and cooling of our buildings, production and processing of food and other products, and transportation of people and goods. In 2022 the world used a total amount of 604 EJ (1 EJ = 10^{18} J) and this amount is still increasing.[1] Most of our energy consumption (82%) is by utilization of fossil fuels, i.e. crude oil, natural gas and coal, as can be inferred from Figure 1.1. Energy consumption is an indicator for economic growth[2] and most of its rise is attributed to increased consumption in developing countries.[1]

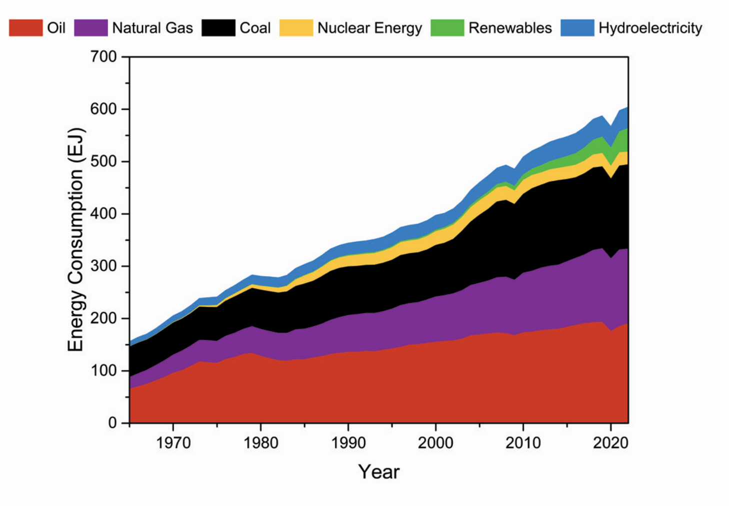

Figure 1.1. Development of the global energy consumption from 1965-2022 per category. Figure based on data from ref.[1] using their Energy Charting tool.[3]

Although the contribution of renewables (including hydroelectricity) is increasing, we are still largely dependent on fossil resources to meet our energy demand. The use of fossil fuels results in the emissions of CO_2. CO_2 is a greenhouse gas, a group of gases that are infamous for their role in global warming.[4] The transport sector is one of the biggest contributors to CO_2 emissions.[5] One of the reasons this sector makes so much use of fossil fuels is the high energy density of liquid hydrocarbons, making them a convenient energy carrier.[6,7] Moreover, these hydrocarbons can be handled and distributed relatively safely and easily.

Fossil sources, such as crude oil, need to undergo refining before they can be applied as fuels. In a modern refinery multiple conversion processes come together. Each of these processes is adjusted to the feedstock that enters the refinery, as the crude oil composition varies from well to well.[8] First, the oil is distilled to separate the different constituents in fractions. The gaseous constituents are sold as Liquefied Petroleum Gas (LPG). All liquid fractions are further treated: undesired heteroatoms sulfur (S) and nitrogen (N) are removed by hydrotreating, reforming is performed to give gasoline the desired properties, and hydrocracking and fluid catalytic cracking are applied to convert the heavier oil fractions into kerosene and diesel fuels.[8,9]

Various raw materials cannot directly be converted into transportation fuels, but can be applied as carbon sources, which can eventually be turned into liquid fuels.[10,11] Examples are natural gas, coal, bitumen-water emulsions, oil sand residues, and heavy petroleum fractions. The processes converting these resources into liquid fuels are often referred to as feed-to-liquids (XTL, in which X could theoretically be any carbon source). XTL is performed on an industrial scale, and mostly via so-called indirect liquefaction. Natural gas is used as a feedstock, but also coal (South Africa, China) is converted. For all indirect liquefaction technologies, independent of the feedstock, synthesis gas (or syngas) is an intermediate. Syngas is a mixture of H_2 and CO and can be obtained from natural gas via, e.g., steam reforming (Eq. 1.1):[12]

$$CH_4 + H_2O \rightleftharpoons CO + 3\ H_2 \qquad \textbf{(Eq. 1.1.)}$$

In order to produce syngas from solid and liquid carbon sources, the feed has to be gasified. During gasification, the carbonaceous feedstock reacts with steam and/or oxygen to yield a gas mixture containing H_2, CO, CO_2 and CH_4.[13] Gasification with steam (Eq. 1.2) and oxygen (Eq. 1.3) can be summarized with the following reaction equations:[13,14]

$$C + H_2O \rightarrow CO + H_2 \qquad \textbf{(Eq. 1.2.)}$$

$$C + \tfrac{1}{2}\ O_2 \rightarrow CO \qquad \textbf{(Eq. 1.3.)}$$

In most gasifiers, the water-gas shift reaction (WGS, Eq. 1.4) and methanation (Eq. 1.5) proceed simultaneously, producing CO_2 and CH_4, respectively:

$$CO + H_2O \rightarrow CO_2 + H_2 \qquad \textbf{(Eq. 1.4.)}$$

$$CO + 3\ H_2 \rightleftharpoons CH_4 + 2\ H_2O \qquad \textbf{(Eq. 1.5.)}$$

The WGS reaction is also used to change the H_2/CO ratio. For the production of fuels from syngas, an H_2/CO ratio of 2/1 is desired.[10,11] Furthermore, during syngas production, the gas mixture has to be purified to remove sulfur and nitrogen compounds.[10,14]

Liquefaction can be carried out via Fischer-Tropsch (FT) synthesis, transforming the syngas into liquid hydrocarbons. A variety of hydrocarbons can be synthesized via FT, and the overall reaction equation for the production of alkanes via FT is:[8,10–12,15,16]

$$(2n{+}1)\ H_2 + n\ CO \rightarrow C_nH_{(2n+2)} + n\ H_2O \qquad \textbf{(Eq. 1.6.)}$$

Products ranging from methane to high molecular weight paraffinic waxes can be obtained via this process.[12] The selectivity towards hydrocarbons with a certain range of molecular weight can be controlled to a certain extent and is dependent on the process conditions. In most cases, however, a mixture of alkanes, alkenes and oxygenates with varying molecular weight is obtained and this mixture forms the syncrude that needs refining.

Syncrude refining – like the refining of crude oil – consists of distillation and separation of the different fractions, and reactions, such as hydrocracking and hydroisomerization, are applied to ensure the resulting fuel meets the required specifications.[10,17] Hydroisomerization, for example, is required to introduce branches in the relatively straight paraffins in the syncrude. These branches improve the octane number of gasoline and give the required cold-flow properties to diesel and jet fuel. Hydrocracking is required to crack the solid waxes into a liquid fraction that is suitable as fuel. Hydrocracking and hydroisomerization are the key reactions discussed in this dissertation and a more thorough description is given in Section 1.5.

A main advantage of syncrude over crude oil is the low metal-, sulfur- and nitrogen content,[10] and therefore, XTL is a promising technology to make ultraclean fuels. Moreover, with the current desire and need to move to more sustainable and renewable energy, biomass[18–20] and municipal solid waste[21–25] are being increasingly used as a resource for the production of liquid fuels.

1.2. Turning Trash into Treasure: Waste to Liquids

In the EU alone, 2.15 billion tons of waste were generated in 2020 by both economic activities (90.6%), such as construction, mining and quarrying, waste and water services, and manufacturing and households (9.4%).[26,27] Worldwide, 2.01 billion tons of municipal solid waste (MSW) were produced by households in 2016 and this amount is projected to increase to 3.40 billion tons in 2050.[28] Most of it (40%) is discarded in landfills.[28] This waste consists of paper, food, plastics, glass, metals, wood, textiles, and other materials. Landfill waste can be converted into fuels, attacking several problems simultaneously:[29] the ever-increasing amounts of waste; the increase of space for agricultural activities, as the amount of land required for landfills decreases; the landfill's greenhouse gas emissions (mainly methane); and the production of transportation fuels from a partially renewable source as on average 49% of the global MSW consists of food, wood and other plant materials.[28]

MSW is one of various raw materials that can be seen as solid carbon sources, which can be turned into liquid fuels in a process referred to as Waste to Liquids (WTL).[15] The chemistry remains largely similar to the production of fuels from other solid carbon materials via XTL as described in Section 1.1: the raw materials are gasified to produce syngas, the syngas is converted in liquid fuels and waxes via the Fischer-Tropsch process, and the liquids and waxes are refined to produce high quality fuels and lubricants. A schematic overview of this process is given in Figure 1.2.

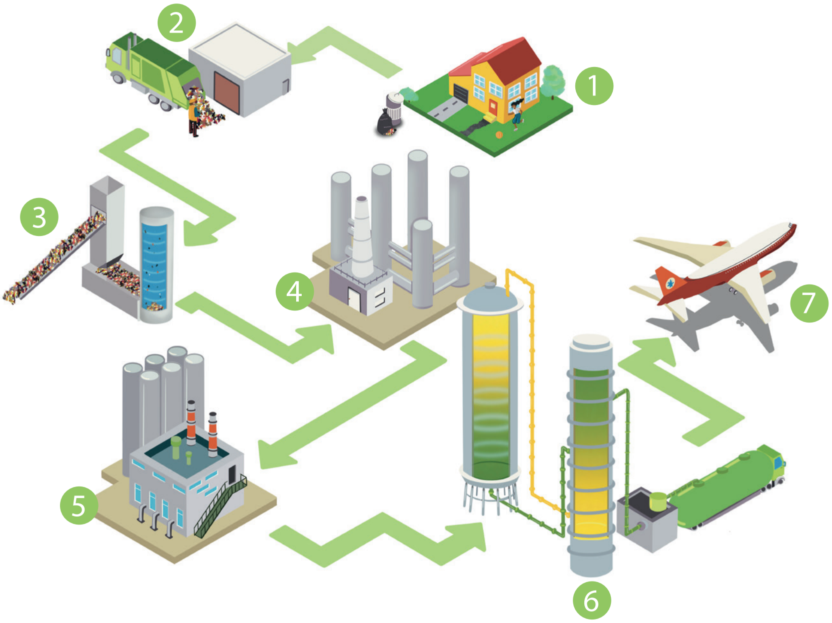

Figure 1.2. Schematic overview of the WTL process in seven steps. 1) Waste is collected from households; 2) the waste from multiple households arrives at a collection facility, ideally close to the WTL-plant; 3) at the WTL-plant, the waste is gasified, producing synthesis gas (CO and H_2); 4) the synthesis gas is purified, unwanted impurities (water, acid gas and particulate matter) are removed in a wet scrubbing process and the CO/H_2 ratio is adjusted; 5) the syngas is converted into a mixture of hydrocarbons (or syncrude) via Fischer-Tropsch synthesis; 6) the syncrude is cracked and isomerized via hydroconversion to produce jet fuel and diesel; 7) the jet fuel (and diesel) is ready to be used for transportation.

Compared to “old” fossil fuel based systems, the WTL refinery could reach a reduction of greenhouse gas emissions of up to 90%.[30] WTL is also an interesting strategy compared to “new” liquid fuel production by hydrogenation of CO_2. This is a result of CO_2 hydrogenation displaying lower energy efficiency and related higher costs of around 1000 USD/barrel,[31] whereas the production of fuels from MSW costs around 100 USD/barrel.[32] Although research endeavors might reduce the former costs, this is not expected to take place in the near future.[3]

The world’s first commercial-scale WTL plant is Fulcrum’s Sierra BioFuels Plant in Nevada (USA), which produced its first synthetic crude oil, a product that can be further refined into transportation fuels, in December 2022.[34] According to a life cycle assessment,[35] its greenhouse gas emissions are more than 60% below a petroleum baseline. Most of the emission prevention was attributed to avoided landfilling of MSW. Therefore, WTL can play a role in the provision of more sustainable energy, mainly in the form of transportation fuels. The processes that are applied in both oil and WTL refineries, and many other processes require catalysts.

1.3. Heterogeneous Catalysis

A catalyst is in a simplified manner defined as “something that makes a reaction go faster, without being consumed in the process”.[36] Additionally, it is very important that the catalyst makes the desired product and that it is stable over longer times. Compared to the substrate, only limited amounts of catalyst are required as a catalyst can participate in multiple consecutive reactions. Many different types of proteins, molecular complexes and solids can act as catalysts, and hence catalysis is divided in three subcategories: biocatalysis, homogeneous catalysis, and heterogeneous catalysis.[9,36]

In biocatalysis, the catalyst is in most cases an enzyme.[9,36] An enzyme is a rather complex protein that catalyzes reactions in living cells. Generally, these enzymes convert one specific reactant into a specific product. Because of their specificity, biocatalysts mainly find applications in the food and pharmaceutical industry. Homogeneous catalysis is one of the two types of “chemical catalysis” and is the name used for processes in which the catalyst and the reactants are in the same phase. In most of the examples, these processes take place in the liquid phase and both catalysts and reactants are in solution. Homogeneous catalysts range from ions, such as protons and hydroxide ions, to organometallic complexes.

The catalysts described in this dissertation are “chemical” catalysts commonly referred to as heterogeneous catalysts. Heterogeneous catalysts are generally solids and the reactants are in the liquid or gas phase. Some books and journals even refer to it as “classical” catalysts, as it is the most widely industrially applied type of catalysis.[36] It is estimated that 85% of all industrial chemical processes makes use of catalysts, and in 80% of these processes a heterogeneous catalyst is used.[37] Most of the heterogeneous catalytic processes known today were developed in petrochemical and bulk chemistry production, where the use of solid catalysts is favorable for the large scale, high temperature, and high pressure processes. An additional advantage is the facile separation of solid catalysts from the liquid or gaseous reactants and products.

Commonly, the active site of a heterogeneous catalyst consists of a metal surface. To make the most use of the metal, and to thus have as much of the metal atoms available at the surface, supported metal nanoparticles are applied. Different metals catalyze different reactions: for example, the aforementioned Fischer-Tropsch process is typically catalyzed by Co or Fe,[38,39] synthesis of methanol from syngas is typically performed with Cu,[40–42] and Pt and Pd are widely applied for hydrogenation and dehydrogenation reactions.[43–45] The support is generally a relatively inert oxide, such as alumina or silica, or a carbon support.[37] Heterogeneous catalysts are not limited to supported metal particles, however. Solid acid materials, such as zeolites[46,47] and amorphous silica-aluminas[48] find applications in cracking and isomerization reactions, for example.

1.4. Zeolites and Zeotypes

Zeolites were first described by the Swedish chemist Axel Cronstedt, who referred to them as boiling stones, and hence gave the name ‘zeolites’ (from Greek: ‘ζεω’ meaning ‘to boil’ and ‘λįθος’ meaning ‘a stone’).[49] They are microporous, crystalline aluminosilicates.[50,51] The pores and cavities in a zeolite are of molecular dimensions, and hence they are also referred to as molecular sieves. They are widely used for industrial applications, such as sorption, catalysis and ion exchange. Zeolites can be found as naturally occurring minerals, but they can also be synthesized. The first successful synthesis of a zeolite material was claimed by Sainte-Claire Deville in 1862 and since the 1940s zeolite synthesis really took off with Richard Barrer and Robert Milton as the founding fathers.[52,53] Ever since, many different synthetic forms have been obtained with a far greater variety than encountered in naturally occurring solids.[53]

The zeolite architecture is based on SiO_4 and AlO_4 tetrahedra as so-called primary building blocks.[54] These tetrahedra can connect in different ways, building up secondary and tertiary building blocks. Examples of these building units are shown in Figure 1.3. Together these building units make up a framework. Zeolite type (or zeotype) materials containing tetrahedrally coordinated Si, Al, P and transition metals or other elements including B, Ga, Fe, Cr, Ti, V, Mn, Co, Zn, Cu and more have also been synthesized.55 Examples of these zeotypes are $AlPO_4$ (aluminophosphate) and SAPO (silicoaluminophosphate), and their respective transition metal containing counterparts MeAPO and MeAPSO. To date, there are about 260 different zeolite and zeotype structures according to the International Zeolite Association.[56] Since every framework has unique properties, several laboratories actively search after new frameworks.

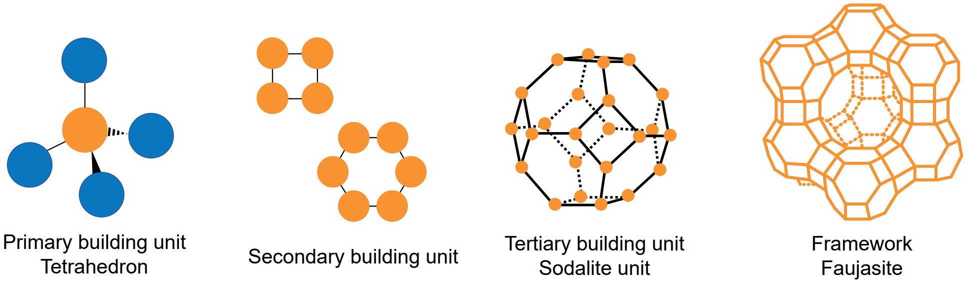
Primary building unit
Tetrahedron

Secondary building unit

Tertiary building unit
Sodalite unit

Framework
Faujasite

Figure 1.3. Examples of primary, secondary and tertiary building blocks of zeolites and the faujasite framework as an example of a zeolite framework.

Substitution of Si^{4+} by Al^{3+} in the zeolite framework results in the creation of a negative charge on the framework, which is compensated for by cations such as Na^+, K^+, NH_4^+ and H^+. Similarly, Si^{4+} substitution for P^{5+} in $AlPO_4$ zeotype framework – which results in the formation of SAPO – creates a negative charge, and hence charge compensation with cations, such as protons.

The catalytic activity of zeolites is mainly due to the Brønsted acidity of protons. A large set of acid-catalyzed chemical reactions can be performed with the help of proton exchanged zeolites. Classically, most of these reactions involve hydrocarbon conversion for the production of high-quality fuels. Other examples include the production of olefins and aromatics from methanol and the production of bulk and fine chemicals.[46] From the group of zeotype materials, SAPO is the most relevant to catalysis. It has a lower acid strength than aluminosilicate zeolites.[57,58] Moreover, these SAPOs can be synthesized to possess structures that are never encountered in aluminosilicate zeolites.[59]

While the focus is shifting from the conversion of petroleum feedstocks to the conversion of renewables, zeolite and zeotype materials will remain relevant. These materials have shown to be useful catalysts during the conversion of biobased compounds[60–62] and plastic recycling[63–66]. Since properties such as the pore architecture, the acidity, and the location of heteroatoms can be tuned, the possibilities with zeolite catalysis are numerous.

1.5. Bifunctional Catalysis for Hydroconversion

If a single catalyst particle contains two or more independent catalytic functions we refer to it as a multifunctional catalyst. Each of these functions has to be active under the same reaction conditions. Other words for multifunctional catalysis are – mostly depending on the field of study − hybrid catalysis,[67–69] and tandem catalysis.[70–72]

Bifunctional catalysts with a metal and an acid function are widely applied in industrial processes, such as catalytic dewaxing, catalytic reforming, hydrocracking and hydroisomerization.[46,53,73] The latter two are also referred to as hydroconversion. During hydroconversion, the metal (oxide or sulfide) catalyzes the dehydrogenation and hydrogenation (DHD/HD) of alkanes and alkene intermediates. The Brønsted acid function catalyzes skeletal rearrangement, i.e. isomerization, and cracking of the alkene intermediates. For DHD/HD classically metal sulfides (CoMoS, NiMoS, MoS_2, WS_2) are used, as they are more resistant to sulfur and nitrogen poisoning.[74–77] Alternatively, for the conversion of ultraclean feedstocks in particular, molybdenum carbide,[78] oxide[79] and oxycarbide,[80,81] nickel oxide and nickel,[82] and platinum and palladium[16,83–85] are used. Ultrastabilized Y Zeolite (USY)[46] and Mordenite[37] typically provide the Brønsted acid function.

The mechanism for hydroconversion is depicted in Figure 1.4. This mechanism is also referred to as classical bifunctional mechanism and was first proposed by Coonradt and Garwood.[86] The reaction is initiated by dehydrogenation of the alkane on a metal site, resulting in the formation of an alkene. This alkene will then diffuse to a Brønsted acid site, where it adsorbs and is protonated to form a carbenium ion. The carbenium ion is transformed into an alkylated cyclopropane molecule which subsequently opens to form a methyl branched alkene (or *i*-alkene) molecule via the molecule via the Protonated Cyclopropane (PCP) mechanism.[87,88] Instead of creating a branch, this mechanism can also lead to the shift of an already present methyl branch along the alkene chain.

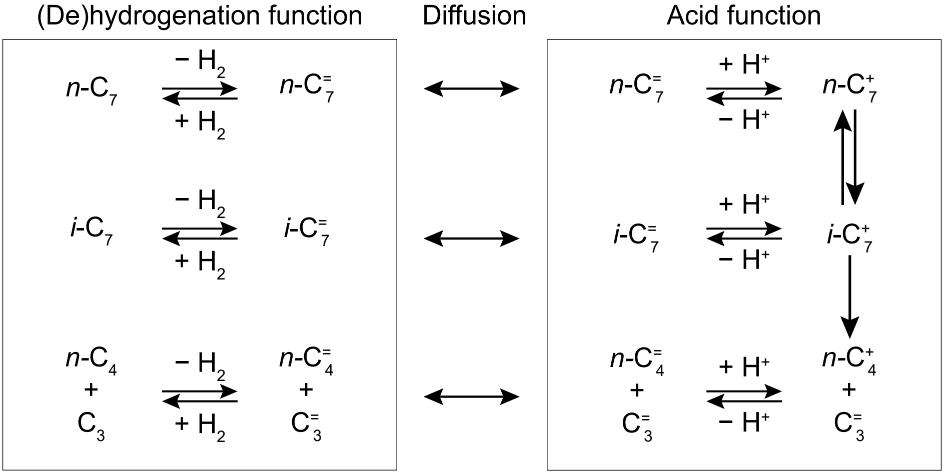

Figure 1.4. The bifunctional mechanism explained using the example of *n*-heptane (*n*-C_7) hydroconversion. Linear alkanes are depicted with '*n*-', branched alkanes are denoted with '*i*-'. The superscripts '+' and '=' denote carbenium ions and alkenes, respectively. Figure adapted from C. Bouchy et al.[17]

The resulting *i*-alkene intermediate may desorb from the acid site and diffuse to a metal site to be hydrogenated to form the saturated *i*-alkane. However, successive reactions on the Brønsted acid site may also occur, which could eventually lead to cracking via β-scission.[89,90] During β-scission, alkylcarbenium ions act as intermediates. Tertiary carbenium ions are the most thermodynamically stable, followed by secondary carbenium ions. As a consequence, cracking of alkenes with multiple branches is fast, resulting in the formation of lighter alkenes that are subsequently hydrogenated towards alkanes. The formation of primary carbenium ions is unfavorable and, in principle, does not take place.[91–93]

Hydrogen has two functions during the hydroconversion process: it is used to saturate (cracked) hydrocarbons towards alkanes, and it prevents the formation of coke, i.e., high molecular weight hydrocarbons that may deactivate the catalyst,[46,94] a major advantage over monofunctional catalytic cracking. Other benefits of hydroconversion with bifunctional catalysis over monofunctional acid alternatives are the milder reaction conditions, e.g. at lower temperatures, and the possibility to control the product distributions with the operating conditions.[73,95] Furthermore, bifunctional catalysts are more selective than monofunctional acid catalysts.[73,94,95]

For preferential hydroisomerization of long chain alkanes, zeolites and zeotypes with unidimensional pores of medium size consisting of 10-membered rings are beneficial.[96–99] ZSM-22 and SAPO-11 are examples of solid acids with these textural properties. The high selectivity towards isomers is attributed to acid catalysis taking place in the pore mouths of the zeolites.[96–101] Pore-mouth catalysis is based on the fact that a hydrocarbon molecule does not need to diffuse fully inside the zeolite pores, but rather adsorbs in the pore entrance where it can react with the zeolite acid sites. This leads to preferential branching at terminal C atoms. Furthermore, hydrocarbons with longer chain lengths can adsorb in multiple pore mouths, in a so-called key-lock mode,[100,102] which in turn can explain branching at more central carbon atoms. Schematics explaining pore mouth and key-lock adsorption are shown in Figure 1.5.

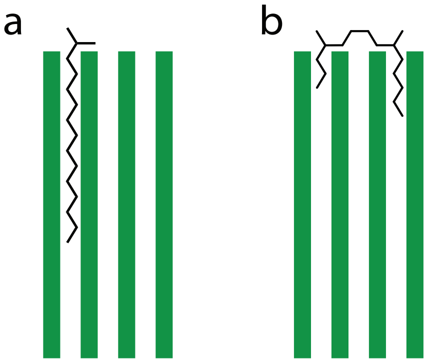

Figure 1.5. Schematic representations of examples of a) pore mouth adsorption, and b) key-lock adsorption of branched hexadecane molecules in unidimensional zeolite/zeotype pores. Micropore walls are drawn in green.

Next to the zeolite pore size and -dimensionality, the zeolite acidity and its balance with the DHD/HD functionality play a key role in bifunctional catalysis. Therefore, the metal-to-acid site (n_M/n_A) ratio is an important factor determining whether or not the bifunctional catalyst is "ideal".[103,104] In an "ideal" bifunctional catalyst the DHD/HD reactions are at thermodynamic equilibrium[104] and the acid-catalyzed reactions are rate-determining.[95,105,106] Already in 1987, Guisnet and co-workers found that catalysts with higher n_M/n_A display higher selectivities towards isomers.[105] Later it was found that even heterogeneities in metal loading and hence n_M/n_A at the nanoscale can impact the catalytic performance in a bifunctional catalysts.[107] It is generally accepted[103,108–110] that the location of the active sites with respect to each other seems to play a key role in bifunctional catalysis.

1.6. Location of Active Sites

There are three key performance criteria that determine the quality of a catalyst: activity, selectivity and stability. In turn, these are largely determined by the density, nature and accessibility of the active sites.[111] Additionally, many of the elements used in solid catalysts are relatively scarce[112] and it is desirable to use all material as efficiently as possible. Rational design of the catalyst helps improving the catalytic performance and prevents the use of excess materials. Multiple studies show that nanoparticle size,[39,43,113,114] nanoparticle composition,[115–117] and metal-support interactions[118–120] can be tweaked for optimal catalytic performance. Optimal use of the available materials in catalysis is traditionally attained by increased metal dispersion, even to the level of single atom catalysts (SAC).[121–123]

Furthermore, the location of the active sites can have a large impact on the performance of the catalyst. In a monofunctional catalyst, location is related to interparticle distance. Prieto et al.[42] showed that maximizing the spacing between Cu nanoparticles greatly increased the catalyst stability during methanol synthesis. In a bifunctional catalyst, the location of the two different active sites with respect to each other − also referred to as the intimacy between active sites or inter-site proximity – can affect the catalytic performance.

Paul Weisz was the first scientist to study the effect of the inter-site proximity in bifunctional catalysts for hydroconversion reactions.[124,125] He demonstrated this effect at the microscale by physically mixing Pt/SiO_2 or Pt/C with silica-alumina in a 50:50 volume ratio.[126] The intimacy between the supported Pt catalyst and silica-alumina was varied by varying the individual particle sizes: both individual catalysts had a particle size of 1000 µm, 70 µm or 5 µm. Furthermore, a catalyst was prepared by impregnation of Pt onto a silica-alumina support, thus preparing a catalyst with the closest proximity between the active sites. During hydroconversion of *n*-heptane, decreasing the catalyst particle diameters, and hence increasing the proximity of active sites, led to improved selectivity towards heptane isomers. The highest *i*-heptane yield was obtained with the impregnated catalyst. As a result, 'the closer the better' was taken for granted for metal-acid catalysts for a long time.[127,128]

More recently, by controlling Pt nanoparticle location at the nanoscale instead of at the microscale, Zečević et al.[129] found that closer does not necessarily mean better. Two catalysts consisting of ultrastable Y zeolite, Pt nanoparticles, and γ-alumina binder were prepared. The catalysts differed in Pt nanoparticle location: the nanoparticles were placed either on/in the zeolite Y crystals or on the γ-alumina binder, as schematically depicted in Figure 1.6. This meant that Pt and acid sites were either in closest proximity, or at nanoscale proximity, respectively. The catalysts with Pt nanoparticles on the binder outperformed the ones with Pt on zeolite Y in terms of selectivity towards isomers during hydroconversion of alkanes. Processes focusing on hydroconversion of long hydrocarbon molecules derived from XTL processes may benefit from this finding.

The impact of the metal nanoparticle location on the selectivity has been studied for several zeolite systems,[129–131] all showing that emplacing Pt nanoparticles in the zeolite can be detrimental for the catalyst selectivity. When mesoporous solid acids were applied, however, no clear difference in catalytic performance was observed.[132] The nanoscale proximity effects are therefore specific to microporous zeolite and zeotype systems. It is hypothesized that these selectivity differences can be attributed to anisotropic diffusion of *i*-alkene intermediates from zeolite acid sites to metal sites. When the metal sites are outside the zeolite crystals, the *i*-alkene is formed in the zeolite pore mouth and can diffuse fast towards the metal site to undergo hydrogenation and form the final *i*-alkane product whereas diffusion deeper into the pores is slow. However, when the metal sites are inside the zeolite crystals, dehydrogenation and subsequent isomerization are more likely to occur inside the micropores, followed by slow diffusion through the pores of zeolites. This slow diffusion might result in the occurrence of multiple reactions on zeolite acid sites, eventually leading to cracking. Figure 1.7 shows a schematic representation of both of these pathways.

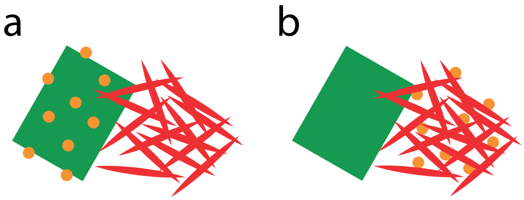

Figure 1.6. Schematic representation of the catalysts prepared and studied by Zečević et al.[129] a) Pt-zeolite Y/γ-Al_2O_3 with Pt nanoparticles in zeolite Y, and b) Pt-γ-Al_2O_3/zeolite Y with Pt on the γ-Al_2O_3 binder material. The Pt nanoparticles (~3 nm), zeolite Y crystal (~500 nm) and γ-Al_2O_3 binder material are drawn as yellow circles, green rectangles and red needles, respectively.

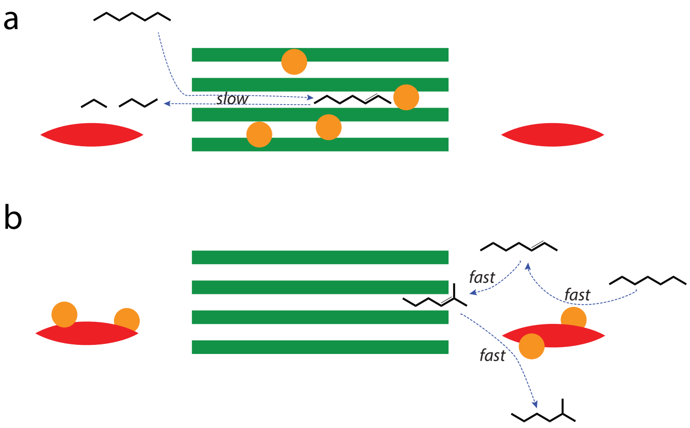

Figure 1.7. Schematic representation of the hydroconversion of *n*-heptane over a) a Pt-zeolite/γ-Al_2O_3 (Pt in zeolite) catalyst, with slow diffusion within the zeolite micropores, and b) a Pt-γ-Al_2O_3/zeolite catalyst, with fast diffusion through the binder macropores and pore-mouth adsorption of the olefin intermediate. The zeolite is drawn in green and possesses a unidimensional micropore structure. The metal nanoparticles and alumina binder are depicted as yellow circles and red needles, respectively.

1.7. Scope of this Thesis

The goal of the research described in this thesis was to study the amount of noble metals required in bifunctional catalysts for hydroconversion by tuning the nanoparticle location, without compromising the catalytic performance. The catalysts that were studied each contained three main components: (noble) metal (oxide) nanoparticles, zeolite or zeotype material, and a binder.

In **Chapter 2** a new tool for controlling the metal nanoparticle location in Pd/zeolite and Pd/zeotype catalysts is described. We show that performing a direct reduction (DR) on ammonium palladate exchanged zeolites/zeotypes results in enrichment of Pd on the outer surface of the solid acid crystallites, whereas slow calcination followed by reduction (CR) resulted in more Pd nanoparticles being confined inside the zeotype crystallites.

The focus in **Chapter 3** is on the minimum amount of platinum required as function of Pt nanoparticle location. Two sets of catalysts were prepared: one set was based on mordenite and the other one on ZSM-22. In the set with mordenite the Pt nanoparticles were either inside the mordenite crystallites or on alumina binder. The ZSM-22 set had the Pt nanoparticles either on the ZSM-22 crystallites or on the alumina binder. Pt weight loadings of 0.005 to 0.5 wt% were used. At loadings of 0.01 wt% catalysts with Pt on alumina binder were much less active. Extensive characterization revealed that this was a result of strong metal-support interaction of the Pt clusters with alumina.

Since the lower catalytic performance of Pt-on-alumina with ≤ 0.01 wt% Pt loadings in Chapter 3 was a result of γ-alumina lacking chemical inertness, we explored the replacement of this binder by silica in **Chapter 4**. Catalysts with 0.005 to 0.5 wt% Pt on ZSM-22 or on silica were prepared and characterized. These catalysts were then applied in the hydroconversion of *n*-heptane. Moreover, for the first time the effect of the low loadings on the catalytic performance during *n*-hexadecane was assessed.

Diminishing noble metal utilization could also mean replacement with earth abundant metals. **Chapter 5** is dedicated to an exploration of nickel based bifunctional catalysts for hydroconversion. We show that Ni based catalysts typically display high hydrogenolysis activity to produce mainly methane. However, the combination of the use of *n*-alkanes with higher molecular weight (e.g. *n*-hexadecane) and emplacing Ni (oxide) nanoparticles at the right place could reduce hydrogenolysis activity and improve *i*-hexadecane selectivity.

Lastly, **Chapter 6** provides a summary & outlook and ‘een Nederlandse samenvatting’ (Dutch summary).

References

(1) Energy Institute. *Statistical Review of World Energy 2023*, 72nd ed.; 2023.

(2) Le, T.-H.; Chang, Y.; Park, D. Renewable and Nonrenewable Energy Consumption, Economic Growth, and Emissions: International Evidence. *Energy J.* **2020**, *41* (2), 73–92.

(3) Energy Institute Statistical Review of World Energy 2023 Energy Charting Tool https://www.energyinst.org/statistical-review/energy-charting-tool/energy-charting-tool (accessed Sep 7, 2023).

(4) Calvin, K.; Dasgupta, D.; Krinner, G.; Mukherji, A.; Thorne, P. W.; Trisos, C.; Romero, J.; Aldunce, P.; Barrett, K.; Blanco, G.; Cheung, W. W. L.; Connors, S.; Denton, F.; Diongue-Niang, A.; Dodman, D.; Garschagen, M.; Geden, O.; Hayward, B.; Jones, C.; Jotzo, F.; Krug, T.; Lasco, R.; Lee, Y.-Y.; Masson-Delmotte, V.; Meinshausen, M.; Mintenbeck, K.; Mokssit, A.; Otto, F. E. L.; Pathak, M.; Pirani, A.; Poloczanska, E.; Pörtner, H.-O.; Revi, A.; Roberts, D. C.; Roy, J.; Ruane, A. C.; Skea, J.; Shukla, P. R.; Slade, R.; Slangen, A.; Sokona, Y.; Sörensson, A. A.; Tignor, M.; van Vuuren, D.; Wei, Y.-M.; Winkler, H.; Zhai, P.; Zommers, Z.; Hourcade, J.-C.; Johnson, F. X.; Pachauri, S.; Simpson, N. P.; Singh, C.; Thomas, A.; Totin, E.; Alegría, A.; Armour, K.; Bednar-Friedl, B.; Blok, K.; Cissé, G.; Dentener, F.; Eriksen, S.; Fischer, E.; Garner, G.; Guivarch, C.; Haasnoot, M.; Hansen, G.; Hauser, M.; Hawkins, E.; Hermans, T.; Kopp, R.; Leprince-Ringuet, N.; Lewis, J.; Ley, D.; Ludden, C.; Niamir, L.; Nicholls, Z.; Some, S.; Szopa, S.; Trewin, B.; van der Wijst, K.-I.; Winter, G.; Witting, M.; Birt, A.; Ha, M. *IPCC, 2023: Climate Change 2023: Synthesis Report. Contribution of Working Groups I, II and III to the Sixth Assessment Report of the Intergovernmental Panel on Climate Change [Core Writing Team, H. Lee and J. Romero (Eds.)]. IPCC, Geneva, Switzerland.*; Arias, P., Bustamante, M., Elgizouli, I., Flato, G., Howden, M., Méndez-Vallejo, C., Pereira, J. J., Pichs-Madruga, R., Rose, S. K., Saheb, Y., Sánchez Rodríguez, R., Ürge-Vorsatz, D., Xiao, C., Yassaa, N., Romero, J., Kim, J., Haites, E. F., Jung, Y., Stavins, R., Birt, A., Ha, M., Orendain, D. J. A., Ignon, L., Park, S., Park, Y., Reisinger, A., Cammaramo, D., Fischlin, A., Fuglestvedt, J. S., Hansen, G., Ludden, C., Masson-Delmotte, V., Matthews, J. B. R., Mintenbeck, K., Pirani, A., Poloczanska, E., Leprince-Ringuet, N., Péan, C., Eds.; 2023.

(5) *EPA (2023) Inventory of U.S. Greenhouse Gas Emissions and Sinks: 1990-2021. U.S. Environmental Protection Agency, EPA 430-R-23-002*.

(6) Friedemann, A. J. *Life after Fossil Fuels*; Lecture Notes in Energy; Springer International Publishing: Cham, 2021; Vol. 81.

(7) Holechek, J. L.; Geli, H. M. E.; Sawalhah, M. N.; Valdez, R. A Global Assessment: Can Renewable Energy Replace Fossil Fuels by 2050? *Sustain.* **2022**, *14* (8), 1–22.

(8) Chorkendorff, I.; Niemantsverdriet, J. W. *Concepts of Modern Catalysis and Kinetics*, 3rd ed.; WILEY-VCH Verlag GmbH & Co. KGaA: Weinheim, 2017.

(9) Hanefeld, U.; Lefferts, L. *Catalysis, An Integrated Textbook for Students*; WILEY-VCH Verlag GmbH & Co. KGaA: Weinheim, Germany, 2018.

(10) de Klerk, A.; Furimsky, E. *Catalysis in the Refining of Fischer-Tropsch Syncrude*, 1st ed.; Royal Society of Chemistry: Cambridge, 2010.

(11) King, D. L.; De Klerk, A. Overview of Feed-to-Liquid (XTL) Conversion. In *ACS Symposium Series*; 2011; Vol. 1084, pp 1–24.

(12) Sousa-Aguiar, E. F.; Noronha, F. B.; Faro, A. The Main Catalytic Challenges in GTL (Gas-to-Liquids) Processes. *Catal. Sci. Technol.* **2011**, *1* (5), 698–713.

(13) Aasberg-Petersen, K.; Christensen, T. S.; Dybkjær, I.; Sehested, J.; Østberg, M.; Coertzen, R. M.; Keyser, M. J.; Steynberg, A. P. Synthesis Gas Production for FT Synthesis. *Stud. Surf. Sci. Catal.* **2004**, *152*, 258–405.

(14) Mondal, P.; Dang, G. S.; Garg, M. O. Syngas Production through Gasification and Cleanup for Downstream Applications - Recent Developments. *Fuel Process. Technol.* **2011**, *92* (8), 1395–1410.

(15) de Klerk, A. Transport Fuel: Biomass-, Coal-, Gas- and Waste-to-Liquids Processes. In *Future Energy: Improved, Sustainable and Clean Options for Our Planet*; Elsevier Ltd, 2020; pp 199–226.

(16) Suárez París, R.; L'Abbate, M. E.; Liotta, L. F.; Montes, V.; Barrientos, J.; Regali, F.; Aho, A.; Boutonnet, M.; Järås, S. Hydroconversion of Paraffinic Wax over Platinum and Palladium Catalysts Supported on Silica–Alumina. *Catal. Today* **2016**, *275*, 141–148.

(17) Bouchy, C.; Hastoy, G.; Guillon, E.; Martens, J. A. Fischer-Tropsch Waxes Upgrading via Hydrocracking and Selective Hydroisomerization. *Oil Gas Sci. Technol.* **2009**, *64* (1), 91–112..

(18) Swain, P. K.; Das, L. M.; Naik, S. N. Biomass to Liquid: A Prospective Challenge to Research and Development in 21st Century. *Renew. Sustain. Energy Rev.* **2011**, *15* (9), 4917–4933.

(19) Liu, D.; Chen, E. Y. X. Integrated Catalytic Process for Biomass Conversion and Upgrading to C 12 Furoin and Alkane Fuel. *ACS Catalysis*. 2014, pp 1302–1310.

(20) Thaker, A. H.; John, M.; Kumar, K.; Kasture, M. W.; Parmar, S.; Newalkar, B. L.; Parikh, P. A. Hydroisomerization of Biomass Derived N-Hexadecane Towards Diesel Pool: Effect of Selective Removal External Surface Sites from Pt/ZSM-22. *Int. J. Chem. React. Eng.* **2016**, *14* (1), 155–165.

(21) Onel, O.; Niziolek, A. M.; Hasan, F. M. F.; Floudas, C. A. Municipal Solid Waste to Liquid Transportation Fuels - Part I: Mathematical Modeling of a Municipal Solid Waste Gasifier. *Comput. Chem. Eng.* **2014**, *71*, 636–647.

(22) Niziolek, A. M.; Onel, O.; Hasan, M. M. F.; Floudas, C. A. Municipal Solid Waste to Liquid Transportation Fuels - Part II: Process Synthesis and Global Optimization Strategies. *Comput. Chem. Eng.* **2015**, *74*, 184–203.

(23) Sharma, V.; Kalam Hossain, A.; Griffiths, G.; Duraisamy, G.; Krishnasamy, A.; Ravikrishnan, V.; Ricardo Sodré, J. Plastic Waste to Liquid Fuel: A Review of Technologies, Applications, and Challenges. *Sustain. Energy Technol. Assessments* **2022**, *53*, 102651.

(24) Geri, J. B.; Wade Wolfe, M. M.; Szymczak, N. K. Borazine-CF3−Adducts for Rapid, Room Temperature, and Broad Scope Trifluoromethylation. *Angew. Chemie - Int. Ed.* **2018**, *57* (5), 1381–1385.

(25) Shahabuddin, M.; Alam, M. T.; Krishna, B. B.; Bhaskar, T.; Perkins, G. A Review on the Production of Renewable Aviation Fuels from the Gasification of Biomass and Residual Wastes. *Bioresour. Technol.* **2020**, *312* (May), 123596.

(26) Generation of waste by waste category https://ec.europa.eu/eurostat/databrowser/view/env_wasgen/default/table?lang=en (accessed Sep 5, 2023).

(27) eurostat Waste Statistics https://ec.europa.eu/eurostat/statistics-explained/index.php?title=Waste_statistics (accessed Oct 6, 2023).

(28) Kaza, S.; Yao, L. C.; Bhada-Tata, P.; Van Woerden, F. *What a Waste 2.0: A Global Snapshot of Solid Waste Management to 2050*; Washington, DC: World Bank, 2018.

(29) Galadima, A.; Muraza, O. Waste to Liquid Fuels: Potency, Progress and Challenges. *Int. J. Energy Res.* **2015**, *39* (11), 1451–1478.

(30) Niziolek, A. M.; Onel, O.; Floudas, C. A. Municipal Solid Waste to Liquid Transportation Fuels, Olefins, and Aromatics: Process Synthesis and Deterministic Global Optimization. *Comput. Chem. Eng.* **2017**, *102*, 169–187.

(31) Kraan, O.; Kramer, G. J.; Haigh, M.; Laurens, C. An Energy Transition That Relies Only on Technology Leads to a Bet on Solar Fuels. *Joule* **2019**, *3* (10), 2286–2290.

(32) Niziolek, A. M.; Onel, O.; Tian, Y.; Floudas, C. A.; Pistikopoulos, E. N. Municipal Solid Waste to Liquid Transportation Fuels – Part III: An Optimization-Based Nationwide Supply Chain Management Framework. *Comput. Chem. Eng.* **2018**, *116*, 468–487.

(33) Detz, R. J.; Ferchaud, C. J.; Kalkman, A. J.; Kemper, J.; Sánchez-Martínez, C.; Saric, M.; Shinde, M. V. Electrochemical CO 2 Conversion Technologies: State-of-the-Art and Future Perspectives. *Sustain. Energy Fuels* **2023**.

(34) Fulcrum BioFuel Plant https://www.fulcrum-bioenergy.com/ (accessed Sep 6, 2023).

(35) Unnasch, S. *Life Cycle GHG Emissions For Fulcrum Sierra BioFuels, LLC ’s MSW-to-Fischer Tropsch Fuel Production Process*; 2015.

(36) Rothenberg, G. *Catalysis, Concepts and Green Applications*; WILEY-VCH Verlag GmbH & Co. KGaA: Weinheim, Germany, 2008.

(37) de Jong, K. P. *Synthesis of Solid Catalysts*; WILEY-VCH Verlag GmbH & Co. KGaA: Weinheim, Germany, 2009.

(38) Khodakov, A. Y.; Chu, W.; Fongarland, P. Advances in the Development of Novel Cobalt Fischer-Tropsch Catalysts for Synthesis of Long-Chain Hydrocarbons and Clean Fuels. *Chem. Rev.* **2007**, *107* (5), 1692–1744.

(39) Xie, J.; Torres Galvis, H. M.; Koeken, A. C. J.; Kirilin, A.; Dugulan, A. I.; Ruitenbeek, M.; De Jong, K. P. Size and Promoter Effects on Stability of Carbon-Nanofiber-Supported Iron-Based Fischer-Tropsch Catalysts. *ACS Catal.* **2016**, *6* (6), 4017–4024..

(40) van den Berg, R.; Parmentier, T. E.; Elkjær, C. F.; Gommes, C. J.; Sehested, J.; Helveg, S.; de Jongh, P. E.; de Jong, K. P. Support Functionalization To Retard Ostwald Ripening in Copper Methanol Synthesis Catalysts. *ACS Catal.* **2015**, *5* (7), 4439–4448.

(41) van den Berg, R.; Prieto, G.; Korpershoek, G.; van der Wal, L. I.; van Bunningen, A. J.; Lægsgaard-Jørgensen, S.; de Jongh, P. E.; de Jong, K. P. Structure Sensitivity of Cu and CuZn Catalysts Relevant to Industrial Methanol Synthesis. *Nat. Commun.* **2016**, *7* (1), 13057.

(42) Prieto, G.; Zečević, J.; Friedrich, H.; De Jong, K. P.; De Jongh, P. E. Towards Stable Catalysts by Controlling Collective Properties of Supported Metal Nanoparticles. *Nat. Mater.* **2013**, *12* (1), 34–39.

(43) Brandt Corstius, O. E.; van der Hoeven, J. E. S.; Sunley, G. J.; de Jongh, P. E. Influence of Particle Size in Pd-Catalysed Selective Hydrogenation of 1,3-Butadiene. *J. Catal.* **2023**, *427*, 115103.

(44) Wei, X.; Cheng, J.; Li, Y.; Cheng, K.; Sun, F.; Zhang, Q.; Wang, Y. Bimetallic Clusters Confined inside Silicalite-1 for Stable Propane Dehydrogenation. *Nano Res.* **2023**, *16* (8), 10881–10889.

(45) Bariås, O. A.; Holmen, A.; Blekkan, E. A. Propane Dehydrogenation over Supported Pt and Pt-Sn Catalysts: Catalyst Preparation, Characterization, and Activity Measurements. *J. Catal.* **1996**, *158* (1), 1–12.

(46) Vogt, E. T. C.; Whiting, G. T.; Dutta Chowdhury, A.; Weckhuysen, B. M. Zeolites and Zeotypes for Oil and Gas Conversion. *Adv. Catal.* **2015**, *58*, 143–314.

(47) Corma, A. Transformation of Hydrocarbons on Zeolite Catalysts. *Catal. Letters* **1993**, *22* (1–2), 33–52.

(48) Busca, G. Silica-Alumina Catalytic Materials: A Critical Review. *Catal. Today* **2020**, *357*, 621–629.

(49) Cronstedt, A. F. Rön Och Beskrifning Om En Obekant Bärg Art, Som Kallas Zeolites. *Kongl. Vetenskaps. Acad. Handl. Stock.* **1756**, *17*, 120.

(50) *Zeolites and Catalysis, Synthesis, Reactions and Applications. Vol. 1*; Čejka, J., Corma, A., Zones, S. I., Eds.; WILEY-VCH Verlag GmbH & Co. KGaA: Weinheim, Germany, 2010.

(51) *Zeolites and Catalyis, Synthesis, Reactions and Applications. Vol. 2*; Čejka, J., Corma, A., Zones, S. I., Eds.; WILEY-VCH Verlag GmbH & Co. KGaA: Weinheim, Germany, 2010.

(52) Cundy, C. S.; Cox, P. A. The Hydrothermal Synthesis of Zeolites: History and Development from the Earliest Days to the Present Time. *Chem. Rev.* **2003**, *103* (3), 663–701.

(53) Chizallet, C.; Bouchy, C.; Larmier, K.; Pirngruber, G. Molecular Views on Mechanisms of Brønsted Acid-Catalyzed Reactions in Zeolites. *Chem. Rev.* **2023**, *123* (9), 6107–6196.

(54) Breck, D. W. Crystalline Molecular Sieves. *J. Chem. Educ.* **1964**, *41* (12), 678.

(55) Corma, A. Inorganic Solid Acids and Their Use in Acid-Catalyzed Hydrocarbon Reactions. *Chem. Rev.* **1995**, *95* (3), 559–614.

(56) International Zeolite Association - Database of Zeolite Structures https://europe.iza-structure.org/IZA-SC/ftc_table.php (accessed Sep 7, 2023).

(57) Lok, B. M.; Messina, C. A.; Patton, R. L.; Gajek, R. T.; Cannan, T. R.; Flanigen, E. M. Silicoaluminophosphate Molecular Sieves: Another New Class of Microporous Crystalline Inorganic Solids. *J. Am. Chem. Soc.* **1984**, *106* (20), 6092–6093.

(58) Barthomeuf, D. Topological Model for the Compared Acidity of SAPOs and SiAl Zeolites. *Zeolites* **1994**, *14* (6), 394–401.

(59) Weitkamp, J. Zeolites and Catalysis. *Solid State Ionics* **2000**, *131* (1–2), 175–188.

(60) Tran, N. H.; Bartlett, J. R.; Kannangara, G. S. K.; Milev, A. S.; Volk, H.; Wilson, M. A. Catalytic Upgrading of Biorefinery Oil from Micro-Algae. *Fuel* **2010**, *89* (2), 265–274.

(61) Peng, B.; Yao, Y.; Zhao, C.; Lercher, J. A. Towards Quantitative Conversion of Microalgae Oil to Diesel-Range Alkanes with Bifunctional Catalysts. *Angew. Chemie - Int. Ed.* **2012**, *51* (9), 2072–2075.

(62) Mäki-Arvela, P.; Martínez-Klimov, M.; Murzin, D. Y. Hydroconversion of Fatty Acids and Vegetable Oils for Production of Jet Fuels. *Fuel* **2021**, *306*.

(63) Kots, P. A.; Vance, B. C.; Vlachos, D. G. Polyolefin Plastic Waste Hydroconversion to Fuels, Lubricants, and Waxes: A Comparative Study. *React. Chem. Eng.* **2022**, *7* (1), 41–54.

(64) Sivagami, K.; Kumar, K. V.; Tamizhdurai, P.; Govindarajan, D.; Kumar, M.; Nambi, I. Conversion of Plastic Waste into Fuel Oil Using Zeolite Catalysts in a Bench-Scale Pyrolysis Reactor. *RSC Adv.* **2022**, *12* (13), 7612–7620.

(65) Daligaux, V.; Richard, R.; Manero, M.-H. Deactivation and Regeneration of Zeolite Catalysts Used in Pyrolysis of Plastic Wastes—A Process and Analytical Review. *Catalysts* **2021**, *11* (7), 770.

(66) Liu, S.; Kots, P. A.; Vance, B. C.; Danielson, A.; Vlachos, D. G. Plastic Waste to Fuels by Hydrocracking at Mild Conditions. *Sci. Adv.* **2021**, *7* (17), 1–10.

(67) Salazar, M.; Becker, R.; Grünert, W. Hybrid Catalysts-an Innovative Route to Improve Catalyst Performance in the Selective Catalytic Reduction of NO by NH3. *Appl. Catal. B Environ.* **2015**, *165*, 316–327.

(68) Kanai, M.; Beller, M. Introduction to Hybrid Catalysis. *Org. Biomol. Chem.* **2021**, *19* (4), 702–704.

(69) Gianotti, E.; Diaz, U.; Velty, A.; Corma, A. Designing Bifunctional Acid–Base Mesoporous Hybrid Catalysts for Cascade Reactions. *Catal. Sci. Technol.* **2013**, *3* (10), 2677.

(70) Fogg, D. E.; Dos Santos, E. N. Tandem Catalysis: A Taxonomy and Illustrative Review. *Coord. Chem. Rev.* **2004**, *248* (21–24), 2365–2379.

(71) Lohr, T. L.; Marks, T. J. Orthogonal Tandem Catalysis. *Nat. Chem.* **2015**, *7* (6), 477–482.

(72) Chang, F.; Vis, C. M.; Bergmeijer, M.; Howes, S. C.; Bruijnincx, P. C. A. Bifunctional Janus Silica Spheres for Pickering Interfacial Tandem Catalysis. *ChemSusChem* **2021**, *14* (23), 5328–5335.

(73) Mirena, J. I.; Thybaut, J. W.; Marin, G. B.; Martens, J. A.; Galvita, V. V. Impact of the Spatial Distribution of Active Material on Bifunctional Hydrocracking. *Ind. Eng. Chem. Res.* **2021**.

(74) Henry, R.; Tayakout-Fayolle, M.; Afanasiev, P.; Lorentz, C.; Lapisardi, G.; Pirngruber, G. Vacuum Gas Oil Hydrocracking Performance of Bifunctional Mo/Y Zeolite Catalysts in a Semi-Batch Reactor. *Catal. Today* **2014**, *220–222*, 159–167.

(75) Pirngruber, G. D.; Maury, S.; Daudin, A.; Alspektor, P. Y.; Bouchy, C.; Guillon, E. Balance between (De)Hydrogenation and Acid Sites: Comparison between Sulfide-Based and Pt-Based Bifunctional Hydrocracking Catalysts. *Ind. Eng. Chem. Res.* **2020**, *59* (28), 12686–12695.

(76) Martínez, C.; Corma, A. Inorganic Molecular Sieves: Preparation, Modification and Industrial Application in Catalytic Processes. *Coordination Chemistry Reviews*. 2011, pp 1558–1580.

(77) Hur, Y. G.; Kim, M. S.; Lee, D. W.; Kim, S.; Eom, H. J.; Jeong, G.; No, M. H.; Nho, N. S.; Lee, K. Y. Hydrocracking of Vacuum Residue into Lighter Fuel Oils Using Nanosheet-Structured WS2 Catalyst. *Fuel* **2014**, *137*, 237–244.

(78) Ledoux, M. J.; Pham-Huu, C.; Dunlop, H.; Guille, J. N-Hexane Isomerization on High Specific Surface Mo2C Activated by an Oxidative Treatment. *Stud. Surf. Sci. Catal.* **1993**, *75* (C), 955–967.

(79) Harmel, J.; Roberts, T.; Zhang, Z.; Sunley, G.; de Jongh, P.; de Jong, K. P. Bifunctional Molybdenum Oxide/Acid Catalysts for Hydroisomerization of n-Heptane. *J. Catal.* **2020**, *390*, 161–169.

(80) Ledoux, M. J.; Del Gallo, P.; Pham-Huu, C.; York, A. P. E. Molybdenum Oxycarbide Isomerization Catalysts for Cleaner Fuel Production. *Catal. Today* **1996**, *27* (1–2), 145–150.

(81) Roy, S.; Bouchy, C.; Pham-Huu, C.; Crouzet, C.; Ledoux, M. J. Slurry Isomerization of N-Hexadecane over MoO3-Carbon-Modified, Pt/β-Zeolite, Pt/ZSM-22 and Pt/SAPO-11 Catalysts at Medium Pressure. *Stud. Surf. Sci. Catal.* **2000**, *130*, 2423–2428.

(82) Kim, J.; Han, S. W.; Kim, J. C.; Ryoo, R. Supporting Nickel to Replace Platinum on Zeolite Nanosponges for Catalytic Hydroisomerization of n -Dodecane. *ACS Catal.* **2018**, *8* (11), 10545–10554.

(83) Martens, J. A.; Verboekend, D.; Thomas, K.; Vanbutsele, G.; Gilson, J. P.; Pérez-Ramírez, J. Hydroisomerization of Emerging Renewable Hydrocarbons Using Hierarchical Pt/H-ZSM-22 Catalyst. *ChemSusChem* **2013**, *6* (3), 421–425.

(84) Höchtl, M.; Jentys, A.; Vinek, H. Hydroisomerization of Heptane Isomers over Pd/SAPO Molecular Sieves: Influence of the Acid and Metal Site Concentration and the Transport Properties on the Activity and Selectivity. *J. Catal.* **2000**, *190* (2), 419–432.

(85) Höchtl, M.; Jentys, A.; Vinek, H. Alkane Conversion over Pd/SAPO Molecular Sieves: Influence of Acidity, Metal Concentration and Structure. *Catal. Today* **2001**, *65* (2–4), 171–177.

(86) Coonradt, H. L.; Garwood, W. E. Mechanism of Hydrocracking. *Ind. Eng. Chem. Process Des. Dev.* **1964**, *3* (1), 38–45.

(87) Weitkamp, J. Isomerization of Long-Chain n-Alkanes on a Pt/CaY Zeolite Catalyst. *Ind. Eng. Chem. Prod. Res. Dev.* **1982**, *21* (4), 550–558.

(88) Jacobs, P. A.; Martens, J. A.; Weitkamp, J.; Beyer, H. K. Shape-Selectivity Changes in High-Silica Zeolites. *Faraday Discuss. Chem. Soc.* **1981**, *72*, 353.

(89) Weitkamp, J.; Jacobs, P. A.; Martens, J. A. Isomerization and Hydrocracking of C9 through C16 N-Alkanes on Pt/HZSM-5 Zeolite. *Appl. Catal.* **1983**, *8* (1), 123–141.

(90) Weitkamp, J. Catalytic Hydrocracking—Mechanisms and Versatility of the Process. *ChemCatChem* **2012**, *4* (3), 292–306.

(91) Martens, J. A.; Jacobs, P. A.; Weitkamp, J. Attempts to Rationalize the Distribution of Hydrocracked Products. I Qualitative Description of the Primary Hydrocracking Modes of Long Chain Paraffins in Open Zeolites. *Appl. Catal.* **1986**, *20* (1–2), 239–281.

(92) Martens, J. A.; Jacobs, P. A.; Weitkamp, J. Attempts to Rationalize the Distribution of Hydrocracked Products. II. Relative Rates of Primary Hydrocracking Modes of Long Chain Paraffins in Open Zeolites. *Appl. Catal.* **1986**, *20* (1–2), 283–303.

(93) Martens, J. A.; Tielen, M.; Jacobs, P. A. Attempts to Rationalize the Distribution of Hydrocracked Products. III. Mechanistic Aspects of Isomerization and Hydrocracking of Branched Alkanes on Ideal Bifunctional Large-Pore Zeolite Catalysts. *Catal. Today* **1987**, *1* (4),

(94) Sartipi, S.; Makkee, M.; Kapteijn, F.; Gascon, J. Catalysis Engineering of Bifunctional Solids for the One-Step Synthesis of Liquid Fuels from Syngas: A Review. *Catal. Sci. Technol.* **2014**, *4* (4), 893–907.

(95) Guisnet, M. "Ideal" Bifunctional Catalysis over Pt-Acid Zeolites. *Catal. Today* **2013**, *218–219*, 123–134.

(96) Mériaudeau, P.; Tuan, V. A.; Nghiem, V. T.; Lai, S. Y.; Hung, L. N.; Naccache, C. SAPO-11, SAPO-31, and SAPO-41 Molecular Sieves: Synthesis, Characterization, and Catalytic Properties in n-Octane Hydroisomerization. *J. Catal.* **1997**, *169* (1), 55–66.

(97) Mériaudeau, P.; Tuan, V. A.; Sapaly, G.; Nghiem, V. T.; Naccache, C. Pore Size and Crystal Size Effects on the Selective Hydroisomerisation of C8 Paraffins over Pt-Pd/SAPO-11, Pt-Pd/SAPO-41 Bifunctional Catalysts. *Catal. Today* **1999**, *49* (1–3), 285–292.

(98) Nghiem, V. T.; Sapaly, G.; Mériaudeau, P.; Naccache, C. Monodimensional Tubular Medium Pore Molecular Sieves for Selective Hydroisomerisation of Long Chain Alkanes: N-Octane Reaction on ZSM and SAPO Type Catalysts. *Top. Catal.* **2000**, *14* (1–4), 131–138.

(99) Sastre, G.; Chica, A.; Corma, A. On the Mechanism of Alkane Isomerisation (Isodewaxing) with Unidirectional 10-Member Ring Zeolites. A Molecular Dynamics and Catalytic Study. *J. Catal.* **2000**, *195* (2), 227–236.

(100) Martens, J. A.; Vanbutsele, G.; Jacobs, P. A.; Denayer, J.; Ocakoglu, R.; Baron, G.; Muñoz Arroyo, J. A.; Thybaut, J.; Marin, G. B. Evidences for Pore Mouth and Key-Lock Catalysis in Hydroisomerization of Long n-Alkanes over 10-Ring Tubular Pore Bifunctional Zeolites. *Catal. Today* **2001**, *65* (2–4), 111–116.

(101) Laxmi Narasimhan, C. S.; Thybaut, J. W.; Marin, G. B.; Martens, J. A.; Denayer, J. F.; Baron, G. V. Pore Mouth Physisorption of Alkanes on ZSM-22: Estimation of Physisorption Enthalpies and Entropies by Additivity Method. *J. Catal.* **2003**, *218* (1), 135–147.

(102) Claude, M. C.; Vanbutsele, G.; Martens, J. A. Dimethyl Branching of Long N-Alkanes in the Range from Decane to Tetracosane on Pt/H-ZSM-22 Bifunctional Catalyst. *J. Catal.* **2001**, *203* (1), 213–231.

(103) Wang, W.; Liu, C.-J.; Wu, W. Bifunctional Catalysts for the Hydroisomerization of N-Alkanes: The Effects of Metal–Acid Balance and Textural Structure. *Catal. Sci. Technol.* **2019**, *9* (16), 4162–4187.

(104) Thybaut, J. W.; Laxmi Narasimhan, C. S.; Denayer, J. F.; Baron, G. V.; Jacobs, P. A.; Martens, J. A.; Marin, G. B. Acid-Metal Balance of a Hydrocracking Catalyst: Ideal versus Nonideal Behavior. *Ind. Eng. Chem. Res.* **2005**, *44* (14), 5159–5169.

(105) Guisnet, M.; Alvarez, F.; Giannetto, G.; Perot, G. Hydroisomerization and Hydrocracking of N-Heptane on PtH Zeolites. Effect of the Porosity and of the Distribution of Metallic and Acid Sites. *Catal. Today* **1987**, *1* (4), 415–433.

(106) Alvarez, F.; Ribeiro, F. R.; Perot, G.; Thomazeau, C.; Guisnet, M. Hydroisomerization and Hydrocracking of Alkanes. *J. Catal.* **1996**, *162* (2), 179–189.

(107) van der Wal, L. I.; Oenema, J.; Smulders, L. C. J.; Samplonius, N. J.; Nandpersad, K. R.; Zečević, J.; de Jong, K. P. Control and Impact of Metal Loading Heterogeneities at the Nanoscale on the Performance of Pt/Zeolite Y Catalysts for Alkane Hydroconversion. *ACS Catal.* **2021**, *11* (7), 3842–3855.

(108) Mendes, P. S. F.; Silva, J. M.; Ribeiro, M. F.; Daudin, A.; Bouchy, C. From Powder to Extrudate Zeolite-Based Bifunctional Hydroisomerization Catalysts: On Preserving Zeolite Integrity and Optimizing Pt Location. *J. Ind. Eng. Chem.* **2018**, *62*, 72–83.

(109) Mendes, P. S. F.; Silva, J. M.; Ribeiro, M. F.; Daudin, A.; Bouchy, C. Bifunctional Intimacy and Its Interplay with Metal-Acid Balance in Shaped Hydroisomerization Catalysts. *ChemCatChem* **2020**, *12* (18), 4582–4592.

(110) Hu, W.; Noh, G.; Iglesia, E. Consequences of Metal-Acid Site Proximity for Alkane Isomerization and β-Scission Mediated by Bifunctional Catalytic Cascades. *J. Catal.* **2023**, *425*, 125–142.

(111) Munnik, P.; De Jongh, P. E.; De Jong, K. P. Recent Developments in the Synthesis of Supported Catalysts. *Chem. Rev.* **2015**, *115* (14), 6687–6718.

(112) Bobba, S.; Carrara, S.; Huisman, J.; Mathieux, F.; Pavel, C. Critical Raw Materials for Strategic Technologies and Sectors in the EU - a Foresight Study. *Publ. Off.* **2020**.

(113) Visser, N. L.; Daoura, O.; Plessow, P. N.; Smulders, L. C. J.; de Rijk, J. W.; Stewart, J. A.; Vandegehuchte, B. D.; Studt, F.; van der Hoeven, J. E. S.; de Jongh, P. E. Particle Size Effects of Carbon Supported Nickel Nanoparticles for High Pressure CO2 Methanation. *ChemCatChem* **2022**, *14* (22).

(114) Barberis, L.; Hakimioun, A. H.; Plessow, P. N.; Visser, N. L.; Stewart, J. A.; Vandegehuchte, B. D.; Studt, F.; de Jongh, P. E. Competition between Reverse Water Gas Shift Reaction and Methanol Synthesis from CO2: Influence of Copper Particle Size. *Nanoscale* **2022**, *14* (37), 13551–13560.

(115) Wang, C.; Tian, Y.; Wu, R.; Li, H.; Yao, B.; Zhao, Y.; Xiao, T. Bimetallic Synergy Effects of Phyllosilicate-Derived NiCu@SiO2 Catalysts for 1,4-Butynediol Direct Hydrogenation to 1,4-Butanediol. *ChemCatChem* **2019**, *11* (19), 4777–4787.

(116) van der Hoeven, J. E. S.; Jelic, J.; Olthof, L. A.; Totarella, G.; van Dijk-Moes, R. J. A.; Krafft, J. M.; Louis, C.; Studt, F.; van Blaaderen, A.; de Jongh, P. E. Unlocking Synergy in Bimetallic Catalysts by Core–Shell Design. *Nat. Mater.* **2021**, *20* (9), 1216–1220.

(117) Schoemaker, S. E.; Welling, T. A. J.; Wezendonk, D. F. L.; Reesink, B. H.; van Bavel, A. P.; de Jongh, P. E. Carbon Nanofiber Growth from Methane over Carbon-Supported NiCu Catalysts: Two Temperature Regimes. *Catal. Today* **2023**, *418*, 114110.

(118) Hernández Mejía, C.; van Deelen, T. W.; de Jong, K. P. Activity Enhancement of Cobalt Catalysts by Tuning Metal-Support Interactions. *Nat. Commun.* **2018**, *9* (1), 1–8.

(119) van Deelen, T. W.; Hernández Mejía, C.; de Jong, K. P. Control of Metal-Support Interactions in Heterogeneous Catalysts to Enhance Activity and Selectivity. *Nat. Catal.* **2019**, *2* (11), 955–

(120) Monai, M.; Jenkinson, K.; Melcherts, A. E. M.; Louwen, J. N.; Irmak, E. A.; Van Aert, S.; Altantzis, T.; Vogt, C.; van der Stam, W.; Duchoň, T.; Šmíd, B.; Groeneveld, E.; Berben, P.; Bals, S.; Weckhuysen, B. M. Restructuring of Titanium Oxide Overlayers over Nickel Nanoparticles during Catalysis. *Science* **2023**, *380* (6645), 644–651.

(121) Kaiser, S. K.; Chen, Z.; Faust Akl, D.; Mitchell, S.; Pérez-Ramírez, J. Single-Atom Catalysts across the Periodic Table. *Chem. Rev.* **2020**, *120* (21), 11703–11809.

(122) Zhang, Z.; Zhu, Y.; Asakura, H.; Zhang, B.; Zhang, J.; Zhou, M.; Han, Y.; Tanaka, T.; Wang, A.; Zhang, T.; Yan, N. Thermally Stable Single Atom Pt/m-Al2O3 for Selective Hydrogenation and CO Oxidation. *Nat. Commun.* **2017**, *8*, 1–10.

(123) Zhang, Z.; Liu, J.; Wang, J.; Wang, Q.; Wang, Y.; Wang, K.; Wang, Z.; Gu, M.; Tang, Z.; Lim, J.; Zhao, T.; Ciucci, F. Single-Atom Catalyst for High-Performance Methanol Oxidation. *Nat. Commun.* **2021**, *12* (1), 1–9.

(124) Weisz, P. B. Stepwise Reaction via Intermediates on Separate Catalytic Centers. *Science* **1956**, *123* (3203), 887–888.

(125) Weisz, P. B.; Swegler, E. W. Stepwise Reaction on Separate Catalytic Centers: Isomerization of Saturated Hydrocarbons. *Science* **1957**, *126* (3262), 31–32.

(126) Weisz, P. B. Polyfunctional Heterogeneous Catalysis. *Adv. Catal.* **1962**, *13* (C), 137–190.

(127) Francis, J.; Guillon, E.; Bats, N.; Pichon, C.; Corma, A.; Simon, L. J. Design of Improved Hydrocracking Catalysts by Increasing the Proximity between Acid and Metallic Sites. *Appl. Catal. A Gen.* **2011**, *409–410*, 140–147.

(128) Batalha, N.; Pinard, L.; Bouchy, C.; Guillon, E.; Guisnet, M. N-Hexadecane Hydroisomerization over Pt-HBEA Catalysts. Quantification and Effect of the Intimacy between Metal and Protonic Sites. *J. Catal.* **2013**, *307*, 122–131.

(129) Zečević, J.; Vanbutsele, G.; de Jong, K. P.; Martens, J. A. Nanoscale Intimacy in Bifunctional Catalysts for Selective Conversion of Hydrocarbons. *Nature* **2015**, *528* (7581), 245–254.

(130) Oenema, J.; Harmel, J.; Vélez, R. P.; Meijerink, M. J.; Eijsvogel, W.; Poursaeidesfahani, A.; Vlugt, T. J. H.; Zečević, J.; de Jong, K. P. Influence of Nanoscale Intimacy and Zeolite Micropore Size on the Performance of Bifunctional Catalysts for N-Heptane Hydroisomerization. *ACS Catal.* **2020**, *10* (23), 14245–14257.

(131) Cheng, K.; van der Wal, L. I.; Yoshida, H.; Oenema, J.; Harmel, J.; Zhang, Z.; Sunley, G.; Zečević, J.; de Jong, K. P. Impact of the Spatial Organization of Bifunctional Metal–Zeolite Catalysts on the Hydroisomerization of Light Alkanes. *Angew. Chemie - Int. Ed.* **2020**, *59* (9), 3592–3600.

(132) Harmel, J.; van der Wal, L. I.; Zečević, J.; de Jongh, P. E.; de Jong, K. P. Influence of Intimacy for Metal-Mesoporous Solid Acids Catalysts for n -Alkanes Hydro-Conversion. *Catal. Sci. Technol.* **2020**, 2111–2119.

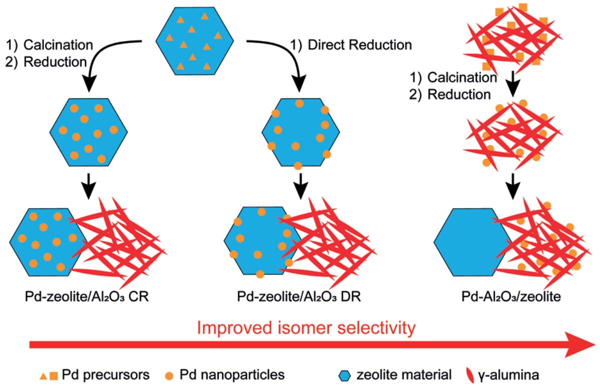
1) Calcination
2) Reduction
1) Direct Reduction
1) Calcination
2) Reduction
Pd-zeolite/Al_2O_3 CR
Pd-zeolite/Al_2O_3 DR
Pd-Al_2O_3/zeolite
Improved isomer selectivity
▲■ Pd precursors
● Pd nanoparticles
⬢ zeolite material
γ-alumina

Chapter 2

Steering the metal precursor location in bifunctional catalysts

Abstract: Bifunctional catalysts containing a dehydrogenation–hydrogenation function and an acidic function are widely applied for the hydroconversion of hydrocarbon feedstocks obtained from both fossil and renewable resources. It is well known that the distance between the two functionalities is important for the performance of the catalyst. In this study, we show that the heat treatment of the catalyst precursor can be used to steer the location of the Pd precursor with respect to the acid sites in SAPO-11 and ZSM-22 zeotype materials when ions are exchanged with $[Pd(NH_3)_4](NO_3)_2$. Two sets of catalysts were prepared based on composite materials of alumina with either SAPO-11 or ZSM-22. Pd was placed on/in the zeotype, followed by a calcination-reduction (CR) or direct reduction (DR) treatment. Furthermore, catalysts with Pd on the alumina binder were prepared. CR results in having more Pd nanoparticles inside the zeotype crystals, whereas DR yields more particles on the outer surface of the zeotype crystals as is confirmed using HAADF-STEM and XPS measurements. The catalytic performance in both n-heptane and n-hexadecane hydroconversion of the catalysts shows that having the Pd nanoparticles on the alumina binder is most beneficial for maximizing the isomer yields. Pd-on-zeotype catalysts prepared using the DR approach show intermediate performances, outperforming their Pd-in-zeotype counterparts that were prepared with the CR approach.

This chapter is based on: Smulders, L.C.J.; van de Minkelis, J.H.; Meeldijk, J.D.; Tang, M.; Liutkova, A.; Cheng, K.; Roberts, S.T.; Sunley, G.J.; Hensen, E.J.M.; de Jongh, P.E.; de Jong, K.P., Steering the metal precursor location in Pd/zeotype catalysts and its implications for catalysis, *Chemistry* **2023**, (5), 348-364

2.1. Introduction

Bifunctional catalysts play a key role in petroleum refining for the production of fuels and chemicals from crude oil.[1–3] Furthermore, they are applied in the conversion of feedstocks such as Fischer–Tropsch wax,[4,5] algae-based hydrocarbons[6,7] and plastic waste[8] into fuels and lubricants. Bifunctional hydroconversion catalysts consist of a metal (sulfide) function for (de)hydrogenation and an acid function for cracking or isomerization.[9–12] Parameters such as the type of acid function, the acidity of the acid materials, the type of metal, the metal-to-acid-site (n_M/n_A) ratio, proximity between the two types of sites and the porosity of the catalyst have an impact on the catalytic performance.[11,13,14] It is well known that the metal particles and the zeolite acid sites need to be in close proximity in order to obtain high catalytic activity.[15,16]

Several studies on the proximity between metal and acid sites have been published, mainly evaluating the difference between placing the metal on alumina binder or on/in the zeolite crystals.[13,17–20] When the metal nanoparticles are located inside the zeolite crystals, their accessibility for larger or bulkier hydrocarbon molecules is limited, since these molecules have a low diffusivity inside the micropores.[21,22] This causes more sequential reactions and hence (over)cracking of the feedstock. On the other hand, locating the particles slightly further away from the acid sites, i.e., on an alumina binder material or on the outer surface of the zeolite crystallites, results in improved selectivity towards the isomerized products.[17,18,23] Apart from zeolites, other zeotype materials can be used in bifunctional hydroconversion catalysts. For example, crystalline aluminium phosphates, SAPO-11 in particular, have been studied for this purpose.[24–28]

Typically, salts containing cations such as $[Pt(NH_3)_4]^{2+}$ and $[Pd(NH_3)_4]^{2+}$ are added to a dispersion of a zeolite/zeotype in water in order to exchange protons with the metal precursor, after which a heat treatment is required to arrive at a catalyst with metal nanoparticles dispersed inside the zeolite crystallites.[29–31] From earlier work, we know that Pt dispersion in Pt/Y catalysts is influenced by the heat treatment conditions. A low calcination ramp (0.2 °C/min) is required to prevent the formation of a mobile $[Pt(NH_3)_2H_2]^0$ complex and hence the formation of larger nanoparticles.[31] To our knowledge, the results obtained with these Pt/Y catalysts have never been correlated to metal nanoparticle location effects and the effect on catalysis has not been studied.

For applications such as hydroconversion, locating the metal nanoparticles (NPs) outside the zeolite micropores is beneficial. Other applications, however, such as propane dehydroaromatization[32] require the confinement of metal NPs inside the zeolite crystals. Furthermore, encapsulation of NPs inside zeolite materials can be used as a strategy to prevent catalyst poisoning.[33] Therefore, control over the metal nanoparticle location is important.

The location of metal nanoparticles can be studied using transmission electron microscopy (TEM).[17,34] However, the disadvantages of TEM are the relatively small sample size, and that it only provides qualitative information about the metal nanoparticle location.[23] Therefore, a complementary and more quantitative characterization method is desirable. X-ray photoelectron spectroscopy (XPS) has proven to be relatively successful. It is a surface-sensitive technique, resulting in the fact that metal atoms located deep inside the zeolite hardly contribute to the signal, whereas metal atoms that are on the outer surface can be detected. Previously, this has been applied to the study of the location of Pd nanoparticles in carbon nanotubes[35] and silicalite-1.[36] Oenema et al.[23] studied Pt/Al ratios in Pt/Y catalysts and used these data to provide quantitative information about the location of the Pt particles. One of the challenges they faced was the overlap between the Pt and Al signal, which is not problematic with Pd since the signal does not overlap with the other elements (Si, Al, P) that are to be determined using XPS.

In this work, we show that the heat treatment of the catalyst precursor can influence the nanoparticle location. Two sets of catalysts were prepared, one based on SAPO-11 and the other based on ZSM-22. These zeotypes both have 1D pore systems consisting of 10-membered rings and are typically used in hydroconversion research.[18,19,26,28] Each set of catalysts consisted of alumina/zeotype composite materials forming the basis of the Pd-on-alumina, Pd-zeotype-direct reduction (DR) and Pd-zeotype-calcination-reduction (CR) catalysts. These catalysts were denoted Pd-γ-Al_2O_3/SAPO-11, Pd-SAPO-11/γ-Al_2O_3 DR, Pd-SAPO-11/γ-Al_2O_3 CR, Pd-γ-Al_2O_3/ZSM-22, Pd-ZSM-22/γ-Al_2O_3 DR and Pd-ZSM-22/γ-Al_2O_3 CR. The Pd nanoparticle location was then studied using transmission electron microscopy (TEM) and X-ray photoelectron spectroscopy (XPS). The hydroconversion performance of the catalysts was assessed using *n*-heptane and *n*-hexadecane as the model feedstocks. This showed that the location of the metal nanoparticle clearly affected the performance in both sets of catalysts.

2.2. Materials and Methods

Materials

SAPO-11 (H^+-form, Si/(Si+Al+P) = 0.15 at/at) and ZSM-22 (H^+-form, Si/Al = 32.5-40 at/at) were purchased from ACS Material. Boehmite was obtained from Harshaw. Tetraaminepalladium (II) nitrate ($[Pd(NH_3)_4](NO_3)_2$) solution (10 wt% in H_2O) and ammonium hexachloropalladate ($(NH_4)_2[PdCl_6]$) were purchased from Sigma-Aldrich. *n*-Heptane (99+%, pure) and *n*-hexadecane (99%, pure) were purchased from ACROS Organics. Acetic acid (glacial, 99+%) was purchased from Alfa Aesar. Hydrochloric acid (37 %) was purchased from Emsure. Silicon carbide (SiC, SIKA ABR I F70, grain size: 220 µm) was supplied by Fiven. H_2 6.0, He 5.0 and N_2 5.0 were obtained from Linde gas.

Catalyst Synthesis

Preparation of Catalysts with Pd on/in Zeotype Crystals

A schematic overview of catalyst synthesis is included in Figure S2.1 in the

Supplementary Materials. SAPO-11 and ZSM-22 were calcined at 550 ˚C in a flow of synthetic air (N_2/O_2, 80/20, *vol*/*vol*) for 3 h. For the preparation of Pd-SAPO-11/γ-Al_2O_3 (DR) and Pd-ZSM-22/γ-Al_2O_3 (DR), 1 g of calcined SAPO-11 or ZSM-22 was dispersed in 300 mL Milli-Q water by stirring at 500 rpm for 1 h. The pH of the dispersion was 4.9 and 6.7 for SAPO-11 and ZSM-22, respectively. A solution with the desired concentration of $[Pd(NH_3)_4](NO_3)_2$ was prepared by taking the required volume of the 10 wt% solution and diluting it in 50 mL Milli-Q water. This solution was then added dropwise to the zeotype dispersion, and the mixture was stirred for 3 h resulting in a pH of 5.9 and 6.6 for SAPO-11 and ZSM-22, respectively. Subsequently, the dispersion was filtered over vacuum and the filter cake was washed with 300 mL Milli-Q water. The filter cake was dried in an oven at 120 ˚C overnight. The pre-catalyst powders were then heat treated in a tubular oven. First, the powders were heated to 150 ˚C with a ramp of 2 ˚C/min to be dried in an N_2 flow of 80 mL/min for 1 h. To produce the DR catalyst, the powder was heated to 600 ˚C with a ramp of 2 ˚C/min in a hydrogen-rich atmosphere (H_2/N_2, 80/20, *vol*/*vol*) for 3 h. To prepare the regular Pd-in-zeotype catalyst, the powder was calcined (N_2/O_2, 80/20, *vol*/*vol*; 0.2 ˚C/min, 350 ˚C, 4 h) prior to reduction with the same reduction conditions. The Pd/zeotype (DR) powder was mixed with boehmite. During typical mixing, 1.428 g of boehmite was mixed with 1.2 mL of Milli-Q water and 0.042 mL of glacial acetic acid until complete wetting was reached using a mortar and pestle. This was followed with the addition of 1.00 g Pd/zeotype pre-catalyst and a few drops of Milli-Q water. It was mixed until a homogeneous paste was obtained. The paste was dried in an oven overnight at 120 ˚C after which it was calcined at 500 ˚C for 2 h (ramp 1 ˚C/min, N_2/O_2, 80/20, *vol*/*vol*).

Preparation of Pd-on-Alumina Catalysts

Pd-γ-Al_2O_3/SAPO-11 and Pd-γ-Al_2O_3/ZSM-22 were prepared using a strong electrostatic adsorption (EA) method as previously described in Cho and Regalbuto.[37] For this, 1 g of γ-Al_2O_3 (obtained from calcination of boehmite) was suspended in 300 mL Milli-Q water and stirred for 1 h using a mechanical stirrer. The suspension was acidified to a pH of 2.5 with 1M HCl solution. A precursor solution of 34.29 mg $(NH_4)_2[PdCl_6]$ in 33 mL Milli-Q water was added dropwise to the suspension and the suspension was stirred at 500 rpm for 3 h. The resulting suspension was then filtered over vacuum and the filter cake was washed with Milli-Q water. The filter cake was then dried in an oven at 120 ˚C overnight. This was followed by calcination (N_2/O_2, 80/20, *vol*/*vol*; 0.2 ˚C/min, 350 ˚C, 4 h) and then reduction (H_2/N_2, 80/20, *vol*/*vol*; 2 ˚C/min, 600 ˚C, 3 h) to obtain the Pd-γ-Al_2O_3 pre-catalyst. The Pd-γ-Al_2O_3 was then mixed with either SAPO-11 or ZSM-22. First, 1 g of calcined (550 ˚C, N_2/O_2, 80/20, *vol*/*vol*, 3 h) SAPO-11 or ZSM-22 was mixed with 1.2 mL Milli-Q water and 0.042 mL acetic acid using mortar and pestle, until complete wetting of the zeotype was reached. Then, 1 g of Pd-γ-Al_2O_3 was added and the paste was mixed with additional Milli-Q water until a homogeneous paste was obtained. This catalyst was then dried and calcined as also described for the Pd-zeotype/γ-Al_2O_3 catalysts.

Catalyst Characterization

Quantification of Metal and Acid Sites

Elemental analysis was performed at Mikroanalytisches Laboratorium Kolbe, Germany, with an inductively coupled plasma (ICP) optical emission spectrometer (PerkinElmer, Waltham, MA, USA) after sample dissolution according to their standard in-house procedures.

Temperature-programmed desorption of ammonia (NH_3-TPD) was performed to determine the number of acid sites. The measurements were performed on a Micromeritics AutoChem II equipped with a thermal conductivity detector (TCD) calibrated for ammonia. For a typical measurement, 100–110 mg of catalyst was dried in a He flow for 1 h at 550 ˚C with a ramp of 10 ˚C/min. The temperature was then lowered to 100 ˚C and ammonia was introduced (10 vol % in He) in a pulse-wise manner. After oversaturation was reached, the physisorbed ammonia was removed by flowing He for 2 h at 100 ˚C. This was followed by monitoring the desorption of ammonia up to 550 ˚C with a ramp of 10 ˚C/min.

Another technique that was applied to obtain information about the acid sites was Fourier Transform Infrared (FT-IR) Spectroscopy. FT-IR was performed in transmission mode on a Thermo iS5 instrument equipped with a DTGS detector. Approximately 15 mg of sample was pressed into a self-supported wafer, which was then placed in a sealed cell with calcium fluoride windows. The wafers were first dried under high vacuum at 550 ˚C (ramp 10 ˚C/min) for 2 h. After cooling down to a temperature of 30–40 ˚C, a spectrum was taken. For each spectrum, 16 scans were taken with a resolution of 4 cm^{-1}. This was followed by the introduction of pyridine (Sigma-Aldrich, 99.8%, probe molecule) at a pressure of 20 mbar, during which spectra were recorded every 2 min for 30 min starting 2 min after initial introduction of the pyridine. A high vacuum of 10−5 mbar was applied for 30 min in order to desorb the pyridine. This was followed with an increase in temperature to 150 ˚C (ramp 2 ˚C/min) and the temperature was kept at this point for 30 min, after which a spectrum was recorded. This was followed by heating the wafer to 250 ˚C with a ramp of 10 ˚C/min, after which an additional spectrum was taken that was used to assess the acidity of the samples. Quantification of acid sites, C (mmol g^{-1}), was performed using band integration of the peaks at 1545 cm^{-1} (Brønsted acid sites, BAS) and 1453 cm^{-1} (Lewis acid sites, LAS) in the spectrum after pyridine desorption at 250 ˚C utilizing Equation 2.1. The integral under the curve is represented by A (cm^{-1}). The results were corrected for the specific molar absorption coefficients and the mass and radius of the wafers. Molar absorption coefficients (A_0) of 1.67 cm/µmol (BAS) and 2.22 cm/µmol (LAS) were used for quantification.[38–40] The mass of the wafer (mg) per cm^2 through which the IR beam was sent was represented by ρ. The stoichiometry of pyridine adsorption was assumed to be 1 molecule of pyridine molecule per LAS and 1 molecule of pyridine per BAS.

$$C = \frac{A}{A_0 \times \rho} \qquad \textbf{(Eq. 2.1.)}$$

Ultramicrotomy of the samples was performed before the samples were studied with (high-resolution) high-angle annular dark-field scanning transmission electron microscopy (HAADF-STEM). Samples were embedded in EpoFix resin and the embedded samples were left to harden in an oven at 60 ˚C overnight. Slices with a thickness of 70 nm were obtained by cutting the resin-embedded sample using a Reichert–Jung Ultracut E ultramicrotome with a Diatome Ultra 35˚ diamond knife. The sections were deposited on a glow-discharged carbon-formvar-coated copper grid (200 mesh). HAADF-STEM and Energy Dispersive X-ray Spectroscopy (EDX) were performed on an FEI Talos F200X electron microscope equipped with a Super-X EDX detector, operating at 200 kV. HR HAADF-STEM was performed on a Thermo Fisher Scientific Spectra 300 S/TEM at 300 kV. Scanning electron microscopy (SEM) on as-received zeotype samples was performed on a Helios G3 UC microscope operated at 10 kV.

X-ray photoelectron spectroscopy was performed using a KAlpha spectrometer from Thermo Fisher Scientific. The spectrometer was equipped with a monochromatic Al Kα X-ray source and a 180˚ double-focusing hemispherical analyzer. The samples were placed on double- sided carbon tape. Spectra were collected using an aluminium anode (Al, Kα = 1486.68 eV) operating at 72 W and a spot size of 400 µm. Survey scans were measured at a constant pass energy of 200 eV. Region scans were measured at 50 eV. The shift in binding energy was calibrated to the C signal (285 eV). Each sample was measured four times. In order to obtain a quantitative value, Pd signals were normalized to the combined Si+Al areas, taking relative sensitivity factors into account.

Nitrogen physisorption isotherms were measured at 196 ˚C on a Micromeritics Tristar II Plus apparatus. First, the samples were dried overnight in a vacuum at 200 ˚C. The accessible surface areas were determined using the Brunauer–Emmett–Teller (BET) and Langmuir methods. Micropore (<2 nm) volumes were determined using a Harkins–Jura thickness curve fitted between 0.32 and 0.40 nm thickness. The total pore volumes were derived from the amount of nitrogen adsorbed at $P/\mathrm{P}_0 = 0.95$.

X-ray diffractograms were recorded using a Bruker-AXS D2 Phaser X-ray Diffractometer in Bragg–Brentano mode, equipped with a Lynxeye detector (Co Kα1,2, λ = 1.790 Å). Recordings were taken at 2θ angles between 5˚ and 80˚ under constant rotation of 15 rpm.

Hydroconversion of *n*-Heptane and *n*-Hexadecane

Catalytic experiments were performed using an Avantium Flowrence 16-parallel fixed-bed reactor setup. Stainless steel reactors (inner diameter = 2 mm) were loaded with a bed height of 2 cm of SiC (220 µm), 30 mg of sieved catalyst (75–212 µm) and another layer of SiC, leaving 2 cm of free space at the top. The products were analyzed using an online GC (Agilent Technologies 7890B). The GC was equipped with an Agilent J&W HP-PONA column and the hydrocarbon products were analyzed using an FID. Prior to the catalytic tests with n-heptane (*n*-C_7), catalysts were reduced at 350 ˚C in H_2/He (25 vol-% H_2). Experiments with *n*-heptane as feedstock were performed with the following reaction conditions: H_2/*n*-heptane molar ratio of 10, total pressure of 10 bar and WHSV of 2.4 $g_{n\text{-C7}} \cdot g_{cat}^{-1} \cdot h^{-1}$. Prior to catalytic tests with n-hexadecane (*n*-C_{16}), catalysts were reduced at 350 ˚C in a pure hydrogen flow. Experiments with n-hexadecane as feedstock were performed with these reaction conditions: H_2/*n*-hexadecane molar ratio of 10, total pressure of 5 bar and WHSV of 2.9 $g_{n\text{-C16}} \cdot g_{cat}^{-1} \cdot h^{-1}$. The conversion of *n*-heptane or *n*-hexadecane ($X_{n\text{-alkane}}$) is calculated by:

$$X_{n\text{-alkane}} = \left(1 - \frac{F_{\text{Cwt.}n-\text{alkane,out}}}{F_{\text{Cwt.}n-\text{alkane,in}}}\right) \cdot 100\% \qquad \textbf{(Eq. 2.2.)}$$

Wherein $F_{\text{Cwt.}n\text{-alkane,out}}$ and $F_{\text{Cwt.}n\text{-alkane,in}}$ are the flows based on carbon weight of *n*-alkane going out or in the reactor, respectively. The isomer yield ($Y_{i\text{-alkane}}$) is calculated by:

$$Y_{i\text{-alkane}} = \left(\frac{F_{\text{Cwt.}i-\text{alkane,out}}}{F_{\text{Cwt.}n-\text{alkane,in}}}\right) \cdot 100\% \qquad \textbf{(Eq. 2.3.)}$$

Similarly, the yield of any cracked product is calculated by:

$$Y_{Cm} = \left(\frac{F_{\text{Cwt.}C\text{m,out}}}{F_{\text{Cwt.}n-\text{alkane,in}}}\right) \cdot 100\% \qquad \textbf{(Eq. 2.4.)}$$

In which C_m is a hydrocarbon molecule with m carbon atoms (m = 1-6 during *n*-heptane conversion and m = 1-14 during *n*-hexadecane conversion).
The selectivity towards *i*-heptane (*i*-C_7) or cracked products (C_m) during *n*-heptane conversion is calculated with the following two equations:

$$S_{i\text{-C7}} = \left(\frac{F_{\text{Cwt.}i-\text{C7,out}}}{F_{\text{Cwt.}n-\text{alkane,in}} - F_{\text{Cwt.}n-\text{alkane,out}}}\right) \cdot 100\% \qquad \textbf{(Eq. 2.5.)}$$

$$S_{Cm} = \left(\frac{F_{\text{Cwt.}C\text{m,out}}}{F_{\text{Cwt.}n-\text{alkane,in}} - F_{\text{Cwt.}n-\text{alkane,out}}}\right) \cdot 100\% \qquad \textbf{(Eq. 2.6.)}$$

The yield in mol-% of each product of *n*-hexadecane is calculated by:

$$Y_{Cm}\,(mol - \%) = \left(\frac{F_{\text{Cwt.}C\text{m,out}}}{F_{\text{Cwt.}n-\text{alkane,in}}}\right) \cdot \left(\frac{16}{m}\right) \cdot 100\% \qquad \textbf{(Eq. 2.7.)}$$

Calculation of Apparent Activation Energies

The apparent activation energies for the hydroconversion of n-heptane and n-hexadecane were calculated based on Arrhenius plots in which ln k was plotted against 1000/T. The results from the catalyst assessment were used to calculate ln k using Equation 2.8, assuming first order kinetics:[41]

$$\ln k = \ln\left(\frac{-\ln(1-X)}{\frac{\mathrm{W}}{F}}\right) \qquad \textbf{(Eq. 2.8.)}$$

In Equation 2.8, k is the first order rate constant (mol · s^{-1} · kg$_{cat}^{-1}$), X is the conversion as a fraction, W is the weight of the catalyst (kg) and F is the molar flow of the reactant (mol s^{-1}). To stay in the kinetically determined regime, only ln k-values derived from X-values between 0.01 and 0.20 were plotted. At least five ln k-values were plotted against their corresponding 1000/T-values (1000 K^{-1}). The slopes of the Arrhenius plots were then multiplied by the gas constant R (8.314 J K^{-1} mol^{-1}) to obtain the apparent activation energy (E_a, kJ mol^{-1}). Standard errors were derived from errors in the fit.

2.3. Results and Discussion

Acidity and Pd Weight Loading of Pd/SAPO-11/γ-Al_2O_3 and Pd/ZSM-22/γ-Al_2O_3 Catalysts

The Pd weight loading is 0.4–0.5 wt% on all catalysts (Table 2.1). This weight loading is sufficient to ensure that the reaction on the acid site is rate-determining, and slight differences in Pd loading do not impact the catalytic performance.[42,43] For a set of catalysts with the same zeotype, NH_3-TPD reveals a similar number of acid sites (Table 2.1). The pyridine-IR results also show the same number of Brønsted acid sites (BAS) within a set of catalysts with the same zeotype material (Table 2.1, Figure 2.1). For quantification of the number of BAS, the band at 1545 cm^{-1} is assigned to the pyridinium ion. The band at 1453 cm^{-1} is typical for coordinately bonded pyridine, indicating the presence of Lewis acid sites (LAS). The presence of the band at 1489 cm^{-1} comes from pyridine adsorbed on both BAS and LAS and can therefore not be used for quantification of acid sites.[38–40] The band at 1576 cm^{-1} can be assigned to pyridine on LAS and overlaps with a band of physisorbed pyridine.[44–46] Since the temperature of 250 °C should be sufficiently high for the desorption of pyridine, this band is most likely indicative of the presence of pyridine on LAS. Because of the rather identical acidity within a set of catalysts, the acidity is not expected to lead to differences in catalytic performance within a set of catalysts. An overview of the results obtained with NH_3-TPD and FT-IR of the catalysts, parent zeotypes and composite materials is presented in Table S2.1.

Table 2.1. Results of catalyst characterization: Pd weight loading, number of acid sites and Pd/(Si+Al) ratios.

Catalyst	Pd weight loading [a] (wt%)	Number of strong acid sites [b] (mmol g^{-1})	Number of Brønsted acid sites [c] (mmol g^{-1})	Pd/(Si+Al) Surface [d] (at/at)	Pd/(Si+Al) Bulk [a] (at/at)
Pd-γ-Al_2O_3/SAPO-11	0.49	0.29	0.015	0.0037 ± 0.0001	0.0036
Pd-SAPO-11/γ-Al_2O_3 DR	0.45	0.26	n.d.	0.0020 ± 0.0001	0.0032
Pd-SAPO-11/γ-Al_2O_3 CR	0.41	0.25	0.018	0.0018 ± 0.0001	0.0028
Pd-γ-Al_2O_3/ZSM-22	0.50	0.37	0.023	0.0028 ± 0.0001	0.0026
Pd-ZSM-22/γ-Al_2O_3 DR	0.44	0.35	n.d.	0.0014 ± 0.0002	0.0023
Pd-ZSM-22/γ-Al_2O_3 CR	0.41	0.33	0.019	0.0010 ± 0.0001	0.0022

[a] Determined using inductively coupled plasma-optical emission spectroscopy on digested samples.

[b] Determined using deconvolution of NH_3-TPD profiles and integration of the peak at higher temperatures ($T \geq 200$ ˚C for SAPO-11 and $T \geq 300$ ˚C for ZSM-22).

[c] Determined using integration of the peak at 1545 cm^{-1} of FT-IR spectra after adsorption and subsequent desorption of pyridine at 250 ˚C, correcting for the sample mass and using a molar absorption coefficient of 1.67 cm/µmol, (n.d. = not determined).

[d] Determined from the areas of Pd, Si and Al peaks from XPS in four separate measurements, taking relative sensitivity factors into account.

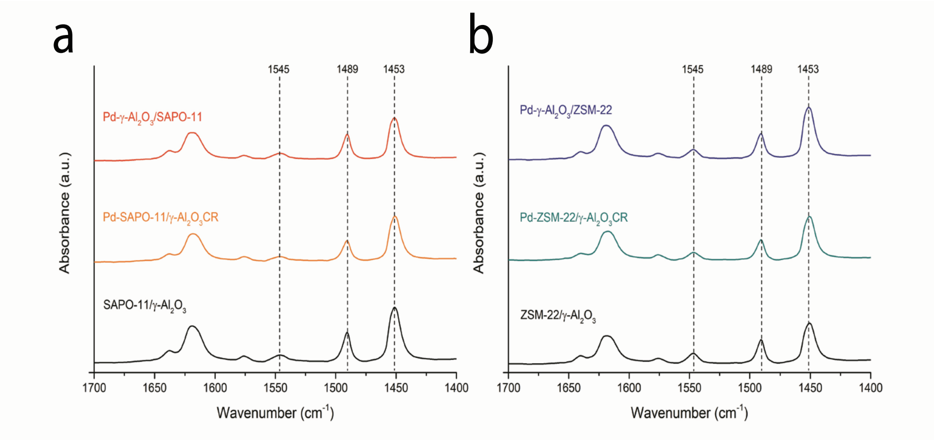

Figure 2.1. FT-IR spectra of the a) SAPO-11 catalysts and b) ZSM-22 catalysts after pyridine adsorption and subsequent desorption at 250 ˚C.

Determination of Pd Nanoparticle Location

The catalysts were embedded in a resin and 70 nm thick slices were prepared by ultramicrotoming. This enabled visualization of the interior of the catalyst particles. As can be seen in Figure 2.2, for the SAPO-11 catalysts, a rather clear distinction can be made between the Pd nanoparticles on the alumina binder (Figure 2.2a) and the Pd particles on/in the SAPO-11 crystals (Figure 2.2c,e). When Figure 2.2c,e are compared, more and larger Pd (~6–7 nm) nanoparticles are present on the outer surface of the SAPO-11 crystals when the catalysts undergo direct reduction (DR), whereas calcination-reduction (CR) results in more nanoparticles inside the SAPO-11 crystals.

This also seems to be the case for the ZSM-22-based catalysts. After CR, more nanoparticles are inside the zeolite crystallite (Figure 2.2d) and after DR more nanoparticles are located on the outer surface of the zeolite crystal and fewer particles are observed inside (Figure 2.2f). When it comes to the average nanoparticle size, only minor differences are observed (Table S2.2).

The imaging of Pd nanoparticles on the alumina binder (Figure 2.2a,b) is very challenging when the samples are ultramicrotomed, as the resolution and contrast are reduced by the presence of the resin. Therefore, it is assumed that the Pd nanoparticles did not change much upon mixing the Pd-γ-Al_2O_3 with the respective zeotype materials. An HAADF-STEM image of the original Pd-γ-Al_2O_3 is included in Figure S2.2.

X-ray photoelectron spectroscopy (XPS) studies were performed to further elaborate on the metal nanoparticle location. Since XPS is a surface-sensitive technique, only Pd atoms residing on the surface of the zeotype crystals or on the alumina binder contribute to the signal in the XPS. When Pd atoms are deeper inside the zeotype crystals, the emitted electrons will not escape from the sample, resulting in a low XPS signal.

In both catalyst series, the highest Pd signal is obtained when Pd is on the alumina binder (Table 2.1, Supplementary Figure S2.3). When Pd is on the zeotype, a lower Pd/(Si+Al) signal is observed. This can have two causes: (1) typically the Pd nanoparticles after direct reduction are larger,[31] which results in relatively fewer Pd atoms contributing to the Pd signal, because only the outer layers of the nanoparticle contribute, and (2) only the Pd nanoparticles that are on the outside contribute to the signal, whereas the particles that reside inside the zeotype crystals will not contribute to the signal. The Pd/(Si+Al) is lowest in both the SAPO-11- and ZSM-22-based catalysts after calcination and reduction. The dispersion in the SAPO-11-based catalysts is higher after calcination-reduction than after DR (Table S2.2), so more Pd atoms can contribute to the XPS signal if they are on the outer surface of the SAPO-11 crystals. For the catalysts with Pd in/on ZSM-22, the dispersions are very similar. Combining these results shows that the calcination-reduction method results in the largest amount of Pd residing inside the zeotype crystals.

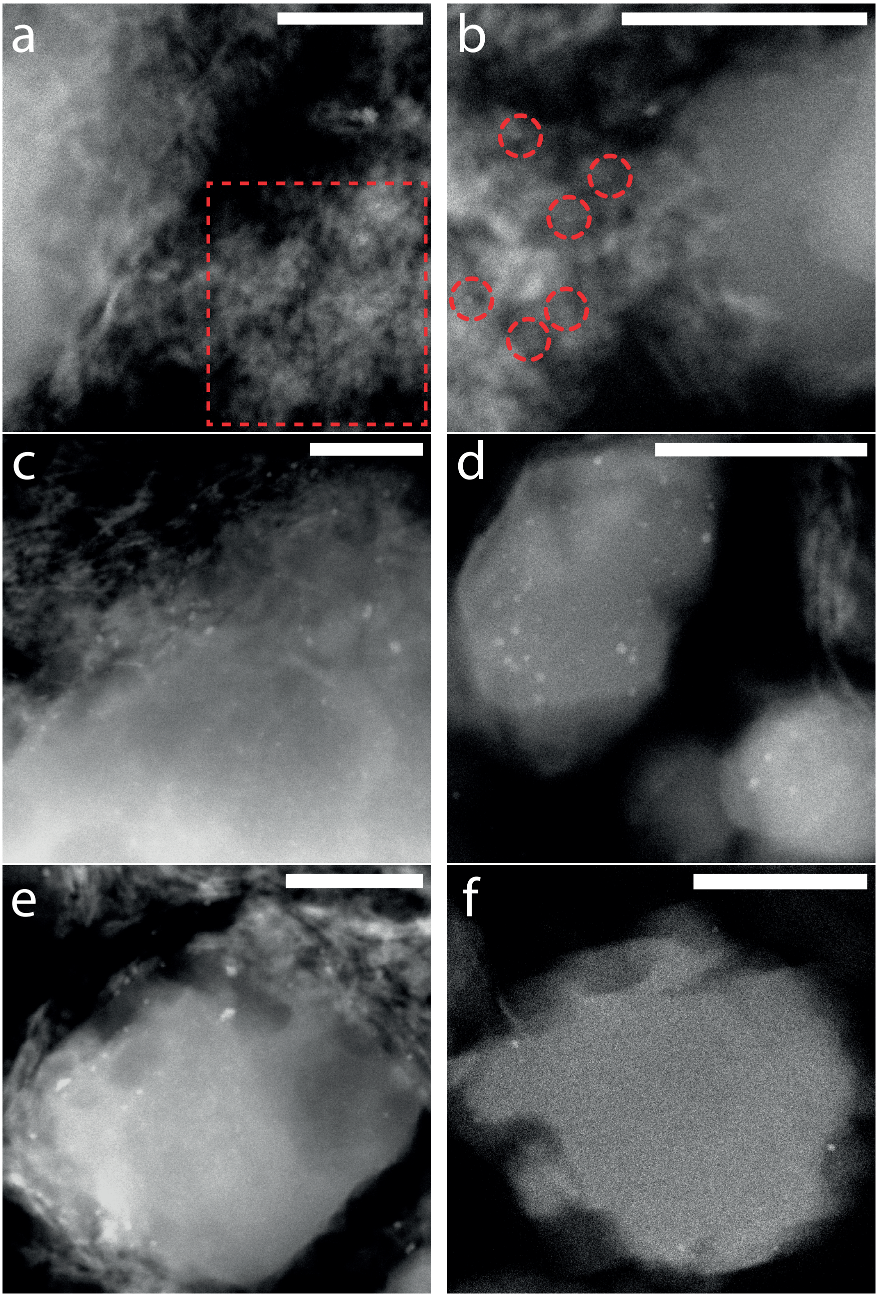

Figure 2.2. HAADF-STEM images of ultramicrotomed (thickness of 70 nm) catalyst samples: a) Pd-γ-Al_2O_3/SAPO-11, b) Pd-γ-Al_2O_3/ZSM-22, c) Pd-SAPO-11/γ-Al_2O_3 CR, d) Pd-ZSM-22/γ-Al_2O_3 CR, with cross sections of ZSM-22 crystals, e) Pd-SAPO-11/γ-Al_2O_3 DR, f) Pd-ZSM-22/γ-Al_2O_3 DR with cross sections of ZSM-22 crystals. Scalebars are 50 nm, red square and circles serve as guide to the eye towards Pd nanoparticles.

Moreover, based on the N_2 physisorption measurements of the samples containing no alumina, the CR procedure indeed leads to more pore blocking than DR, decreasing the BET surface area (Table S2.3). This is the case even while the DR samples have higher amounts of Pd than the CR samples used for these measurements.

Although CR and DR clearly affect the Pd nanoparticle location as observed with HAADF-STEM and XPS, STEM-EDX mapping reveals Pd nanoparticles on the outer surface of SAPO-11 in the Pd-SAPO-11/γ-Al_2O_3 CR catalysts as well (Figure 2.3). In these catalysts, some Pd nanoparticles are present on silica, which is not in the SAPO-11 framework. The placement of Pd on this extraframework silica diminishes the differences in Pd nanoparticle location between the SAPO-11-based catalysts.

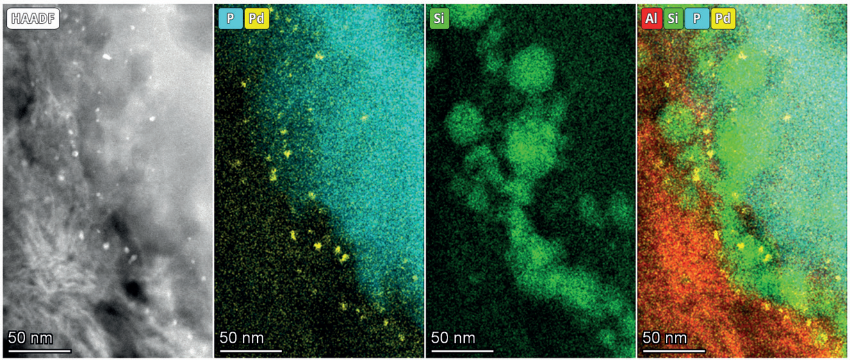

Figure 2.3. HAADF-STEM image and EDX-maps of an ultramicrotomed sample of reduced Pd-SAPO-11/γ-Al_2O_3 catalyst prepared with the calcination-reduction (CR) method. The elements Pd, P, Si and Al are depicted in yellow, blue, green and red, respectively.

The Effect of the Metal Nanoparticle Location on *n*-Heptane Conversion

The effect of the different catalyst preparation methods and hence the location was assessed during the hydroconversion of *n*-heptane. As can be seen in Figure 2.4a, the preparation method has only a limited impact on the catalytic activity of the different SAPO-11-based catalysts. Considering the selectivity (Figure 2.4b), at conversions above 60% the catalyst with Pd inside the SAPO-11 crystals (Pd-SAPO-11/γ-Al_2O_3 CR) is somewhat less selective towards *i*-heptane. This is in line with findings from previous works where lower isomer selectivity (and hence more cracking) is observed when Pt is in the zeolite crystals compared to catalysts with Pt on the alumina binder,[13,17,18] provided that the metal weight loading is high enough.[19] Surprisingly, the activity is slightly lower and the isomer selectivity is higher when the Pd nanoparticles are on the SAPO-11 crystals, which is the case for the Pd-SAPO-11/γ-Al_2O_3 DR catalyst.

When the hydroconversion of the ZSM-22-based catalysts is considered (Figure 2.4c,d), there are more distinct differences in the catalytic performance caused by a difference in the Pd nanoparticle location. Placing Pd on the alumina binder is clearly beneficial for the catalytic activity and selectivity. The catalytic activity and isomer selectivity is the lowest when Pd is located inside the ZSM-22 crystals, as is the case for Pd-ZSM-22/γ-Al_2O_3 CR catalysts. Interestingly, placing Pd particles on the outer surface of the ZSM-22 crystals by means of direct reduction can already partially induce the benefits of placing Pd on the alumina binder, as is shown by the in-between activity and selectivity of the Pd-ZSM-22/γ-Al_2O_3 DR catalyst. This result is further evidence for the effect of the heat treatment on the Pd location.

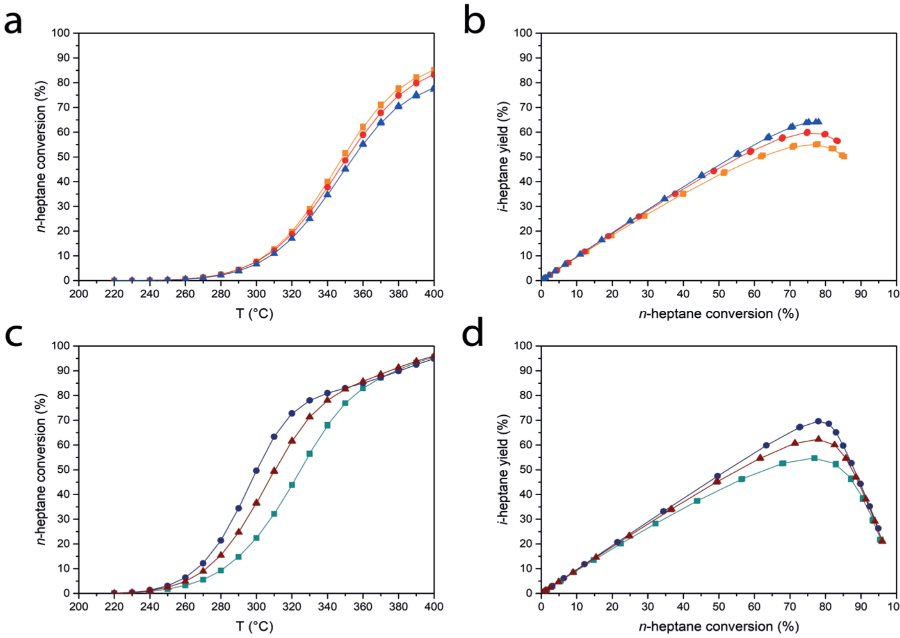

Figure 2.4. Results of the hydroconversion of *n*-heptane. a) *n*-heptane conversion as function of the temperature and b) *i*-heptane yield as function of the *n*-heptane conversion for Pd-SAPO-11/γ-Al_2O_3 CR (orange squares), Pd-γ-Al_2O_3/SAPO-11 (red circles) and Pd-SAPO-11/γ-Al_2O_3 DR (blue triangles). c) *n*-heptane conversion as function of the temperature and d) *i*-heptane yield as function of *n*-heptane conversion for Pd-ZSM-22/γ-Al_2O_3 CR (cyan squares), Pd-γ-Al_2O_3/ZSM-22 (dark blue circles) and Pd-ZSM-22/γ-Al_2O_3 DR (brown triangles).

However, unlike the results obtained with the SAPO-11-based catalysts, the DR catalyst shows intermediate performance in the ZSM-22 case. A tentative explanation is that after DR, there are still Pd nanoparticles present in the zeotype micropores, impeding intracrystalline diffusion and enlarging residence times, which causes (over)cracking. The differences in the maximum isomer yield in the SAPO-11-based catalysts are small compared to the differences exhibited by the ZSM-22 catalysts. This may be caused by the presence of Pd nanoparticles on extraframework silica, limiting the difference in Pd nanoparticle location in the SAPO-11-based catalysts.

The Effect of the Metal Nanoparticle Location on *n*-Hexadecane Conversion

If we compare the conversion of *n*-hexadecane for all SAPO-11-based catalysts (Figure 2.5a), the activity of the three catalysts is rather similar although at the highest temperatures some differences are apparent. Furthermore, if *i*-hexadecane selectivity is considered (Figure 2.5b), the highest isomer yield is observed when Pd is on the alumina binder. This is followed by the DR catalyst and the lowest isomer yield is obtained when the catalyst with Pd inside the SAPO-11 crystals is used. This is again in line with the results from previous work.[13,17,18,23] However, it slightly differs from the *n*-heptane results in which the DR catalyst shows the highest i-heptane selectivity. This difference can be attributed to the fact that fewer Pd nanoparticles are outside the SAPO-11 crystals in the DR catalyst compared to the catalyst with Pd on the alumina binder. The diffusivity of the longer molecule towards the Pd nanoparticles inside the crystals is impeded; hence the ratio between the available Pd sites and acid sites is lower than the overall n_{Pd}/n_A ratio. This is in line with previous results, which suggest that a higher n_M/n_A ratio is required to obtain the desired products during the conversion of longer hydrocarbon feedstocks.[34] Note that SAPO-11-based catalysts deactivate at higher temperatures. This may be caused by the presence of impurities in the SAPO-11 samples as evidenced by differences in the XRD patterns (Figure S2.4), SEM (Figure S2.5) and the aforementioned presence of extraframework silica (Figure 2.3).

For the ZSM-22-based catalysts, the catalyst with Pd on the alumina binder (Pd-γ-Al_2O_3/ZSM-22) displays the highest activity and *i*-hexadecane selectivity (Figure 2.5c,d). This catalyst is by far the most selective with a maximum isomer yield of over 70%. When Pd is mainly present inside the ZSM-22 crystals (Pd-ZSM-22/γ-Al_2O_3 CR), the isomer yield does not even reach 10%. This suggests that the majority of the Pd nanoparticles in this catalyst are inside the ZSM-22 crystals, thus giving rise to overcracking. The elevated isomer yield of the Pd-ZSM-22/γ-Al_2O_3 DR catalyst of about 30% shows that the DR results in a larger fraction of Pd on the outside of the ZSM-22 catalysts, allowing for more isomerization to occur. Note that at low conversion levels (< 5%), the isomer yields are very similar, whereas at higher conversion levels the isomer yields differ substantially.

The Effect of the Metal Nanoparticle Location on Hydrocracking Selectivities

The cracking patterns are compared by plotting the selectivity for each product against the product carbon number. Figure 2.6 shows the product selectivities over the Pd/zeotype/γ-Al_2O_3 catalysts during both *n*-heptane and *n*-hexadecane conversion. Next to isomerization, the main reactions are acid cracking, hydrogenolysis and dimerization cracking.[18] During the hydroconversion of *n*-heptane, the main products that are formed next to *i*-heptane are propane, *n*-butane and *i*-butane (Figure 2.6a,b). As *i*-butane and *n*-butane are products of different β-scission mechanisms,[3] their respective ratios tell us more about the mechanisms involved. For SAPO-11-based catalysts, *n*-butane yields are very low, resulting in high *i*-butane/*n*-butane (*i*-C_4/*n*-C_4) ratios. It shows that in all three catalysts, hydrocracking mainly occurs via

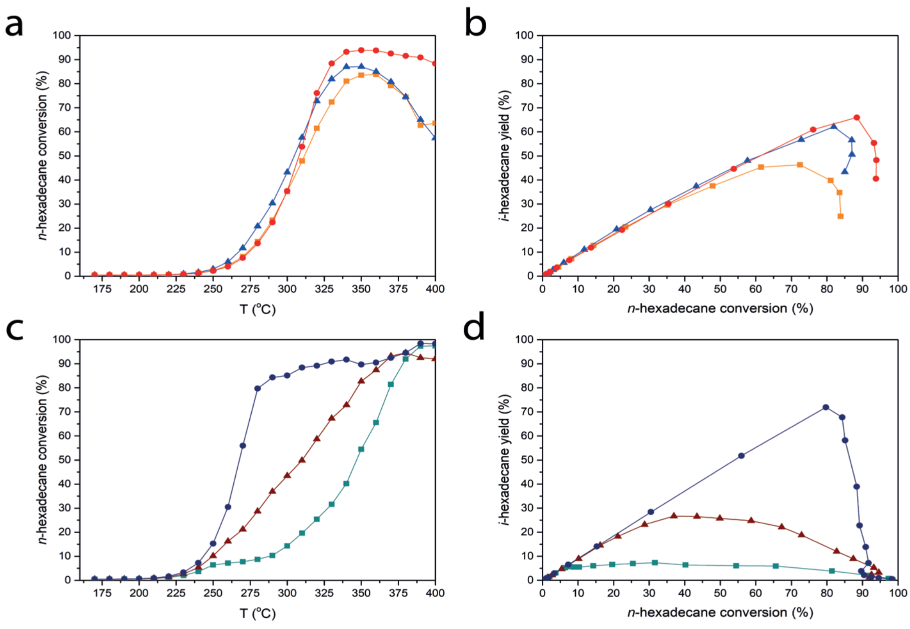

Figure 2.5. Results of the hydroconversion of *n*-hexadecane. a) *n*-hexadecane conversion as function of the temperature and b) *i*-hexadecane yield as function of the *n*-hexadecane conversion for Pd-SAPO-11/γ-Al_2O_3 CR (orange squares), Pd-γ-Al_2O_3/SAPO-11 (red circles) and Pd-SAPO-11/γ-Al_2O_3 DR (blue triangles). c) *n*-hexadecane conversion as function of the temperature and d) *i*-hexadecane yield as function of *n*-hexadecane conversion for Pd-ZSM-22/γ-Al_2O_3 CR (cyan squares), Pd-γ-Al_2O_3/ZSM-22 (dark blue circles) and Pd-ZSM-22/γ-Al_2O_3 DR (brown triangles).

the type B β-scission mechanism. This is a result of the relatively mild acidity of SAPO-11,[47,48] decreasing its ability to catalyze the energetically less favorable type C β-scission. ZSM-22 catalysts, on the contrary, produce less *i*-butane, with *i*-C_4/*n*-C_4 ratios ranging between 1.3 and 1.7, approaching a 50:50 ratio. This indicates that type B and type C β-scission mechanisms[3,49] occur to a rather similar extent. The higher acidity of ZSM-22 allows for more type C β-scission producing *n*-butane. Furthermore, the *i*-C_4/*n*-C_4 ratios for this set of catalysts increases when more Pd nanoparticles are assumed to be outside the ZSM-22 crystals, which is in line with previously obtained results.[13,18] When more metal nanoparticles are inside the zeolite crystals, the cracking reactions are more prone to confinement effects, also known as shape-selectivity, resulting in improved *n*-butane yields.

For the hydrocracking of *n*-hexadecane, as shown in Figure 2.6c,d, the more symmetrical these plots are, i.e., the more 'bell-shaped' the curve is (for every C_{10} molecule, a C_6 molecule is formed and for every C_8 molecule another C_8 molecule is formed, etc.), the more "ideal" hydrocracking takes place.[3] Ideal hydrocracking means that a catalyst tends to perform only one cracking step. If the selectivity peak is shifted towards lower carbon numbers, the catalyst performs more secondary cracking, resulting in the production of more shorter hydrocarbons. In practice, this is undesired as overcracking of the feedstock yields small hydrocarbons not suitable for gasoline, jet fuel or diesel applications. Although SAPO-11-based catalysts show relatively high isomer selectivity, the cracked products mainly originate from secondary cracking as can be observed in Figure 2.4c. This may be caused by the shape and size of the SAPO-11 pores (10MR, 0.39 nm x 0.63 nm). When hexadecane isomers reside inside these pores, diffusivities are very low, resulting in high residence time and the increased probability of secondary reactions such as cracking.

For both Pd-ZSM-22 catalysts, clearly not all Pd is outside the zeolite crystals as the selectivity towards the cracked products is still high and the isomer yield of only 30% is much lower than the isomer yield obtained when the Pd nanoparticles are on the alumina binder. As can be seen in Figure 2.6d, the Pd nanoparticle location impacts the cracking behavior of the ZSM-22-based catalysts. The catalyst with Pd on the alumina binder acts more like an “ideal” hydrocracking catalyst, as the plot is most similar to a bell-shaped carbon distribution.[3] If more of the Pd nanoparticles are present inside the ZSM-22 crystals — as is the case to some extent for the DR catalyst and even more for the Pd-ZSM-22/γ-Al_2O_3 CR catalyst — more secondary cracking occurs.

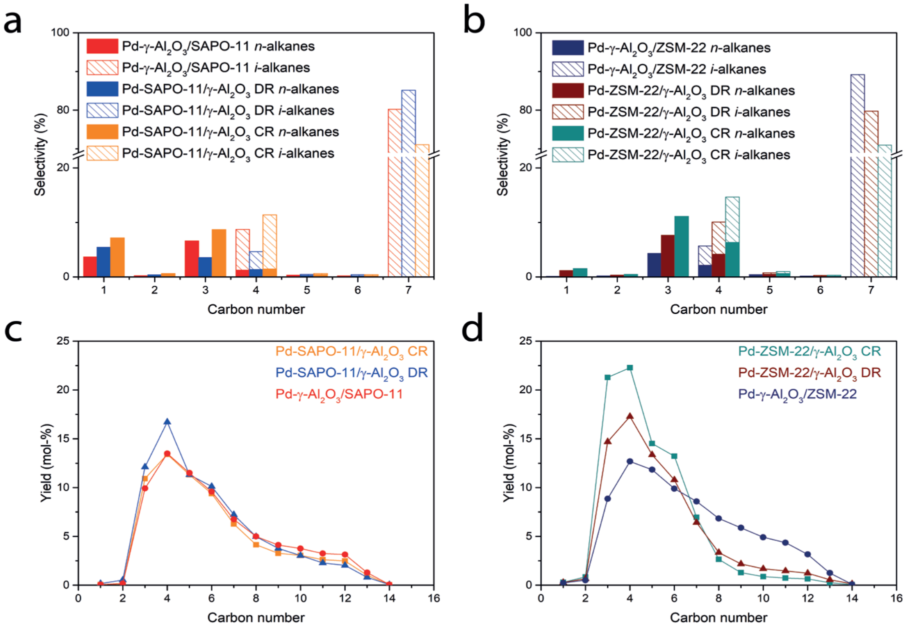

Figure 2.6. Distribution of products obtained during a) hydroconversion of *n*-heptane over SAPO-11-based catalysts at 75–77% conversion, b) hydroconversion of *n*-heptane over ZSM-22-based catalysts at 77–78% conversion, c) hydroconversion of *n*-hexadecane over Pd-SAPO-11/γ-Al_2O_3 (orange squares at T = 340 ˚C), Pd-γ-Al_2O_3/SAPO-11 (red circles at T = 350 ˚C) and Pd-SAPO-11/γ-Al_2O_3 DR (blue triangles at T = 380 ˚C) at 26–28% cracking yield and d) hydroconversion of *n*-hexadecane over Pd-ZSM-22/γ-Al_2O_3 (cyan squares at T = 340 ˚C), Pd-γ-Al_2O_3/ZSM-22 (dark blue circles at T = 320 ˚C) and Pd-ZSM-22/γ-Al_2O_3 DR (brown triangles at T = 330 ˚C) at 25–32% cracking yield.

In Table 2.2, an overview of the apparent activation energies for hydroconversion over the different catalysts is presented. These activation energies are derived from Arrhenius plots (Figure S2.6). The activation energies in the set of SAPO-11-based catalysts are virtually identical, indicating that there is no difference in diffusivity as a result of a difference in Pd location. This is in line with the fact that the catalytic activity of these catalysts is not impacted by the Pd location, possibly caused by the presence of Pd particles on the extraframework silica in the SAPO-11 catalysts. Furthermore, this extraframework silica can have a rate-enhancing effect, increasing the transport of molecules of which the intracrystalline diffusion is not limited.[50] This possibly results in similar diffusion rates for all three catalysts.

For the ZSM-22-based catalysts, however, the Pd location has a great impact on the activity and the apparent activation energy of both *n*-heptane and *n*-hexadecane conversion. This difference in activation energy is most probably a result of the diffusion effects caused by a difference in the Pd nanoparticle location.[18] Here, the DR catalyst shows activation energies that are in between the activation energies of the Pd-on-alumina and the Pd-in- ZSM-22 catalysts, indicating that as a result of the DR treatment indeed more of the Pd nanoparticles are located *on* the ZSM-22 crystals.

Table 2.2. Apparent activation energies (E_a) for the hydroconversion of *n*-heptane and *n*-hexadecane over each catalyst.

Catalyst	E_a *n*-Heptane Conversion (kJ mol^{-1})	E_a *n*-Hexadecane Conversion (kJ mol^{-1})
Pd-γ-Al_2O_3/SAPO-11	148 ± 1	143 ± 4
Pd-SAPO-11/γ-Al_2O_3 DR	152 ± 1	140 ± 2
Pd-SAPO-11/γ-Al_2O_3 CR	150 ± 1	140 ± 1
Pd-γ-Al_2O_3/ZSM-22	173 ± 4	148 ± 8
Pd-ZSM-22/γ-Al_2O_3 DR	160 ± 4	119 ± 2
Pd-ZSM-22/γ-Al_2O_3 CR	135 ± 1	85 ± 1

Overall, the effect of the heat treatment during the preparation of the Pd-ZSM-22 catalysts is more profound than in the Pd-SAPO-11 catalysts. This effect is found in all product distributions. The apparent activation energies for both *n*-heptane and *n*-hexadecane conversion are also largely impacted by the Pd nanoparticle location in the ZSM-22-based catalysts, whereas they are not affected in the SAPO-11-based catalysts (Table 2.2). This can be a result of the fact that in general, more of the Pd nanoparticles end up on the outside of the SAPO-11 crystals regardless of the heat treatment as evidenced by the comparison of the Pd/(Si+Al) surface versus bulk ratios (Table 2.1) and the presence of Pd on extraframework silica revealed with EDX (Figure 2.3).

2.4. Conclusions

The heat treatment of zeotypes that underwent IE with $[Pd(NH_3)_4](NO_3)_2$ impacted the final location of the Pd nanoparticles with respect to the acid sites. Although in both cases, metal nanoparticles seemed to be inside and on the zeotype crystals, our results showed that a slow calcination followed by a reduction resulted in more Pd particles inside the zeotype crystals. Direct reduction, on the other hand, caused more Pd nanoparticles to end up on the zeotype crystals. This was further investigated using TEM and XPS. For the SAPO-11-based catalysts, HAADF-STEM showed to be a tool to investigate the differences in location. The XPS revealed more clear differences in nanoparticle location for the ZSM-22 catalysts. In turn, the hydroconversion of *n*-heptane and *n*-hexadecane clearly showed differences in Pd nanoparticle location, as having more Pd nanoparticles on the outside was beneficial for the activity and selectivity towards the isomers for both sets of catalysts. Having Pd on the alumina binder was still the most beneficial for the hydroconversion performance. Direct reduction could be used to prepare catalysts with more Pd on the outer surface of the zeotype crystals, resulting in an intermediate hydroconversion performance. The calcination-reduction treatment was a strategy to encapsulate Pd nanoparticles inside the crystals of the zeolitic materials, and was disadvantageous for hydroconversion purposes.

Acknowledgements

The authors thank Dennie Wezendonk, Jan Willem de Rijk and Remco Dalebout for their help commissioning the Flowrence setup. Claudia Keijzer is thanked for SEM imaging. Remco Dalebout, Laura Barberis, Kristiaan Helfferich and Suzan Schoemaker are acknowledged for performing the N_2 physisorption measurements.

References

(1) Martínez, C.; Corma, A. Inorganic Molecular Sieves: Preparation, Modification and Industrial Application in Catalytic Processes. *Coordination Chemistry Reviews*. 2011, pp 1558–1580.

(2) Mäki-Arvela, P.; Khel, T. A. K.; Azkaar, M.; Engblom, S.; Murzin, D. Y. Catalytic Hydroisomerization of Long-Chain Hydrocarbons for the Production of Fuels. *Catalysts* **2018**, *8* (11).

(3) Weitkamp, J. Catalytic Hydrocracking—Mechanisms and Versatility of the Process. *ChemCatChem* **2012**, *4* (3), 292–306.

(4) Bouchy, C.; Hastoy, G.; Guillon, E.; Martens, J. A. Fischer-Tropsch Waxes Upgrading via Hydrocracking and Selective Hydroisomerization. *Oil Gas Sci. Technol.* **2009**, *64* (1), 91–112.

(5) Sousa-Aguiar, E. F.; Noronha, F. B.; Faro, A. The Main Catalytic Challenges in GTL (Gas-to-Liquids) Processes. *Catal. Sci. Technol.* **2011**, *1* (5), 698–713.

(6) Tran, N. H.; Bartlett, J. R.; Kannangara, G. S. K.; Milev, A. S.; Volk, H.; Wilson, M. A. Catalytic Upgrading of Biorefinery Oil from Micro-Algae. *Fuel* **2010**, *89* (2), 265–274.

(7) Peng, B.; Yao, Y.; Zhao, C.; Lercher, J. A. Towards Quantitative Conversion of Microalgae Oil to Diesel-Range Alkanes with Bifunctional Catalysts. *Angew. Chemie - Int. Ed.* **2012**, *51* (9), 2072–2075.

(8) Kots, P. A.; Vance, B. C.; Vlachos, D. G. Polyolefin Plastic Waste Hydroconversion to Fuels, Lubricants, and Waxes: A Comparative Study. *React. Chem. Eng.* **2022**, *7* (1), 41–54.

(9) Corma, A. Transformation of Hydrocarbons on Zeolite Catalysts. *Catal. Letters* **1993**, *22* (1–2), 33–52.

(10) Vogt, E. T. C.; Whiting, G. T.; Dutta Chowdhury, A.; Weckhuysen, B. M. Zeolites and Zeotypes for Oil and Gas Conversion. *Adv. Catal.* **2015**, *58*, 143–314.

(11) Wang, W.; Liu, C.-J.; Wu, W. Bifunctional Catalysts for the Hydroisomerization of N-Alkanes: The Effects of Metal–Acid Balance and Textural Structure. *Catal. Sci. Technol.* **2019**, *9* (16), 4162–4187.

(12) Del Campo, P.; Martínez, C.; Corma, A. Activation and Conversion of Alkanes in the Confined Space of Zeolite-Type Materials. *Chem. Soc. Rev.* **2021**, *50* (15), 8511–8595.

(13) Oenema, J.; Harmel, J.; Vélez, R. P.; Meijerink, M. J.; Eijsvogel, W.; Poursaeidesfahani, A.; Vlugt, T. J. H.; Zečević, J.; de Jong, K. P. Influence of Nanoscale Intimacy and Zeolite Micropore Size on the Performance of Bifunctional Catalysts for N-Heptane Hydroisomerization. *ACS Catal.* **2020**, *10* (23), 14245–14257.

(14) Mendes, P. S. F.; Silva, J. M.; Ribeiro, M. F.; Daudin, A.; Bouchy, C. Bifunctional Intimacy and Its Interplay with Metal-Acid Balance in Shaped Hydroisomerization Catalysts. *ChemCatChem* **2020**, *12* (18), 4582–4592.

(15) Weisz, P. B. Stepwise Reaction via Intermediates on Separate Catalytic Centers. *Science* **1956**, *123* (3203), 887–888.

(16) Weisz, P. B.; Swegler, E. W. Stepwise Reaction on Separate Catalytic Centers: Isomerization of Saturated Hydrocarbons. *Science* **1957**, *126* (3262), 31–32.

(17) Zečević, J.; Vanbutsele, G.; de Jong, K. P.; Martens, J. A. Nanoscale Intimacy in Bifunctional Catalysts for Selective Conversion of Hydrocarbons. *Nature* **2015**, *528* (7581), 245–254.

(18) Cheng, K.; van der Wal, L. I.; Yoshida, H.; Oenema, J.; Harmel, J.; Zhang, Z.; Sunley, G.; Zečević, J.; de Jong, K. P. Impact of the Spatial Organization of Bifunctional Metal–Zeolite Catalysts on the Hydroisomerization of Light Alkanes. *Angew. Chemie - Int. Ed.* **2020**, *59* (9), 3592–3600.

(19) Cheng, K.; Smulders, L. C. J.; van der Wal, L. I.; Oenema, J.; Meeldijk, J. D.; Visser, N. L.; Sunley, G.; Roberts, T.; Xu, Z.; Doskocil, E.; Yoshida, H.; Zheng, Y.; Zečević, J.; de Jongh, P. E.; de Jong, K. P. Maximizing Noble Metal Utilization in Solid Catalysts by Control of Nanoparticle Location. *Science* **2022**, *377* (6602), 204–208.

(20) Kim, J.; Kim, W.; Seo, Y.; Kim, J. C.; Ryoo, R. N-Heptane Hydroisomerization over Pt/MFI Zeolite Nanosheets: Effects of Zeolite Crystal Thickness and Platinum Location. *J. Catal.* **2013**, *301*, 187–197.

(21) Noh, G.; Shi, Z.; Zones, S. I.; Iglesia, E. Isomerization and Β-Scission Reactions of Alkanes on Bifunctional Metal-Acid Catalysts: Consequences of Confinement and Diffusional Constraints on Reactivity and Selectivity. *J. Catal.* **2018**, *368*, 389–410.

(22) Noh, G.; Zones, S. I.; Iglesia, E. Isomer Sieving and the Selective Formation of Terminal Methyl Isomers in Reactions of Linear Alkanes on One-Dimensional Zeolites. *J. Catal.* **2019**, *377*, 255–270.

(23) Oenema, J.; Hofmann, J. P.; Hensen, E. J. M.; Zečević, J.; de Jong, K. P. Assessment of the Location of Pt Nanoparticles in Pt/Zeolite Y/γ-Al2O3 Composite Catalysts. *ChemCatChem* **2020**, *12* (2), 615–622.

(24) Höchtl, M.; Jentys, A.; Vinek, H. Hydroisomerization of Heptane Isomers over Pd/SAPO Molecular Sieves: Influence of the Acid and Metal Site Concentration and the Transport Properties on the Activity and Selectivity. *J. Catal.* **2000**, *190* (2), 419–432.

(25) Höchtl, M.; Jentys, A.; Vinek, H. Alkane Conversion over Pd/SAPO Molecular Sieves: Influence of Acidity, Metal Concentration and Structure. *Catal. Today* **2001**, *65* (2–4), 171–177.

(26) Wang, D.; Liu, J.; Cheng, X.; Kang, X.; Wu, A.; Tian, C.; Fu, H. Trace Pt Clusters Dispersed on SAPO-11 Promoting the Synergy of Metal Sites with Acid Sites for High-Effective Hydroisomerization of N-Alkanes. *Small Methods* **2019**, *3* (5), 1800510.

(27) Sinha, A. K.; Sivasanker, S. Hydroisomerization of N-Hexane over Pt-SAPO-11 and Pt-SAPO-31 Molecular Sieves. *Catal. Today* **1999**, *49* (1–3), 293–302.

(28) Wang, Z.; Tian, Z.; Teng, F.; Wen, G.; Xu, Y.; Xu, Z.; Lin, L. Hydroisomerization of Long-Chain Alkane over Pt/SAPO-11 Catalysts Synthesized from Nonaqueous Media. *Catal. Letters* **2005**, *103* (1–2), 109–116.

(29) van den Broek, A. C. M.; van Grondelle, J.; van Santen, R. A. Preparation of Highly Dispersed Platinum Particles in HZSM-5 Zeolite: A Study of the Pretreatment Process of [Pt(NH3)4]2+. *J. Catal.* **1997**, *167* (2), 417–424.

(30) Reagan, W. J.; Chester, A. W.; Kerr, G. T. Studies of the Thermal Decomposition and Catalytic Properties of Some Platinum and Palladium Ammine Zeolites. *J. Catal.* **1981**, *69* (1), 89–100.

(31) de Graaf, J.; van Dillen, A. J.; de Jong, K. P.; Koningsberger, D. C. Preparation of Highly Dispersed Pt Particles in Zeolite Y with a Narrow Particle Size Distribution: Characterization by Hydrogen Chemisorption, TEM, EXAFS Spectroscopy, and Particle Modeling. *J. Catal.* **2001**, *203* (2), 307–321.

(32) Chen, H.; Li, W.; Zhang, M.; Wang, W.; Zhang, X. H.; Lu, F.; Cheng, K.; Zhang, Q.; Wang, Y. Boosting Propane Dehydroaromatization by Confining PtZn Alloy Nanoparticles within H-ZSM-5 Crystals. *Catal. Sci. Technol.* **2022**, *12* (24), 7281–7292.

(33) Goel, S.; Wu, Z.; Zones, S. I.; Iglesia, E. Synthesis and Catalytic Properties of Metal Clusters Encapsulated within Small-Pore (SOD, GIS, ANA) Zeolites. *J. Am. Chem. Soc.* **2012**, *134* (42), 17688–17695.

(34) van der Wal, L. I.; Oenema, J.; Smulders, L. C. J.; Samplonius, N. J.; Nandpersad, K. R.; Zečević, J.; de Jong, K. P. Control and Impact of Metal Loading Heterogeneities at the Nanoscale on the Performance of Pt/Zeolite Y Catalysts for Alkane Hydroconversion. *ACS Catal.* **2021**, *11* (7), 3842–3855.

(35) Winter, F.; Bezemer, G. L.; van der Spek, C.; Meeldijk, J. D.; van Dillen, A. J.; Geus, J. W.; de Jong, K. P. TEM and XPS Studies to Reveal the Presence of Cobalt and Palladium Particles in the Inner Core of Carbon Nanofibers. *Carbon* **2005**, *43* (2), 327–332.

(36) Wang, N.; Sun, Q.; Bai, R.; Li, X.; Guo, G.; Yu, J. In Situ Confinement of Ultrasmall Pd Clusters within Nanosized Silicalite-1 Zeolite for Highly Efficient Catalysis of Hydrogen Generation. *J. Am. Chem. Soc.* **2016**, *138* (24), 7484–7487.

(37) Cho, H. R.; Regalbuto, J. R. The Rational Synthesis of Pt-Pd Bimetallic Catalysts by Electrostatic Adsorption. *Catal. Today* **2015**, *246*, 143–153.

(38) Emeis, C. A. Determination of Integrated Molar Extinction Coefficients for Infrared Absorption Bands of Pyridine Adsorbed on Solid Acid Catalysts. *J. Catal.* **1993**, *141* (2), 347–354.

(39) Busca, G. Spectroscopic Characterization of the Acid Properties of Metal Oxide Catalysts. *Catal. Today* **1998**, *41* (1–3), 191–206.

(40) Velthoen, M. E. Z.; Nab, S.; Weckhuysen, B. M. Probing Acid Sites in Solid Catalysts with Pyridine UV-Vis Spectroscopy. *Phys. Chem. Chem. Phys.* **2018**, *20* (33), 21647–21659.

(41) Agarwal, U.; Rigutto, M. S.; Zuidema, E.; Jansen, A. P. J.; Poursaeidesfahani, A.; Sharma, S.; Dubbeldam, D.; Vlugt, T. J. H. Kinetics of Zeolite-Catalyzed Heptane Hydroisomerization and Hydrocracking with CBMC-Modeled Adsorption Terms : Zeolite Beta as a Large Pore Base Case. **2022**, *415*, 37–50.

(42) Guisnet, M.; Alvarez, F.; Giannetto, G.; Perot, G. Hydroisomerization and Hydrocracking of N-Heptane on PtH Zeolites. Effect of the Porosity and of the Distribution of Metallic and Acid Sites. *Catal. Today* **1987**, *1* (4), 415–433.

(43) Alvarez, F.; Ribeiro, F. R.; Perot, G.; Thomazeau, C.; Guisnet, M. Hydroisomerization and Hydrocracking of Alkanes. *J. Catal.* **1996**, *162* (2), 179–189.

(44) Bagshaw, S. A.; Cooney, R. P. FTIR Surface Site Analysis of Pillared Clays Using Pyridine Probe Species. *Chem. Mater.* **1993**, *5* (8), 1101–1109.

(45) Barzetti, T.; Selli, E.; Moscotti, D.; Forni, L. Pyridine and Ammonia as Probes for FTIR Analysis of Solid Acid Catalysts. *J. Chem. Soc. - Faraday Trans.* **1996**, *92* (8), 1401–1407.

(46) Velthoen, M. E. Z.; Muñoz-Murillo, A.; Bouhmadi, A.; Cecius, M.; Diefenbach, S.; Weckhuysen, B. M. The Multifaceted Role of Methylaluminoxane in Metallocene-Based Olefin Polymerization Catalysis. *Macromolecules* **2018**, *51* (2), 343–355.

(47) Lok, B. M.; Messina, C. A.; Patton, R. L.; Gajek, R. T.; Cannan, T. R.; Flanigen, E. M. Silicoaluminophosphate Molecular Sieves: Another New Class of Microporous Crystalline Inorganic Solids. *J. Am. Chem. Soc.* **1984**, *106* (20), 6092–6093.

(48) Martens, J. A.; Grobet, P. J.; Jacobs, P. A. Catalytic Activity and Si, Al, P Ordering in Microporous Silicoaluminophosphates of the SAPO-5, SAPO-11, and SAPO-37 Type. *J. Catal.* **1990**, *126* (1), 299–305.

(49) Martens, J. A.; Tielen, M.; Jacobs, P. A. Attempts to Rationalize the Distribution of Hydrocracked Products. III. Mechanistic Aspects of Isomerization and Hydrocracking of Branched Alkanes on Ideal Bifunctional Large-Pore Zeolite Catalysts. *Catal. Today* **1987**, *1* (4), 435–453.

(50) Gobin, O. C.; Reitmeier, S. J.; Jentys, A.; Lercher, J. A. Role of the Surface Modification on the Transport of Hexane Isomers in ZSM-5. *J. Phys. Chem. C* **2011**, *115* (4), 1171–1179.

Supporting Information

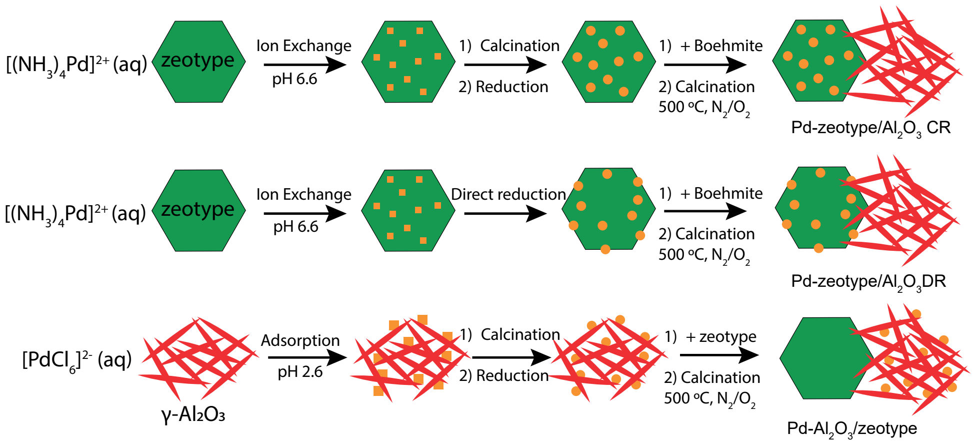

Figure S2.1. Schematic overview of catalyst synthesis.

Table S2.1. Number of acid sites as determined using NH_3-TPD and FT-IR using pyridine (Py) as probe molecule.

Material	NH_3-TPD (mmol g^{-1})			Py-FT-IR (mmol g^{-1})	
	Weak	**Medium/ Strong**	**Total**	**BAS**	**LAS**
SAPO-11	0.17	0.22	0.40	0.082	0.021
ZSM-22	0.20	0.28	0.48	0.081	0.016
γ-Al_2O_3	-	-	0.46	0	0.226
SAPO-11/γ-Al_2O_3	0.08	0.27	0.35	0.020	0.096
ZSM-22/γ-Al_2O_3	0.14	0.35	0.49	0.025	0.086
Pd-γ-Al_2O_3/SAPO-11	0.08	0.29	0.37	0.015	0.112
Pd-SAPO-11/γ-Al_2O_3 DR	0.08	0.26	0.34	n.d.	n.d.
Pd-SAPO-11/γ-Al_2O_3 CR	0.07	0.25	0.32	0.018	0.117
Pd-γ-Al_2O_3/ZSM-22	0.17	0.37	0.53	0.023	0.149
Pd-ZSM-22/γ-Al_2O_3 DR	0.14	0.35	0.49	n.d.	n.d.
Pd-ZSM-22/γ-Al_2O_3 CR	0.15	0.33	0.48	0.019	0.108

Table S2.2. Palladium loading, palladium nanoparticle properties and acid properties of each catalyst.

Material	Pd weight loading [a] (wt%)	Pd size, d_{Pd} [b] (nm)	D [c] (%)	n_{Pd} [d] (mmol g^{-1})	n_A [e] (mmol g^{-1})	n_{Pd}/n_A
Pd-γ-Al_2O_3/SAPO-11	0.49	2.0 ± 0.4	56	0.026	0.29	0.088
Pd-SAPO-11/γ-Al_2O_3 DR	0.45	2.3 ± 0.9	48	0.020	0.26	0.079
Pd-SAPO-11/γ-Al_2O_3 CR	0.41	1.7 ± 0.4	65	0.025	0.25	0.101
Pd-γ-Al_2O_3/ZSM-22	0.50	2.0 ± 0.4	56	0.024	0.37	0.064
Pd-ZSM-22/γ-Al_2O_3 DR	0.44	1.9 ± 0.4	59	0.024	0.35	0.069
Pd-ZSM-22/γ-Al_2O_3 CR	0.41	2.1 ± 0.4	53	0.020	0.33	0.062

[a] By inductively coupled plasma optical emission spectroscopy on digested samples.

[b] Number average particle size by measurement Pd nanoparticle diameter of at least 400 particles in STEM images.

[c] Dispersion of Pd nanoparticles using Dispersion = 1.112/dPd

[d] Calculated based on the ICP weight loading of Pd and the dispersion.

[e] By deconvolution of NH3-TPD profiles and integration of the peak at higher temperatures (T ≥ 200 °C for SAPO-11 and T ≥ 300 °C for ZSM-22).

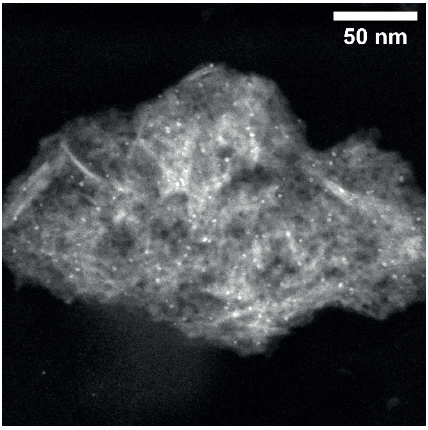

Figure S2.2. HAADF-STEM image of Pd/γ-Al_2O_3 before mixing with a zeotype material.

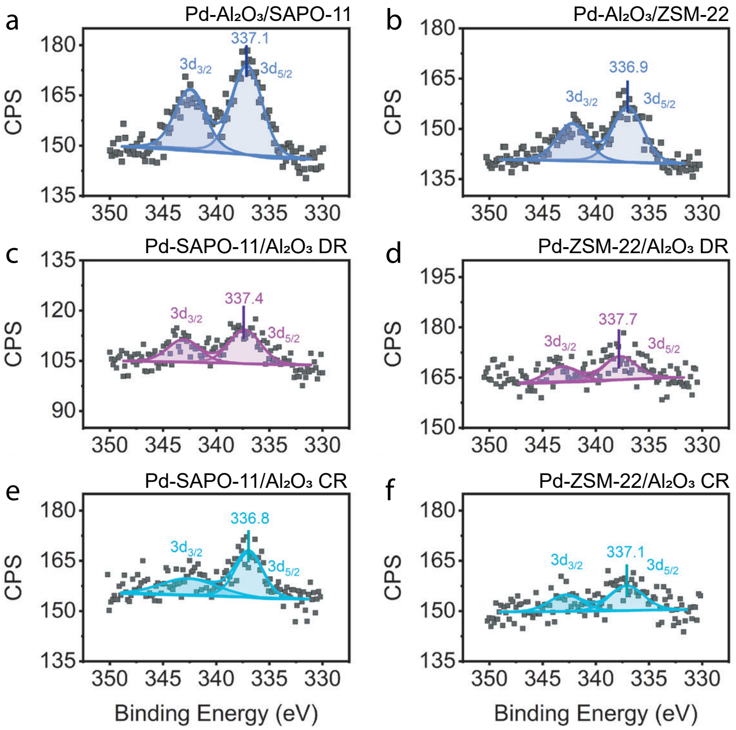

Figure S2.3. XPS spectra of Pd in all catalysts.

Table S2.3. N_2 physisorption on samples without γ-alumina.

Sample	S_{BET} **(m² g⁻¹)**	S_{micro} **(m² g⁻¹)**	S_{ext} **(m² g⁻¹)**	V_{total} **(cm³ g⁻¹)**	V_{micro} **(cm³ g⁻¹)**	S_{langmuir} **(m² g⁻¹)**
SAPO-11	134	56	78	0.17	0.024	147
0.5Pd-SAPO-11 CR	122	58	64	0.16	0.024	129
1Pd-SAPO-11 DR	131	68	64	0.16	0.028	142
ZSM-22	126	70	56	0.19	0.029	136
0.5Pd-ZSM-22 CR	138	83	55	0.32	0.033	144
0.9Pd-ZSM-22 DR	174	93	83	0.22	0.040	194

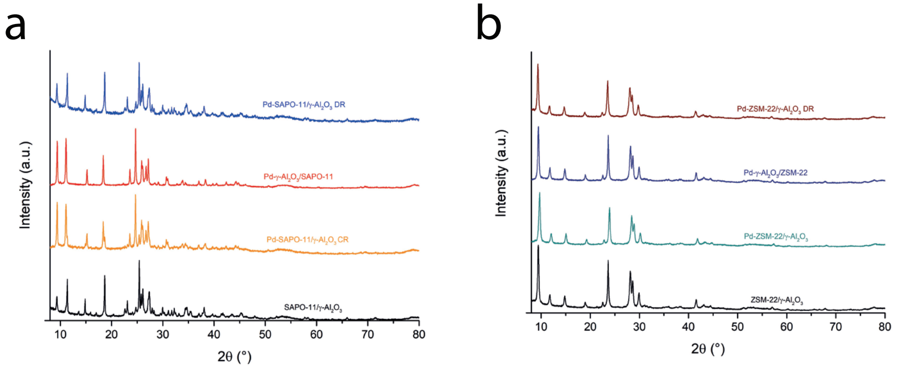

Figure S2.4. XRD patterns of a) SAPO-11 based catalysts and b) ZSM-22 based catalysts each catalyst and zeotype/alumina composite materials.

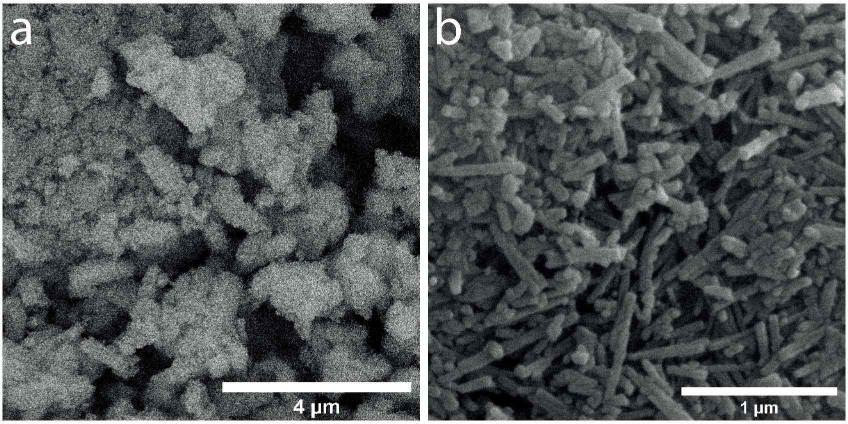

Figure S2.5. SEM images of as-received a) SAPO-11 and b) ZSM-22. As can be seen in a) the SAPO-11 sample contains both the typical cuboid SAPO-11 crystals, as well as a less crystalline component (top right). In b) the needle-like shape of ZSM-22 is evident.

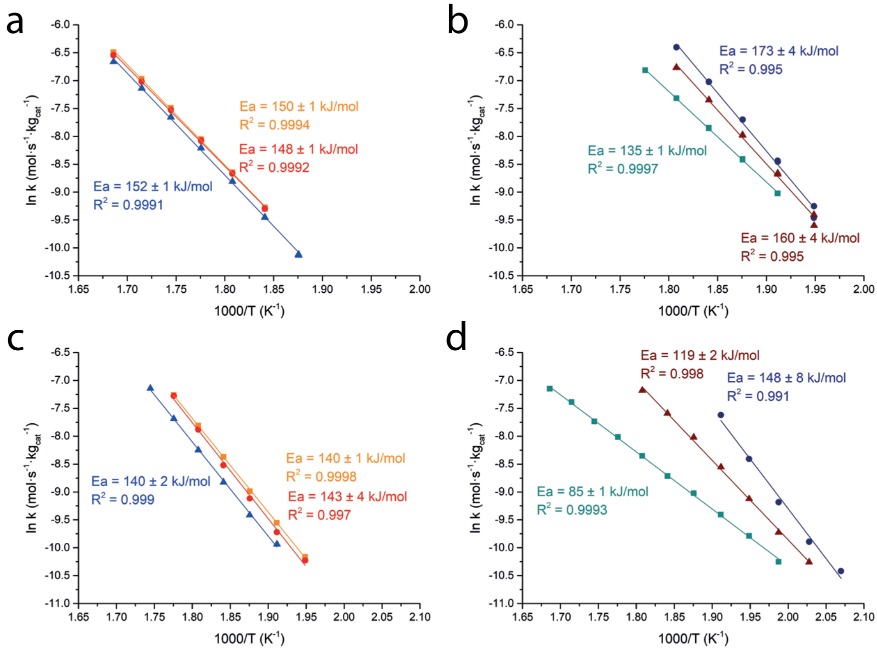

Figure S2.6. Arrhenius plots of a) *n*-heptane conversion over SAPO-11 based catalysts, b) *n*-heptane conversion over ZSM-22 based catalysts, c) *n*-hexadecane conversion over SAPO-11 based catalysts and d) *n*-hexadecane conversion over ZSM-22 based catalysts. The catalysts are depicted as follows: Pd-SAPO-11/γ-Al_2O_3 (CR) (orange squares), Pd-γ-Al_2O_3/SAPO-11 (red circles), Pd-SAPO-11/γ-Al_2O_3 (DR) (blue triangles), Pd-ZSM-22/γ-Al_2O_3 (CR) (dark cyan squares), Pd-γ-Al_2O_3/ZSM-22 (dark blue circles) and Pd-ZSM-22/γ-Al_2O_3 (DR) (brown triangles). The plots are based on measurements below 20 % conversion. Reaction conditions of *n*-heptane conversion: P = 10 bar, H_2/*n*-heptane = 10 : 1 (mol/mol), WHSV = 2.4 $g_{n\text{-}C7} \cdot g_{cat}^{-1} \cdot h^{-1}$. Reaction conditions of *n*-hexadecane conversion: P = 5 bar, H_2/*n*-heptane = 10 : 1 (mol/mol), WHSV = 2.9 $g_{n\text{-}C16} \cdot g_{cat}^{-1} \cdot h^{-1}$.

Chapter 3

Maximizing noble metal utilization in bifunctional catalysts by control of metal nanoparticle location

Abstract: Maximizing the utilization of noble metals is crucial for applications such as catalysis. We found that the minimum loading of platinum for optimal performance in the hydroconversion of *n*-alkanes for industrially relevant bifunctional catalysts could be reduced by a factor of 10 or more through the rational arranging of functional sites at the nanoscale. Intentionally depositing traces of platinum nanoparticles on the alumina binder or the outer surface of zeolite crystals, instead of inside the zeolite crystals, enhanced isomer selectivity without compromising activity. Separation between platinum and zeolite acid sites preserved the metal and acid functions by limiting micropore blockage by metal clusters and enhancing access to metal sites. Reduced platinum nanoparticles were more active than platinum single atoms strongly bonded to the alumina binder.

This chapter is based on: Cheng K.*; Smulders, L.C.J.*; van der Wal, L.I.; Oenema, J.; Meeldijk, J.D.; Visser, N.L.; Sunley, G.J.; Roberts, S.T.; Xu, Z.; Doskocil, E.; Yoshida, H.; Zheng, Y.; Zecevic, J.; de Jongh, P.E.; de Jong, K.P., Maximizing noble metal utilization in solid catalysts by control of nanoparticle location, *Science* **2022**, (377), 204-208.

*These authors contributed equally.

3.1. Introduction

Noble metals (NMs) are widely used in a variety of commercial and emerging technologies, including catalytic converters in automobiles; electrocatalysts in hydrogen fuel cells; and, as described in Chapter 1, catalysts for petroleum, biomass, and waste conversion.[1–5] Increasing demand for NMs in these applications is driving approaches that make more efficient use of NMs,[6–9] including so-called single-atom catalysts (SACs) in which isolated single metal atoms or ions are stabilized by the support.[10–13] However, strong metal-support interactions often lead to limited reducibility and in some cases low reactivity. Confinement of NMs inside zeolite channels or cages can benefit the adsorption of reagents and stabilization of reaction intermediates to improve catalytic activity, product selectivity, or both.[14–16] Successful examples of confinement effects have been demonstrated for the conversion of small molecules, including carbon monoxide (CO) oxidation, methane (CH_4) oxidation, and the water-gas shift reaction.[17–19]

In the petrochemical industry, platinum (Pt) is frequently used in combination with acidic zeolites for the hydroconversion of linear alkanes to enhance the quality of liquid fuels (Figure S3.1), and its performance is influenced by the Pt nanoparticle (NP) size and distribution, metal-support interactions, and acidic properties.[20–23] To describe the required Pt loading sufficient to maintain the bifunctional metal-acid balance in hydroconversion catalysts, Guisnet and coworkers proposed a widely applied parameter of the surface Pt sites to Brønsted acid sites ratio (n_{Pt}/n_A).[24] To meet this criterion, the typical Pt loading for bifunctional catalysts is in the range of 0.3 to 3 wt%.[25–27] For integrating two functional components, Weisz's intimacy criterion, which is often interpreted as "the closer the better," has been applied to spatial organization.[28]

Recently, we have shown at Pt loadings around 0.5 wt% that separation of Pt and acid sites at the nanoscale enhanced the isomer selectivity in hydroisomerization of linear alkanes, whereas placing Pt inside zeolite crystals with closest proximity promoted acid-catalyzed cracking or overcracking reactions because of the high concentrations of intracrystalline carbenium ions.[29–31] With this concept of nanoscale intimacy, we found that lowering the Pt loading holds potential,[30] which inspired us to a study of the lower limit of NMs for catalysis as a function of the Pt NP location.

We controlled the Pt location and loading on industrially relevant platinum-zeolite-alumina (Al_2O_3) composite catalysts to decrease the Pt loading for hydroisomerization while maintaining optimal performance. We used *n*-heptane as a model molecule relevant to gasoline upgrading. We used the one-dimensional (1D) zeolites HZSM-22 and HMOR to construct bifunctional catalysts. To provide mechanical stability and to avoid the high-pressure drop in industrial fixed-bed reactors, zeolite catalysts need to be shaped into composites—for example, as extrudates with the use of a binder such as clay.[32] The location of Pt sites in these composite catalysts can be roughly classified into three types: (i) on the outer surface of zeolite crystals; (ii) inside the zeolite crystals; and (iii) on the binder.

3.2. Materials and Methods

Materials

NH_4-MOR (CBV 21A, Si/Al = 10 at/at) was purchased from Zeolyst. HZSM-22 (Si/Al = 32.5–40 at/at) was purchased from ACS Material. Boehmite (70 wt% Al_2O_3) was supplied by Shell Technology. $[Pt(NH_3)_4](NO_3)_2$ (99.995% purity), $H_2[PtCl_6]\cdot 6H_2O$ (≥ 37.5 wt% Pt), Pluronic P123 (Mn ~5,800), acetic acid, and aluminum isopropoxide (≥ 98%) were purchased from SigmaAldrich.

Catalyst Preparation

Both NH_4-MOR and HZSM-22 were calcined at 500 °C for 5 h with a heating ramp of 1 °C min^{-1}. A zeolite-alumina composite (50 wt% / 50 wt%) was prepared using acetic acid as a peptizing agent to deagglomerate boehmite particles and enhance the interaction of zeolite crystals and alumina binder. For 10 g of product, 7.14 g of boehmite was first mixed with 6 mL of Milli-Q H_2O and 0.21 mL of acetic acid using a pestle and mortar.[33] After complete wetting of boehmite powder, 5 g of zeolite was added to the mortar. The mixture was further pestled for 10 minutes with additional Milli-Q H_2O until a homogenous paste was obtained. Then, the paste was dried in an oven at 120 °C for 12 h, followed by crushing and calcination at 500 °C for 2 h with a heating ramp of 5 °C min^{-1}. For comparison, a zeolite+alumina composite was prepared without using acetic acid only to reveal the function of acetic acid in dispersing boehmite.

Pt-Al_2O_3/zeolite catalyst with platinum deposited on alumina binder was prepared by an ion adsorption (IA) method.[29] 1.5 g of zeolite-alumina composite was first added into 450 mL Milli-Q H_2O and stirred for 30 min at room temperature, after which the pH of the suspension was adjusted to 2.6 by adding 1 M HCl solution. The surface of the alumina binder was positively charged at this pH value (Figure S3.4). Then, a given volume of $H_2[PtCl_6]\cdot 6H_2O$ aqueous solution (0.17 mg_{Pt} mL^{-1}) was added dropwise to the suspension to obtain platinum weight loadings from 0.005 wt% to 0.5 wt% (Table S3.1). After 3 h of stirring, the suspension was filtered and washed with 500 mL of Milli-Q H_2O . The filter cake was dried at 120 °C overnight. The catalyst powder was reduced in H_2/N_2 (20/80 *vol*/*vol*) flow at 500 °C for 3 h with a heating ramp of 1 °C min^{-1}, and then further treated for 2 h at 500 °C in O_2/N_2 (20/80 *vol*/*vol*) flow.

Pt-zeolite/Al_2O_3 catalysts with platinum deposited on/inside zeolite crystals were prepared by an ion-exchange (IE) method. First, 0.75 g of zeolite powder was dispersed in 225 mL Milli-Q H_2O at room temperature and stirred for 30 min, after which a given volume of $[Pt(NH_3)_4](NO_3)_2$ aqueous solution (0.30 mg_{Pt} mL^{-1}) was added dropwise to the suspension. After 3 h of stirring, the suspension was filtered without further washing and the filtrate was collected for a repetitive IE. The filter cake was dried at 60 °C overnight, followed by a reduction in H_2/N_2 (20/80 *vol*/*vol*) flow at 500 °C for 3 h, with a heating ramp of 1 °C min^{-1}. After cooling to room temperature, the powders were put back into the collected filtrate, which still contained certain amounts of $[Pt(NH_3)_4]^{2+}$ ions. Then the IE was conducted again with stirring, filtration, drying, and reduction. Finally, the Pt-zeolite powders were obtained. By this repetitive IE step, most $[Pt(NH_3)_4]^{2+}$ ions in an aqueous solution can be loaded on/inside the zeolites. The composite Pt-zeolite/Al_2O_3 catalyst was prepared by the same method for preparing zeolite-alumina composite, but with a heating ramp of 1 °C min^{-1} in the calcination step. With this method, zeolite crystals can be well dispersed and fastened by alumina binder.

The single-atom Pt-Al_2O_3 with a 1.0 wt% (or 0.2 wt%) loading, named SAC-1.0Pt-Al_2O_3, was synthesized according to a recipe reported by Zhang et al.[34] 4.2 g Pluronic P123 was dissolved in 20 mL ethanol at room temperature. Then, 6.4 ml 67% nitric acid and 8.16 g aluminum isopropoxide were also dissolved in 20 mL ethanol. The two solutions were mixed under vigorous stirring for 30 min, after which a solution containing 6 mL ethanol and 55 mg (or 11 mg) $H_2[PtCl_6]\cdot 6H_2O$ was added to the mixture under stirring overnight. After evaporation for 72 h in an oven at 60 °C, the final gel was calcined at 400 °C for 4 h with a ramp of 1 °C min^{-1}. The SAC1.0Pt-Al_2O_3 was further physically mixed with HMOR in a mortar with a zeolite-alumina weight ratio of 1:1.

Catalyst Characterization

Ammonia temperature-programmed desorption (NH_3-TPD) measurements were conducted on a Micromeritics AutoChem II 2920 instrument equipped with a thermal conductivity detector (TCD). Typically, 0.1 g of sample was pretreated in a quartz reactor with He flow at 600 °C for 2 h. The adsorption of NH_3 was carried out at 100 °C in an NH_3–He mixture (10 vol % NH_3 in He) for 1 h, and TPD was performed in He flow by raising the temperature to 600 °C with a heating ramp of 10 °C min^{-1}.

N_2 physisorption measurements were performed at –196 °C on a Micromeritics Tristar 3000 Surface Area Analyzer; before N_2 adsorption, the sample was degassed under vacuum at 300 °C overnight. ICP analysis of platinum was performed at Kolbe Mikroanalytisches Laboratorium using an ICP-optical emission spectrometer (Perkin Elmer) after sample dissolution according to standard in-house procedures. The Si/Al molar ratio of zeolites was determined by X-ray fluorescence (XRF) spectroscopy on a Panalytical Axois Petro XRF instrument with rhodium target (50 kV, 50 mA).

Scanning electron microscopy (SEM) measurements were performed on a Hitachi S-4800 operated at 15 kV. HAADF-STEM images and EDX mapping were collected on an FEI TALOS F200X transmission electron microscope equipped with a Super-XTM EDX detector. To expose cross-sections that contain purely the zeolite or alumina components, ultramicrotomy of resin embedded catalysts was carried out. For this, the sample was first embedded in Epofix resin, put in an oven overnight at 60 °C, and cut to 70-nm sections using a diamond knife.[30] Cross-sections were deposited on carbon-coated copper TEM grids (200 mesh). The platinum particle size was determined by analyzing more than 200 particles. The platinum distribution and particle sizes over catalysts with platinum loading lower than 0.1 wt% were analyzed on an aberration-corrected Spectra 300 S/TEM from Thermo Fisher Scientific with an accelerating voltage of 300 kV.

X-ray photoelectron spectroscopy (XPS) measurements were carried out on an Omicron XPS System using Al Kα X-rays as the excitation source at a voltage of 15 kV and a power of 300 W. Samples were reduced in situ under hydrogen flow at 500 °C and atmospheric pressure for 2 hours. The binding energy was corrected by taking C1s line at 284.5 eV as an internal standard.

X-ray Absorption Spectroscopy (XAS) was carried out at the Insertion Device line of sector 10 at the Advanced Photon Source (APS), Argonne National Laboratory at the Pt L_3 edge, in fluorescence mode. The experiments were performed using a double crystal monochromator with direct drive air bearings and two sets of crystals: Si (111) and Si (311). Higher harmonics present in the X-ray beam were avoided by a 60 cm long flat harmonic rejection mirror. Approximately 100 mg of sample was pressed into a pellet in a special sample holder 45^o facing the beam direction. The sample holder was placed in an *in situ* temperature-programmable sample cell operated under ambient pressure. The samples were reduced under a flow 100 mL min^{-1} consisting of 3.5 vol% H_2 in He, at a temperature of 350 °C for 1 hour then cooled down to room temperature when the XAS measurements were taken. Fluorescence data were collected with an ion chamber Lytle detector, with a step size of 0.5 eV and an acquisition time of 0.1 s per point. XANES spectra were processed using the Athena program (Demeter 0.9.26) by averaging 12 scans for each sample. For XANES processing, normalization was done by dividing the absorption intensities by the height of the absorption edge and subtracting the background using cubic spline routines. The Pt oxidation state composition was determined from Linear Combination Fitting from Athena in the derivative space of μ(E), with PtO_2 used as a reference standard for Pt^{4+}; $[Pt(NH_3)_4](NO_3)_2$ for Pt^{2+} and the Pt metal foil for Pt^0 while allowing E0 to fit. The fitting was performed in the range of 20 eV below and 30 eV above the Pt L_3 edge. The EXAFS fitting was performed by converting the spectra in k-space with k-weight of 2 and in the range of 2.0–11 Å^{-1}, followed by a conversion into the R space with the following Forward Fourier transform parameters: *k* range of 2.0–11 Å^{-1} , d_k of 0.5, R range of 1.3–3.0 Å, d_r of 0.5, and a Hanning window. Multiple shell fitting was used involving Pt–Pt and Pt–O paths in the R space. Data for the backscattering amplitudes were obtained from the FEFFIT calculation built within Artemis (Demeter 0.9.26) software. The amplitude reduction factor was calibrated and fixed at $S_0^2 = 0.70$ from Pt metal foil at L_3 edge.

Catalyst Evaluation

Before reaction, the bifunctional catalysts were pressed, crushed, and sieved to obtain particles in the range 75–212 μm. Then, 30 mg or 15 mg of catalyst was loaded in stainless steel reactors (internal diameter, 2 mm). The hydroconversion of *n*-heptane was performed on an Avantium Flowrence 16 parallel reactor setup.

Catalysts were first reduced *in situ* for 3 h at 350 °C in 90 vol% H_2 in helium at 1 bar, using a ramp of 10 °C min^{-1}. An HPLC pump was used to inject the *n*-heptane feedstock, which was vaporized in an evaporator and mixed with H_2 with an H_2/*n*-heptane molar ratio of 10. After the reduction, the reactors were cooled to 200 ˚C and the H_2/*n*-heptane mixture was distributed into 16 reactors by capillary columns, with weight hourly space velocity (WHSV) of 2.1 $g_{n\text{-C7}}\ g_{cat}^{-1}\ h^{-1}$ (30 mg) or 4.2 $g_{n\text{-C7}}\ g_{cat}^{-1}\ h^{-1}$ (15 mg). Simultaneously, the pressure was increased to 10 bar to start the reaction. For all reactors, the temperature was increased stepwise, product analysis was conducted after 4 h at each temperature platform when the reaction had reached a steady state. The hydrocarbon products were analyzed online with an Agilent 7890A GC equipped with a flame ionization detector (FID). A capillary column (Agilent J&W Pora-BOND-Q) was used to separate the hydrocarbon products.

3.3. Results and Discussion

Metal Loading and Metal Nanoparticle Location

The Pt location on the composite catalysts consisting of a mixture of HZSM-22 or HMOR (SEM images of pristine zeolites provided in Figure S3.2) with alumina, could be controlled through either ion exchange (IE) by using $[Pt(NH_3)_4](NO_3)_2$ as Pt precursor or ion adsorption (IA) by using $H_2[PtCl_6]$ (Figure S3.3). IE led to the emplacement of Pt nanoparticles on/in the zeolite material and IA led to Pt emplacement on the alumina binder. The structural properties of the supports are summarized in Table S3.2. The actual weight loading of Pt was determined by means of inductively coupled plasma (ICP) spectrometry (Tables S3.3 and S3.4). Because all raw materials are based on commercial products and the IE and IA methods are commonly applied in industry, no major barriers are foreseen for the catalyst preparation on a large scale.

High-angle annular dark-field scanning transmission electron microscopy (HAADF-STEM) imaging combined with ultramicrotomy can expose cross sections of zeolite crystals or shaped catalysts and enables the visualization of the spatial distribution of Al_2O_3 binder, zeolite crystals, and Pt sites.[29] Because the kinetic diameter of the $[Pt(NH_3)_4]^{2+}$ (0.48 nm) is comparable with the HZSM-22 pore size (0.45 by 0.55 nm) and HMOR pore size (0.67 by 0.70 nm), the diffusion of $[Pt(NH_3)_4]^{2+}$ ions into the micropores during the IE process could be limited. The STEM images of Pt-HZSM-22 slices confirmed that after reduction, most Pt NPs were present on the external crystal surfaces, regardless of the Pt loading, and a small fraction was located inside the HZSM-22 crystals (Figure 3.1a,b). The average sizes of Pt NPs for 0.2Pt-HZSM-22 (where 0.2 is Pt loading in weight percent) and 1.0Pt-HZSM-22were 1.5 and 1.7 nm, respectively. For 0.2Pt-HMOR and 1.0Pt-HMOR, the average diameters of Pt NPs were 1.2 and 1.6 nm, respectively, and the Pt NPs were exclusively deposited inside HMOR crystals (Figure 3.1d,e). The Pt NPs were larger than the micropores of the zeolite and were likely accommodated by the local destruction of micropores during NP growth, an effect confirmed in previous studies.[35]

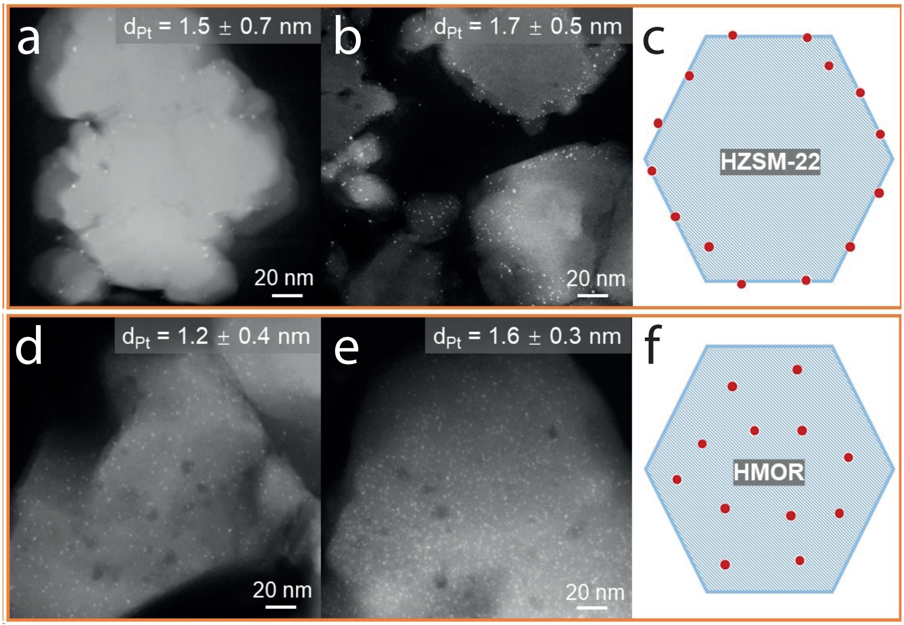

Figure 3.1. HAADF-STEM images of ultramicrotomed 70 nm-thick sections of a) 0.2Pt-HZSM-22, b) 1.0Pt-HZSM-22 and c) scheme for Pt distribution over HZSM-22. And HAADF-STEM images of sections of d) 0.2Pt-HMOR e), 1.0Pt-HMOR and f) scheme for Pt distribution over HMOR. The red dots and blue hexagons indicate Pt NPs and zeolite crystals, respectively.

The zeolite powders containing Pt NPs were then mixed with boehmite and acetic acid to prepare bifunctional catalysts with a zeolite-to-Al2O3weight ratio of 1/1. The zeolite-Al_2O_3 composite, by use of acetic acid as a peptizing agent in this work, exhibited a uniform distribution of zeolite crystals, which were coated and stabilized by the Al_2O_3 binder (Figure 3.2a). By contrast, large agglomerates of zeolites and Al_2O_3 were observed over zeolite+Al_2O_3 composite without acetic acid (Figure S3.4). The TEM imaging revealed that for IE-prepared Pt-HZSM-22/Al_2O_3, most Pt NPs remained on the HZSM-22 crystal surfaces with only a few NPs inside the HZSM-22 crystals, and those NPs were near NPs present on HZSM-22 surfaces; no NPs were observed on the mesoporous Al_2O_3 binder (Figure 3.2b and d, and Figure S3.5a). Conversely, almost all of the Pt NPs were located on the Al_2O_3 binder for Pt-Al_2O_3/HZSM-22 prepared with the IA method (Figure 3.2c and e, and Figure S3.5b). Correspondingly, the Pt NPs were still exclusively present inside the HMOR crystals for IE-prepared Pt-HMOR/Al_2O_3 (Figure 3.2f), and all of the Pt NPs were deposited on the Al_2O_3 binder for IA-prepared Pt-Al_2O_3/HMOR (Figure 3.2g). With this methodology, we prepared a series of composite catalysts with different Pt loadings and locations (Table S3.4). The Pt loading in all cases had a minor effect on the catalyst acidity (Figure S3.6).

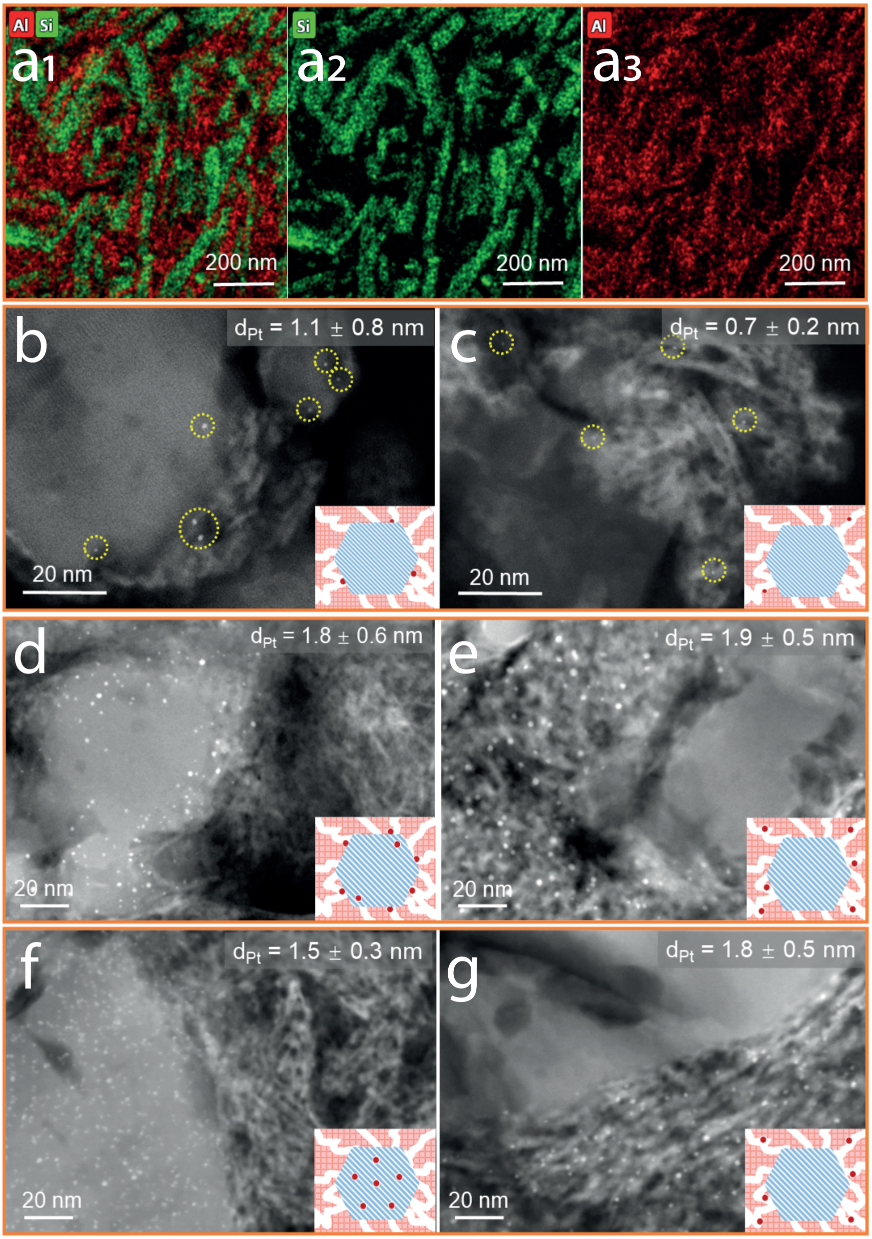

Figure 3.2. HAADF-STEM and STEM-energy dispersive x-ray (EDX) images of ultramicrotomed 70 nm-thick sections of catalysts. a) HZSM-22/Al_2O_3 composite by using acetic acid as a peptizing agent. The images a1-a3 show to location of silicon (green) and aluminum (red), which is indicative of the presence of HZSM-22 and Al_2O_3 components. b) 0.01Pt-HZSM-22/Al_2O_3, c) 0.01Pt-Al_2O_3/HZSM-22, d) 0.5Pt-HZSM-22/Al_2O_3, e) 0.5Pt-Al_2O_3/HZSM-22, f) 0.5Pt-HMOR/Al_2O_3 g) 0.5Pt-Al_2O_3/HMOR. In the schematic representations, the pink areas, the red dots and blue hexagons indicate Al_2O_3 binder, Pt NPs and zeolite crystals, respectively.

Hydroconversion of *n*-Heptane

The catalytic performance of HZSM-22–based catalysts in the hydroisomerization of *n*-heptane (*n*-C_7) was strongly affected by the Pt loading and distribution, especially at loading of 0.005 to 0.05 wt% (Figure 3.3 and Figure S3.7). With an increase of Pt loading, the *n*-C_7 conversion compared at identical temperature and weight hourly space velocity (WHSV) increased first and then reached a plateau. Unexpectedly, with the Pt-on–HZSM-22 configuration, an ultralow Pt loading of 0.01 wt% was sufficient to maintain the *n*-C_7 conversion and selectivity of C_7 isomers (Figure 3.3a). Such a low Pt loading is usually insufficient for catalyzing this reaction. However, 0.01Pt-Al_2O_3/HZSM-22 exhibited inferior activity and selectivity (Figure 3.3b). The C_7 isomers consisted of monobranched and traces of dibranched C_7 isomers (mono-C_7 and di-C_7,respectively), and the main side products were propane, *n*-butane, and *i*-butane from acid-catalyzed hydrocracking.[30]

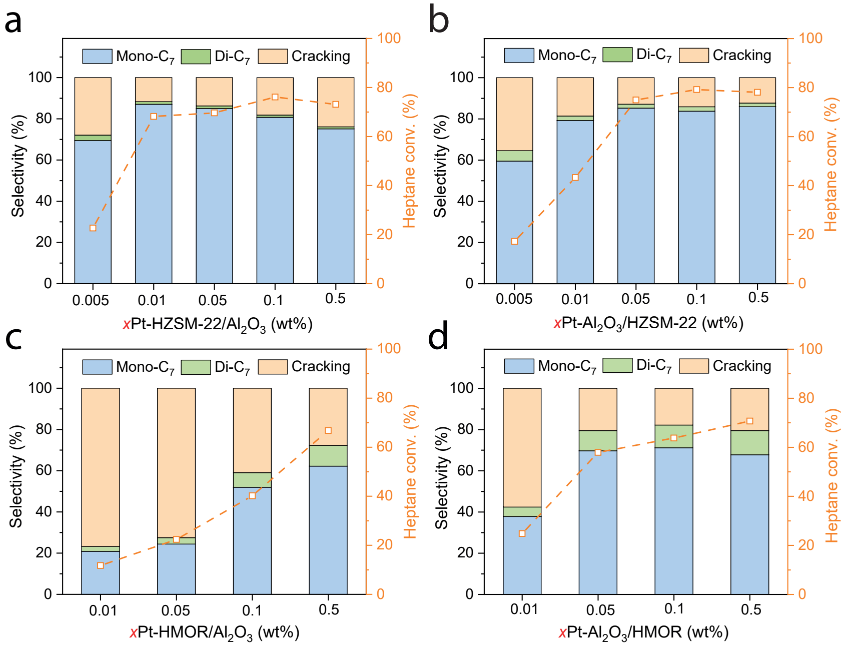

Figure 3.3. Hydroconversion of *n*-heptane over bifunctional catalysts with different Pt loadings and locations. a) Pt-HZSM-22/Al_2O_3 with Pt on the HZSM-22 crystals and b) Pt-Al_2O_3/ZSM-22 with Pt on the Al_2O_3 binder. c) Pt-HMOR/Al2O3 with Pt inside the HMOR crystals and d) Pt-Al_2O_3/HMOR with Pt on the Al_2O_3 binder. Data are partly from Cheng et al.[30] Reaction conditions: P = 10 bar, H_2/*n*-C_7 = 10/1 mol/mol, WHSV = 2.1 $g_{n\text{-}C7} \cdot g_{cat}^{-1} \cdot h^{-1}$, and T = 320 ˚C for HZSM-22-based catalysts and T = 280 ˚C for HMOR-based catalysts.

At similar conversion levels, 0.01Pt-HZSM-22/Al_2O_3 also provided higher selectivity of C_7 isomers than did 0.01Pt-Al_2O_3/HZSM-22 (Figure S3.8). Increasing the Pt loading > 0.01 wt% decreased the selectivity of C_7 isomers, which was likely the result of more Pt NPs sited in the pore mouth region of HZSM-22, which would promote cracking reactions.[30] For Pt-Al_2O_3/HZSM-22 with Pt-on-Al_2O_3, both the n-C_7 conversion and selectivity of C_7 isomers increased steadily and then reached a plateau as Pt loading increased to 0.05 wt% (Figure 3.3b).With Pt-on-binder, therefore, a minimum loading of 0.05 wt% was required to sustain the n-heptane conversion and the selectivity of C_7 isomers, to ensure the equilibrium of the dehydrogenation-hydrogenation reaction. Over HMOR-based catalysts, both the n-C_7 conversion and the selectivity of C_7 isomers increased with the Pt loading, and overall, the performance of catalysts with Pt inside HMOR crystals was more strongly influenced by the Pt loading (Figure 3.3c and d, and Figure S3.7). At the same Pt loading, the specific n-C_7 conversion over Pt-HMOR/Al_2O_3 was lower than the corresponding Pt-Al_2O_3/HMOR, probably because of pore blockage or poor accessibility of Pt NPs.[36] With a 10-fold increase of Pt loading from 0.05 to 0.5%, the n-C_7 conversion increased from 58 to 71% with a selectivity of C_7 isomers ~80% over Pt-Al_2O_3/HMOR, whereas the n-C_7 conversion increased from 22 to 67% and the selectivity of C_7 isomers increased from 28 to 72% over Pt-HMOR/Al_2O_3. Regardless of the Pt loading and location over the composite catalysts, after more than 100 hours, we observed virtually no catalyst deactivation for both HZSM-22– and HMOR-based catalysts (Figures S3.9 and S3.10).

The dependence of the maximum yield of C_7 isomers, an important performance indicator in alkane hydroisomerization,[26] on the platinum loading is summarized in Figure 3.4. The acid density of HMOR is much higher than that of HZSM-22. Therefore, HMOR-based catalysts required more Pt sites to obtain the same n_{Pt}/n_A ratio (Figure S3.11). A composite catalyst with Pt-on–HZSM-22 exhibited an optimum loading of only 0.01 wt% for maximizing the yield of C_7 isomers (≈64%) (Figure 3.4a). For Pt-Al_2O_3/HZSM-22 with Pt-on-binder, the increase of Pt loading above 0.05 wt% maximized the yield of C_7 isomers toward 68%. Likewise, the maximum yield of C_7 isomers for Pt-Al_2O_3/HMOR went up with Pt loading, and relative to HZSM-22, a much higher loading of Pt (≈0.1 wt %) was needed to provide maximum yields of C_7 isomers (Figure 3.4b). Disadvantageous for the yield of C_7 isomers was to confine the Pt inside HMOR crystals, which promoted the cracking reaction and prevented the conversion of n-C_7. The maximum yield of C_7 isomers over 0.05Pt-Al_2O_3/HMOR was near that over 0.5Pt-HMOR/Al_2O_3, suggesting that a rational placement of Pt could lead to a 10-fold reduction in its usage.

In the low loading range (≤ 0.01 wt%), Pt placed on the Al_2O_3 binder was less effective than on HZSM-22 crystals (Figures 3.3a and b, and 3.4a). Highly dispersed Pt sites stabilized by the alumina (Pt–O–Al) could be difficult to reduce and not be sufficiently active for dehydrogenation of n-heptane. To investigate this, we intentionally prepared a SAC-Pt-Al_2O_3/HMOR catalyst with single-atom Pt dispersed on Al_2O_3, which was almost inactive in n-heptane hydroconversion (Figure 3.5).

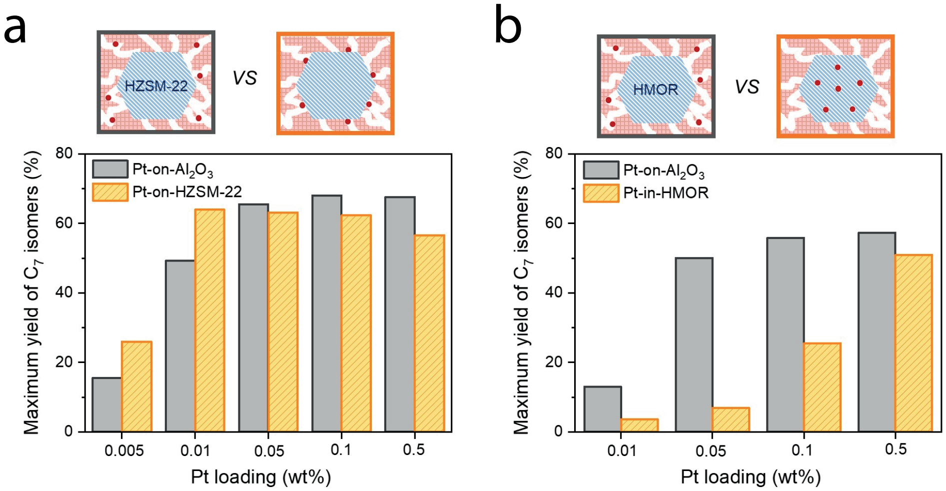

Figure 3.4. The effect of the Pt loading on the maximum yield of C_7 isomers. a) Pt/HZSM-22/Al2O3 composite catalysts, with Pt NPs placed either on Al_2O_3 binder or on HZSM-22 crystals, and b) Pt/HMOR/Al_2O_3, with Pt NPs placed either on Al_2O_3 binder or inside HMOR crystals. Reaction conditions: P = 10 bar, H_2/*n*-C_7 = 10/1 mol/mol, WHSV = 2.1 $g_{n\text{-}C7} \cdot g_{cat}^{-1} \cdot h^{-1}$. The pink areas, the red dots and blue hexagons indicate Al_2O_3 binder, Pt NPs and zeolite crystals, respectively.

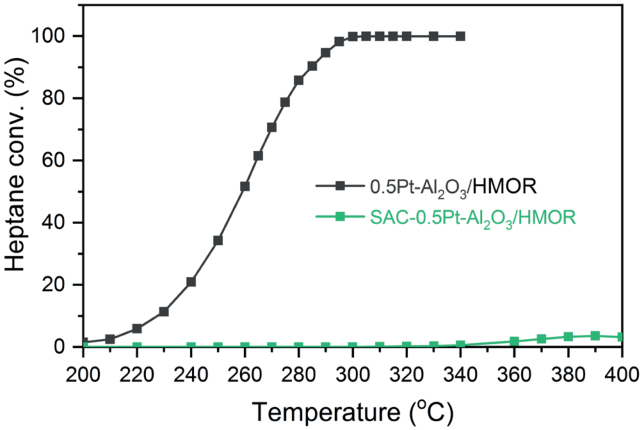

Figure 3.5. Hydroconversion of *n*-heptane over 0.5Pt-Al_2O_3/HMOR and SAC-0.5PtAl$_2$O$_3$/HMOR. SAC-0.5Pt-Al_2O_3/HMOR was prepared by physical mixing of SAC-1.0Pt-Al_2O_3 with HMOR powders (wt/wt = 1/1) in a mortar. Reaction condition: P = 10 bar, H_2/*n*-heptane = 10:1 mol/mol, WHSV = 2.1 $g_{n\text{-}C7} \cdot g_{cat}^{-1} \cdot h^{-1}$.

Chemical State of Pt in Catalysts with Ultralow Pt Loadings

The x-ray absorption spectroscopy (XAS) shows the k^2-weighted (where k is photoelectron wave number), phase-corrected extended x-ray absorption fine structure (EXAFS) spectra of reduced Pt catalysts together with Pt standards (Figure 3.6a). The scattering from the first shell of Pt–O led to the scattering path below 2.0 Å, whereas the scattering Pt–Pt in the Pt foil resulted in peaks at 2.4 and 2.9 Å.[7] The scattering path at 2.2 Å observed with a bond distance shorter than that of Pt–Pt may indicate the formation of Pt dimers.[37]

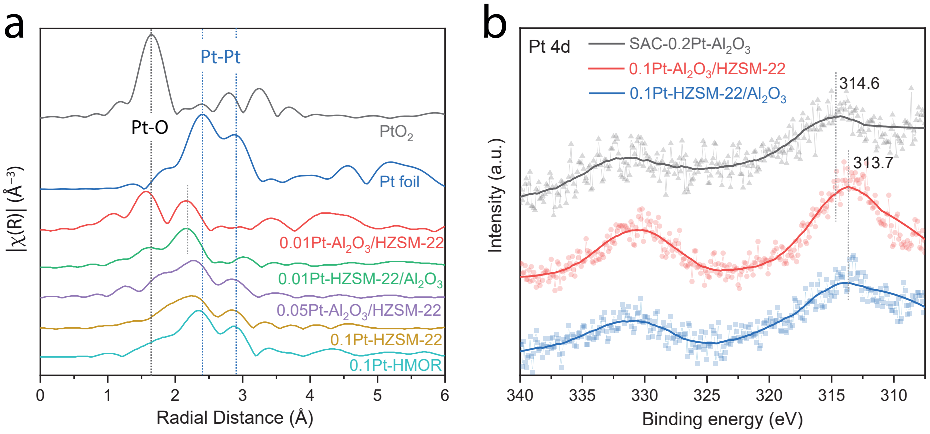

Figure 3.6. Chemical state of Pt. a) The k^2-weighted Pt L_3 edge EXAFS spectra in R space of bifunctional catalysts. Catalysts were reduced under 3.5 vol% H_2 flow at 350 ° C for 1 h. PtO_2 and Pt foil were used as Pt standards. b) XPS spectra of reduced catalysts.

Strong Pt–Pt scattering for 0.1Pt-HMOR and 0.1Pt-HZSM-22 with 0.1 wt% loadings could be observed (Figure 3.6a), which is indicative of the formation of metallic Pt NPs or clusters. A Pt–O scattering peak was observed over $0.01Pt-HZSM-22/Al_2O_3$ and $0.01Pt-Al_2O_3/HZSM-22$, indicating that single-atom Pt (ions) was present within the two samples together with Pt NPs observed with electron microscopy (Figure 3.2b and c). More than half of Pt was metallic over $0.01Pt-HZSM-22/Al_2O_3$, which exhibited higher reactivity in *n*-C_7 conversion than that of $0.01Pt-Al_2O_3/HZSM-22$ that contained mainly oxidized Pt (Figure S3.12 and Table S3.5). As the Pt loading on the Al_2O_3 binder increased from 0.01 to 0.05 wt%, the Pt–O scattering became negligible, and Pt–Pt scattering appeared, which suggested the formation of larger numbers of small Pt NPs or clusters in line with electron microscopy results (Figure 3.2).The *in situ* x-ray photoelectron spectroscopy (Figure 3.6b) further suggested reduced $0.1Pt-HZSM-22/Al_2O_3$ and $0.1Pt-Al_2O_3/HZSM-22$ to mainly contain metallic Pt (313.7 eV), whereas the atomically dispersed Pt on Al_2O_3 ($SAC-0.2Pt-Al_2O_3$) was in a partially oxidized state (314.6 eV).[38] The weaker Pt signals of $0.1Pt-HZSM-22/Al_2O_3$ than those of $0.1Pt-Al_2O_3/HZSM-22$ imply that a fraction of Pt NPs might be confined in the micropores of HZSM-22, causing cracking reactions at high

(≥ 0.1 wt %) Pt loadings (Figure 3.3a).

3.4. Conclusions

To increase the Pt utilization over bifunctional Pt-zeolite catalysts, we have varied the proximity between sites by controlling the spatial distribution of Pt NPs. Because of the low diffusivity of alkanes and alkenes, Pt sites should be placed in an accessible location in solid catalysts rather than in the micropores of a zeolite, such as on a mesoporous alumina binder or the outer surface of the zeolite crystals. Additionally, maintaining a separation between Pt and zeolite acid sites can preserve the metal and acid functions to the greatest extent through three main mechanisms: (i) limiting micropore blockage by metal clusters, (ii) enhancing accessibility of metal sites, and (iii) favoring pore mouth catalysis to reduce secondary cracking reactions. Furthermore, reducible Pt ensemble sites were confirmed to be more active as the dehydrogenation-hydrogenation function than Pt SAC, which was strongly bonded by the alumina binder, especially at low platinum loadings. Our findings generally agree with the classical criterion that a minimum amount of NMs is necessary to maintain the metal-acid balance and ensure a quasi-equilibration of the dehydrogenation-hydrogenation reactions, but this study confirms that the required loading for NMs is profoundly affected by how functional sites are arranged at the nanoscale.

Statement of author contributions

Kang Cheng conducted the catalyst preparation, catalytic evaluation; sample characterization by NH_3-TPD, SEM, and XRF, and drafted the manuscript. Luc Smulders assessed the catalyst stability, maintained the reaction unit, performed additional characterization, and helped revise the manuscript. Lars van der Wal, Hans Meeldijk, Nienke Visser, and Hideto Yoshida performed STEM imaging. Jogchum Oenema guided the catalyst preparation and maintained the reaction unit. Glenn Sunley, Tegan Roberts, Petra de Jongh, and Jovana Zecevic contributed to the discussion of all the results. Zhuoran Xu and Eric Doskocil performed the XAS measurements and analyzed the data. Yanping Zheng performed XPS analysis. Krijn de Jong initiated and supervised the project and manuscript writing. All authors approved the final version of the manuscript.

Acknowledgements

Nikos Nikolopoulos, Giorgio Totarella and Silvia Zanoni are acknowledged for N_2 physisorption measurements. This work has been supported by BP plc and Topsector Chemie Consortia for Knowledge and Innovation (TKIs).

References

(1) Wang, A.; Li, J.; Zhang, T. Heterogeneous Single-Atom Catalysis. *Nat. Rev. Chem.* **2018**, *2* (6), 65–81.

(2) Chong, L.; Wen, J.; Kubal, J.; Sen, F. G.; Zou, J.; Greeley, J.; Chan, M.; Barkholtz, H.; Ding, W.; Liu, D. J. Ultralow-Loading Platinum-Cobalt Fuel Cell Catalysts Derived from Imidazolate Frameworks. *Science* **2018**, *362* (6420), 1276–1281.

(3) Hannagan, R. T.; Giannakakis, G.; Réocreux, R.; Schumann, J.; Finzel, J.; Wang, Y.; Michaelides, A.; Deshlahra, P.; Christopher, P.; Flytzani-Stephanopoulos, M.; Stamatakis, M.; Sykes, E. C. H. First-Principles Design of a Single-Atom-Alloy Propane Dehydrogenation Catalyst. *Science* **2021**, *372* (6549), 1444–1447.

(4) Zhang, F.; Zeng, M.; Yappert, R. D.; Sun, J.; Lee, Y. H.; LaPointe, A. M.; Peters, B.; Abu-Omar, M. M.; Scott, S. L. Polyethylene Upcycling to Long-Chain Alkylaromatics by Tandem Hydrogenolysis/Aromatization. *Science* **2020**, *370* (6515), 437–441.

(5) Huang, Z.; Zhao, Z.; Zhang, C.; Lu, J.; Liu, H.; Luo, N.; Zhang, J.; Wang, F. Enhanced Photocatalytic Alkane Production from Fatty Acid Decarboxylation via Inhibition of Radical Oligomerization. *Nat. Catal.* **2020**, *3* (2), 170–178.

(6) DeRita, L.; Resasco, J.; Dai, S.; Boubnov, A.; Thang, H. V.; Hoffman, A. S.; Ro, I.; Graham, G. W.; Bare, S. R.; Pacchioni, G.; Pan, X.; Christopher, P. Structural Evolution of Atomically Dispersed Pt Catalysts Dictates Reactivity. *Nat. Mater.* **2019**, *18* (7), 746–751.

(7) Jeong, H.; Kwon, O.; Kim, B. S.; Bae, J.; Shin, S.; Kim, H. E.; Kim, J.; Lee, H. Highly Durable Metal Ensemble Catalysts with Full Dispersion for Automotive Applications beyond Single-Atom Catalysts. *Nat. Catal.* **2020**, *3* (4), 368–375.

(8) Rasmussen, K. D.; Wenzel, H.; Bangs, C.; Petavratzi, E.; Liu, G. Platinum Demand and Potential Bottlenecks in the Global Green Transition: A Dynamic Material Flow Analysis. *Environ. Sci. Technol.* **2019**, *53* (19), 11541–11551.

(9) Hughes, A. E.; Haque, N.; Northey, S. A.; Giddey, S. Platinum Group Metals: A Review of Resources, Production and Usage with a Focus on Catalysts. *Resources* **2021**, *10* (9), 1–40.

(10) Qiao, B.; Wang, A.; Yang, X.; Allard, L. F.; Jiang, Z.; Cui, Y.; Liu, J.; Li, J.; Zhang, T. Single-Atom Catalysis of CO Oxidation Using Pt1/FeOx. *Nat. Chem.* **2011**, *3* (8), 634–641.

(11) Mitchell, S.; Vorobyeva, E.; Pérez-Ramírez, J. The Multifaceted Reactivity of Single-Atom Heterogeneous Catalysts. *Angew. Chemie - Int. Ed.* **2018**, *57* (47), 15316–15329.

(12) Li, Z.; Ji, S.; Liu, Y.; Cao, X.; Tian, S.; Chen, Y.; Niu, Z.; Li, Y. Well-Defined Materials for Heterogeneous Catalysis: From Nanoparticles to Isolated Single-Atom Sites. *Chem. Rev.* **2020**, *120* (2), 623–682.

(13) Xiong, H.; Datye, A. K.; Wang, Y. Thermally Stable Single-Atom Heterogeneous Catalysts. *Adv. Mater.* **2021**, *33* (50), 1–19.

(14) Kistler, J. D.; Chotigkrai, N.; Xu, P.; Enderle, B.; Praserthdam, P.; Chen, C. Y.; Browning, N. D.; Gates, B. C. A Single-Site Platinum CO Oxidation Catalyst in Zeolite KLTL: Microscopic and Spectroscopic Determination of the Locations of the Platinum Atoms. *Angew. Chemie - Int. Ed.* **2014**, *53* (34), 8904–8907.

.

(15) Kosinov, N.; Liu, C.; Hensen, E. J. M.; Pidko, E. A. Engineering of Transition Metal Catalysts Confined in Zeolites. *Chem. Mater.* **2018**, *30* (10), 3177–3198.

(16) Liu, L.; Lopez-Haro, M.; Lopes, C. W.; Li, C.; Concepcion, P.; Simonelli, L.; Calvino, J. J.; Corma, A. Regioselective Generation and Reactivity Control of Subnanometric Platinum Clusters in Zeolites for High-Temperature Catalysis. *Nat. Mater.* **2019**, *18* (8), 866–873.

(17) Wu, S. M.; Yang, X. Y.; Janiak, C. Confinement Effects in Zeolite-Confined Noble Metals. *Angew. Chemie - Int. Ed.* **2019**, *58* (36), 12340–12354.

(18) Zhang, J.; Wang, L.; Zhang, B.; Zhao, H.; Kolb, U.; Zhu, Y.; Liu, L.; Han, Y.; Wang, G.; Wang, C.; Su, D. S.; Gates, B. C.; Xiao, F. S. Sinter-Resistant Metal Nanoparticle Catalysts Achieved by Immobilization within Zeolite Crystals via Seed-Directed Growth. *Nat. Catal.* **2018**, *1* (7), 540–546.

(19) Jin, Z.; Wang, L.; Zuidema, E.; Mondal, K.; Zhang, M.; Zhang, J.; Wang, C.; Meng, X.; Yang, H.; Mesters, C.; Xiao, F. S. Hydrophobic Zeolite Modification for in Situ Peroxide Formation in Methane Oxidation to Methanol. *Science* **2020**, *367* (6474), 193–197.

(20) Liu, L.; Corma, A. Metal Catalysts for Heterogeneous Catalysis: From Single Atoms to Nanoclusters and Nanoparticles. *Chem. Rev.* **2018**, *118* (10), 4981–5079.

(21) Zhang, B.; Sun, G.; Ding, S.; Asakura, H.; Zhang, J.; Sautet, P.; Yan, N. Atomically Dispersed Pt1-Polyoxometalate Catalysts: How Does Metal-Support Interaction Affect Stability and Hydrogenation Activity? *J. Am. Chem. Soc.* **2020**, *141* (20), 8185–8197.

(22) van Deelen, T. W.; Hernández Mejía, C.; de Jong, K. P. Control of Metal-Support Interactions in Heterogeneous Catalysts to Enhance Activity and Selectivity. *Nat. Catal.* **2019**, *2* (11), 955–970.

(23) van der Wal, L. I.; Oenema, J.; Smulders, L. C. J.; Samplonius, N. J.; Nandpersad, K. R.; Zečević, J.; de Jong, K. P. Control and Impact of Metal Loading Heterogeneities at the Nanoscale on the Performance of Pt/Zeolite Y Catalysts for Alkane Hydroconversion. *ACS Catal.* **2021**, *11* (7), 3842–3855.

(24) Giannetto, G. E.; Perot, G. R.; Guisnet, M. R. Hydroisomerization and Hydrocracking of N-Alkanes. 1. Ideal Hydroisomerization PtHY Catalysts. *Ind. Eng. Chem. Prod. Res. Dev.* **1986**, *25* (3), 481–490.

(25) van den Broek, A. C. M.; van Grondelle, J.; van Santen, R. A. Preparation of Highly Dispersed Platinum Particles in HZSM-5 Zeolite: A Study of the Pretreatment Process of [Pt(NH3)4]2+. *J. Catal.* **1997**, *167* (2), 417–424.

(26) Martens, J. A.; Verboekend, D.; Thomas, K.; Vanbutsele, G.; Gilson, J. P.; Pérez-Ramírez, J. Hydroisomerization of Emerging Renewable Hydrocarbons Using Hierarchical Pt/H-ZSM-22 Catalyst. *ChemSusChem* **2013**, *6* (3), 421–425.

(27) Guo, Z.; Li, X.; Hu, S.; Ye, G.; Zhou, X.; Coppens, M. O. Understanding the Role of Internal Diffusion Barriers in Pt/Beta Zeolite Catalyzed Isomerization of n-Heptane. *Angew. Chemie - Int. Ed.* **2020**, *59* (4), 1548–1551.

(28) Weisz, P. B.; Swegler, E. W. Stepwise Reaction on Separate Catalytic Centers: Isomerization of Saturated Hydrocarbons. *Science* **1957**, *126* (3262), 31–32.

(29) Zečević, J.; Vanbutsele, G.; de Jong, K. P.; Martens, J. A. Nanoscale Intimacy in Bifunctional Catalysts for Selective Conversion of Hydrocarbons. *Nature* **2015**, *528* (7581), 245–254.

(30) Cheng, K.; van der Wal, L. I.; Yoshida, H.; Oenema, J.; Harmel, J.; Zhang, Z.; Sunley, G.; Zečević, J.; de Jong, K. P. Impact of the Spatial Organization of Bifunctional Metal–Zeolite Catalysts on the Hydroisomerization of Light Alkanes. *Angew. Chemie - Int. Ed.* **2020**, *59* (9), 3592–3600.

(31) Oenema, J.; Harmel, J.; Vélez, R. P.; Meijerink, M. J.; Eijsvogel, W.; Poursaeidesfahani, A.; Vlugt, T. J. H.; Zečević, J.; de Jong, K. P. Influence of Nanoscale Intimacy and Zeolite Micropore Size on the Performance of Bifunctional Catalysts for N-Heptane Hydroisomerization. *ACS Catal.* **2020**, *10* (23), 14245–14257.

(32) Michels, N. L.; Mitchell, S.; Pérez-Ramírez, J. Effects of Binders on the Performance of Shaped Hierarchical MFI Zeolites in Methanol-to-Hydrocarbons. *ACS Catal.* **2014**, *4* (8), 2409–2417.

(33) Whiting, G. T.; Chung, S. H.; Stosic, D.; Chowdhury, A. D.; Van Der Wal, L. I.; Fu, D.; Zecevic, J.; Travert, A.; Houben, K.; Baldus, M.; Weckhuysen, B. M. Multiscale Mechanistic Insights of Shaped Catalyst Body Formulations and Their Impact on Catalytic Properties. *ACS Catal.* **2019**, *9* (6), 4792–4803.

(34) Zhang, Z.; Zhu, Y.; Asakura, H.; Zhang, B.; Zhang, J.; Zhou, M.; Han, Y.; Tanaka, T.; Wang, A.; Zhang, T.; Yan, N. Thermally Stable Single Atom Pt/m-Al2O3 for Selective Hydrogenation and CO Oxidation. *Nat. Commun.* **2017**, *8*, 1–10.

(35) Zečević, J.; Van Der Eerden, A. M. J.; Friedrich, H.; De Jongh, P. E.; De Jong, K. P. Heterogeneities of the Nanostructure of Platinum/Zeolite y Catalysts Revealed by Electron Tomography. *ACS Nano* **2013**, *7* (4), 3698–3705.

(36) Guisnet, M.; Alvarez, F.; Giannetto, G.; Perot, G. Hydroisomerization and Hydrocracking of N-Heptane on PtH Zeolites. Effect of the Porosity and of the Distribution of Metallic and Acid Sites. *Catal. Today* **1987**, *1* (4), 415–433.

(37) Müller, U.; Sattler, K.; Xhie, J.; Venkateswaran, N.; Raina, G. A Scanning Tunneling Microscope Study of Single Platinum Atoms, Platinum Dimers and Trimers on Highly-Oriented Pyrolytic Graphite. *Zeitschrift für Phys. D Atoms, Mol. Clust.* **1991**, *19* (4), 319–321.

(38) Huizinga, T.; van 'T Blik, H. F. J.; Vis, J. C.; Prins, R. XPS Investigations of Pt and Rh Supported on γ-Al2O3 and TiO2. *Surf. Sci.* **1983**, *135* (1–3), 580–596.

(39) Choudhury, I. R.; Hayasaka, K.; Thybaut, J. W.; Laxmi Narasimhan, C. S.; Denayer, J. F.; Martens, J. A.; Marin, G. B. Pt/H-ZSM-22 Hydroisomerization Catalysts Optimization Guided by Single-Event MicroKinetic Modeling. *J. Catal.* **2012**, *290*, 165–176.

(40) Kim, J.; Kim, W.; Seo, Y.; Kim, J. C.; Ryoo, R. N-Heptane Hydroisomerization over Pt/MFI Zeolite Nanosheets: Effects of Zeolite Crystal Thickness and Platinum Location. *J. Catal.* **2013**, *301*, 187–197.

Supporting Information

Table S3.1. Details for the preparation of 1.5 g of Pt-zeolite-alumina composite catalysts with different Pt locations and loadings.

Catalyst	**Pt source** [a]	**Conc.** [b] **(mg_{Pt} mL^{-1})**	**Volume (mL)**	**Pt intake (wt%)**	**Heat treatment**
0.5Pt-HZSM-22/Al_2O_3	PTA	0.30	37.5	0.75	H_2/N_2 500 ˚C/3h
0.1Pt-HZSM-22/Al_2O_3	PTA	0.30	5	0.1	H_2/N_2 500 ˚C/3h
0.05Pt-HZSM-22/Al_2O_3	PTA	0.30	3	0.06	H_2/N_2 500 ˚C/3h
0.01Pt-HZSM-22/Al_2O_3	PTA	0.30	0.6	0.012	H_2/N_2 500 ˚C/3h
0.005Pt-HZSM-22/Al_2O_3	PTA	0.30	0.3	0.006	H_2/N_2 500 ˚C/3h
0.5Pt-Al_2O_3/HZSM-22	CPA	0.17	50	0.56	$H_2/N_2 \rightarrow O_2/N_2$ 500 ˚C
0.1Pt-Al_2O_3/HZSM-22	CPA	0.17	10	0.11	$H_2/N_2 \rightarrow O_2/N_2$ 500 ˚C
0.05Pt-Al_2O_3/HZSM-22	CPA	0.17	5	0.056	$H_2/N_2 \rightarrow O_2/N_2$ 500 ˚C
0.01Pt-Al_2O_3/HZSM-22	CPA	0.17	1	0.012	$H_2/N_2 \rightarrow O_2/N_2$ 500 ˚C
0.005Pt-Al_2O_3/HZSM-22	CPA	0.17	0.5	0.005	$H_2/N_2 \rightarrow O_2/N_2$ 500 ˚C
0.5Pt-HMOR/Al_2O_3	PTA	0.30	37.5	0.75	H_2/N_2 500 ˚C/3h
0.1Pt-HMOR/Al_2O_3	PTA	0.30	5	0.1	H_2/N_2 500 ˚C/3h
0.05Pt-HMOR/Al_2O_3	PTA	0.30	3	0.06	H_2/N_2 500 ˚C/3h
0.01Pt-HMOR/Al_2O_3	PTA	0.30	0.6	0.012	H_2/N_2 500 ˚C/3h
0.5Pt-Al_2O_3/HMOR	CPA	0.17	50	0.56	$H_2/N_2 \rightarrow O_2/N_2$ 500 ˚C
0.1Pt-Al_2O_3/HMOR	CPA	0.17	10	0.11	$H_2/N_2 \rightarrow O_2/N_2$ 500 ˚C
0.05Pt-Al_2O_3/HMOR	CPA	0.17	5	0.056	$H_2/N_2 \rightarrow O_2/N_2$ 500 ˚C
0.01Pt-Al_2O_3/HMOR	CPA	0.17	1	0.012	$H_2/N_2 \rightarrow O_2/N_2$ 500 ˚C

[a] PTA and CPA denote $[Pt(NH_3)_4](NO_3)_2$ and $H_2[PtCl_6]\cdot H_2O$, respectively.

[b] Concentration of platinum in solution.

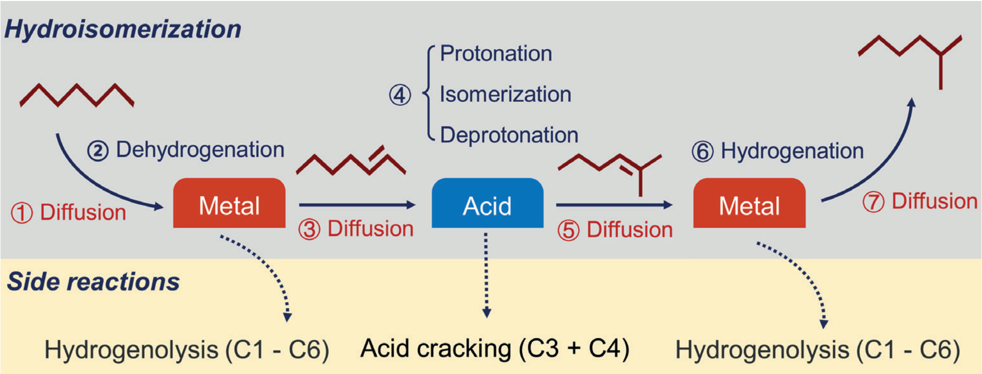

Figure S3.1. Simplified reaction mechanism for *n*-heptane hydroisomerization and side reactions as well. Because the reaction involves several diffusion steps, the distance between metal and acid sites plays a key role in catalysis.

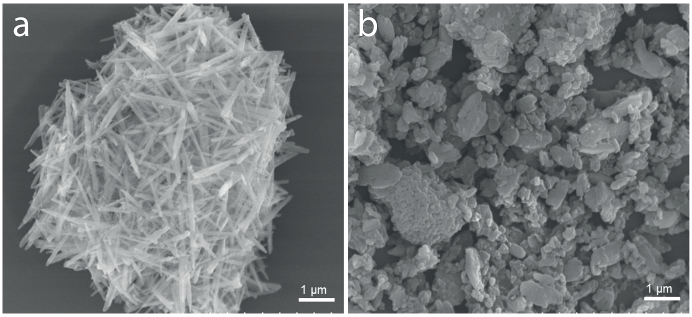

Figure S3.2. SEM images of parent a) HZSM-22 and b) HMOR. Note: Both HZSM-22 and HMOR were composed of sub-micron-sized crystals agglomerated into larger particles. HZSM-22 had a typical rod-like morphology, with the micropore channels (10- membered ring, 10MR) along the length of zeolite crystals.[39] HMOR consisted of agglomerates of crystals of variable sizes

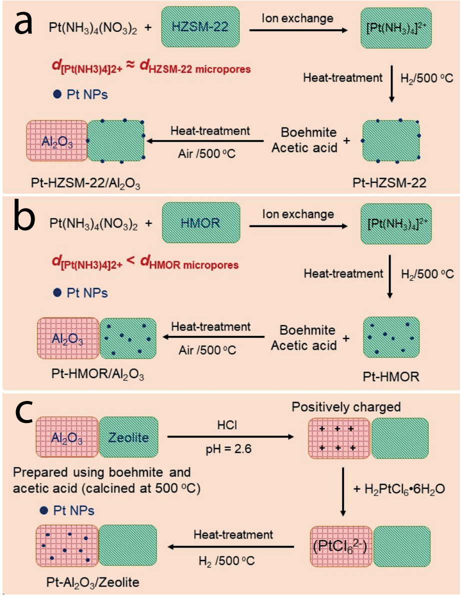

Figure S3.3. Preparation schemes of a) Pt-HZSM-22/Al_2O_3, b) Pt-HMOR/Al_2O_3 and c) Pt-Al_2O_3/Zeolite with a different platinum location. Black dots, red and green squares denote Pt NPs, alumina binder, and zeolite crystals, respectively.

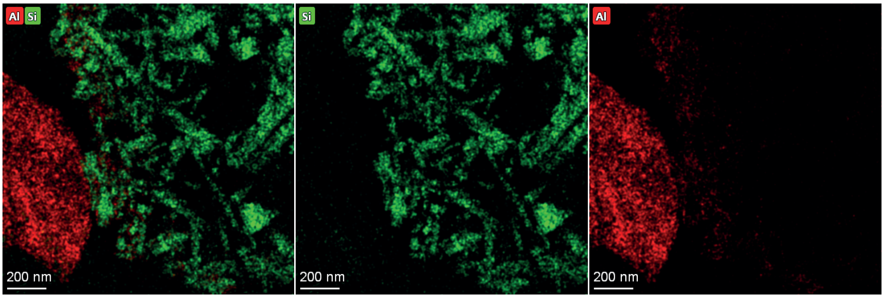

Figure S3.4. Distribution of zeolite HZSM-22 and alumina components for HZSM-22+Al_2O_3. This composite catalyst was prepared without using acetic acid as a peptizing agent. The images show the location of silicon (green) and aluminum (red), which is indicative of the presence of the HZSM-22 and alumina components. EDX mapping was acquired over a 70-nm-thick section of catalyst grains.

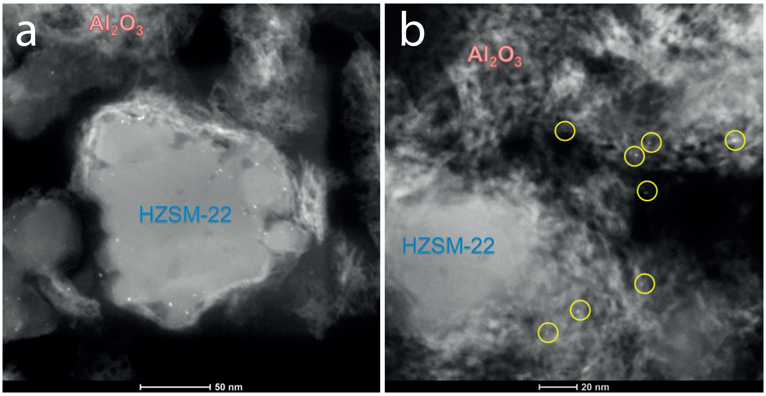

Figure S3.5. STEM images of a) 0.1Pt-HZSM-22/Al_2O_3 and b) Pt-Al_2O_3/ZSM-22

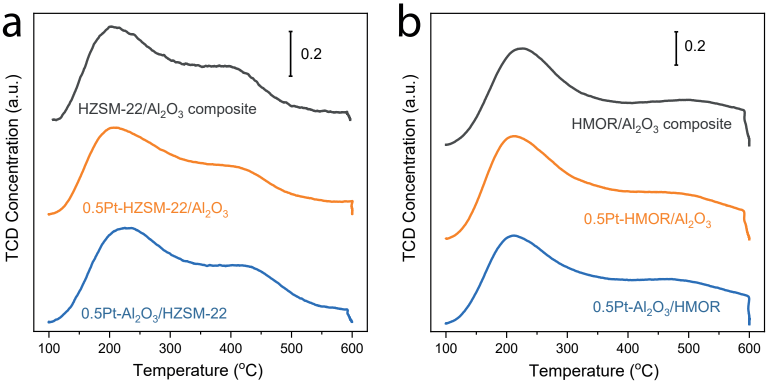

Figure S3.6. NH_3-TPD profiles of a) 0.5Pt-HZSM-22/Al_2O_3, 0.5Pt-Al_2O_3/HZSM-22 and HZSM-22/Al_2O_3 composite without platinum, and b) 0.5Pt-HMOR/Al_2O_3, 0.5Pt-Al_2O_3/HMOR, and HMOR/Al_2O_3 composite without platinum.

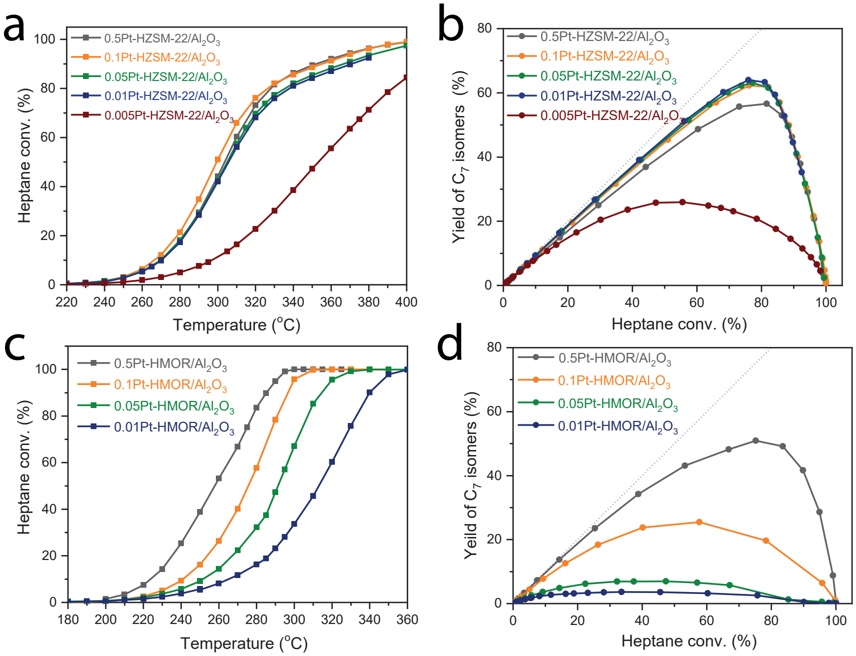

Figure S3.7. The effect of platinum loading on the hydroisomerization of *n*-heptane. a, b) Pt-HZSM-22/Al_2O_3 with platinum particles placed *on* the HZSM-22 crystals and c, d) Pt-HMOR/Al_2O_3 with platinum particles *inside* the HMOR crystals. Reaction condition: P = 10 bar, H_2/*n*-heptane = 10/1 mol/mol, WHSV = 2.1 $g_{n\text{-C7}}\ g_{cat}^{-1}\ h^{-1}$.

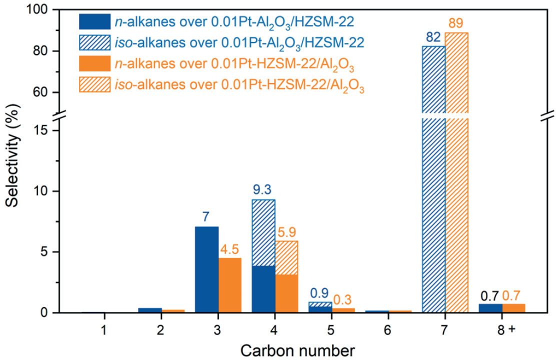

Figure S3.8. Product selectivity over 0.01Pt-Al_2O_3/HZSM-22 (blue) at 320 °C and WHSV of 2.1 $g_{n\text{-C7}}\ g_{cat}^{-1}\ h^{-1}$ at the *n*-heptane conversion of 38.2%, and 0.01Pt-HZSM-22/Al_2O_3 (orange) at 310 °C and WHSV of 4.2 $g_{n\text{-C7}}\ g_{cat}^{-1}\ h^{-1}$ at the *n*-heptane conversion of 35.9%. C_{8+} denotes hydrocarbon products with a carbon number of 8 or higher.

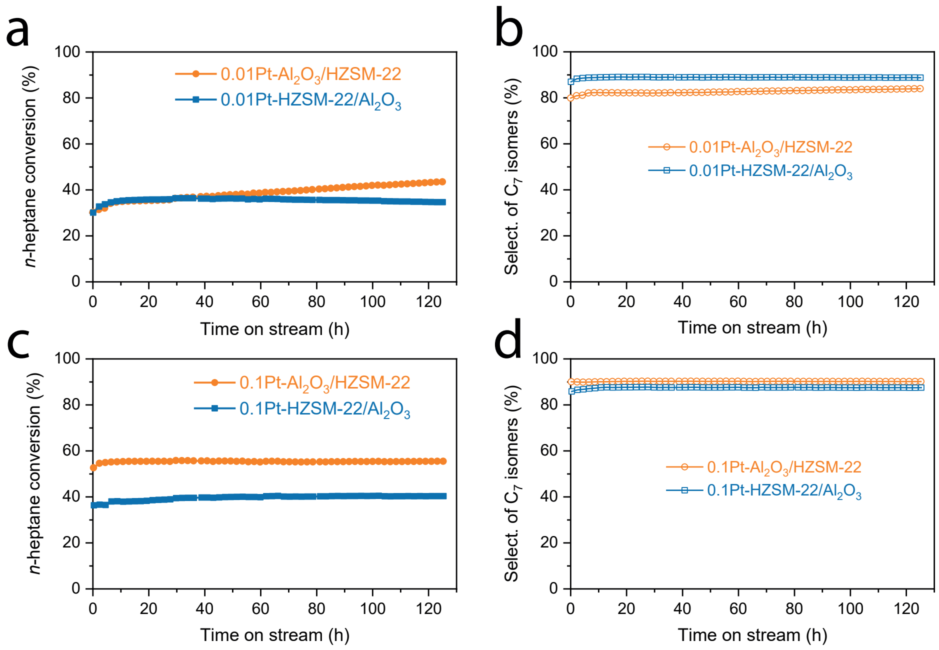

Figure S3.9. Catalytic performance with time-on-stream of HZSM-22 based catalysts. a,b) *n*-C_7 conversion and selectivity of C_7 isomers over 0.01Pt-Al_2O_3/HZSM-22 (WHSV 2.1 $g_{n\text{-}C7}$ g_{cat}^{-1} h^{-1}) and 0.01Pt-HZSM-22/Al_2O_3 (WHSV 4.2 $g_{n\text{-}C7}$ g_{cat}^{-1} h^{-1}). c,d) *n*-C_7 conversion and selectivity of C7 isomers over 0.1Pt-Al_2O_3/HZSM-22 (WHSV 4.2 $g_{n\text{-}C7}$ g_{cat}^{-1} h^{-1}) and 0.1Pt-HZSM-22/Al_2O_3 (WHSV 4.2 $g_{n\text{-}C7}$ g_{cat}^{-1} h^{-1}). Reaction condition: P = 10 bar, T = 310 °C. H_2/*n*-C_7 = 10/1.

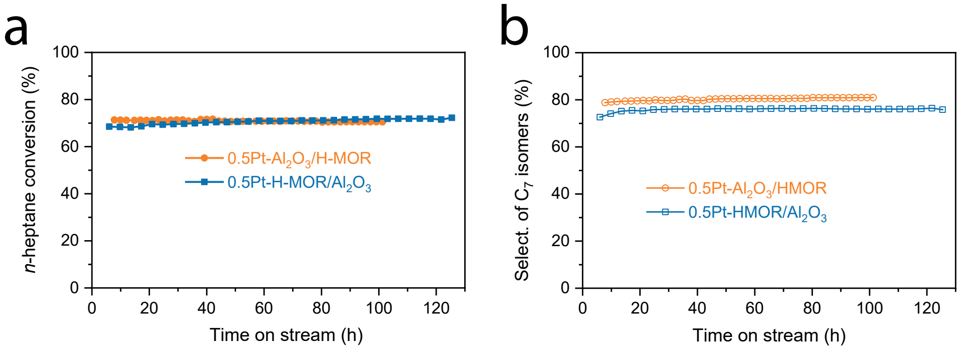

Figure S3.10. Catalytic performance with time-on-stream of HMOR based catalysts. a) *n*-C_7 conversion and b) selectivity of C7 isomers over 0.5Pt-Al_2O_3/HMOR and 0.5Pt-HMOR/Al_2O_3. Reaction condition: P = 10 bar, T = 270 °C. H_2/*n*-C_7 = 10/1, WHSV = 2.1 $g_{n\text{-}C7}$ g_{cat}^{-1} h^{-1}.

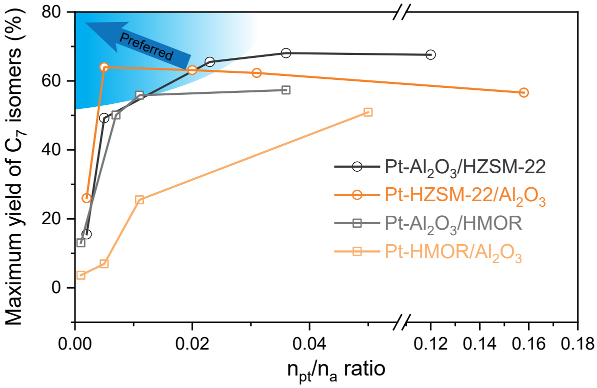

Figure S3.11. Maximum yield of C_7 isomers versus the ratio of n_{Pt}/n_a over different catalysts. The calculation of n_{Pt}/n_A is shown in Table S3.4.

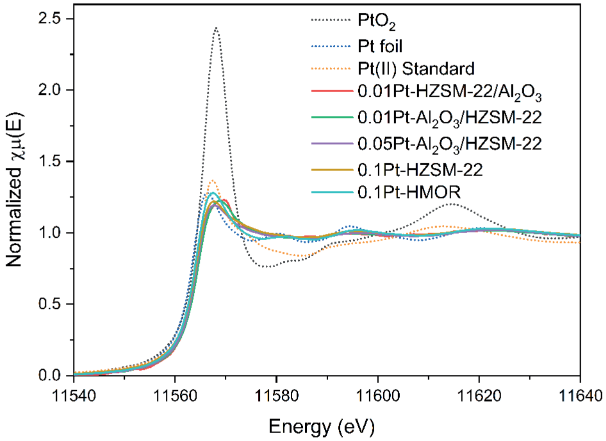

Figure S3.12. X-ray absorption near edge structure (XANES) spectra of bifunctional catalysts after reduction at 350 °C for 1 hour together with platinum standards at the Pt L_3 edge.

Table S3.2. The textural properties of samples from nitrogen physisorption experiments.

Sample	**Si/Al** [a]	S_{BET}	S_{micro} [b]	S_{ext} [b]	V_{total} [c]	V_{micro} [b]	V_{meso} [d]
	(at/at)	**($m^2\ g^{-1}$)**	**($m^2\ g^{-1}$)**	**($m^2\ g^{-1}$)**	**($cm^3\ g^{-1}$)**	**($cm^3\ g^{-1}$)**	**($cm^3\ g^{-1}$)**
HZSM-22	37	175	133	42	0.16	0.06	0.10
HMOR	9.7	449	390	59	0.25	0.18	0.07
Al_2O_3 binder	-	321	34	287	0.70	0.01	0.69

[a] By X-ray Fluorescence Spectroscopy, [b] t-plot method, [c] single point desorption total pore volume, $P/P_0 = 0.996$, [d] $V_{meso} = V_{total} - V_{micro}$.

Table S3.3. Platinum loading and particle size of Pt-zeolite catalysts before peptizing with boehmite.

Catalyst	**Pt intake [a]** **(wt%)**	**Pt loading by ICP** **(wt%)**	**Pt size by STEM** **(nm)**	***D*** **[b]** **(%)**
1.0Pt-HZSM-22	1.5	1.2	1.7 ± 0.5	66
0.2Pt-HZSM-22	0.2	0.24	1.5 ± 0.6	75
0.1Pt-HZSM-22	0.12	0.09	1.4 ± 0.4	81
0.02Pt-HZSM-22	0.024	0.03	1.1 ± 0.8	100
0.01Pt-HZSM-22	0.012	n.a. [c]	n.a. [c]	-
1.0Pt-HMOR	1.5	1.2	1.6 ± 0.3	71
0.2Pt-HMOR	0.2	0.2	1.2 ± 0.4	94
0.1Pt-HMOR	0.12	0.10	1.0 ± 0.3	100
0.02Pt-HMOR	0.024	0.02	n.a. [c]	-

[a] Metallic platinum content in aqueous solution of $Pt(NH_3)_4(NO_3)_2$ for ion exchange.

[b] $D = 1.13/d_{Pt}$.[40] Dispersion of platinum nanoparticles with a particle size smaller than 1.13 nm was assumed to be 100%.

[c] Not analyzed.

Note: The platinum particle sizes of Pt-HZSM-22 were generally larger than those of Pt-HMOR, because HMOR provided a much larger available surface area in the micropores than the external surface of the zeolite crystals. It also can be evidence that platinum NPs are located inside the restricted HMOR crystals, while the majority of platinum NPs are on the outer surface of HZSM-22 crystals.

Table S3.4. Platinum and acid properties of bifunctional catalysts (n.a. denotes 'not analyzed' due to the platinum amount being under the limit of detection.

Catalyst	Pt intake [a] (wt%)	Pt loading [b] (wt%)	Pt size [d] (nm)	D (%)	n_{Pt} [g] (μmol g^{-1})	n_A [h] (μmol g^{-1})	n_{Pt}/n_A
0.5Pt-HZSM-22/Al2O3	0.75	0.59 [c]	1.7 ± 0.5	66 [e]	20	127	0.158
0.1Pt-HZSM-22/Al2O3	0.1	0.12 [c]	1.5 ± 0.6	75 [e]	3.9	127	0.031
0.05Pt-HZSM-22/Al2O3	0.06	0.07 [c]	1.4 ± 0.4	81 [e]	2.5	127	0.020
0.01Pt-HZSM-22/Al2O3	0.012	0.015 [c]	1.1 ± 0.8	100 [e]	0.6	127	0.005
0.005Pt-HZSM-22/Al2O3	0.006	n.a.	n.a.	100 [f]	0.2	127	0.002
0.5Pt-Al2O3/HZSM-22	0.56	0.46	1.9 ± 0.5	59 [e]	15	127	0.120
0.1Pt-Al2O3/HZSM-22	0.11	0.16	1.4 ± 0.6	81 [e]	4.6	127	0.036
0.05Pt-Al2O3/HZSM-22	0.056	0.055	0.9 ± 0.4	100 [e]	2.9	127	0.023
0.01Pt-Al2O3/HZSM-22	0.012	0.017	0.7 ± 0.2	100 [e]	0.6	127	0.005
0.005Pt-Al2O3/HZSM-22	0.005	n.a.	n.a.	100 [f]	0.3	127	0.002
0.5Pt-HMOR/Al2O3	0.75	0.61 [c]	1.6 ± 0.3	71 [e]	23	453	0.050
0.1Pt-HMOR/Al2O3	0.1	0.10 [c]	1.2 ± 0.4	94 [e]	4.8	453	0.011
0.05Pt-HMOR/Al2O3	0.06	0.05 [c]	1.0 ± 0.3	100 [e]	2.5	453	0.005
0.01Pt-HMOR/Al2O3	0.012	0.01 [c]	n.a.	100 [f]	0.5	453	0.001
0.5Pt-Al2O3/HMOR	0.56	0.63	1.8 ± 0.5	63 [e]	16.5	453	0.036
0.1Pt-Al2O3/HMOR	0.11	0.12	1.4 ± 0.5	81 [e]	5.0	453	0.011
0.05Pt-Al2O3/HMOR	0.056	0.06	0.9 ± 0.3	100 [e]	3.1	453	0.007
0.01Pt-Al2O3/HMOR	0.012	0.01	n.a.	100 [f]	0.5	453	0.001

[a] Metallic platinum content in $[Pt(NH_3)_4](NO_3)_2$ or $H_2[PtCl_6]$ aqueous solutions used.

[b] By inductively coupled optical emission spectroscopy of digested samples.

[c] Since the Pt-zeolite/Al_2O_3 catalysts were prepared by mixing Pt-zeolite with boehmite with a zeolite/Al_2O_3 weight ratio of 1/1, the value of platinum loading was calculated from the platinum ICP loading in Table S3.3 divided by 2.

[d] Average platinum size with standard deviations analyzed by more than 200 particles from STEM images.

[e] Dispersion = $1.13/d_{Pt}$. Dispersion of catalyst with particle size smaller than 1.13 nm was estimated to be 100%.

[f] Based on the fact that no obvious Pt–Pt scattering was observed over platinum catalysts with 0.01 wt% loading by XAS, as a result, catalysts with lower platinum loadings could be considered to have 100% dispersion.

[g] n_{pt} denotes the density of surface Pt atoms, calculated by Pt ICP loadings (If not detected, using Pt intake) and dispersion.

[h] By deconvolution of NH_3-TPD profiles and integration of high-temperature (≥ 300 °C) peak.

Table S3.5. Quantification of XANES LCF results.

Sample	**Pt^0** **(wt%)**	**$Pt^{\delta+}$** **(wt%)**	**R-factor**
0.01Pt-Al_2O_3/HZSM-22	28.9 ± 2.9	71.1 ± 4.1	0.032
0.01Pt-HZSM-22/Al_2O_3	69.6 ± 1.6	30.4 ± 3.2	0.016
0.05Pt-Al_2O_3/HZSM-22	81.9 ± 1.4	18.1 ± 3.8	0.017
0.1Pt-HZSM-22	76.7 ± 2.3	23.3 ± 4.2	0.024
0.1Pt-HMOR	77.6 ± 2.1	22.4 ± 4.1	0.004

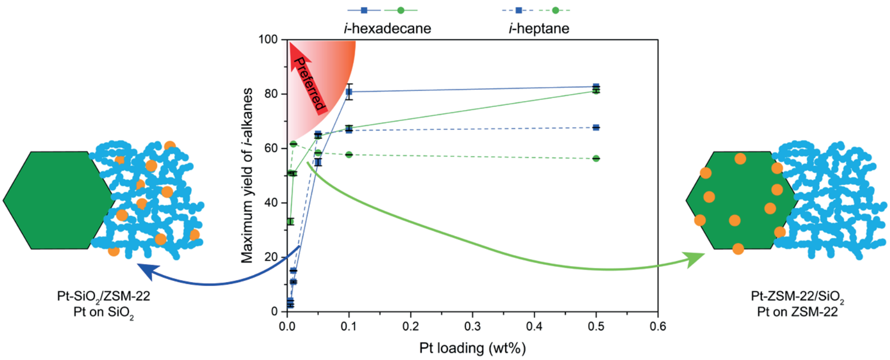
i-hexadecane
i-heptane
Preferred
Maximum yield of i-alkanes
Pt loading (wt%)
0
20
40
60
80
100
0.0
0.1
0.2
0.3
0.4
0.5
0.6
Pt-SiO$_2$/ZSM-22
Pt on SiO$_2$
Pt-ZSM-22/SiO$_2$
Pt on ZSM-22

Chapter 4

Silica as support and binder in bifunctional catalysts with ultralow Pt loadings

Abstract: Hydroconversion is a key step in the production of ultraclean fuels from renewable sources. This reaction is carried out using a bifunctional catalyst consisting of a base metal sulfide or a noble metal and a solid acid. In Chapter 3, we have shown that for Pt/Al_2O_3/ZSM-22 catalysts with low Pt loadings ($\leq$ 0.01 wt%) it is advantageous – to both the activity as well as the isomer selectivity – to emplace the Pt on the zeolite crystallites instead of on the Al_2O_3 binder. When these low loadings of Pt were on the alumina binder, small clusters or even single atoms were present which were hard to reduce leading to inactivity of the catalysts. In this chapter, we explore the replacement of alumina by silica, and the performance of catalysts with ultralow Pt loadings on the conversion of longer-chain hydrocarbons. A series of Pt/SiO_2/ZSM-22 catalysts with varying Pt weight loadings (0.001, 0.005, 0.01, 0.05, 0.1 and 0.5 wt%) and location (on silica or on ZSM-22) was prepared and characterized using ICP, NH_3-TPD, HAADF-STEM and XAS. Their hydroconversion performance was evaluated using *n*-heptane and *n*-hexadecane as model feedstocks. As for the Pt/Al_2O_3/ZSM-22 catalysts systems, for Pt/SiO_2/ZSM-22 catalysts with low Pt loadings ($\leq$ 0.01 wt% for *n*-heptane conversion) it was beneficial to have the Pt nanoparticles on the ZSM-22 crystals. Hydroconversion of *n*-hexadecane over Pt/SiO_2/ZSM-22 and Pt/Al_2O_3/ZSM-22 catalysts showed that for feedstocks with a higher molecular weight, higher Pt loadings ($\geq$ 0.05 wt%) are required for sufficient catalytic performance. For the conversion of *n*-hexadecane it was beneficial to locate these higher amounts of Pt on the binder.

This chapter is based on: Smulders, L.C.J.; Beeuwkes, A.J.; Cheng, K.; Meeldijk, J.D.; Xu, Z.; Tierney, G.F.; Doskocil, E.; Roberts, S.T.; Sunley, G.J.; de Jongh, P.E.; de Jong, K.P., Silica as support and binder in bifunctional catalysts with ultralow Pt loadings for the hydroconversion of *n*-alkanes, *Catalysis Today*, **2024** (429), 114508.

4.1. Introduction

Platinum group metals (PGMs) are indispensable for several emerging and established technologies. Platinum, for example, is utilized in fuel cells,[1,2] electrolysers,[3] catalytic converters[4] and refinery catalysts.[5] Although their applicability is large, their reserves are not and supply of PGMs is considered to be at risk.[6,7] Therefore, it is necessary to look into ways to improve recycling and to maximize their utilization.

As shown in the previous chapters, one refinery process requiring PGMs is the hydroconversion of alkane feedstocks. This is a key step in the production of ultraclean fuels and lubricants from renewable sources, such as Fischer-Tropsch waxes,[8,9] biobased fatty acids[10] or plastic waste.[11–13] Hydroconversion is performed with a bifunctional catalyst consisting of a metal (sulfide) function and an acid function, for dehydrogenation-hydrogenation and isomerization-cracking, respectively.[14,15] These roles are typically fulfilled by base metal sulfides or Pt, in combination with amorphous silica-aluminas, zeolites or zeotypes.[16] Previous research regarding hydroconversion focused on the ideal distance between these two functions,[17–20] and their respective ratio, known as the metal-to-acid-site (n_M/n_A) ratio.[21–23]

To optimize PGM utilization in hydroconversion catalysts, we previously studied the optimal Pt weight loading as a function of the Pt location. This study is described in Chapter 3. At regular weight loadings of 0.1 – 0.5 wt%, it is beneficial to have the metal function on the alumina binder, at nanoscale distance from the zeolite acid sites.[19,24–27] However, for Pt/Al_2O_3/ZSM-22 catalysts the loading could be reduced to 0.01 wt% Pt when the Pt nanoparticles were placed on the zeolite crystals, without compromising catalytic activity, selectivity towards isomers, or stability during the hydroconversion of *n*-heptane. For hydroconversion of longer chain hydrocarbons, e.g. *n*-hexadecane, the n_M/n_A ratio has to be higher for an optimal performance.[28,29] Although the reactivity of these longer hydrocarbons differs from the shorter ones,[29–31] optimal Pt weight loading as function of the Pt location has not been studied for feedstocks with higher molecular weight yet.

Additionally, characterization of the low (0.01 wt% Pt) loaded catalysts in our previous study[24] – after reduction − revealed the presence of Pt-O species when Pt was on the alumina binder. These Pt-O species are most probably inactive as (de)hydrogenation catalysts. This was confirmed by the assessment of the performance of bifunctional catalysts containing Pt single atoms. It was concluded that reduced Pt nanoparticles are required for (de)hydrogenation and hence hydroconversion activity.

Another, albeit less often utilized inorganic binder is silica. It is used in both industrial and academic research.[32–36] Although extrudates prepared with silica have been shown to undergo solid ion exchange, decreasing the Brønsted acidity of the zeolites,[37–39] silica is also known to aid in the retainment of zeolite structural stability.[40] Another possible advantage is that metal nanoparticles supported on silica are typically more readily reduced than nanoparticles of the same composition on alumina.[41,42]

In this work, we explored the replacement of the alumina binder material by a silica binder material and we assess the optimal Pt location for the conversion of longer chain hydrocarbons when ultralow Pt loadings are used.

4.2. Materials and Methods

Materials

ZSM-22 (H^+-form, Si/Al = 32.5-40 at/at) was purchased from ACS Material. Aerosil 380 silica was purchased from Evonik. Boehmite (70 wt% Al_2O_3) was supplied by Shell Technology. Tetraamine platinum (II) nitrate ($[Pt(NH_3)_4](NO_3)_2$, 99.995% pure), chloroplatinic acid ($H_2[PtCl_6] \cdot 6\ H_2O$, ≥ 37.5 wt% Pt) and acetic acid were purchased from Sigma-Aldrich. *n*-Heptane (99+%, pure) and *n*-hexadecane (99%, pure) were obtained from ACROS Organics. Ammonia solution (NH_4OH, 25%) was obtained from Emsure. Silicon carbide (SiC, SIKA ABR I F70, grain size: 220 µm) was supplied by Fiven. H_2 6.0, He 5.0 and N_2 5.0, were obtained from Linde gas.

Catalyst Preparation

Preparation of Pt/SiO_2/ZSM-22 Catalysts

ZSM-22 was calcined in a flow of synthetic air (N_2/O_2, 80/20, *vol*/*vol*) at 500 ˚C (ramp 5 ˚C min^{-1}) for 5 h. Solutions containing 6.0 mM and 0.6 mM of tetraamine platinum nitrate (PTA) were prepared by dissolving in Milli-Q water. Pt-SiO_2/ZSM-22 catalysts were prepared using an electrostatic adsorption method adapted from Regalbuto et al.[43] 500 mg of silica was dispersed in 300 mL Milli-Q water by mechanical stirring at 400 rpm for 1 h. Subsequently, the required volume of the 6.0 mM or 0.6 mM PTA solution was further diluted with 50 mL Milli-Q water and added dropwise to the dispersion, after which the pH was increased to 7 using a 0.15 M aqueous ammonia solution. The resulting dispersion was stirred for 3 additional hours. This dispersion was then filtered over vacuum. The filter cake was dried overnight in a static oven at 120 ˚C. Once dried, it was crushed and transferred to a tubular reactor. The dried catalyst precursor was then calcined in a total flow of 100 mL min^{-1} of synthetic air (N_2/O_2, 80/20, *vol*/*vol*) at 350 ˚C (ramp: 0.2 ˚C min^{-1}) for 2 h and reduced in a H_2 rich atmosphere (H_2/N_2, 80/20, *vol*/*vol*) at 600 ˚C (ramp: 5 ˚C min^{-1}) for 3 h. After cooling down to room temperature the resulting powder was mixed with calcined ZSM-22. For this, the ZSM-22 was first mixed with 100 µL of a 1.5 mM aqueous ammonia solution and 250 µL Milli-Q water using a mortar and pestle for 15 min. After this the Pt/SiO_2 powder was added and mixed for an additional 15 min. The resulting paste was dried in a static oven at 120 ˚C overnight and calcined (N_2/O_2, 80/20, *vol*/*vol*) at 500 ˚C (ramp: 5 ˚C min^{-1}) for 2 h.

Pt-ZSM-22/SiO_2 catalysts were prepared via ion exchange (IE). First, 500 mg of calcined ZSM-22 was dispersed in 300 mL Milli-Q water by stirring mechanically at 400 rpm for 1 h. Meanwhile, the required volume of 6 mM PTA solution was further diluted with Milli-Q water to obtain a PTA solution of 50 mL with the desired concentration. This solution was added dropwise to the dispersion, and stirred for an additional 3 h. The dispersion was filtered over vacuum and the resulting filter cake was dried in a static oven at 120 °C overnight. The powder was then transferred to a tubular reactor and calcined in a flow (100 mL min^{-1}) of synthetic air (N_2/O_2, 80/20, *vol*/*vol*) at 350 ˚C (ramp: 0.2 ˚C min^{-1}) for 2 h. This was followed by reduction in a H_2 rich atmosphere (H_2/N_2, 80/20, *vol*/*vol*) at 600 ˚C (ramp: 5 ˚C min^{-1}) for 3 h and cooling down to room temperature. 500 mg of Aerosil 380 was then mixed with 100 µL of a 1.5 mM aqueous ammonia solution and 250 µL Milli-Q water using a mortar and pestle for 15 min, after which the Pt/ZSM-22 catalyst was added to the mortar. The powders were stirred for additional 15 min. The resulting paste was again dried in a static oven at 120 ˚C overnight and calcined (N_2/O_2, 80/20, *vol*/*vol*) at 500 ˚C (ramp: 5 ˚C min^{-1}) for 2 h.

Preparation of Pt/γ-Al_2O_3/ZSM-22 Catalysts

Pt/γ-Al_2O_3/ZSM-22 catalysts were prepared as previously reported.[24] ZSM-22 was calcined in a flow of synthetic air (N_2/O_2, 80/20, *vol*/*vol*) at 500 °C for 5 h with a ramp of 1 °C min^{-1}. Zeolite-alumina composite (1/1, *wt*/*wt*) material was prepared by mixing using acetic acid for the deagglomeration of boehmite. In order to obtain 10 g of composite, firstly, 7.14 g of boehmite was mixed with 6 mL Milli-Q H_2O and 0.21 mL acetic acid using mortar and pestle. When wetting of the boehmite was complete, 5 g of ZSM-22 was added to the mortar. Then, the mixture was mixed for 10 minutes using a mortar and pestle and additional Milli-Q H_2O was added until a homogeneous paste was obtained. The resulting paste was dried overnight in an oven at 120 °C. The dried powder was crushed and calcined for 2 h at 500 °C using a ramp of 5 °C min^{-1}.

Pt-γ-Al_2O_3/ZSM-22 catalysts with varying Pt weight loadings (0.005 – 0.5 wt%) were prepared via electrostatic adsorption.[24,43] For this, 1.5 g of the composite material was dispersed in 450 mL Milli-Q H_2O and stirred for 30 min. The pH of the dispersion was adjusted to 2.6 using a 1 M aqueous solution of hydrochloric acid. At this pH value, the surface of the Al_2O_3 is positively charged. A given volume of an aqueous solution of chloroplatinic acid (0.17 mg$_{Pt}$ mL^{-1}) was added dropwise. The dispersion was stirred for 3 h, after which it was filtered and washed with 500 mL Milli-Q H_2O. The filter cake was dried overnight in an oven at 120 °C. The resulting catalyst powder was reduced in a flow of H_2/N_2 (20/80, *vol*/*vol*) at 500 °C for 3 h using a heating ramp of 1 °C min^{-1} and calcined for 2 h at 500 °C in a flow of synthetic air (N_2/O_2, 80/20, *vol*/*vol*).

For the preparation of Pt-ZSM-22/γ-Al_2O_3, firstly, 0.75 g of ZSM-22 was dispersed in 225 mL Milli-Q H_2O and stirred for 30 min. Then a given volume of the PTA solution was added dropwise and the mixture was stirred for 3 h. The dispersion was filtered without further washing and both the filtrate and the filter cake were collected. The filter cake was dried in an oven at 60 °C and reduced (H_2/N_2, 20/80, *vol*/*vol*) at 500 °C for 3 h with a ramp of 1 °C min^{-1}. When cooled to room temperature the resulting powders were redispersed in the filtrate that still contained PTA. The IE procedure including stirring, filtration, drying and reduction was performed a second time. The Pt-ZSM-22/γ-Al_2O_3 composite catalyst was then prepared by mixing the Pt/ZSM-22 catalyst with boehmite, using acetic acid as peptizing agent, followed by drying and calcination as described for the preparation of ZSM-22/γ-Al_2O_3 composite, but now with a heating ramp of 1 °C min^{-1} during calcination.

Catalyst Characterization

Quantification of Metal and Acid Sites

Analysis of the elemental composition of the catalysts was performed at Mikroanalytisches Laboratorium Kolbe, Germany, using an inductively coupled plasma optical emission spectrometer (ICP-OES). Prior to measurements, samples were dissolved according to their standard in-house procedures.

Temperature programmed desorption of ammonia (NH_3-TPD) was performed to quantify the number of acid sites in each catalyst. The measurements were performed on a Micromeritics AutoChem II equipped with a thermal conductivity detector (TCD) calibrated for ammonia. For a typical measurement 80 – 110 mg of catalyst was dried in a helium flow for 1 h at 600 °C with a ramp of 10 °C min^{-1}. This was followed by lowering the temperature to 100 °C after which ammonia (10 vol% in He) was introduced in a pulse-wise manner until oversaturation was accomplished. After this, the physisorbed ammonia was removed by flushing He for 2 h at 100 °C. Subsequently, the desorption of ammonia up to 600 °C with a ramp of 10 °C min^{-1} was monitored.

Nitrogen Physisorption

Measurements of N_2 physisorption isotherms were performed at -196 °C on a Micromeritics Tristar II Plus apparatus. Prior to the measurement, the samples were dried in a nitrogen flow at 300 °C. The accessible surface areas of the catalysts were determined with the Brunauer-Emmett-Teller (BET) method. A Harkins-Jura thickness curve fitted between 0.32 and 0.40 nm thickness was used to determine micropore (< 2 nm) volumes. Total pore volumes were derived from the volume of N_2 adsorbed at $P/P_0 = 0.95$.

Electron Microscopy

Prior to studying the samples with electron microscopy, the samples were ultramicrotomed. Firstly, the samples were embedded in EpoFix resin, and then left to harden in an oven at 60 °C overnight. To obtain slices with a thickness of 70 nm, the resin-embedded samples were cut using a Reichert-Jung Ultracut E ultramicrotome and a Diatome Ultra 35° diamond knife. The resulting sections were deposited on glow-discharged carbon-formvar-coated copper grids (200 mesh). High-resolution high-angle annular dark-field scanning transmission electron microscopy (HAADF-STEM) was performed on a Thermo Fisher Scientific Spectra 300 S/TEM operating at 300 kV. The number average particle size (d_n) of the Pt nanoparticles was determined by measuring the nanoparticle diameter using ImageJ software, followed by a calculation using Equation 4.1. Furthermore, the surface average particle size (d_s) in each catalyst sample was calculated using Equation 4.2.

$$d_{\mathrm{n}} \pm \sigma_{\mathrm{dn}} = \frac{1}{N}\sum_{i=1}^{N} d_i \pm \sqrt{\frac{1}{N}\sum_{i=1}^{N}(d_{\mathrm{n}} - d_i)^2} \qquad \textbf{(Eq. 4.1.)}$$

$$d_{\mathrm{s}} \pm \sigma_{\mathrm{ds}} = \frac{\sum_{i=1}^{N} d_i{}^3}{\sum_{i=1}^{N} d_i{}^2} \pm \sqrt{\frac{1}{N}\sum_{i=1}^{N}(d_{\mathrm{s}} - d_i)^2} \qquad \textbf{(Eq. 4.2.)}$$

X-ray Absorption Spectroscopy

X-ray Absorption Spectroscopy was performed at the Advanced Photon Source (APS), Argonne National Lab, USA, at the Insertion Device of sector 10. Measurements were performed at the Pt L_3 edge (11.563 keV) in fluorescence mode, using a double monochromator with direct drive air bearings and two sets of crystals: Si (111) and Si (311). To filter out the higher harmonics present in the X-ray beam, a 60 cm long flat harmonic rejection mirror was used. Approximately 100 mg of sample was pressed into a pellet and placed in a sample holder at 45° to the beam direction. The holder was placed in an *in situ* temperature programmable sample cell operated under ambient pressure. The samples were reduced for 1 h in a gas flow of 100 mL min^{-1} containing 3.5 vol% H_2/He at 400 °C, after which they were cooled to room temperature. Fluorescence data were collected with an ion chamber Lytle detector with a step size of 0.5 eV and an acquisition time of 0.1 s per point. XANES spectra were processed using Athena software (Demeter 0.9.26) by averaging 12 scans for each sample.[44,45] For the 0.01Pt-SiO_2/ZSM-22 sample 58 scans were averaged to improve the low Pt signal/noise. Normalization of the XANES data was done by dividing the absorption intensities by the height of the absorption edge and subtracting the background using cubic spline routines. The oxidation state of Pt was determined from Linear Combination Fitting (LCF) from Athena in the derivative space of μ(E). For this, PtO_2 $[Pt(NH_3)_4](NO_3)_2$ and Pt foil were used as reference standards for Pt^{4+}, Pt^{2+} and Pt^0, respectively. The data was fitted to the references in the range of 20 eV below and 30 eV above the Pt L_3 edge energy. EXAFS fitting was performed by converting the spectra in *k*-space with *k*-weight 2 and in the range of 2.0-11 Å^{-1}, d_k of 0.5, R range of 1.3-3.0 Å, d_r of 0.5, and a Hanning window. Multiple shell fitting was performed involving Pt-Pt and Pt-O paths in R space. Data for back scattering amplitudes were obtained with the built-in FEFFIT calculation using the Artemis software.[45] Prior to fitting of the acquired EXAFS data, the amplitude reduction factor ($S_0{}^2$) was calculated by fitting a Pt^0 reference foil using a Pt FCC *.cif* file taken from an online source (Materials Project, mp-126), yielding a value of 0.7 applied to all fitted Pt L_3 edge datasets.

Hydroconversion of *n*-Heptane and *n*-Hexadecane

The hydroconversion performance of the catalysts was assessed using an Avantium Flowrence 16 parallel fixed bed reactor setup with *n*-heptane (*n*-C_7) and *n*-hexadecane (*n*-C_{16}) as feedstock. Stainless steel reactors (inner diameter = 2 mm) were loaded with SiC (220 µm) until it reached a bed height of 2 cm. On top of this SiC bed, 30 mg of sieved catalyst (75 – 212 µm) was loaded. This was followed by adding more of the SiC, leaving 2 cm of free space at the top of the reactor. Analysis of the products was performed using an online GC (Agilent Technologies 7890B) equipped with an Agilent J&W HP-PONA column. The hydrocarbon products were analyzed using an FID. Prior to the catalytic tests with *n*-heptane the catalysts were reduced in H_2/He (90 vol% H_2) at 400 °C for 2 h. When *n*-hexadecane was studied, activation was caried out in pure H_2 at 400 °C for 3 h. Experiments with *n*-heptane feedstock were performed with the following reaction conditions: H_2/*n*-heptane molar ratio of 10, total pressure of 10 bar and WHSV of 2.4 $g_{n\text{-C7}} \cdot g_{cat}^{-1} \cdot h^{-1}$. When *n*-hexadecane was used as a feedstock, the following reactions conditions were applied: H_2/*n*-hexadecane molar ratio of 10, total pressure of 5 bar and WHSV of 2.9 $g_{n\text{-C16}} \cdot g_{cat}^{-1} \cdot h^{-1}$. These pressures were chosen to prevent alkane condensation during reaction.

The conversion of *n*-heptane or *n*-hexadecane ($X_{n\text{-alkane}}$) was calculated using:

$$X_{n\text{-alkane}} = \left(1 - \frac{F_{\mathrm{Cwt.}n-\mathrm{alkane,out}}}{F_{\mathrm{Cwt.}n-\mathrm{alkane,in}}}\right) \cdot 100\% \qquad \textbf{(Eq. 4.3.)}$$

Where $F_{\mathrm{Cwt.}n\text{-alkane,out}}$ and $F_{\mathrm{Cwt.}n\text{-alkane,in}}$ are the flows based on carbon weight of *n*-alkane going out or in the reactor, respectively. The isomer yield ($Y_{i\text{-alkane}}$) was calculated using:

$$Y_{i\text{-alkane}} = \left(\frac{F_{\mathrm{Cwt.}i-\mathrm{alkane,out}}}{F_{\mathrm{Cwt.}n-\mathrm{alkane,in}}}\right) \cdot 100\% \qquad \textbf{(Eq. 4.4.)}$$

Similarly, the yield of any cracked product was calculated using:

$$Y_{Cm} = \left(\frac{F_{\mathrm{Cwt.}Cm\mathrm{,out}}}{F_{\mathrm{Cwt.}n-\mathrm{alkane,in}}}\right) \cdot 100\% \qquad \textbf{(Eq. 4.5.)}$$

In which C_m is a hydrocarbon molecule with m carbon atoms (*m* = 1-6 during *n*-heptane conversion and *m* = 1-14 during *n*-hexadecane conversion).

For *n*-hexadecane, the yield in mol-% of a product with m carbon atoms was calculated as follows:

$$Y_{Cm}\,(mol-\%) = \left(\frac{F_{C\mathrm{wt}.Cm,\mathrm{out}}}{F_{C\mathrm{wt}.n-\mathrm{alkane,in}}}\right)\cdot\left(\frac{16}{m}\right)\cdot 100\% \qquad \textbf{(Eq. 4.6.)}$$

The selectivity towards *i*-heptane (*i*-C_7), *i*-hexadecane (*i*-C_{16}) or cracked products (C_m) during hydroconversion was calculated with the following two equations:

$$S_{i\text{-}C7} = \left(\frac{F_{C\mathrm{wt}.i-\mathrm{C7,out}}}{F_{C\mathrm{wt}.n-\mathrm{alkane,in}} - F_{C\mathrm{wt}.n-\mathrm{alkane,out}}}\right)\cdot 100\% \qquad \textbf{(Eq. 4.7.)}$$

$$S_{i\text{-}C16} = \left(\frac{F_{C\mathrm{wt}.i-\mathrm{C16,out}}}{F_{C\mathrm{wt}.n-\mathrm{alkane,in}} - F_{C\mathrm{wt}.n-\mathrm{alkane,out}}}\right)\cdot 100\% \qquad \textbf{(Eq. 4.8.)}$$

$$S_{Cm} = \left(\frac{F_{C\mathrm{wt}.Cm,\mathrm{out}}}{F_{C\mathrm{wt}.n-\mathrm{alkane,in}} - F_{C\mathrm{wt}.n-\mathrm{alkane,out}}}\right)\cdot 100\% \qquad \textbf{(Eq. 4.9.)}$$

4

It should be noted that the C_{15} peaks overlap with *i*-C_{16} peaks in the chromatogram, and therefore it is assumed that Y_{C1} (mol-%) = Y_{C15} (mol-%). This holds when hydrogenolysis activity is low, which is the case for the Pt based catalysts. The signals for 'C_{15}' and *i*-C_{16} peaks are ascribed to *i*-C_{16} products.

4.3. Results and Discussion

Quantification of Metal and Acid Sites

The platinum weight loadings and number of acid sites are summarized in Table 4.1. The actual Pt weight loading was close to the intended weight loading resulting in a series of Pt-SiO_2/ZSM-22 (Pt-on-silica) and Pt-ZSM-22/SiO_2 (Pt-on-ZSM-22) catalysts with weight loadings of 0.005, 0.01, 0.05, 0.1 and 0.5 wt%. The number of acid sites as determined by temperature programmed desorption of ammonia (NH_3-TPD) was in all cases between 0.14 and 0.19 mmol g^{-1} with no clear correlation with Pt loading.

The Pt weight loadings were similar to the weight loadings on the Pt/Al_2O_3/ZSM-22 catalysts as previously reported.[24] The numbers of acid sites in the Pt/SiO_2/ZSM-22 were slightly higher compared to those of the Pt/Al_2O_3/ZSM-22 catalysts, which might have been caused by using a different batch of ZSM-22 or by effects caused by the binder.[35,37] It is not expected that these differences were caused by dealumination of the zeolite as has been observed with silica binders before,[34,38] since the number of acid sites per gram of composite (50/50 zeolite/binder by mass) material was approximately half of the number of acid sites in pristine ZSM-22 (0.280 mmol g^{-1}, Table S4.1).

Table 4.1. Results of quantification of metal and acid sites; Pt weight loading, particle size and dispersion, and number of strong acid sites.

Catalyst	Intended Pt loading (wt%)	Pt loading [a] (wt%)	Number of strong acid sites [b] (mmol g^{-1})	$d_n \pm \sigma_n$ [c] (nm)	$d_s \pm \sigma_s$ [d] (nm)	D [e] (%)	n_{Pt}/n_A
0.005Pt-SiO$_2$/ZSM-22	0.005	0.004	0.160	n.d.	n.d.	100 [f]	0.001
0.01Pt-SiO$_2$/ZSM-22	0.01	0.012	0.139	~0.8 [g]	~1.3 [g]	100	0.004
0.05Pt-SiO$_2$/ZSM-22	0.05	0.041	0.142	1.2 ± 1.1	4.0 ± 1.6	94	0.014
0.1Pt-SiO$_2$/ZSM-22	0.1	0.013	0.182	2.6 ± 3.6	12.3 ± 4.5	43	0.016
0.5Pt-SiO$_2$/ZSM-22	0.5	0.46	0.158	1.1 ± 0.9	4.1 ± 1.5	100	0.15
0.005Pt-ZSM-22/SiO$_2$	0.005	0.004	0.166	1.1 ± 0.4	1.3 ± 1.1	100	0.001
0.01Pt-ZSM-22/SiO$_2$	0.01	0.009	0.154	0.9 ± 0.4	1.6 ± 1.0	100	0.003
0.05Pt-ZSM-22/SiO$_2$	0.05	0.054	0.136	1.3 ± 1.9	10.1 ± 2.3	86	0.018
0.1Pt-ZSM-22/SiO$_2$	0.1	0.11	0.145	1.4 ± 1.7	7.4 ± 2.3	82	0.032
0.5Pt-ZSM-22/SiO$_2$	0.5	0.41	0.189	1.1 ± 0.3	1.3 ± 1.2	100	0.11

[a] Determined by inductively coupled plasma optical emission spectroscopy on digested samples.

[b] Determined by deconvolution of NH$_3$-TPD profiles and integration of the peak at $T \geq 300$ °C.

[c] Number average size of Pt nanoparticles as determined using HAADF STEM, based on at least 150 counts.

[d] Surface average particle size as determined using HAADF STEM followed by calculation using Equation 4.2.

[e] Dispersion = $1.13/d_{Pt}$.[46] Dispersion of Pt with $d_{TEM} < 1.13$ nm was estimated to be 100%.

[f] Based on the absence of observable Pt nanoparticles or clusters in HAADF STEM and the lower weight loading than the 0.01Pt-SiO$_2$/ZSM-22 catalyst.

[g] Average diameter of Pt nanoparticles based on 3 nanoparticles.

Location and Size of Pt Nanoparticles

The location and size of Pt nanoparticles were determined by high resolution HAADF-STEM. Prior to the measurement, most of the catalysts were ultramicrotomed to sections with a thickness of 70 nm. This allowed for looking “inside” the catalyst grains and distinguishing Pt nanoparticles on the ZSM-22 from Pt nanoparticles on the silica binder (Figure 4.1). The resolution and contrast for Pt-SiO$_2$/ZSM-22 catalysts with a weight loading ≤ 0.01 wt% were not high enough to distinguish Pt nanoparticles unambiguously, due to a combination of a high Pt dispersion, ultralow Pt loadings, and the use of a resin. The 0.01Pt-SiO$_2$/ZSM-22 was imaged without performing ultramicrotomy, with the sample deposited onto a TEM grid by dipping the grid into a small sieve fraction (< 75 µm) of the sample (Figure 4.1f). This ensured the deposition of a very thin layer.

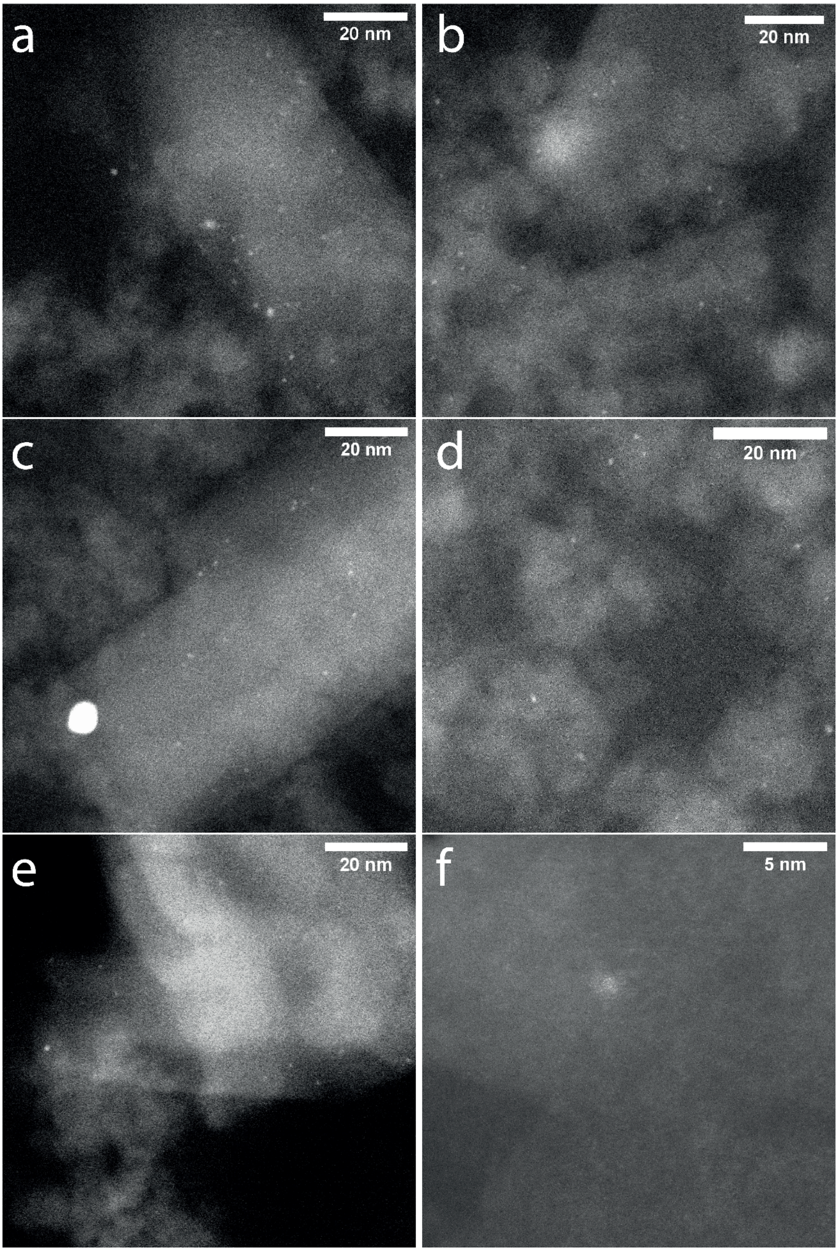

Figure 4.1. HAADF-STEM images of ultramicrotomed samples of a) 0.5Pt-ZSM-22/SiO$_2$, b) 0.5Pt-SiO$_2$/ZSM-22, c) 0.1Pt-ZSM-22/SiO$_2$, d) 0.1Pt-SiO$_2$/ZSM-22, e) 0.01Pt-ZSM-22/SiO$_2$, f) (not ultramicrotomed, mind the different scale) 0.01Pt-SiO$_2$/ZSM-22.

Based on the HAADF-STEM images the average Pt particle diameter was determined and the corresponding dispersion was calculated (Table 4.1). All samples displayed well dispersed Pt nanoparticles on either the ZSM-22, both in and on the zeolite crystals (Figure 4.1a, c and e), or on the silica binder (Figure 4.1b, d and f). However, in several images, a few larger Pt nanoparticles with a diameter up to 10 nm were observed as illustrated in Figure 4.1c and as inferred from the standard deviations in the average Pt particle diameters (Table 4.1), in particular for 0.1Pt-SiO_2/ZSM-22. This may have been caused by redissolution of platinum by the NH_3 peptizing agent, followed by rapid drying and calcination of the paste. HAADF-STEM on a physical mixture of 0.4Pt/SiO_2+ZSM-22, prepared without the use of a peptizing agent (Figure S4.1), was performed to investigate the impact of the use of NH_3. The images that were obtained showed well-dispersed Pt nanoparticles, confirming that the larger Pt nanoparticles have formed in the peptizing and (re-)calcination process. During the preparation of 0.1Pt-SiO_2/ZSM-22 there might have been a temporary higher concentration of NH_3 if the additional Milli-Q water was not added immediately afterwards, causing increased redissolution leading to a larger increase of particle size compared to the other catalysts. Since the few larger particles were outnumbered by smaller particles and because they were mainly present in samples with higher weight loadings, their overall impact on the n_{Pt}/n_A ratios is limited. Furthermore, the textural properties of the zeolite-binder mixtures, also when Pt was included, were all very alike as observed with N_2-physisorption (Table S4.2). The bifunctional catalysts therefore differ in platinum particle location and platinum weight loading, whereas the acidic properties are similar in all cases.

X-ray Absorption Spectroscopy to Study the Nature of Pt Sites

X-ray absorption spectroscopy was performed in order to obtain more information on the nature of the Pt sites after reduction. Linear Combination Fitting (LCF) of the Pt L_3 edge X-ray absorption near edge structure (XANES, Figure S4.1) was used to determine the average Pt oxidation state for the various catalysts (Table 4.2).

Table 4.2. Quantification from XANES Linear Combination Fitting (LCF) and corresponding R-factor.

Catalyst	Pt^0 (%)	Pt^{4+} (%)	R-factor
0.1Pt-SiO_2/ZSM-22	100	0	0.007
0.05Pt-SiO_2/ZSM-22	93.2 ± 2.2	6.8 ± 2.2	0.014
0.01Pt-SiO_2/ZSM-22	97.6 ± 0.8	2.4 ± 0.8	0.0077
0.1Pt-ZSM-22/SiO_2	95.1 ± 1.8	4.9 ± 1.8	0.0088
0.05Pt-ZSM-22/SiO_2	95.7 ± 1.0	4.3 ± 1.0	0.0035
0.01Pt-ZSM-22/SiO_2	88.7 ± 3.9	11.3 ± 3.9	0.037
0.005Pt-ZSM-22/SiO_2	87.0 ± 4.2	13.0 ± 4.2	0.043

Interestingly, the XANES LCF results of the Pt-on-SiO_2 catalysts all show that the Pt was predominantly present as Pt^0 (Table 4.2), unlike that of the Pt-on-Al_2O_3 catalysts prepared previously.[24] This is in agreement with the fact that silica supported nanoparticles are more readily reduced than similar particles supported on alumina.[41,42] Also for the samples with Pt on ZSM-22, the majority of Pt is zero-valent. In particular for the ZSM-22 series, decreasing the metal loading led to an increase in Pt^{4+} in these samples.

Based on the Extended X-ray Absorption Fine Structure (EXAFS) in Figure 4.2, qualitative information about the average local environment of the absorbing Pt atoms was derived.

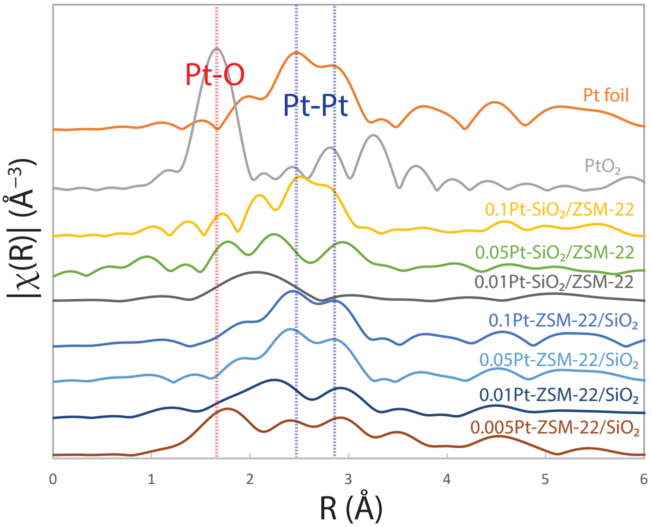

Figure 4.2. Fourier Transforms of Pt L_3 edge EXAFS spectra in R space of reduced bifunctional catalysts with different Pt weight loadings and Pt nanoparticle locations.

When Pt was deposited on silica, both Pt-Pt (scattering paths at 2.4 and 2.9 Å) and Pt-O (scattering path below 2.0 Å) scattering[24,47] were observed at a weight loading of 0.1 wt%. At a loading of 0.05 wt%, Pt-Pt scattering became less apparent and a greater magnitude of Pt-O scattering was observed. This is in line with the results obtained with Linear Combination Fitting (Table 4.2) of the XANES (Figure S4.2), showing that increased amounts of Pt^{4+} are present when decreasing the weight loading from 0.1 to 0.05 wt%. Decreasing the Pt weight loading to 0.01 wt% resulted in the absence of clear similarity with the reference spectra, and only a scattering path at a radial distance of 2.1 Å was observed. This could be indicative for the presence of Pt dimers[48] a hypothesis which is supported by the presence of small Pt clusters and low density of Pt nanoparticles in this sample (Figure 4.1f).

Strong Pt-Pt scattering was observed for all catalysts with Pt on ZSM-22, regardless of the weight loading, proving the presence of metallic Pt nanoparticles in all of these catalysts, which can be seen in the HAADF-STEM images (Figure 4.1a, c, e). At loadings < 0.05 wt%, a Pt-O scattering was observed, which can indicate covalently bound oxygen, or the interaction of Pt^0 with support oxygen, or a combination thereof.[49,50] This is likely a result of the presence of small clusters or even some single atoms of Pt.

Catalytic Performance in *n*-Heptane Hydroconversion

The performance of all $Pt/SiO_2/ZSM\text{-}22$ catalysts for the hydroconversion of *n*-heptane is summarized in Figure 4.3 and Figure S4.3. At 330 °C the *n*-heptane conversion in all cases was higher at higher Pt weight loadings. The selectivity towards isomers, however, displayed a maximum with Pt loading, also when the catalysts were compared at the same conversion level. At weight loadings of 0.1 wt% or higher it was beneficial to the isomer selectivity to have the Pt nanoparticles on the binder, in line with previous research.[19,25–27] At a weight loading of 0.01 wt% or lower, placing the Pt on the silica greatly lowered the selectivity and conversion, whereas $Pt\text{-}ZSM\text{-}22/SiO_2$ maintained reasonable activity and even outperformed its Pt-on-SiO_2 counterpart in terms of isomer selectivity. Most likely this is caused by the shortage of Pt nanoparticles in $0.01Pt\text{-}SiO_2/ZSM\text{-}22$, as evidenced by the low density of metal nanoparticles in HAADF-STEM images and absence of Pt-Pt scattering in EXAFS, and not by the chemical state of the Pt as inferred from XANES. On the contrary, the $0.01Pt\text{-}ZSM\text{-}22/SiO_2$ catalysts contained a sufficient number of Pt nanoparticles to balance (de)hydrogenation with the acid-catalyzed isomerization and cracking.

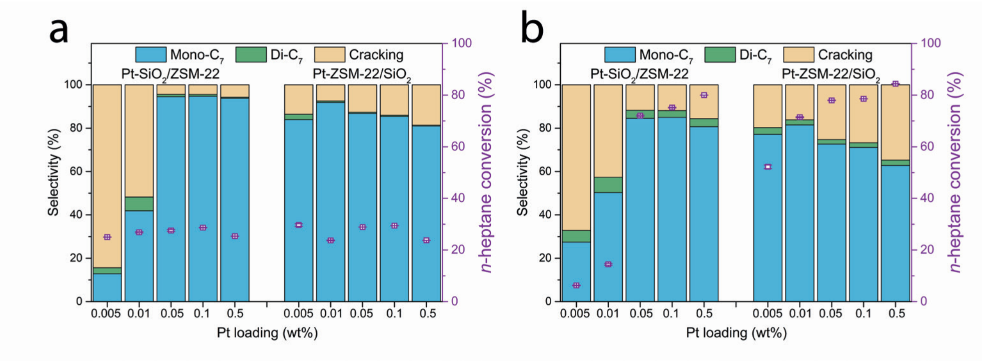

Figure 4.3. Hydroconversion of *n*-heptane over $Pt/SiO_2/ZSM\text{-}22$ bifunctional catalysts with different Pt loadings and locations at a) similar conversion levels of 24-30% and b) at the same temperature of 330 °C. Reaction conditions: P = 10 bar, $H_2/n\text{-}C_7 = 10/1$ mol/mol, and WHSV = 2.5 $g_{n\text{-}C7} \cdot g_{cat}^{-1} \cdot h^{-1}$. Mono-$C_7$ indicates monobranched *i*-heptane, Di-C_7 indicates dibranched *i*-heptane, and Cracking indicates the products that have fewer than 7 carbon atoms in their molecular structure. Error bars indicate standard deviations.

For the production of dibranched isomers of *n*-heptane, it was beneficial to place Pt on the binder. This can be rationalized by shape selectivity of the zeolite and very low inward diffusivity of bulky hydrocarbons inside of the 10 MR zeolites. In Pt-SiO_2/ZSM-22 the dibranched intermediates were likely formed in the pore mouth,[51–53] allowing for enhanced outward diffusion to the metal sites, preventing cracking. In other words, when formed too deep inside the zeolite pores, these intermediates cannot diffuse rapidly out of the zeolite, enhancing the formation of smaller hydrocarbons via cracking.

Catalytic Performance in *n*-Hexadecane Hydroconversion and Comparison with Pt/Al_2O_3/ZSM-22 Catalysts

To study the effect of the location and loading of the Pt nanoparticles in Pt/SiO_2/ZSM-22 in more detail, their catalytic performance was also assessed using *n*-hexadecane as a feedstock. Furthermore, the effect of the silica binder was investigated by comparing the results to those obtained with Pt/Al_2O_3/ZSM-22 catalysts prepared previously.[24] In general, the conversion of *n*-hexadecane requires lower temperatures than the conversion of *n*-heptane when the metal loading is sufficient (Figure S4.3 and S4.4), which is a result of the enhanced adsorption of the heavier molecule onto the catalyst. In Figure 4.4 the temperature to reach 50% *n*-hexadecane conversion (T_{50}) is shown as a function of Pt weight loading. These T_{50} values were acquired by interpolation of *n*-hexadecane conversions as function of the temperature (Figure S4.4).

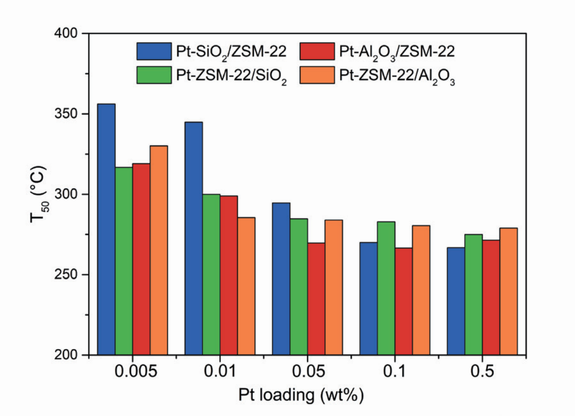

Figure 4.4. Temperature to reach 50% *n*-hexadecane conversion as function of the Pt weight loading of Pt-SiO_2/ZSM-22 (blue), Pt-ZSM-22/SiO_2 (green), Pt-Al_2O_3/ZSM-22 (red), Pt-ZSM-22/Al_2O_3 (orange) catalysts.

When Pt was on the binder (either silica or alumina), the T_{50} of the low loaded catalysts was significantly higher than the T_{50} for catalysts with higher Pt loadings. When Pt was on the ZSM-22, the T_{50} does not further decrease at loadings higher than 0.01 wt% (Figure 4.4). This finding is in line with what was observed with *n*-heptane hydroconversion, where Pt loadings of 0.01 wt% were sufficient to maintain catalytic activity, when the Pt was located on the ZSM-22 (Figure 4.3 and ref.[24]).

The type of binder and/or support also seems to play a key role in the hydroconversion activity of catalysts with low loadings. When Pt was located on the silica, the T_{50} increased and the activity of the catalyst was drastically lower when the Pt loading was lowered from 0.5 wt% to 0.05 wt% (Figure S4.4). Contrary to this, the 0.05Pt-Al_2O_3/ZSM-22 had a T_{50} that is comparable to that of the 0.5Pt-Al_2O_3/ZSM-22 catalyst in terms of activity (Figure 4.4). Since n_{Pt}/n_A ratios for the SiO_2 and Al_2O_3 catalysts were similar, the cause of this difference should be ascribed to another phenomenon. A possible explanation is that, although oxidized to an extent, the XAS of 0.01Pt-Al_2O_3/ZSM-22 catalyst showed Pt-Pt scattering and in HAADF-STEM the Pt particles were clearly present. Conversely, the 0.01Pt-SiO_2/ZSM-22 catalyst exhibited no clear Pt-Pt scattering with very few Pt particles present in the HAADF-STEM images acquired. The combination of the very high dispersion and very low loading of Pt can explain the low activity. This, in turn, also leads to a decrease in isomer selectivity at lower conversion levels and maximum isomer yield (Figure 4.5, Figure S4.5).

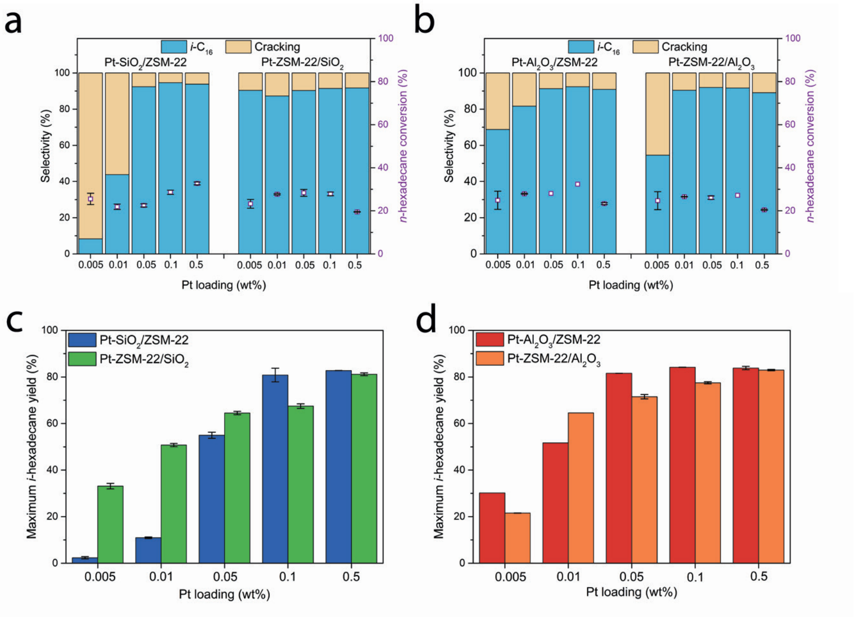

Figure 4.5. a) Pt/SiO_2/ZSM-22 catalyst selectivity during *n*-hexadecane conversion at similar conversion levels (20-32%), b) Pt/Al_2O_3/ZSM-22 catalyst selectivity during *n*-hexadecane conversion at similar conversion levels (20-32%), and maximum *i*-hexadecane yields obtained with c) Pt/SiO_2/ZSM-22 catalysts and d) Pt/Al_2O_3/ZSM-22 catalysts as function of the Pt loading. Reaction conditions: P = 5 bar, $H_2/n\text{-}C_{16}$ = 10/1 mol/mol, and WHSV = 2.9 $g_{n\text{-}C16} \cdot g_{cat}^{-1} \cdot h^{-1}$. Error bars indicate standard deviations.

In Figure 4.5a and b the selectivity of the catalysts at a conversion level of 20-32% is compared. At these conversion levels, catalysts with low Pt loadings (≤ 0.01 wt%) on a silica or alumina binder displayed poor isomer selectivities compared to most of their counterparts in which the Pt was placed on/in ZSM-22. Therefore, at low loadings and at relatively low conversion levels (20-32%) it was typically beneficial for the isomer selectivity to have the Pt deposited on the zeolite.

Nevertheless, maximum yields (attained at different temperatures, Table S4.3) of branched hexadecane (Figure 4.5c,d) required relatively high weight loadings of > 0.1 wt% with Pt on the binder. When alumina was used as binder, a Pt weight loading of 0.05 wt% (Figure 4.5b) did not significantly compromise the isomer yield compared to higher loadings. At lower loadings (< 0.05 wt%), however, it was beneficial to have the Pt on ZSM-22. Generally speaking, catalysts with Pt on ZSM-22 maintained relatively high isomer yields when the Pt weight loading was decreased. When Pt was on the binder, particularly on SiO_2, low Pt loadings were detrimental to the isomer yield. In combination with the decreased activity of Pt-on-binder catalysts with low loadings with respect to the Pt-on-ZSM-22 catalysts (Figure 4.4), it is concluded that it is beneficial to locate Pt on the zeolite when ultralow (≤ 0.01 wt%) loadings of Pt are used. In terms of overall catalytic performance, a loading of 0.05 wt% or higher was required to sustain decent catalytic performance. This is a higher weight loading than for the *n*-heptane hydroconversion reaction, which is in line with the fact that generally higher n_{Pt}/n_A ratios are required for adequate catalytic performance during the hydroconversion of longer hydrocarbons.[29] However, the experiments with the *n*-hexadecane feedstock were conducted at a total pressure of 5 bar, whereas *n*-heptane hydroconversion experiments were performed at 10 bar. Both the heavier hydrocarbon feedstock and the lower hydrogen partial pressure with hexadecane experiments are expected to increase the required metal loading[29,54] and the effects could not be disentangled based on these experiments.

Looking at the catalysts with Pt loadings ≥ 0.05 wt% for the alumina binder and ≥ 0.1 wt% for the silica binder, it was preferred to keep the Pt located on the binder. This can be rationalized by the lower diffusivities of longer and bulkier hydrocarbons within the zeolite micropores.[51–53,55] Decreasing the n_{Pt}/n_A ratio resulted in catalysts that favored overcracking of the feedstock (Figure S4.6) and the carbon distribution started to deviate substantially from a distribution that would be obtained during "ideal" hydrocracking.[56] The minimum Pt weight loading and preferred nanoparticle location in bifunctional metal-acid catalysts are affected by both the process conditions and the molecular weight of the hydrocarbon feedstock.

4.4. Conclusions

A set of Pt/SiO_2/ZSM-22 catalysts with differing Pt weight loadings and nanoparticle locations were prepared and characterized. Pt weight loadings of 0.01 wt% and lower led to fewer visible Pt nanoparticles (HR HAADF-STEM) and limited Pt-Pt coordination (XAS) when located on the silica binder, while at the same loading of Pt on the ZSM-22, the catalysts had abundant observable Pt nanoparticles. Their catalytic performance during the hydroconversion of *n*-heptane was assessed and at low loadings (0.01 wt%) the catalytic activity and selectivity benefited from Pt being present on the ZSM-22 crystals, which is likely a result of the presence of Pt nanoparticles in sufficient numbers at that location. The hydroconversion of longer-chain hydrocarbons (*n*-hexadecane) over catalysts with ultralow amounts of Pt at different locations was assessed for the first time and the performance of Pt/SiO_2/ZSM-22 catalysts was compared to that of Pt/Al_2O_3/ZSM-22 catalysts. For the hydroconversion of *n*-hexadecane a Pt weight loading of ≥ 0.05 wt%, preferentially placed on the binder, was desired. Decreasing the Pt loading led to a decrease in catalytic activity, regardless of the Pt location. Pt-on-SiO_2 catalysts displayed very low activity at loadings of 0.01 wt% or lower, whereas Pt-on-Al_2O_3 catalysts still show activity and selectivity at these loadings. Based on the XAS and STEM results for 0.01Pt-SiO_2/ZSM-22 catalysts, although predominantly present as Pt^0, the Pt dispersion appeared to be too high and the loading too low on these catalysts leading to a poor catalytic performance. Silica therefore was not a better binder and support for bifunctional hydroconversion catalysts with ultralow platinum loadings.

Acknowledgements

The authors thank Dennie Wezendonk, Jan Willem de Rijk and Remco Dalebout for their help commissioning the Flowrence setup. Tom Welling and Karan Kotalgi are thanked for performing the N_2 physisorption measurements. This research was funded by BP plc.

References

(1) Chong, L.; Wen, J.; Kubal, J.; Sen, F. G.; Zou, J.; Greeley, J.; Chan, M.; Barkholtz, H.; Ding, W.; Liu, D. J. Ultralow-Loading Platinum-Cobalt Fuel Cell Catalysts Derived from Imidazolate Frameworks. *Science* **2018**, *362* (6420), 1276–1281.

(2) Reverdiau, G.; Le Duigou, A.; Alleau, T.; Aribart, T.; Dugast, C.; Priem, T. Will There Be Enough Platinum for a Large Deployment of Fuel Cell Electric Vehicles? *Int. J. Hydrogen Energy* **2021**, *46* (79), 39195–39207.

(3) Monteiro, M. C. O.; Goyal, A.; Moerland, P.; Koper, M. T. M. Understanding Cation Trends for Hydrogen Evolution on Platinum and Gold Electrodes in Alkaline Media. *ACS Catal.* **2021**, *11* (23), 14328–14335.

(4) Kritsanaviparkporn, E.; Baena-Moreno, F. M.; Reina, T. R. Catalytic Converters for Vehicle Exhaust: Fundamental Aspects and Technology Overview for Newcomers to the Field. *Chem.* **2021**, *3* (2), 630–646.

(5) Mäki-Arvela, P.; Khel, T. A. K.; Azkaar, M.; Engblom, S.; Murzin, D. Y. Catalytic Hydroisomerization of Long-Chain Hydrocarbons for the Production of Fuels. *Catalysts* **2018**, *8* (11).

(6) Bobba, S.; Carrara, S.; Huisman, J.; Mathieux, F.; Pavel, C. Critical Raw Materials for Strategic Technologies and Sectors in the EU - a Foresight Study. *Publ. Off.* **2020**.

(7) Hughes, A. E.; Haque, N.; Northey, S. A.; Giddey, S. Platinum Group Metals: A Review of Resources, Production and Usage with a Focus on Catalysts. *Resources* **2021**, *10* (9), 1–40.

(8) Böhringer, W.; Kotsiopoulos, A.; de Boer, M.; Knottenbelt, C.; Fletcher, J. C. Q. Selective Fischer-Tropsch Wax Hydrocracking - Opportunity for Improvement of Overall Gas-to-Liquids Processing. *Stud. Surf. Sci. Catal.* **2007**, *163*, 345–365.

(9) Bouchy, C.; Hastoy, G.; Guillon, E.; Martens, J. A. Fischer-Tropsch Waxes Upgrading via Hydrocracking and Selective Hydroisomerization. *Oil Gas Sci. Technol.* **2009**, *64* (1), 91–112.

(10) Mäki-Arvela, P.; Martínez-Klimov, M.; Murzin, D. Y. Hydroconversion of Fatty Acids and Vegetable Oils for Production of Jet Fuels. *Fuel* **2021**, *306*, 121673.

(11) Kots, P. A.; Vance, B. C.; Vlachos, D. G. Polyolefin Plastic Waste Hydroconversion to Fuels, Lubricants, and Waxes: A Comparative Study. *React. Chem. Eng.* **2022**, *7* (1), 41–54.

(12) Rorrer, J. E.; Ebrahim, A. M.; Questell-Santiago, Y.; Zhu, J.; Troyano-Valls, C.; Asundi, A. S.; Brenner, A. E.; Bare, S. R.; Tassone, C. J.; Beckham, G. T.; Román-Leshkov, Y. Role of Bifunctional Ru/Acid Catalysts in the Selective Hydrocracking of Polyethylene and Polypropylene Waste to Liquid Hydrocarbons. *ACS Catal.* **2022**, *12* (22), 13969–13979.

.

(13) Lee, W. T.; van Muyden, A.; Bobbink, F. D.; Mensi, M. D.; Carullo, J. R.; Dyson, P. J. Mechanistic Classification and Benchmarking of Polyolefin Depolymerization over Silica-Alumina-Based Catalysts. *Nat. Commun.* **2022**, *13* (1), 1–13.

(14) Corma, A. Transformation of Hydrocarbons on Zeolite Catalysts. *Catal. Letters* **1993**, *22* (1–2), 33–52.

(15) Vogt, E. T. C.; Whiting, G. T.; Dutta Chowdhury, A.; Weckhuysen, B. M. Zeolites and Zeotypes for Oil and Gas Conversion. *Adv. Catal.* **2015**, *58*, 143–314.

(16) Wang, W.; Liu, C.-J.; Wu, W. Bifunctional Catalysts for the Hydroisomerization of N-Alkanes: The Effects of Metal–Acid Balance and Textural Structure. *Catal. Sci. Technol.* **2019**, *9* (16), 4162–4187.

(17) Weisz, P. B. Stepwise Reaction via Intermediates on Separate Catalytic Centers. *Science* **1956**, *123* (3203), 887–888.

(18) Weisz, P. B.; Swegler, E. W. Stepwise Reaction on Separate Catalytic Centers: Isomerization of Saturated Hydrocarbons. *Science* **1957**, *126* (3262), 31–32.

(19) Zečević, J.; Vanbutsele, G.; de Jong, K. P.; Martens, J. A. Nanoscale Intimacy in Bifunctional Catalysts for Selective Conversion of Hydrocarbons. *Nature* **2015**, *528* (7581), 245–254.

(20) Batalha, N.; Pinard, L.; Bouchy, C.; Guillon, E.; Guisnet, M. N-Hexadecane Hydroisomerization over Pt-HBEA Catalysts. Quantification and Effect of the Intimacy between Metal and Protonic Sites. *J. Catal.* **2013**, *307*, 122–131.

(21) Guisnet, M.; Alvarez, F.; Giannetto, G.; Perot, G. Hydroisomerization and Hydrocracking of N-Heptane on PtH Zeolites. Effect of the Porosity and of the Distribution of Metallic and Acid Sites. *Catal. Today* **1987**, *1* (4), 415–433.

(22) Alvarez, F.; Ribeiro, F. R.; Perot, G.; Thomazeau, C.; Guisnet, M. Hydroisomerization and Hydrocracking of Alkanes. *J. Catal.* **1996**, *162* (2), 179–189.

(23) Mirena, J. I.; Thybaut, J. W.; Marin, G. B.; Martens, J. A.; Galvita, V. V. Impact of the Spatial Distribution of Active Material on Bifunctional Hydrocracking. *Ind. Eng. Chem. Res.* **2021**, *60* (18), 6357–6378.

(24) Cheng, K.; Smulders, L. C. J.; van der Wal, L. I.; Oenema, J.; Meeldijk, J. D.; Visser, N. L.; Sunley, G.; Roberts, T.; Xu, Z.; Doskocil, E.; Yoshida, H.; Zheng, Y.; Zečević, J.; de Jongh, P. E.; de Jong, K. P. Maximizing Noble Metal Utilization in Solid Catalysts by Control of Nanoparticle Location. *Science* **2022**, *377* (6602), 204–208.

(25) Oenema, J.; Hofmann, J. P.; Hensen, E. J. M.; Zečević, J.; de Jong, K. P. Assessment of the Location of Pt Nanoparticles in Pt/Zeolite Y/γ-Al2O3 Composite Catalysts. *ChemCatChem* **2020**, *12* (2), 615–622.

(26) Cheng, K.; van der Wal, L. I.; Yoshida, H.; Oenema, J.; Harmel, J.; Zhang, Z.; Sunley, G.; Zečević, J.; de Jong, K. P. Impact of the Spatial Organization of Bifunctional Metal–Zeolite Catalysts on the Hydroisomerization of Light Alkanes. *Angew. Chemie - Int. Ed.* **2020**, *59* (9), 3592–3600.

(27) Smulders, L. C. J.; van de Minkelis, J. H.; Meeldijk, J. D.; Tang, M.; Liutkova, A.; Cheng, K.; Roberts, S. T.; Sunley, G. J.; Hensen, E. J. M.; de Jongh, P. E.; de Jong, K. P. Steering the Metal Precursor Location in Pd/Zeotype Catalysts and Its Implications for Catalysis. *Chemistry* **2023**, *5* (1), 348–364.

(28) van der Wal, L. I.; Oenema, J.; Smulders, L. C. J.; Samplonius, N. J.; Nandpersad, K. R.; Zečević, J.; de Jong, K. P. Control and Impact of Metal Loading Heterogeneities at the Nanoscale on the Performance of Pt/Zeolite Y Catalysts for Alkane Hydroconversion. *ACS Catal.* **2021**, *11* (7), 3842–3855.

(29) Wei, C.; Zhang, G.; Zhao, L.; Gao, J.; Xu, C. Effect of Metal–Acid Balance and Textual Modifications on Hydroisomerization Catalysts for n-Alkanes with Different Chain Length: A Mini-Review. *Fuel* **2022**, *315*, 122809.

(30) Weitkamp, J. Isomerization of Long-Chain n-Alkanes on a Pt/CaY Zeolite Catalyst. *Ind. Eng. Chem. Prod. Res. Dev.* **1982**, *21* (4), 550–558.

(31) Weitkamp, J. The Influence of Chain Length in Hydrocracking and Hydroisomerization of n -Alkanes. In *American Chemical Society, Division of Petroleum Chemistry, Preprints*; 1975; Vol. 20, pp 1–27.

(32) Lee, K. Y.; Lee, H. K.; Ihm, S. K. Influence of Catalyst Binders on the Acidity and Catalytic Performance of HZSM-5 Zeolites for Methanol-to-Propylene (MTP) Process: Single and Binary Binder System. *Top. Catal.* **2010**, *53* (3–4), 247–253.

(33) Michels, N. L.; Mitchell, S.; Pérez-Ramírez, J. Effects of Binders on the Performance of Shaped Hierarchical MFI Zeolites in Methanol-to-Hydrocarbons. *ACS Catal.* **2014**, *4* (8), 2409–2417.

(34) Bingre, R.; Louis, B.; Nguyen, P. An Overview on Zeolite Shaping Technology and Solutions to Overcome Diffusion Limitations. *Catalysts* **2018**, *8* (4).

(35) Asgar Pour, Z.; Abduljawad, M. M.; Alassmy, Y. A.; Cardon, L.; Van Steenberge, P. H. M.; Sebakhy, K. O. A Comparative Review of Binder-Containing Extrusion and Alternative Shaping Techniques for Structuring of Zeolites into Different Geometrical Bodies. *Catalysts* **2023**, *13* (4), 656.

(36) Vajglová, Z.; Kumar, N.; Mäki-Arvela, P.; Eränen, K.; Peurla, M.; Hupa, L.; Murzin, D. Y. Effect of Binders on the Physicochemical and Catalytic Properties of Extrudate-Shaped Beta Zeolite Catalysts for Cyclization of Citronellal. *Org. Process Res. Dev.* **2019**, *23* (11), 2456–2463.

(37) Mitchell, S.; Michels, N. L.; Pérez-Ramírez, J. From Powder to Technical Body: The Undervalued Science of Catalyst Scale Up. *Chem. Soc. Rev.* **2013**, *42* (14), 6094–6112.

(38) Whiting, G. T.; Meirer, F.; Mertens, M. M.; Bons, A. J.; Weiss, B. M.; Stevens, P. A.; De Smit, E.; Weckhuysen, B. M. Binder Effects in SiO2- and Al2O3-Bound Zeolite ZSM-5-Based Extrudates as Studied by Microspectroscopy. *ChemCatChem* **2015**, *7* (8), 1312–1321.

(39) Yang, K.; Zhang, D.; Zou, M.; Yu, L.; Huang, S. The Known and Overlooked Sides of Zeolite-Extrudate Catalysts. *ChemCatChem* **2021**, *13* (6), 1414–1423.

(40) Guo, S.; Yu, S.; Tian, H.; Da, Z. Mechanistic Insights into the Interaction between Binders and Y-Type Zeolites in Fluid Catalytic Cracking. *Fuel* **2022**, *324*, 124640.

(41) Bariås, O. A.; Holmen, A.; Blekkan, E. A. Propane Dehydrogenation over Supported Pt and Pt-Sn Catalysts: Catalyst Preparation, Characterization, and Activity Measurements. *J. Catal.* **1996**, *158* (1), 1–12.

(42) Penner, S.; Wang, D.; Su, D. S.; Rupprechter, G.; Podloucky, R.; Schlögl, R.; Hayek, K. Platinum Nanocrystals Supported by Silica, Alumina and Ceria: Metal-Support Interaction Due to High-Temperature Reduction in Hydrogen. *Surf. Sci.* **2003**, *532–535*, 276–280.

(43) Cho, H. R.; Regalbuto, J. R. The Rational Synthesis of Pt-Pd Bimetallic Catalysts by Electrostatic Adsorption. *Catal. Today* **2015**, *246*, 143–153.

(44) Newville, M. EXAFS Analysis Using FEFF and FEFFIT. *J. Synchrotron Radiat.* **2001**, *8* (2), 96–100.

(45) Ravel, B.; Newville, M. ATHENA, ARTEMIS, HEPHAESTUS: Data Analysis for X-Ray Absorption Spectroscopy Using IFEFFIT. *J. Synchrotron Radiat.* **2005**, *12* (4), 537–541.

(46) Kim, J.; Kim, W.; Seo, Y.; Kim, J. C.; Ryoo, R. N-Heptane Hydroisomerization over Pt/MFI Zeolite Nanosheets: Effects of Zeolite Crystal Thickness and Platinum Location. *J. Catal.* **2013**, *301*, 187–197.

(47) Jeong, H.; Kwon, O.; Kim, B. S.; Bae, J.; Shin, S.; Kim, H. E.; Kim, J.; Lee, H. Highly Durable Metal Ensemble Catalysts with Full Dispersion for Automotive Applications beyond Single-Atom Catalysts. *Nat. Catal.* **2020**, *3* (4), 368–375.

(48) Müller, U.; Sattler, K.; Xhie, J.; Venkateswaran, N.; Raina, G. A Scanning Tunneling Microscope Study of Single Platinum Atoms, Platinum Dimers and Trimers on Highly-Oriented Pyrolytic Graphite. *Zeitschrift für Phys. D Atoms, Mol. Clust.* **1991**, *19* (4), 319–321.

(49) Vaarkamp, M.; Modica, F. S.; Miller, J. T.; Koningsberger, D. C. Influence of Hydrogen Pretreatment on the Structure of the Metal-Support Interface in Pt/Zeolite Catalysts. *J. Catal.* **1993**, *144* (2), 611–626.

(50) Finzel, J.; Sanroman Gutierrez, K. M.; Hoffman, A. S.; Resasco, J.; Christopher, P.; Bare, S. R. Limits of Detection for EXAFS Characterization of Heterogeneous Single-Atom Catalysts. *ACS Catal.* **2023**, *13* (9), 6462–6473.

(51) Martens, J. A.; Souverijns, W.; Verrelst, W.; Parton, R.; Froment, G. F.; Jacobs, P. A. Selective Isomerization of Hydrocarbon Chains on External Surfaces of Zeolite Crystals. *Angew. Chemie Int. Ed. English* **1995**, *34* (22), 2528–2530.

(52) Martens, J. A.; Vanbutsele, G.; Jacobs, P. A.; Denayer, J.; Ocakoglu, R.; Baron, G.; Muñoz Arroyo, J. A.; Thybaut, J.; Marin, G. B. Evidences for Pore Mouth and Key-Lock Catalysis in Hydroisomerization of Long n-Alkanes over 10-Ring Tubular Pore Bifunctional Zeolites. *Catal. Today* **2001**, *65* (2–4), 111–116.

(53) Chizallet, C.; Bouchy, C.; Larmier, K.; Pirngruber, G. Molecular Views on Mechanisms of Brønsted Acid-Catalyzed Reactions in Zeolites. *Chem. Rev.* **2023**, *123* (9), 6107–6196.

(54) Thybaut, J. W.; Laxmi Narasimhan, C. S.; Denayer, J. F.; Baron, G. V.; Jacobs, P. A.; Martens, J. A.; Marin, G. B. Acid-Metal Balance of a Hydrocracking Catalyst: Ideal versus Nonideal Behavior. *Ind. Eng. Chem. Res.* **2005**, *44* (14), 5159–5169.

(55) Noh, G.; Zones, S. I.; Iglesia, E. Isomer Sieving and the Selective Formation of Terminal Methyl Isomers in Reactions of Linear Alkanes on One-Dimensional Zeolites. *J. Catal.* **2019**, *377*, 255–270.

(56) Weitkamp, J. Catalytic Hydrocracking—Mechanisms and Versatility of the Process. *ChemCatChem* **2012**, *4* (3), 292–306.

Supporting Information

Table S4.1. Results of temperature programmed desorption of ammonia (NH_3-TPD) of catalysts and pristine silica and ZSM-22.

Sample	**Total number of acid sites (mmol g^{-1})**	**Number of weak acid sites (mmol g^{-1})**	**Number of strong acid sites (mmol g^{-1})**
Aerosil 380 SiO_2	0.025	0.025	0
ZSM-22	0.481	0.201	0.280
0.005Pt-SiO_2/ZSM-22	0.250	0.090	0.160
0.01Pt-SiO_2/ZSM-22	0.217	0.079	0.139
0.05Pt-SiO_2/ZSM-22	0.216	0.075	0.142
0.1Pt-SiO_2/ZSM-22	0.256	0.073	0.182
0.5Pt-SiO_2/ZSM-22	0.281	0.123	0.158
0.005Pt-ZSM-22/SiO_2	0.270	0.104	0.166
0.01Pt-ZSM-22/SiO_2	0.235	0.081	0.154
0.05Pt-ZSM-22/SiO_2	0.202	0.066	0.136
0.1Pt-ZSM-22/SiO_2	0.219	0.074	0.145
0.5Pt-ZSM-22/SiO_2	0.312	0.123	0.189

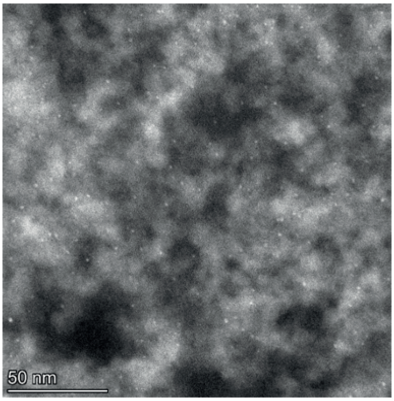

Figure S4.1. HAADF-STEM image of an ultramicrotomed sample of a physical mixture consisting of 0.4Pt/SiO_2+ZSM-22, prepared by dry mixing without a peptizing agent, $d_{Pt} = 1.3 \pm 0.3$ nm.

Table S4.2. N_2 physisorption results.

Sample	s_{BET} **(m² g⁻¹)**	s_{ext} **(m² g⁻¹)**	V_{total} **(cm³ g⁻¹)**	V_{micro} **(cm³ g⁻¹)**	$s_{Langmuir}$ **(m² g⁻¹)**
ZSM-22	247	50	0.31	0.08	455
SiO_2	409	391	1.22	0.003	2116
SiO_2/ZSM-22	261	229	0.97	0.01	1672
0.1Pt-SiO_2/ZSM-22	260	181	0.88	0.03	1515
0.1Pt-ZSM-22/SiO_2	281	208	0.77	0.03	1472
γ-Al_2O_3	317	305	0.92	0.003	2570
γ-Al_2O_3/ZSM-22	282	184	0.58	0.04	1188
0.1Pt-γ-Al_2O_3/ZSM-22	255	167	0.59	0.04	1177
0.1Pt-ZSM-22/γ-Al_2O_3	278	174	0.54	0.04	1077

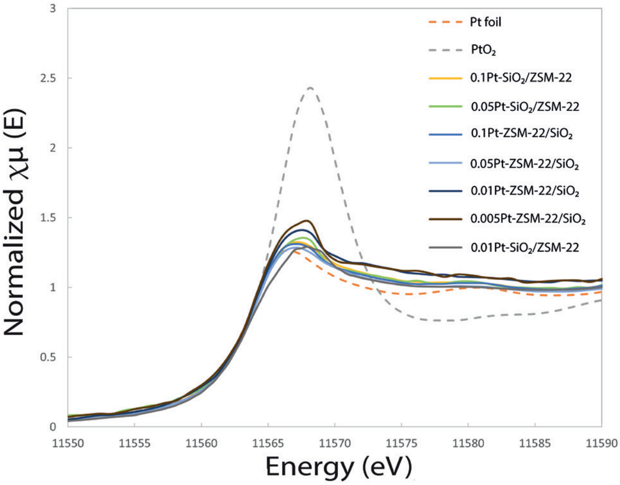

Figure S4.2. X-ray absorption near edge structure (XANES) spectra of bifunctional catalysts after reduction at 400 °C for 1 h and Pt standards, measured at the Pt L_3 edge.

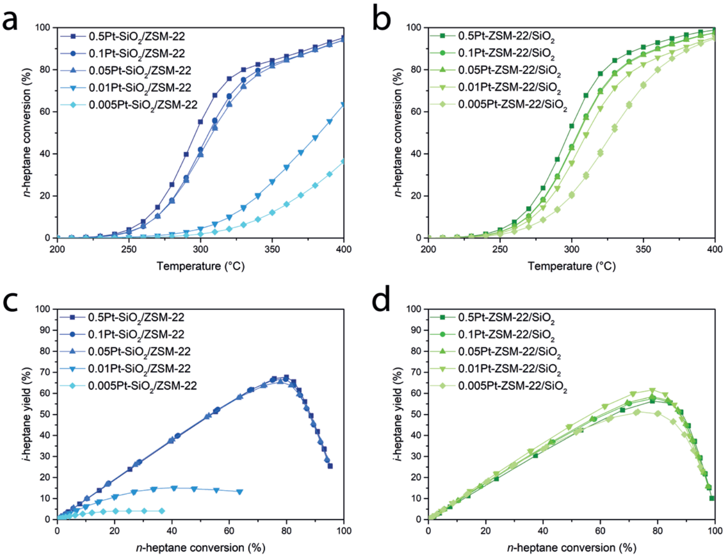

Figure S4.3. Hydroconversion of *n*-heptane as a function of temperature for a) Pt-SiO_2/ZSM-22 catalysts (blue), b) Pt-ZSM-22/SiO_2 catalysts (green), and *i*-heptane yield as function of *n*-heptane conversion for c) Pt-SiO_2/ZSM-22 catalysts (blue) and d) Pt-ZSM-22/SiO_2 catalysts (green). Pt weight loadings are: 0.5 wt% (■), 0.1 wt% (●), 0.05 wt% (▲), 0.01 wt% (▼) and 0.005 wt% (◆).

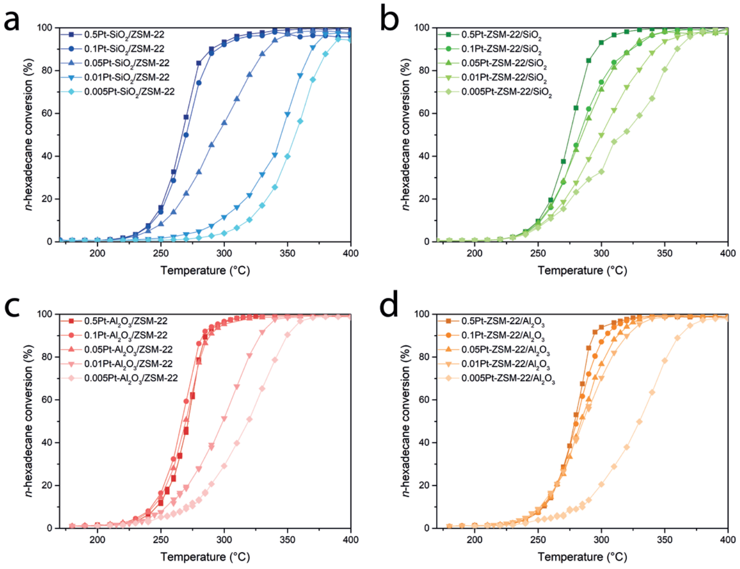

Figure S4.4. Hydroconversion of *n*-hexadecane as a function of temperature for a) Pt-SiO_2/ZSM-22 catalysts (blue), b) Pt-ZSM-22/SiO_2 catalysts (green), c) Pt-Al_2O_3/ZSM-22 catalysts (red) and d) Pt-ZSM-22/Al_2O_3 catalysts (orange) with different Pt weight loadings: 0.5 wt% (■), 0.1 wt% (●), 0.05 wt% (▲), 0.01 wt% (▼) and 0.005 wt% (◆).

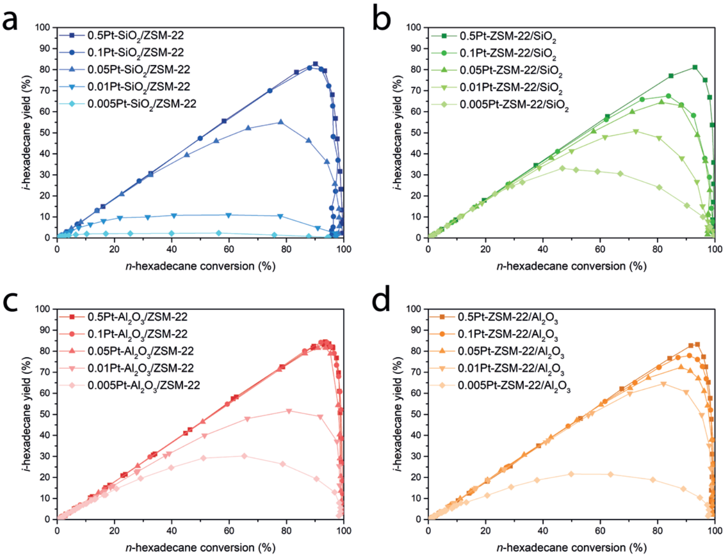

Figure S4.5. Yield of hexadecane isomers as a function of *n*-hexadecane conversion for a) Pt-SiO_2/ZSM-22 catalysts (blue), b) Pt-ZSM-22/SiO_2 catalysts (green), c) Pt-Al_2O_3/ZSM-22 catalysts (red) and d) Pt-ZSM-22/Al_2O_3 catalysts (orange) with different Pt weight loadings: 0.5 wt% (■), 0.1 wt% (●), 0.05 wt% (▲), 0.01 wt% (▼) and 0.005 wt% (◆).

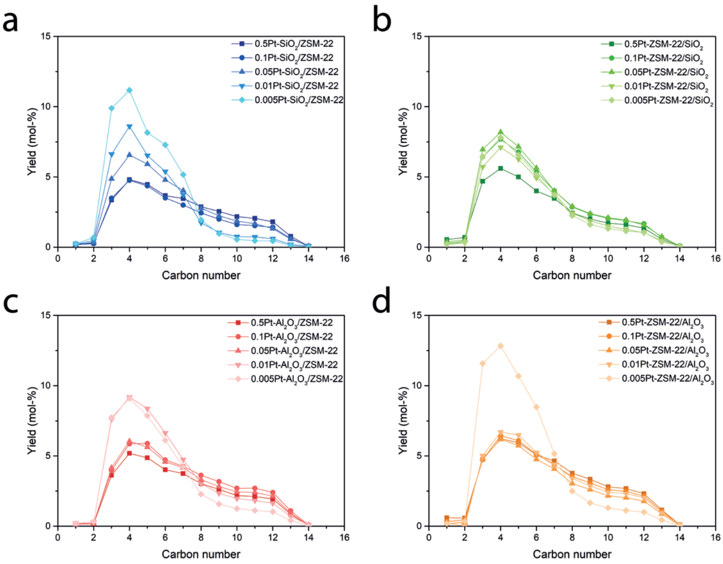

Figure S4.6. Molar yield of hydrocarbons obtained from cracking of *n*-hexadecane for a) Pt-SiO_2/ZSM-22 catalysts (blue) at 12-17% cracking conversion, b) Pt-ZSM-22/SiO_2 catalysts (green) at 13-17% cracking conversion, c) Pt-Al_2O_3/ZSM-22 catalysts (red) at 15-19% cracking conversion and d) Pt-ZSM-22/Al_2O_3 catalysts (orange) at 15-19% cracking conversion. Pt weight loadings are: 0.5 wt% (■), 0.1 wt% (●), 0.05 wt% (▲), 0.01 wt% (▼) and 0.005 wt% (◆).

Table S4.3. Maximum *i*-hexadecane (*i*-C_{16}) yields and the corresponding temperatures at which they are attained.

Catalyst	**Maximum** *i*-C_{16} **Yield** **(%)**	**Temperature** **(°C)**
0.005Pt-SiO_2/ZSM-22	2	360
0.01Pt-SiO_2/ZSM-22	11	350
0.05Pt-SiO_2/ZSM-22	55	320
0.1Pt-SiO_2/ZSM-22	81	290
0.5Pt-SiO_2/ZSM-22	83	290
0.005Pt-ZSM-22/SiO_2	33	310
0.01Pt-ZSM-22/SiO_2	51	320
0.05Pt-ZSM-22/SiO_2	65	310
0.1Pt-ZSM-22/SiO_2	68	310
0.5Pt-ZSM-22/SiO_2	81	300
0.005Pt-Al_2O_3/ZSM-22	30	330
0.01Pt-Al_2O_3/ZSM-22	52	320
0.05Pt-Al_2O_3/ZSM-22	82	290-295
0.1Pt-Al_2O_3/ZSM-22	84	285-290
0.5Pt-Al_2O_3/ZSM-22	85	290
0.005Pt-ZSM-22/Al_2O_3	22	330-340
0.01Pt-ZSM-22/Al_2O_3	65	310
0.05Pt-ZSM-22/Al_2O_3	72	310-315
0.1Pt-ZSM-22/Al_2O_3	78	300-305
0.5Pt-ZSM-22/Al_2O_3	83	300

Chapter 5

Location effects in Ni based bifunctional catalysts

Abstract: In previous chapters we described location effects in bifunctional catalysts which contain the noble metals Pd and Pt. Ni is an earth-abundant alternative with a major challenge of its hydrogenolysis activity leading to the production of methane and thus decreasing hydroisomerization selectivity. In this work, we studied several Ni based bifunctional catalysts, using ZSM-22 as solid acid function. The Ni was either placed on SiO_2, or on/in ZSM-22 crystals or it was present in the Ni phyllosilicate framework. Pt/ZSM-22 and Pt/SiO_2+ZSM-22 catalysts were prepared for comparison. The catalysts were characterized using HAADF-STEM, NH_3-TPD, ICP-OES, N_2-physisorption and TPR. Their catalytic performances were assessed using *n*-heptane and *n*-hexadecane as feedstocks. All Ni based catalysts displayed hydrogenolysis activity, during both *n*-heptane and *n*-hexadecane hydroconversion. The hydrogenolysis activity of Ni/ZSM-22, however, was significantly lower when *n*-hexadecane was used as a feedstock, while it displayed the highest hydrogenolysis activity of all Ni based catalysts during the hydroconversion of *n*-heptane. When the Ni (oxide) was exclusively present outside the ZSM-22 crystals, i.e. on SiO_2 or in a Ni phyllosilicate framework, the impact of the feedstock molecular weight on the hydrogenolysis activity was limited. We hypothesize that the Ni nanoparticle location inside the ZSM-22 crystals in the Ni/ZSM-22 catalysts in combination with the bulkier hydrocarbon feedstock led to diffusion limitation for hydrogenolysis. This finding is of great relevance for the further development of (noble metal free) bifunctional catalysts for the conversion of FT wax and plastic waste.

5.1. Introduction

Bifunctional catalysts play a key role in the production of fuels and chemicals from crude oil or renewable sources.[1–5] One of the processes in which a bifunctional catalyst is used, is the hydroconversion of hydrocarbon feedstocks into fuels. These catalysts consist of a metal (sulfide) function for dehydrogenation/hydrogenation (DHD/HD) and an acid function for isomerization and cracking. Traditionally, for the conversion of crude oil, metal sulfides (CoMoS, NiMoS, MoS_2, WS_2) are used, as they are resistant to sulfur poisoning.[6–9] Renewable hydrocarbon sources, such as Fischer-Tropsch (FT) wax, are ultraclean[10,11] and the presence of sulfur in the catalyst becomes undesired. Therefore, the focus has shifted towards Pt and Pd as DHD/HD function.

Chapters 3 and 4 show that it is possible to go to ultralow loadings of these noble metals, without compromising on catalytic performance. However, still a non-abundant noble metal is used in the catalysts described in those chapters. Hence, exploration of the utilization of more earth-abundant elements is expedient. Researchers have focused on the use of transition metals and their respective oxides and carbides, such as molybdenum carbide,[12] -oxide[13] and -oxycarbide,[14] and Ni and NiO,[15–18] since the main prerequisite for clean feedstocks is having a sulfur free DHD/HD function.

Hydroisomerization and hydrocracking are the main goals during the hydroconversion for the production of fuels from oil or FT waxes. Ni tends to catalyze hydrogenolysis, which is considered to be an undesired side reaction and scientists actively look into ways to suppress that.[16,19] However, the hydrogenolysis reaction gained new interest, with the current focus on chemical recycling of plastic waste in particular.[20–25] Many of the polyolefin waste valorization studies are performed with high noble metal weight loadings of up to 5 wt%,[24–27] making replacement with earth-abundant metals that could perform hydrogenolysis, such as Ni, also attractive in this field.[28]

In this explorative study we show that the combination of Ni nanoparticle location and feedstock can have a tremendous effect on the hydroisomerization versus hydrogenolysis selectivity. Several Ni- and ZSM-22 based bifunctional catalysts were prepared and characterized, and their hydroconversion performances were compared to those of their Pt-based counterparts. The Ni was present on SiO_2, in/on ZSM-22 crystals, or in a Ni phyllosilicate framework, and similarly, Pt/ZSM-22 and Pt/SiO_2+ZSM-22 were studied.

5.2. Materials and Methods

Materials

ZSM-22 (H^+-form, Si/Al = 32.5-40 at/at) was purchased from ACS Material. Aerosil 380 and Aerosil OX50 silica were purchased from Evonik. Tetraamine platinum (II) nitrate ($[Pt(NH_3)_4](NO_3)_2$, 99.995% pure), nickel (II) nitrate ($Ni(NO_3)_2 \cdot 6\ H_2O$, 99.999% pure), and urea were purchased from Sigma-Aldrich. Nitric acid (HNO_3, 65%) was purchased from VWR Chemicals. Ammonia solution (NH_4OH, 25%) was obtained from Emsure. *n*-Heptane (99+%, pure) and *n*-hexadecane (99%, pure) were obtained from ACROS Organics. Silicon carbide (SiC, SIKA ABR I F60, grain size: 250 µm) was supplied by Fiven. H_2 6.0, He 5.0 and N_2 5.0, were obtained from Linde gas.

Catalyst Preparation

Preparation of Ni/ZSM-22 and Ni/SiO$_2$+ZSM-22 Catalysts

ZSM-22 was calcined in a flow of 100 mL min^{-1} synthetic air (N_2/O_2, 80/20, *vol*/*vol*) at 500 ˚C (ramp 5˚C min^{-1}) for 5 h, before metal deposition. To prepare Ni/ZSM-22, Ni was introduced via incipient wetness impregnation. Typically, 0.5 g of calcined ZSM-22 was dried in a round-bottom flask for 4 h at 90 °C, while stirring under dynamic vacuum. A solution with the intended amount of nickel nitrate in Milli-Q water was prepared. The dried ZSM-22 was impregnated with 0.18 mL $g_{ZSM\text{-}22}{}^{-1}$ (90% of the pore volume of calcined ZSM-22 as determined using N_2 physisorption) under static vacuum while stirring, to ensure homogeneous distribution of the nickel nitrate solution over the zeolite powder. The sample was stirred under static vacuum for 1 h. The resulting powder was transferred to an oven dish and dried in an oven at 120 °C overnight. The powder was transferred to a plug-flow reactor and heated to 150 °C under N_2 flow of 80 mL min^{-1} (2 °C min^{-1}, 3 h). Subsequently, reduction was performed in the same reactor at 400 °C (2 °C min^{-1}, 6 h) under a flow of H_2/N_2 of 100 mL min^{-1} (80/20, *vol*/*vol*). After cooling down, the catalyst was slowly exposed to air in order to passivate the Ni nanoparticles.

Ni/SiO_2 catalysts were prepared in a similar fashion. Aerosil 380 was used as SiO_2 support and was impregnated with 1.1 mL $g_{silica}{}^{-1}$ of a nickel nitrate solution. It underwent the same drying and heat treatment. An intimate physical mixture was prepared as described before:[29] The resulting Ni/SiO_2 catalyst was then mixed with calcined ZSM-22 in a mortar in a 50/50 wt. ratio. Subsequently, the mixture was pelletized, crushed and sieved into a fraction of 75-212 µm.

Preparation of Ni phyllosilicate+ZSM-22 Catalysts

Nickel phyllosilicate was synthesized by deposition precipitation via urea hydrolysis as described in literature.[30–33] For this, 6.1 g of Aerosil OX50 was added to a five-neck 500 mL baffled flask. A solution of 15.2 g nickel nitrate was dissolved in 350 mL distilled water and the solution was added to the baffled flask and it was stirred vigorously with an overhead stirrer. The reaction was monitored using a thermometer and a pH meter. The flask necks were not sealed and therefore evaporation of water and loss of CO_2 (as product of urea decomposition) could occur. The reaction mixture was heated to 90 °C and acidified with a few drops of HNO_3 to a pH of 2 – 3. A solution of 9.4 g of urea in 100 mL distilled water was prepared and added to the reaction mixture. The temperature of the contents of the flask was maintained at 87 – 92 °C. Initially, the pH rose to a value of 5.4 at which it stabilized. The water level in the reaction mixture was regularly topped up using a pipette to compensate for the evaporation. After 4 h of reaction, the phyllosilicates were filtered, washed with water until the filtrate ran clear and dried overnight at 120 °C in a static air oven. Intimate physical mixtures of Ni phyllosilicate and calcined ZSM-22 were prepared by dry mixing in a mortar in a 10/90, 30/70 and 50/50 wt. ratio. The resulting mixtures were then pelletized, crushed and sieved into a fraction of 75-212 μm.

Preparation of Pt/ZSM-22 and Pt/SiO_2+ZSM-22 Catalysts

A Pt/ZSM-22 catalyst was prepared via ion exchange. First, 1 g of calcined ZSM-22 was dispersed in 300 mL Milli-Q water by stirring mechanically at 400 rpm for 1 h. A solution containing 50.8 mg $[Pt(NH_3)_4](NO_3)_2$ in 50 mL Milli-Q water was added dropwise. The mixture was stirred for another 3 h. Subsequently, the dispersion was filtered over vacuum and the filter cake was washed with additional Milli-Q water and dried in a static air oven at 120 °C overnight. The obtained solid was crushed and the resulting powder was transferred to a plug-flow reactor and calcined in a flow (100 mL min^{-1}) of synthetic air (N_2/O_2, 80/20, *vol*/*vol*) at 350 °C (ramp: 0.2 °C min^{-1}). This was followed by reduction in H_2 rich atmosphere with a flow of 100 mL min^{-1} (H_2/N_2, 80/20, *vol*/*vol*) at 600 °C (ramp: 5 °C min^{-1}).

Pt/SiO_2+ZSM-22 was prepared via an electrostatic adsorption method adapted from Regalbuto et al.[34] using $[Pt(NH_3)_4](NO_3)_2$ as Pt precursor. 1 g of Aerosil 380 was dispersed in 300 mL Milli-Q water and mechanically stirred at 500 rpm for 1 h. A solution containing 20.06 mg of $[Pt(NH_3)_4](NO_3)_2$ in 50 mL Milli-Q water was added dropwise to the dispersion and the pH was increased to 7.1 using a few drops of ammonia (0.25% NH_4OH, prepared by diluting 25% NH_4OH in Milli-Q water). The reaction mixture was mixed for 3 additional hours, after which it was filtered over vacuum. The filter cake was washed with additional Milli-Q water and dried in a static air oven at 120 °C overnight. This was followed by crushing to form a powder and the resulting powder was transferred to a plug flow reactor. Calcination was performed in synthetic air (N_2/O_2, 80/20, *vol*/*vol*) with a total flow of 100 mL min^{-1} at 350 ˚C (ramp: 0.2 ˚C min^{-1}) for 2 h. After calcination, the catalyst was reduced in a H_2 rich atmosphere (H_2/N_2, 80/20, *vol*/*vol*) at 600 ˚C (ramp: 5 ˚C min^{-1}) for 3 h. After cooling to room temperature, the Pt/SiO_2 was mixed with calcined ZSM-22 in a 50/50 weight ratio using mortar and pestle, pressed into a pellet, crushed and sieved until an intimate physical mixture in a fraction of 75 – 212 μm was obtained.

Catalyst Characterization

The elemental composition of the catalysts was analyzed with ICP-OES and the acidity of the catalysts was probed with NH_3-TPD as described in sections 2.2, 3.2 and 4.2.

Temperature programmed reduction (TPR) by H_2 on the catalysts was performed on a Micromeritics Autochem II 2920 apparatus. To get an understanding of the chemical state of the Ni (oxide) after *in situ* activation of the catalysts, this was performed on reduced and passivated catalysts. Before measurement, approximately 90 mg of reduced and passivated catalyst was dried *in situ* in an argon flow of 50 mL min^{-1} at 120 °C for 30 min. After drying, the sample was cooled down to room temperature. Reduction profiles were recorded using a TCD while the sample was heated to 800 °C with a ramp of 5 °C min^{-1} in a flow of 5% H_2 in Ar of 25 mL min^{-1}. The water that had formed during reduction was captured with a cold trap that was cooled with a mixture of dry ice and isopropanol.

Measurements of N_2 physisorption isotherms were performed at -196 °C on a Micromeritics Tristar II Plus apparatus. Prior to the measurement, the reduced and passivated samples were dried in a nitrogen flow at 300 °C. The accessible surface areas of the catalysts were determined with the Brunauer-Emmett-Teller (BET) method. A Harkins-Jura thickness curve fitted between 0.32 and 0.40 nm thickness was used to determine micropore (< 2 nm) volumes. Total pore volumes were derived from the volume of N_2 adsorbed at $P/P_0 = 0.95$.

Before studying the samples with electron microscopy, the (reduced and passivated) samples were ultramicrotomed. Samples were embedded in EpoFix resin and left to harden in a static air oven at 60 °C overnight. The resin-embedded samples were cut using a Reichert-Jung Ultracut E ultramicrotome and a Diatome Ultra 35° diamond knife, and sections with a thickness of 70 nm were obtained. These sections were deposited on glow-discharged holy-carbon-coated copper grids (200 mesh). High-angle annular dark-field scanning transmission electron microscopy (HAADF-STEM) was performed on an FEI Talos F200X transmission electron microscope operating at 200 kV.

Hydroconversion of *n*-Heptane and *n*-Hexadecane

The hydroconversion performance of the catalysts was assessed using an Avantium Flowrence 16 parallel fixed bed reactor setup with *n*-heptane (n-C_7) or *n*-hexadecane (n-C_{16}) as feedstock. Stainless steel reactors (inner diameter = 2 mm) were loaded with SiC (220 µm) until it reached a bed height of 2 cm. On top of this SiC bed, 30 mg of sieved catalyst (75 – 212 µm) was loaded. This was followed by adding more of the SiC, leaving 2 cm of free space at the top of the reactor. Analysis of the products was performed using an online GC (Agilent Technologies 7890B) equipped with an Agilent J&W HP-PONA column. The hydrocarbon products were analyzed using an FID. Prior to the catalytic tests with *n*-heptane the catalysts were reduced in H_2/He (90 vol% H_2) at 400 °C for 2 h. When *n*-hexadecane was studied, activation was caried out in pure H_2 at 400 °C for 3 h. Experiments with *n*-heptane feedstock were performed with the following reaction conditions: H_2/*n*-heptane molar ratio of 10, total pressure of 10 bar and WHSV of 2.4 $g_{n\text{-C7}} \cdot g_{cat}^{-1} \cdot h^{-1}$. When *n*-hexadecane was used as a feedstock, the following reactions conditions were applied: H_2/*n*-hexadecane molar ratio of 10, total pressure of 5 bar and WHSV of 2.9 $g_{n\text{-C16}} \cdot g_{cat}^{-1}$ h^{-1}.

The conversion of *n*-heptane or *n*-hexadecane ($X_{n\text{-alkane}}$) was calculated using:

$$X_{n\text{-alkane}} = \left(1 - \frac{F_{\mathrm{Cwt}.n-\mathrm{alkane,out}}}{F_{\mathrm{Cwt}.n-\mathrm{alkane,in}}}\right) \cdot 100\% \qquad \textbf{(Eq. 5.1.)}$$

Where $F_{\mathrm{Cwt}.n\text{-alkane,out}}$ and $F_{\mathrm{Cwt}.n\text{-alkane,in}}$ are the flows based on carbon weight of *n*-alkane going out or in the reactor, respectively. The isomer yield ($Y_{i\text{-alkane}}$) was calculated using:

$$Y_{i\text{-alkane}} = \left(\frac{F_{\mathrm{Cwt}.i-\mathrm{alkane,out}}}{F_{\mathrm{Cwt}.n-\mathrm{alkane,in}}}\right) \cdot 100\% \qquad \textbf{(Eq. 5.2.)}$$

Similarly, the yield of any cracked product was calculated using:

$$Y_{Cm} = \left(\frac{F_{\mathrm{Cwt}.C\mathrm{m,out}}}{F_{\mathrm{Cwt}.n-\mathrm{alkane,in}}}\right) \cdot 100\% \qquad \textbf{(Eq. 5.3.)}$$

In which C_m is a hydrocarbon molecule with m carbon atoms ($m = 1$-6 during *n*-heptane conversion and $m = 1$-14 during *n*-hexadecane conversion). The selectivity towards *i*-heptane (*i*-C_7) or cracked products (C_m) in mol-% during *n*-heptane conversion was calculated with the following two equations:

$$S_{i\text{-C7}}\,(\%\ or\ mol-\%) = \left(\frac{F_{\mathrm{Cwt}.i-\mathrm{C7,out}}}{F_{\mathrm{Cwt}.n-\mathrm{alkane,in}} - F_{\mathrm{Cwt}.n-\mathrm{alkane,out}}}\right) \cdot 100\% \qquad \textbf{(Eq. 5.4.)}$$

$$S_{Cm}\,(mol-\%) = \left(\frac{F_{\mathrm{Cwt}.C\mathrm{m,out}}}{F_{\mathrm{Cwt}.n-\mathrm{alkane,in}} - F_{\mathrm{Cwt}.n-\mathrm{alkane,out}}}\right) \cdot \left(\frac{7}{m}\right) \cdot 100\% \qquad \textbf{(Eq. 5.5.)}$$

For *n*-hexadecane, the yield in mol-% of a product with m carbon atoms was calculated as follows:

$$Y_{Cm}\,(mol-\%) = \left(\frac{F_{\mathrm{Cwt}.C\mathrm{m,out}}}{F_{\mathrm{Cwt}.n-\mathrm{alkane,in}}}\right) \cdot \left(\frac{16}{m}\right) \cdot 100\% \qquad \textbf{(Eq. 5.6.)}$$

Note that for every mol of heptane, multiple mols of shorter alkanes can be formed, e.g. 1 mol of heptane could theoretically lead to the production of 7 mol of methane. Therefore, selectivities or yields in mol-% could exceed a value of 100 %.

Calculation of Apparent Activation Energies

Apparent activation energies for the hydroconversion of *n*-heptane and *n*-hexadecane were calculated using Arrhenius plots in which ln k was plotted against 1000/T. Equation 5.7 was used to calculate ln k-values using the results of the evaluation of the catalytic performance, assuming first order kinetics.[35]

$$\ln k = \ln\left(\frac{-\ln(1-X)}{\frac{W}{F}}\right) \qquad \textbf{(Eq. 5.7.)}$$

In Equation 5.7, k is the first order rate constant (mol s^{-1} kg_{cat}^{-1}), X is the conversion as a fraction, W is the weight of the catalyst (kg) and F is the molar flow of the reactant (mol s^{-1}). Only ln k-values derived from X-values between 0.01 and 0.20 were plotted, in order to stay in the kinetically determined regime. At least 4 ln k-values were plotted against their corresponding 1000/T-values (1000 K^{-1}). The slopes of the Arrhenius plots were multiplied with the gas constant R (8.314 J K^{-1} mol^{-1}) to obtain the apparent activation energy (E_a, kJ mol^{-1}). E_a-values for methane production were calculated in a similar fashion. However, in that case, X in Equation 5.7 was replaced by the fractional yield of methane (Y_{C1}), thus assuming methane to be a primary product of n-alkane hydrogenolysis.

5.3. Results and Discussion

Quantification of Metal and Acid Sites

Catalysts with different Ni (nanoparticle) nature and location were prepared. The metal weight loadings and number of acid sites in each catalyst are summarized in Table 5.1. They were studied with inductively coupled plasma optical emission spectroscopy (ICP-OES) and temperature programmed desorption of ammonia (NH_3-TPD), respectively. Typically, for the Ni based catalysts, higher metal weight loadings were used than for the Pt based catalysts as in view of the lower dehydrogenation-hydrogenation (DHD/HD) activity of Ni. Ni phyllosilicate to ZSM-22 weight ratios were varied to investigate how much of the Ni in the phyllosilicate framework would be needed.

Structural Properties of the Catalysts

The textural properties of the pristine silica, zeolite, and as-obtained phyllosilicate the dry mixed (phyllosilicate+ZSM-22) catalysts and reduced and passivated (other) catalysts were analyzed with N_2 physisorption (Table 5.2) and HAADF-STEM (Figure 5.1). Emplacing Ni or Pt on/in ZSM-22 led to a significant decrease in BET surface area and the micropore volume compared to pristine ZSM-22. This decrease can be ascribed to pore blocking by metal nanoparticles, suggesting that a part of the metal nanoparticles was placed inside the ZSM-22 crystals, as has been observed before with Pd-SAPO catalysts.[38] The textural properties of the physical mixtures of ZSM-22 with either silica supported catalysts or phyllosilicates show surface areas and pore volumes which are in between the values obtained for the pristine components.

Table 5.1. Results of quantification of metal and acid sites; Ni and Pt weight loading, particle size and dispersion, and number of strong acid sites.

Catalyst	Ni weight loading [a] (wt%)	Pt weight loading [a] (wt%)	Number of strong acid sites [b] (mmol g^{-1})	d_{TEM} [c] (nm)	D [d] (%)	n_M/n_A
Ni/ZSM-22	2.13	n/a	0.46	4.2 ± 1.4	23	0.18
2Ni/SiO_2+ZSM-22 (50/50)	0.94	n/a	0.18	2.7 ± 1.1	36	0.32
4Ni/SiO_2+ZSM-22 (50/50)	1.88	n/a	0.20	4.1 ± 2.0	24	0.38
Ni phyllosilicate+ZSM-22 (5/45)	2.62	n/a	0.24	n/a	100*	1.86
Ni phyllosilicate+ZSM-22 (15/35)	7.98	n/a	0.23	n/a	100*	5.91
Ni phyllosilicate+ZSM-22 (50/50)	14.12	n/a	0.27	n/a	100*	8.91
Pt/ZSM-22	n/a	0.39	0.25	1.1 ± 0.3	100	0.080
0.8Pt/ SiO_2+ZSM-22 (50/50)	n/a	0.41	0.15	1.3 ± 0.3	87	0.12

n/a is not applicable. * used for calculation of n_M/n_A.

[a] Determined by ICP-OES on digested samples.

[b] Determined by deconvolution of NH_3-TPD profiles and integration of the peak at T ≥ 300 °C.

[c] Average particle diameter as determined using HAADF-STEM, based on at least 200 counts.

[d] $\text{Dispersion}_{Pt} = 1.13/d_{Pt}$ [36] and $\text{Dispersion}_{Ni} = 0.971/d_{Ni}$ [17,37]. Dispersion of Pt with $d_{TEM} < 1.13$ nm and dispersion of Ni in Ni phyllosilicate framework were estimated to be 100%.

Table 5.2. Quantitative information derived from N_2 physisorption isotherms for as obtained SiO_2, ZSM-22, Ni phyllosilicate and Ni phyllosilicate+ZSM-22 physical mixtures, and the other reduced and passivated catalysts.

Catalyst	s_{BET} ($m^2\,g^{-1}$)	s_{ext} ($m^2\,g^{-1}$)	V_{total} ($cm^3\,g^{-1}$)	V_{micro} ($cm^3\,g^{-1}$)
Aerosil 380 SiO_2	409	391	1.22	0.00
ZSM-22	247	50	0.31	0.08
Ni/ZSM-22	93	64	0.21	0.01
2Ni/SiO_2+ZSM-22 (50/50)	262	203	0.84	0.02
4Ni/SiO_2+ZSM-22 (50/50)	245	182	0.77	0.03
Ni phyllosilicate	158	133	0.57	0.01
Ni phyllosilicate+ZSM-22 (5/45)	157	77	0.28	0.03
Ni phyllosilicate+ZSM-22 (15/35)	144	88	0.30	0.02
Ni phyllosilicate+ZSM-22 (50/50)	180	101	0.47	0.03
Pt/ZSM-22	190	69	0.22	0.05
0.8Pt/ SiO_2+ZSM-22 (50/50)	228	181	0.78	0.02

[a] Determined using the t-plot method, [b] Single point desorption total pore volume $P/P_0 = 0.995$.

Figure 5.1 shows the representative HAADF-STEM images of a series of selected catalysts. The ZSM-22 crystals were determined to be ~200 nm in length and ~40 nm in width. The metal particle sizes and the corresponding metal dispersion are listed in Table 5.1. When ZSM-22 was impregnated with $Ni(NO_3)_2$, subsequent reduction led to Ni nanoparticles nicely distributed over the ZSM-22 support (Figure 5.1a). A combination of small (1 – 2 nm) and larger (4 – 5 nm) was obtained, and these smaller nanoparticles were presumed to be inside the ZSM-22. Since the fresh Ni phyllosilicate based catalysts did not show Ni nanoparticles (Figure 5.1b), the Ni was assumed to be distributed as nickel ions in the Ni phyllosilicate framework, and Ni dispersion was assumed to be 100% for calculation purposes only. When Ni was deposited on SiO_2 via impregnation and a physical mixture of Ni/SiO_2 and ZSM-22 was prepared, catalysts were obtained with Ni nanoparticles nicely dispersed on the silica support (Figure 5.1c,d). Because of the low z-contrast, however, it was difficult to clearly distinguish Ni nanoparticles, in particular for the 2 wt% loading. At 4 wt% Ni loading, an increase in the number of larger nanoparticles was observed (Figure 5.1d, Table 5.1). In case of the Pt-based catalysts, Pt was clearly deposited on/in ZSM-22 (Figure 5.1e), or on silica when a Pt/SiO_2+ZSM-22 physical mixture was prepared (Figure 5.1f).

Temperature programmed reduction in 1 bar 5% H_2/Ar of the passivated Ni based catalysts was carried out in order to know whether the Ni is completely reduced during catalysis (activation in H_2 at 400 °C (P = 1 bar), and catalysis in H_2 rich atmosphere at $170\ °C \leq T \leq 400\ °C$ and $P_{C16\text{-conversion}} = 5$ bar, $P_{C7\text{-conversion}} = 10$ bar). The Ni phyllosilicate did not show reduction until a temperature of 300 °C was reached and most of the Ni phyllosilicate reduction occurred at $T > 400$ °C (Figure 5.2), in line with what was found previously for calcined samples.[33] This suggests that the unreduced Ni is still present in the Ni phyllosilicate framework and only few, if any, nanoparticles would be present during catalysis. However, during catalysis Ni nanoparticles had formed from the Ni phyllosilicate. This has been observed in the Ni phyllosilicate+ZSM-22 (5/45) catalyst after it was used for the hydroconversion of *n*-hexadecane (Figure 5.3). Also for the Ni-on-SiO_2 a broad reduction peak between 200 °C and 500 °C was observed, meaning that a significant amount of Ni is still present as Ni cations during catalysis. Interestingly, for the Ni/ZSM-22 catalyst, a relatively sharp reduction peak at 200 °C was observed, suggesting that the NiO had been fully reduced and is present as Ni^0 during catalysis. Kim et al. observed a similar reduction peak for Ni on commercial ZSM-5 and ascribed it to the reduction of NiO that weakly interacts with the support.[17,39]

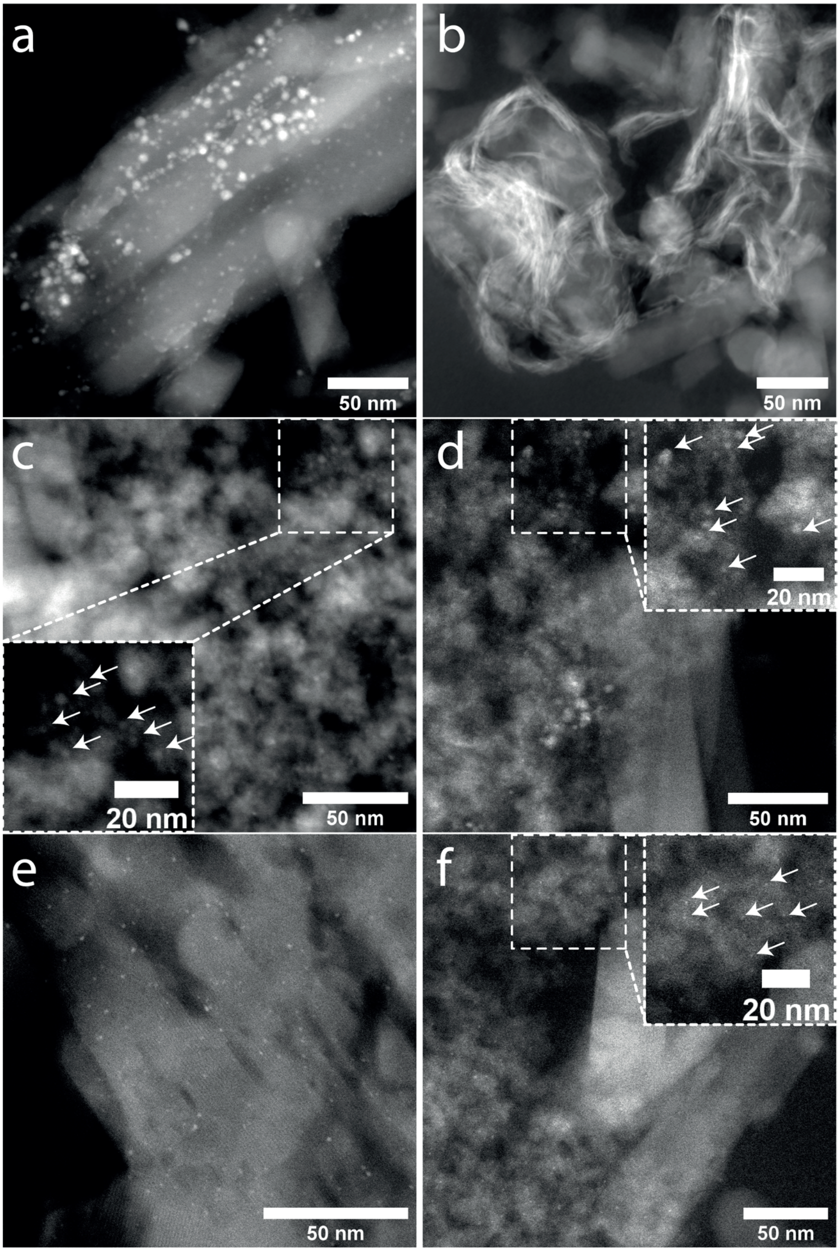

Figure 5.1. HAADF-STEM images of ultramicrotomed (section thickness: 70 nm) samples of catalysts: a) Ni/ZSM-22, b) dry mixture of as obtained Ni phyllosilicate+ZSM-22 (5/45), c) 2Ni/SiO$_2$+ZSM-22 (50/50), d) 4Ni/SiO$_2$+ZSM-22 (50/50), e) Pt/ZSM-22, and f) Pt/SiO$_2$+ZSM-22 (50/50). Insets and arrows pointing at individual nanoparticles serve as guide to the eye. All catalysts were reduced and passivated, except for the Ni phyllosilicate+ZSM-22 catalysts which consisted of a physical mixture of the as prepared Ni phyllosilicate and calcined ZSM-22.

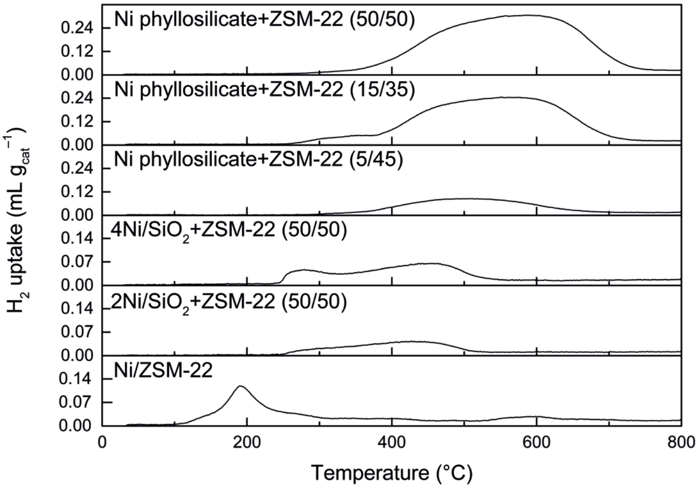

Figure 5.2. Reduction profiles of NiO$_x$ in selected catalysts as obtained via temperature programmed reduction (TPR) with H$_2$. These profiles are measured after passivation of the reduced and passivated Ni/SiO$_2$+ZSM-22 and Ni/ZSM-22 catalysts, and after dry mixing of the as prepared Ni phyllosilicate with ZSM-22 in varying weight ratios.

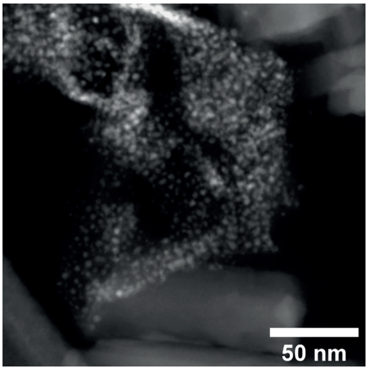

Figure 5.3. HAADF-STEM image of an ultramicrotomed (section thickness: 70 nm) sample of used Ni phyllosilicate+ZSM-22 (5/45) after *n*-hexadecane hydroconversion.

Hydroconversion of *n*-Heptane

The hydroconversion performance of the catalysts was evaluated using *n*-heptane as a feedstock. Overall, the Ni catalysts were slightly more active than the Pt catalysts (Figure 5.4a). However, the *i*-heptane selectivity for the Pt based catalysts than for the Ni based catalysts (Figure 5.4b-d). The highest selectivity towards isomers was obtained with the Pt/SiO$_2$+ZSM-22 catalyst. This is in line with the results in Chapters 2, 3 and 4, where it was beneficial to place Pt (or Pd) on the binder or an external support instead of in the zeolite crystals at metal loadings of about 0.5

wt%.[29,40–42] When Pt was placed on/in ZSM-22 crystals, as is the case for the Pt/ZSM-22 catalysts, loss in *i*-heptane selectivity was caused by an increased tendency towards hydrocracking. This was evidenced by the increased amounts of propane and butanes that had formed (Figure 5.4b). Decrease of the isomer selectivity in Ni-based catalysts was a result of hydrogenolysis, as evidenced by the high selectivity towards methane and hexanes. The selectivities towards methane and hexanes were also higher than the selectivity towards the products that would typically be the product of heptane hydrocracking (C_3 and C_4).

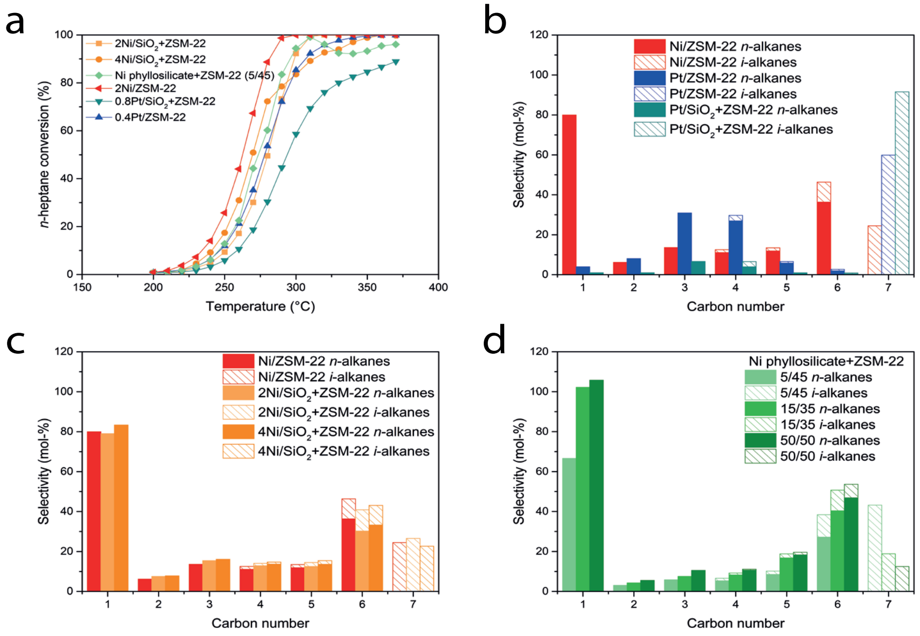

Figure 5.4. *n*-Heptane hydroconversion. a) *n*-heptane conversion as a function of the temperature, and distribution of the products obtained during hydroconversion of *n*-heptane over b) Ni/ZSM-22, Pt/ZSM-22 and Pt/SiO_2+ZSM-22 at 68-72% conversion, c) Ni/ZSM-22, 2Ni/SiO_2+ZSM-22 and 4Ni/SiO_2+ZSM-22 at 68-73% conversion, and d) Ni phyllosilicate+ZSM-22 catalysts in different weight ratios at 67-69% conversion.

All Ni catalysts showed a relatively high hydrogenolysis selectivity (Figure 5.4c,d), regardless of the Ni oxidation state or Ni location. Based on the results from *n*-heptane conversion, the Ni loading affected the hydrogenolysis selectivity, as was mainly shown by the increased hydrogenolysis when the amount of Ni phyllosilicate increased (Figure 5.4d). Furthermore, a graph showing the *i*-heptane/methane molar ratio at low conversion levels (Figure 5.5) confirms this statement. This can be explained by the fact that there is more metal (oxide) present in the sample, and hence more hydrogenolysis[43] – also referred to as metal cracking[44] – can take place. Interestingly, the Ni phyllosilicate+ZSM-22 (5/45) catalyst shows a relatively high selectivity towards *i*-heptane as compared to the other Ni catalysts with similar loadings. This could be rationalized by the fact that less metallic Ni is present in the phyllosilicate based catalyst compared to the Ni/ZSM-22 and Ni/SiO_2+ZSM-22 catalysts as evidenced by the TPR profile (Figure 5.2).

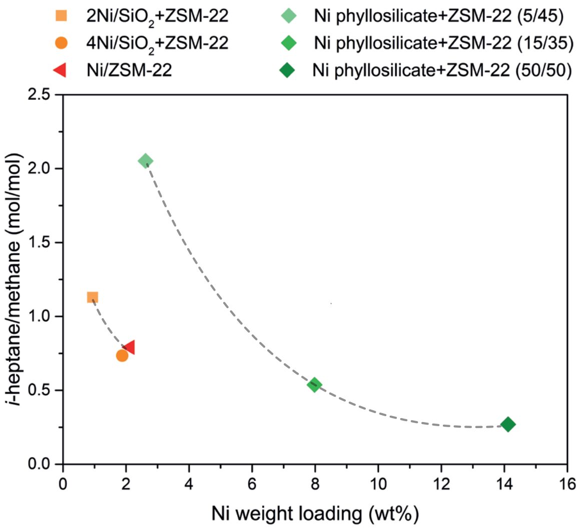

Figure 5.5. Molar ratio between *i*-heptane and methane in the product stream as function of the Ni weight loading in the catalysts at 14-19% *n*-heptane conversion. The dashed lines serve as guide to the eye.

Hydroconversion of *n*-Hexadecane

The catalytic performance was also assessed using *n*-hexadecane as feedstock. Again, the Ni catalysts were slightly more active than the Pt based catalysts (Figure 5.6a), whereas the Pt based catalysts were more selective towards *i*-hexadecane and therefore showed higher *i*-hexadecane yields (Figure 5.6b). The maximum *i*-hexadecane yield of Pt/SiO_2+ZSM-22 was 86% and was only slightly higher than the maximum yield over Pt/ZSM-22 of 84%, in line with what was observed previously at these weight loadings.[45] This suggests that a significant fraction of Pt was present on the external surface of the ZSM-22 crystals, sufficient for DHD/HD on the external surface followed by isomerization in the pore mouth of the zeolite micropores. Most Ni based catalysts showed low *i*-hexadecane yields (Figure 5.4b). Interestingly, however, the Ni/ZSM-22 catalysts did show a maximum *i*-hexadecane yield of 68%.

The carbon number distribution obtained during the hydroconversion of *n*-hexadecane (Figure 5.7), shows that the Ni/ZSM-22 catalyst (Figure 5.7a) displayed lower methane and C_{14} yields compared to most of the other Ni based catalysts. In particular the methane yield at the highest conversion levels depicted in figure 5.7 (Table 5.3) was the lowest for Ni/ZSM-22 and Ni/SiO_2+ZSM-22. Note, however, that the conversion at which this methane yield was taken, was higher over Ni/ZSM-22 than over 2Ni/SiO_2+ZSM-22. A methane yield of 57 mol-% was obtained with Ni/ZSM-

22 at 92% conversion, which is significantly lower than the methane yield with 2Ni/SiO_2+ZSM-22 at 93% conversion. The high *i*-hexadecane yield obtained with Ni/ZSM-22 can therefore be ascribed to a lower hydrogenolysis activity.

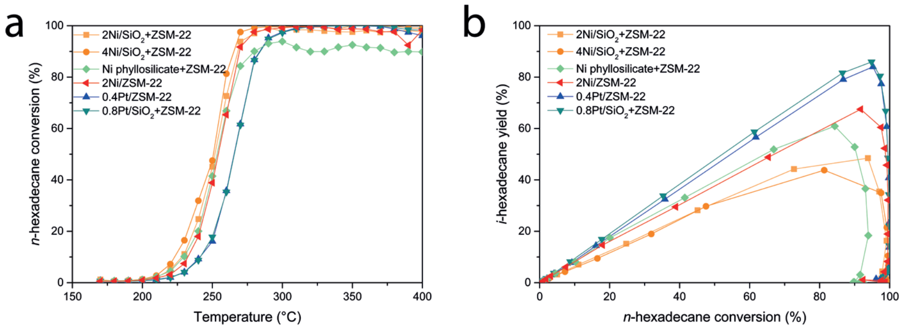

Figure 5.6. Results of *n*-hexadecane hydroconversion. a) *n*-hexadecane conversion as function of the temperature and b) *i*-hexadecane yield as function of the *n*-hexadecane conversion.

Furthermore, the carbon number distribution of Ni/ZSM-22 (Figure 5.7a), showed similarities with that obtained with Pt/ZSM-22 (Figure 5.7g), with peaks at C_3 and C_4 products. This is a result of increased secondary cracking, which is a consequence of having more metal nanoparticles inside the ZSM-22 crystals.[42] The Ni/SiO_2+ZSM-22 (Figure 5.7b,c) and Pt/SiO_2+ZSM-22 (Figure 5.7h) on the contrary, showed more resemblance with the bell-shaped curve indicative for "ideal" cracking.[42,44] Increasing the Ni weight loading results in a shift towards a relatively flat carbon number distribution referred to as a "hammock-shaped" distribution,[44] as evidenced by the Ni phyllosilicate based catalysts (Figure 5.7d-f). The latter is a result of extensive hydrogenolysis.

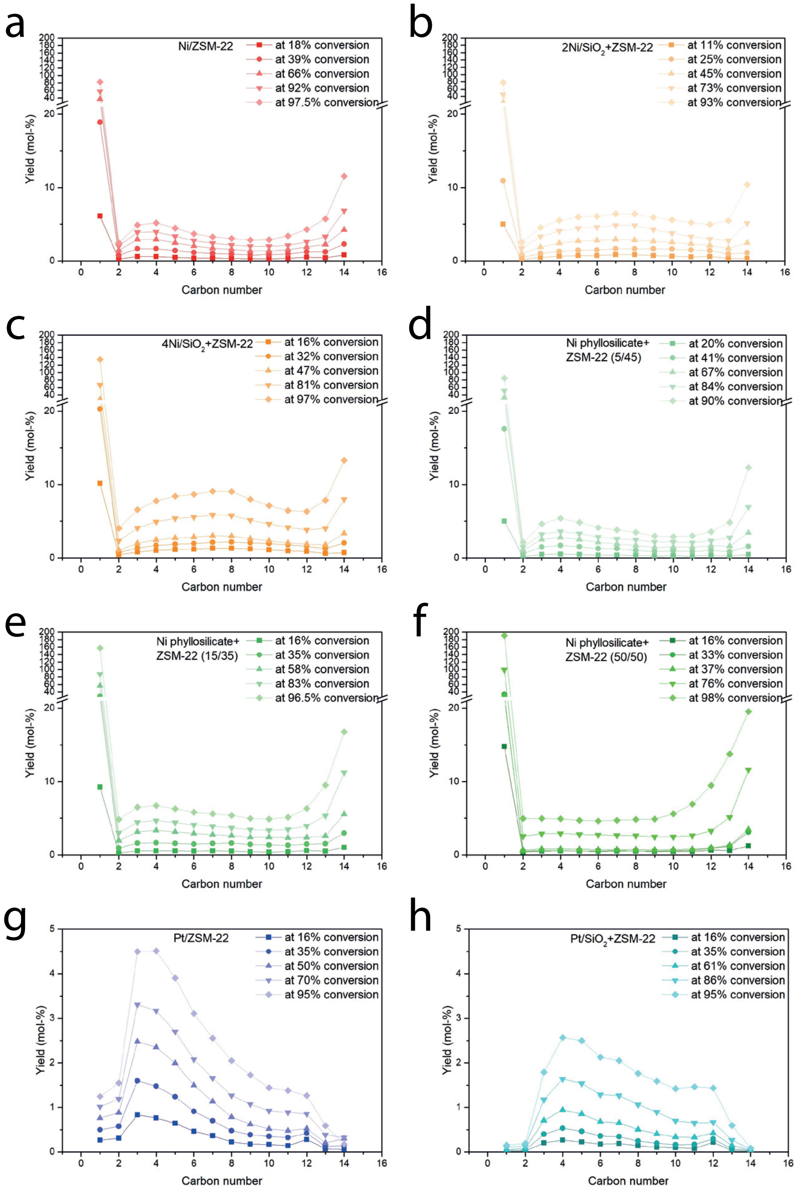

Figure 5.7. Development of carbon number distributions with increasing conversion levels over a) Ni/ZSM-22, b) 2Ni/SiO_2+ZSM-22, c) 4Ni/SiO_2+ZSM-22, d) Ni phyllosilicate+ZSM-22 (5/45), e) Ni phyllosilicate+ZSM-22 (15/35), f) Ni phyllosilicate+ZSM-22 (50/50), g) Pt/ZSM-22 and h) Pt/SiO_2+ZSM-22.

Table 5.3. Methane yield (in mol-% and in %C of the total amount of carbon in product stream) at the highest conversion level depicted in Figure 5.7 for each catalyst.

Catalyst	***n*-hexadecane conversion (%)**	**methane yield (mol-%)**	**methane yield (%C)**
Ni/ZSM-22	97.5	82	12
2Ni/SiO_2+ZSM-22 (50/50)	93	78	11
4Ni/SiO_2+ZSM-22 (50/50)	97	135	19
Ni phyllosilicate+ZSM-22 (5/45)	90	85	12
Ni phyllosilicate+ZSM-22 (15/35)	97	158	23
Ni phyllosilicate+ZSM-22 (50/50)	98	191	27
Pt/ZSM-22	95	1.2	0.2
0.8Pt/ SiO_2+ZSM-22 (50/50)	95	< 0.2	< 0.03

Hydrogenolysis Activity

Hydrogenolysis rather than hydrocracking is the main cause for the formation of side products over Ni based catalysts during the hydroisomerization of both *n*-heptane and *n*-hexadecane. The extent of hydrogenolysis, however, was dependent on the feedstock, in particular for the Ni/ZSM-22 catalyst (Figure 5.8). Even though the hydrogenolysis rate is expected to increase with increasing hydrocarbon chain length,[46] our results show something different, in particular for the Ni/ZSM-22 catalyst. Ni/ZSM-22 was the most active hydrogenolysis catalyst during heptane conversion (Figure 5.8a) and the least active Ni based hydrogenolysis catalyst during hexadecane conversion (Figure 5.8b).

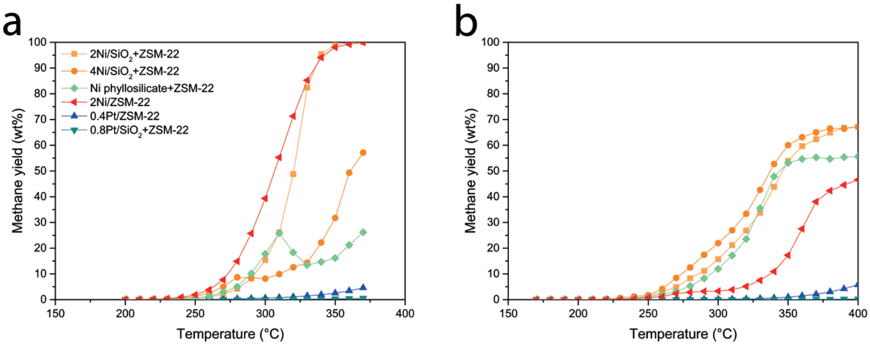

Figure 5.8. Methane yield as function of the temperature during a) *n*-heptane conversion and b) *n*-hexadecane conversion.

This suggests that the methane production from hexadecane over Ni/ZSM-22 is affected by diffusion phenomena. *n*-Heptane reaches the Ni particles in Ni/ZSM-22 more readily than *n*-hexadecane. This hypothesis is supported by the decreased activation energy and much lower pre-exponential factor for the production of methane from *n*-hexadecane for the Ni/ZSM-22 catalyst (Table 5.4). Nevertheless, it is important to note that the Ni/ZSM-22 catalyst was prepared via incipient wetness impregnation and with this method and with the Ni particle sizes obtained with STEM (Figure 5.1, Table 5.1), it is unlikely that the Ni was exclusively deposited inside the ZSM-22 crystals.

Table 5.4. Apparent activation energies (E_a) of *n*-heptane (n-C_7) conversion, *n*-hexadecane (n-C_{16}) conversion, and methane (C_1) production (prod.) during hydroconversion of each of the feedstocks, and the pre-exponential factor (A) for methane production during *n*-hexadecane conversion. The depicted errors correspond to errors in the fit.

Catalyst	**E_a n-C_7 Conv. (kJ mol^{-1})**	**E_a C_1 prod. from n-C_7 (kJ mol^{-1})**	**E_a n-C_{16} Conv. (kJ mol^{-1})**	**E_a C_1 prod. from n-C_{16} (kJ mol^{-1})**	**A C_1 prod. from n-C_{16} (mol kg_{cat}^{-1} s^{-1})**
Ni/ZSM-22	145 ± 5	170 ± 1	165 ± 15	91 ± 6	$7.3 \cdot 10^4$
2Ni/SiO_2+ZSM-22 (50/50)	145 ± 5	177 ± 1	153 ± 14	113 ± 7	$1.2 \cdot 10^7$
4Ni/SiO_2+ZSM-22 (50/50)	148 ± 9	161 ± 5	175 ± 8	144 ± 6	$1.9 \cdot 10^{10}$
Ni phyllosilicate+ZSM-22 (5/45)	156 ± 3	171 ± 4	150 ± 5	119 ± 2	$3.2 \cdot 10^7$
Ni phyllosilicate+ZSM-22 (15/35)	173 ± 19	158 ± 7	141 ± 1	133 ± 1	$2.4 \cdot 10^9$
Ni phyllosilicate+ZSM-22 (50/50)	146 ± 1	169 ± 6	160 ± 9	143 ± 17	$2.0 \cdot 10^{10}$
Pt/ZSM-22	130 ± 3	93 ± 1	143 ± 8	137 ± 2	$9.4 \cdot 10^6$
0.8Pt/ SiO_2+ZSM-22 (50/50)	134 ± 4	89 ± 1	154 ± 6	90 ± 2	$9.1 \cdot 10^1$

The formation of methane and ethane can also be ascribed to (s,p)-β-scission reaction, i.e. acid cracking of a secondary alkylcarbenium ion into primary ones, as was described by Choudhury et al.[47] for Pt/ZSM-22 catalysts. This is expected to only occur under severe confinement and a high density of acid sites, such as in the micropores of zeolites like ZSM-22. The methane formation can therefore be indicative for either cracking occurring inside the micropores and/or hydrogenolysis. This would also explain the production of methane over Pt/ZSM-22 and the absence of methane production over Pt/SiO_2+ZSM-22 (Table 5.3, Figure 5.8), which is a result of Pt/ZSM-22 having Pt nanoparticles inside the ZSM-22 crystals. However, if the methane production from the (s,p)-β-scission was dominant, one would expect that the methane yield and the apparent activation energy for methane production over all Ni-based catalysts would be more or less equally affected, which is not the case. This shows that hydrogenolysis was still one of the key side reactions during hydroconversion of *n*-heptane and *n*-hexadecane over Ni based catalysts.

5.4. Conclusions

Several Ni+ZSM-22 based bifunctional catalysts were prepared, characterized and assessed in hydroconversion studies. The catalysts differed in Ni nanoparticle location, Ni nature and Ni weight loading: the Ni was present in/on ZSM-22, on SiO_2 or in the Ni phyllosilicate framework. Pt/ZSM-22 and Pt/SiO_2+ZSM-22 catalysts were prepared and assessed for comparison. All Ni based catalysts displayed methane production from hydrogenolysis at the expense of hydroisomerization selectivity, irrespective of the nature of the Ni species as determined using TPR. Interestingly, unlike the other Ni based catalysts, the Ni/ZSM-22 catalyst showed a selectivity towards *i*-hexadecane that was almost comparable to that of the Pt/ZSM-22 and Pt/SiO_2+ZSM-22 catalysts. However, when *n*-heptane was converted, the Ni/ZSM-22 showed poor isomerization performance, which is ascribed to very high hydrogenolysis activity. We postulate that this difference originates from diffusion limitations of *n*-hexadecane towards the Ni nanoparticles inside the ZSM-22 crystals, leaving fewer Ni nanoparticles available for hydrogenolysis. Hence, the hydrogenolysis versus the hydroisomerization selectivity is dependent both on the metal (oxide) nanoparticle location and the molecular weight of the hydrocarbon feedstock. These findings are relevant for the further development of catalysts for hydroconversion of FT waxes and valorization of plastic waste.

Acknowledgements

Jan Willem de Rijk, Dennie Wezendonk and Remco Dalebout are acknowledged for their help with the commissioning of the Flowrence setup. The authors thank Savannah Turner for synthesizing and providing the nickel phyllosilicate. Sergei Cherniak and Karan Kotalgi are thanked for N_2 physisorption measurements.

References

(1) Martens, J. A.; Verboekend, D.; Thomas, K.; Vanbutsele, G.; Gilson, J. P.; Pérez-Ramírez, J. Hydroisomerization of Emerging Renewable Hydrocarbons Using Hierarchical Pt/H-ZSM-22 Catalyst. *ChemSusChem* **2013**, *6* (3), 421–425.

(2) Tran, N. H.; Bartlett, J. R.; Kannangara, G. S. K.; Milev, A. S.; Volk, H.; Wilson, M. A. Catalytic Upgrading of Biorefinery Oil from Micro-Algae. *Fuel* **2010**, *89* (2), 265–274.

(3) Peng, B.; Yao, Y.; Zhao, C.; Lercher, J. A. Towards Quantitative Conversion of Microalgae Oil to Diesel-Range Alkanes with Bifunctional Catalysts. *Angew. Chemie - Int. Ed.* **2012**, *51* (9), 2072–2075.

(4) Kong, X.; Zhu, Y.; Zheng, H.; Li, X.; Zhu, Y.; Li, Y. W. Ni Nanoparticles Inlaid Nickel Phyllosilicate as a Metal-Acid Bifunctional Catalyst for Low-Temperature Hydrogenolysis Reactions. *ACS Catal.* **2015**, *5* (10), 5914–5920.

(5) Del Campo, P.; Martínez, C.; Corma, A. Activation and Conversion of Alkanes in the Confined Space of Zeolite-Type Materials. *Chem. Soc. Rev.* **2021**, *50* (15), 8511–8595.

(6) Pirngruber, G. D.; Maury, S.; Daudin, A.; Alspektor, P. Y.; Bouchy, C.; Guillon, E. Balance between (De)Hydrogenation and Acid Sites: Comparison between Sulfide-Based and Pt-Based Bifunctional Hydrocracking Catalysts. *Ind. Eng. Chem. Res.* **2020**, *59* (28), 12686–12695.

(7) Martínez, C.; Corma, A. Inorganic Molecular Sieves: Preparation, Modification and Industrial Application in Catalytic Processes. *Coordination Chemistry Reviews*. 2011, pp 1558–1580.

(8) Henry, R.; Tayakout-Fayolle, M.; Afanasiev, P.; Lorentz, C.; Lapisardi, G.; Pirngruber, G. Vacuum Gas Oil Hydrocracking Performance of Bifunctional Mo/Y Zeolite Catalysts in a Semi-Batch Reactor. *Catal. Today* **2014**, *220–222*, 159–167.

(9) Hur, Y. G.; Kim, M. S.; Lee, D. W.; Kim, S.; Eom, H. J.; Jeong, G.; No, M. H.; Nho, N. S.; Lee, K. Y. Hydrocracking of Vacuum Residue into Lighter Fuel Oils Using Nanosheet-Structured WS 2 Catalyst. *Fuel* **2014**, *137*, 237–244.

(10) Bouchy, C.; Hastoy, G.; Guillon, E.; Martens, J. A. Fischer-Tropsch Waxes Upgrading via Hydrocracking and Selective Hydroisomerization. *Oil Gas Sci. Technol.* **2009**, *64* (1), 91–112.

(11) Sousa-Aguiar, E. F.; Noronha, F. B.; Faro, A. The Main Catalytic Challenges in GTL (Gas-to-Liquids) Processes. *Catal. Sci. Technol.* **2011**, *1* (5), 698–713.

(12) Ledoux, M. J.; Pham-Huu, C.; Dunlop, H.; Guille, J. N-Hexane Isomerization on High Specific Surface Mo2C Activated by an Oxidative Treatment. *Stud. Surf. Sci. Catal.* **1993**, *75* (C), 955–967.

(13) Harmel, J.; Roberts, T.; Zhang, Z.; Sunley, G.; de Jongh, P.; de Jong, K. P. Bifunctional Molybdenum Oxide/Acid Catalysts for Hydroisomerization of n-Heptane. *J. Catal.* **2020**, *390*, 161–169.

(14) Ledoux, M. J.; Del Gallo, P.; Pham-Huu, C.; York, A. P. E. Molybdenum Oxycarbide Isomerization Catalysts for Cleaner Fuel Production. *Catal. Today* **1996**, *27* (1–2), 145–150.

(15) Lugstein, A.; Jentys, A.; Vinek, H. Hydroisomerization and Cracking of N-Octane and C8 Isomers on Ni-Containing Zeolites. *Appl. Catal. A Gen.* **1999**, *176* (1), 119.

(16) de Haan, R.; Joorst, G.; Mokoena, E.; Nicolaides, C. P. Non-Sulfided Nickel Supported on Silicated Alumina as Catalyst for the Hydrocracking of n-Hexadecane and of Iron-Based Fischer-Tropsch Wax. *Appl. Catal. A Gen.* **2007**, *327* (2), 247–254.

(17) Kim, J.; Han, S. W.; Kim, J. C.; Ryoo, R. Supporting Nickel to Replace Platinum on Zeolite Nanosponges for Catalytic Hydroisomerization of n -Dodecane. *ACS Catal.* **2018**, *8* (11), 10545–10554.

(18) Yang, Y.; Lyu, Y.; Zhao, L.; Zhan, W.; Fan, L.; Li, F.; Liu, X. Ligand Assistance via Solid-State Coordination for Promoting Nickel Dispersion over the Ni/Beta Hydroisomerization Catalyst. *Fuel* **2022**, *318* (February), 123568.

(19) Yang, Z.; Liu, Y.; Li, Y.; Zeng, L.; Liu, Z.; Liu, X.; Liu, C. Effect of Preparation Method on the Bimetallic NiCu/SAPO-11 Catalysts for the Hydroisomerization of n-Octane. *J. Energy Chem.* **2019**, *28*, 23–30.

(20) Kots, P. A.; Vance, B. C.; Vlachos, D. G. Polyolefin Plastic Waste Hydroconversion to Fuels, Lubricants, and Waxes: A Comparative Study. *React. Chem. Eng.* **2022**, *7* (1), 41–54.

(21) Xie, T.; Wittreich, G. R.; Vlachos, D. G. Multiscale Modeling of Hydrogenolysis of Ethane and Propane on Ru(0001): Implications for Plastics Recycling. *Appl. Catal. B Environ.* **2022**, *316*, 121597..

(22) Lee, W. T.; van Muyden, A.; Bobbink, F. D.; Mensi, M. D.; Carullo, J. R.; Dyson, P. J. Mechanistic Classification and Benchmarking of Polyolefin Depolymerization over Silica-Alumina-Based Catalysts. *Nat. Commun.* **2022**, *13* (1), 1–13.

(23) Zichittella, G.; Ebrahim, A. M.; Zhu, J.; Brenner, A. E.; Drake, G.; Beckham, G. T.; Bare, S. R.; Rorrer, J. E.; Román-Leshkov, Y. Hydrogenolysis of Polyethylene and Polypropylene into Propane over Cobalt-Based Catalysts. *JACS Au* **2022**, *2* (10), 2259–2268.

(24) Rorrer, J. E.; Ebrahim, A. M.; Questell-Santiago, Y.; Zhu, J.; Troyano-Valls, C.; Asundi, A. S.; Brenner, A. E.; Bare, S. R.; Tassone, C. J.; Beckham, G. T.; Román-Leshkov, Y. Role of Bifunctional Ru/Acid Catalysts in the Selective Hydrocracking of Polyethylene and Polypropylene Waste to Liquid Hydrocarbons. *ACS Catal.* **2022**, *12* (22), 13969–13979.

(25) Kang, Q.; Chu, M.; Xu, P.; Wang, X.; Wang, S.; Cao, M.; Ivasenko, O.; Sham, T. K.; Zhang, Q.; Sun, Q.; Chen, J. Entropy Confinement Promotes Hydrogenolysis Activity for Polyethylene Upcycling. *Angew. Chemie - Int. Ed.* **2023**, *215123*.

(26) Rorrer, J. E.; Beckham, G. T.; Román-Leshkov, Y. Conversion of Polyolefin Waste to Liquid Alkanes with Ru-Based Catalysts under Mild Conditions. *JACS Au* **2021**, *1* (1), 8–12.

(27) Jaydev, S. D.; Martín, A. J.; Pérez-Ramírez, J. Direct Conversion of Polypropylene into Liquid Hydrocarbons on Carbon-Supported Platinum Catalysts. *ChemSusChem* **2021**, *14* (23), 5179–5185.

(28) Vance, B. C.; Kots, P. A.; Wang, C.; Granite, J. E.; Vlachos, D. G. Ni/SiO2 Catalysts for Polyolefin Deconstruction via the Divergent Hydrogenolysis Mechanism. *Appl. Catal. B Environ.* **2023**, *322*, 122138.

(29) Oenema, J.; Harmel, J.; Vélez, R. P.; Meijerink, M. J.; Eijsvogel, W.; Poursaeidesfahani, A.; Vlugt, T. J. H.; Zečević, J.; de Jong, K. P. Influence of Nanoscale Intimacy and Zeolite Micropore Size on the Performance of Bifunctional Catalysts for N-Heptane Hydroisomerization. *ACS Catal.* **2020**, *10* (23), 14245–14257.

(30) Hermans, L. A. M.; Geus, J. W. Interaction Of Nickel Ions With Silica Supports During Deposition-Precipitation. *Stud. Surf. Sci. Catal.* **1979**, *3C*, 113–130.

(31) Burattin, P.; Che, M.; Louis, C. Characterization of the Ni(II) Phase Formed on Silica upon Deposition-Precipitation. *J. Phys. Chem. B* **1997**, *101* (36), 7060–7074.

(32) Van Der Lee, M. K.; Van Jos Dillen, A.; Bitter, J. H.; De Jong, K. P. Deposition Precipitation for the Preparation of Carbon Nanofiber Supported Nickel Catalysts. *J. Am. Chem. Soc.* **2005**, *127* (39), 13573–13582.

(33) Turner, S. J.; Wezendonk, D. F. L.; Terorde, R. J. A. M.; de Jong, K. P. In Situ TEM Study of the Genesis of Supported Nickel Catalysts. *J. Phys. Chem. C* **2023**, *127* (16), 7772–7783.

(34) Cho, H. R.; Regalbuto, J. R. The Rational Synthesis of Pt-Pd Bimetallic Catalysts by Electrostatic Adsorption. *Catal. Today* **2015**, *246*, 143–153.

(35) Agarwal, U.; Rigutto, M. S.; Zuidema, E.; Jansen, A. P. J.; Poursaeidesfahani, A.; Sharma, S.; Dubbeldam, D.; Vlugt, T. J. H. Kinetics of Zeolite-Catalyzed Heptane Hydroisomerization and Hydrocracking with CBMC-Modeled Adsorption Terms : Zeolite Beta as a Large Pore Base Case. **2022**, *415*, 37–50.

(36) Kim, J.; Kim, W.; Seo, Y.; Kim, J. C.; Ryoo, R. N-Heptane Hydroisomerization over Pt/MFI Zeolite Nanosheets: Effects of Zeolite Crystal Thickness and Platinum Location. *J. Catal.* **2013**, *301*, 187–197.

(37) Mustard, D. G.; Bartholomew, C. H. Determination of Metal Crystallite Size and Morphology in Supported Nickel Catalysts. *J. Catal.* **1981**, *67* (1), 186–206.

(38) Wu, Q.; Yuan, J.; Guo, C.; Liu, Z.; Li, X.; Liu, Z.; Wang, W.; Wu, W. The Hydroisomerization of N-Hexadecane over Pd/SAPOs Bifunctional Catalysts with Different Opening Size: Features of the Diffusion Properties in Pore Channels and the Metal-Acid Synergistic Catalysis. *Fuel Process. Technol.* **2023**, *244*, 107692.

(39) Li, C.; Chen, Y. W. Temperature-Programmed-Reduction Studies of Nickel Oxide/Alumina Catalysts: Effects of the Preparation Method. *Thermochim. Acta* **1995**, *256* (2), 457–465.

(40) Zečević, J.; Vanbutsele, G.; de Jong, K. P.; Martens, J. A. Nanoscale Intimacy in Bifunctional Catalysts for Selective Conversion of Hydrocarbons. *Nature* **2015**, *528* (7581), 245–254.

(41) Cheng, K.; van der Wal, L. I.; Yoshida, H.; Oenema, J.; Harmel, J.; Zhang, Z.; Sunley, G.; Zečević, J.; de Jong, K. P. Impact of the Spatial Organization of Bifunctional Metal–Zeolite Catalysts on the Hydroisomerization of Light Alkanes. *Angew. Chemie - Int. Ed.* **2020**, *59* (9), 3592–3600.

(42) Smulders, L. C. J.; van de Minkelis, J. H.; Meeldijk, J. D.; Tang, M.; Liutkova, A.; Cheng, K.; Roberts, S. T.; Sunley, G. J.; Hensen, E. J. M.; de Jongh, P. E.; de Jong, K. P. Steering the Metal Precursor Location in Pd/Zeotype Catalysts and Its Implications for Catalysis. *Chemistry* **2023**, *5* (1), 348–364.

(43) Regali, F.; Liotta, L. F.; Venezia, A. M.; Boutonnet, M.; Järås, S. Hydroconversion of N-Hexadecane on Pt/Silica-Alumina Catalysts: Effect of Metal Loading and Support Acidity on Bifunctional and Hydrogenolytic Activity. *Appl. Catal. A Gen.* **2014**, *469*, 328–339.

(44) Weitkamp, J. Catalytic Hydrocracking—Mechanisms and Versatility of the Process. *ChemCatChem* **2012**, *4* (3), 292–306.

(45) Smulders, L. C. J.; Beeuwkes, A. J.; Cheng, K.; Meeldijk, J. D.; Xu, Z.; Tierney, G. F.; Doskocil, E.; Roberts, S. T.; Sunley, G. J.; de Jongh, P. E.; de Jong, K. P. Silica as Support and Binder in Bifunctional Catalysts with Ultralow Pt Loadings for the Hydroconversion of N-Alkanes. *Catal. Today* **2024** (429), 114508.

(46) Hibbitts, D. D.; Flaherty, D. W.; Iglesia, E. Effects of Chain Length on the Mechanism and Rates of Metal-Catalyzed Hydrogenolysis of n-Alkanes. *J. Phys. Chem. C* **2016**, *120* (15), 8125–8138.

(47) Choudhury, I. R.; Hayasaka, K.; Thybaut, J. W.; Laxmi Narasimhan, C. S.; Denayer, J. F.; Martens, J. A.; Marin, G. B. Pt/H-ZSM-22 Hydroisomerization Catalysts Optimization Guided by Single-Event MicroKinetic Modeling. *J. Catal.* **2012**, *290*, 165–176.

Chapter 6a

Summary, concluding remarks & outlook

6.1. Summary and Concluding Remarks

The catalysts studied in this thesis play a key role in the production of fuels. Fuels are of utmost importance to modern society. The fact that we can heat our buildings and that we can move goods and people through countries, continents and even around the world is largely by using fuels. Most of the fuels we consume now are based on fossil resources. This leads to an unprecedented increase of CO_2 concentrations in the atmosphere. Simultaneously, billions of tons of solid waste are produced by humankind on a yearly basis. Large amounts of waste are landfilled, leading to pollution, a decrease of useful earth surface space, and increased emissions of methane. Both CO_2 and methane are potent greenhouse gases and increased atmospheric concentrations cause global warming.

The solid waste that is landfilled contains carbon-containing molecules. Plastic waste, cardboard and biomass, for example, can be used as solid sources of carbon. These feedstocks can be gasified to produce synthesis gas (a mixture of H_2 and CO) and this syngas can be transformed into paraffins, olefins and oxygenates via the Fischer-Tropsch (FT) process. Some of the products are directly suitable as fuels. However, also paraffinic waxes are produced, which need further treatment. Like the heavy fractions of crude oil, these waxes can be cracked and isomerized via hydroconversion to produce gasoline, diesel and jet fuel. Overall this process is referred to as Waste-To-Liquids (WTL) which is a low carbon footprint technology for transportation fuels.

Hydroconversion is performed with bifunctional catalysts, which typically consist of a metal (oxide or sulfide) as dehydrogenation/hydrogenation function and a (crystalline) solid acid for isomerization and cracking. In particular when the feed is ultraclean, which is the case for FT wax, the metal function can be noble metals such as Pt or Pd. However, these metals are scarce and expensive, and their supply is considered to be at risk. Therefore, it is important to use these metals as efficiently as possible. Classically, in a catalyst, the metal nanoparticles are small and metal dispersion is high, meaning that the surface-to-volume ratio of a metal nanoparticle is high and most of the metal atoms are on the outer surface. Making these nanoparticles as small as possible is a way to make as efficient use of the required materials as possible.

In a bifunctional catalyst another strategy for efficient use of materials can be applied. The metal nanoparticle location with respect to the acid site location can be chosen in such a way that the catalyst displays good catalytic performance. Paul Weisz showed that supported Pt catalysts in combination with silica-alumina showed the highest selectivity towards branched alkanes (*i*-alkanes) when the individual components were small ($d = 5$ µm), or – even better – the Pt was directly impregnated on an acidic silica-alumina support. As a consequence, for a long time it was thought that the two functionalities should be as close to one another as possible. Later, developments in the science of catalyst preparation allowed for placing Pt with nanoscale precision on a zeolite Y/alumina extrudate, and catalysts were prepared with the Pt either in the zeolite Y or on the alumina binder material. The catalyst with Pt on the alumina binder showed improved catalytic performance as this catalyst displayed improved selectivity towards isomers. When Pt was located in the zeolite Y, on the other hand, the catalyst displayed more cracking towards smaller hydrocarbons. Additional studies with different zeolites confirmed this location-dependent catalytic performance in bifunctional catalysts.

The research described in this thesis aimed at improving the metal utilization in bifunctional catalysts by controlling the metal nanoparticle location. In **Chapter 2** we describe the effect of the heat treatment conditions on the final Pd nanoparticle location in ZSM-22 and SAPO-11. We found that direct reduction (DR) of tetraamine palladium nitrate ($[Pd(NH_3)_4](NO_3)_2$) exchanged zeotypes results in enrichment of Pd on the outer surface of the zeotype crystals, whereas slow calcination followed by reduction (CR) leads to confinement of Pd nanoparticles inside the zeotype crystals. For comparison, catalysts with Pd on γ-alumina binder mixed with empty zeotype crystals were prepared. Differences in location were confirmed using HAADF-STEM and XPS. The catalytic performance of these catalysts clearly showed that the more the Pd was on the outside, i.e. on the zeotype crystals or on the binder material, the higher the yield of *i*-heptane and *i*-hexadecane. The catalysts with Pd on the alumina binder performed best, followed by the DR catalysts and lastly the CR catalysts. This showed that heat treatment is a useful synthesis tool to control metal nanoparticle location.

Chapter 3 is devoted to finding the minimum amount of Pt that is required in a bifunctional catalyst. Specifically, this minimum amount as function of the metal nanoparticle location was studied. Catalysts were prepared consisting of Pt, γ-alumina and either ZSM-22 or mordenite as zeolites. The Pt/Al_2O_3/ZSM-22 and Pt/Al_2O_3/MOR varied in Pt location (on Al_2O_3, on ZSM-22 or in MOR) and Pt weight loading (0.005, 0.01, 0.05, 0.1, 0.5 wt%). Regardless of the metal loading, placing Pt nanoparticles in MOR was detrimental to the selectivity of the catalyst towards *i*-heptane, and hence it was beneficial to place Pt on alumina in Pt/Al_2O_3/MOR catalysts. Pt/Al_2O_3/ZSM-22 with a loading ≥ 0.05 wt% displayed similar behavior and improved isomer yields were obtained when Pt was on alumina. However, when an ultralow loading of 0.01 wt% was applied the Pt-on-alumina catalyst displayed a limited catalytic performance. Extensive characterization with HAADF-STEM, XAS and XPS implied that this 0.01Pt-Al_2O_3/ZSM-22 had relatively small ($d_{Pt} = 0.7$ nm) nanoparticles that were harder to reduce and present as Pt in a more oxidized state. Comparison with a single atom catalyst (SAC) with Pt on alumina revealed that indeed Pt nanoparticles are required and that small clusters or single atoms display a too strong interaction with the alumina support, leading to decreased activity in catalysis. The 0.01Pt-ZSM-22/Al_2O_3 catalyst, on the other hand, showed very good catalytic activity, selectivity and stability. Emplacing ultralow loadings of Pt on the outer surface of ZSM-22 showed that the amount of noble metal could be lowered with a factor of 10 or more compared to industrially used catalysts.

In **Chapter 4** we describe the replacement of alumina with silica as binder in bifunctional catalysts with ultralow Pt loadings. As silica is a more inert support material, it was expected that Pt nanoparticles or clusters would be reduced more readily on silica and hence Pt-on-silica bifunctional catalysts with ultralow Pt loadings would be more active than Pt-on-alumina catalysts. A set of Pt/SiO_2/ZSM-22 catalysts with 0.005, 0.01, 0.05, 0.1 and 0.5 wt% Pt on either silica or ZSM-22 was prepared and characterized. XAS showed that indeed even at 0.01 wt% Pt the Pt supported on silica showed to be in a more reduced state. However, this did not lead to improved performance in *n*-heptane hydroisomerization, and at this loading it was still beneficial to emplace Pt on ZSM-22. Additionally, the *n*-hexadecane conversion over the Pt/SiO_2/ZSM-22 catalysts and the Pt/Al_2O_3/ZSM-22 catalysts of Chapter 3 was assessed. A Pt loading of at least 0.05 wt% was desired in that case, preferentially present on the binder material where the reactant and intermediate molecules had easy access to the Pt particles. Fewer Pt particles were observed in HAADF-STEM images when Pt was on silica and higher Pt loadings were required in that case, compared to the other catalysts. Although present as Pt^0, the metal nanoparticle dispersion was too high and the loading too low, which resulted in poor catalytic performance. Silica therefore did not show to be a better support and binder in bifunctional catalysts with ultralow Pt loadings.

In **Chapter 5** the replacement of the noble metals with Ni (oxide) is treated. Ni (oxide) is active as a dehydrogenation and hydrogenation catalyst. The main drawback of using Ni (oxide), however, is its hydrogenolysis activity. The Ni was present in different chemical states and different locations in the catalyst: It was deposited on silica, on/in ZSM-22, or added in the form of a Ni phyllosilicate. During the hydroconversion of both *n*-heptane and *n*-hexadecane, all Ni based catalysts displayed hydrogenolysis activity at the expense of hydroisomerization selectivity. This was irrespective of the nature of the Ni species as determined using TPR. Interestingly, however, Ni/ZSM-22 displayed high isomerization selectivity during the hydroconversion of *n*-hexadecane, whereas it showed the lowest *i*-heptane selectivity. We postulate that this difference is caused by diffusion limitations of *n*-hexadecane towards Ni nanoparticles inside ZSM-22 crystals, leaving fewer Ni nanoparticles available for hydrogenolysis. To conclude, the hydrogenolysis versus the hydroisomerization selectivity is dependent both on the Ni (oxide) nanoparticle location and the molecular weight of the hydrocarbon feedstock. This finding is important to hydroconversion of Fischer-Tropsch wax and valorization of polyolefin waste using non-noble metals.

6.2. Outlook

The research described in this thesis heavily relied on advanced characterization methods to determine metal nanoparticle location. Particularly, when catalysts containing ultralow amounts of metal (oxide) are studied, the techniques are forced to work close to their detection limits. Complementary methods could be applied to unequivocally determine metal nanoparticle locations. To provide more information about the metal nanoparticles being present in or on zeolite crystals, one could perform electron tomography. The main issue with this method is the prolonged exposure of the zeolite crystals to the electron beam, leading to destruction of the crystal in the process of image collection. One way to circumvent this is by performing the measurements in a cryo-holder and direct-electron detection cameras. Other methods that could provide additional information on the metal nanoparticle location are FT-IR with probe molecules, X-ray microtomography, and different probe reactions.

In Chapter 2 the effect of the heat treatment conditions on the final metal nanoparticle location was studied. We showed that ‘direct reduction’ in hydrogen atmosphere led to enrichment of Pd on the outer surface of the zeotype crystals, whereas a slow calcination step prior to reduction led to an increase of Pd nanoparticles inside the crystals. These results in combination with the fact that the cation was exchanged with the zeotype protons suggest that the tetraamine palladium cation was present inside the crystals before heat treatment was performed. That would mean that direct reduction leads to ions and/or atoms moving out of the crystals. This has to our knowledge never been studied directly. *In situ* spectroscopic techniques of tetraamine palladium exchanged zeolites undergoing the heat treatment could shed a light on this process.

The research described in Chapters 3 and 4 showed that the Pt loading could be decreased by factor of 10 or more for the hydroconversion of *n*-heptane if Pt was located on the outer surface of the zeolite. Additionally, for the hydroconversion of *n*-hexadecane the amount of Pt can be lowered drastically. It is important to keep in mind that these results were obtained with catalyst powders. Already under these conditions, the type of zeolite, the feedstock and the operating conditions impact the exact amount of Pt that is required for uncompromised catalytic performance. In industry, catalysts are typically shaped into larger bodies, such as extrudates. The nanoscale phenomena observed in this thesis might have different outcomes under industrial operating conditions. Additional research on a larger scale and under industrially relevant conditions has to be performed in order to find out how much the metal loading could be lowered in an industrial hydroconversion catalyst. The catalyst grain size, for example, could also impact the selectivity of the catalysts. Additionally, under industrial conditions, issues with the catalyst stability are to be expected.

The utilization of Ni as dehydrogenation/hydrogenation function in bifunctional catalysts was explored in Chapter 5. We showed that the Ni (oxide) location in combination with the feedstock can impact the selectivity during hydroconversion, mainly by manipulating the hydrogenolysis activity. However, no catalysts were prepared with Ni selectively deposited *on* or *in* the zeolite crystals. Impregnation of a zeolite with Ni colloids could be applied to selectively deposit the Ni on the outer surface of the zeolite. If this indeed leads to increased hydrogenolysis during *n*-hexadecane hydroconversion, additional evidence for the diffusion limitations observed with Ni/ZSM-22 is obtained. Furthermore, it is well-known that the nature of the Ni species could also impact the hydrogenolysis activity. Hydrogenolysis is for example suppressed by adding Cu, forming NiCu nanoalloys. The formation of nanoalloys is also a strategy to dilute noble metals in earth abundant metals. Attempts towards the optimization of noble metal utilization can therefore also focus on diluting Pt or Pd in Ni. This might lead to improved selectivity and activity of the metal function, while simultaneously suppressing hydrogenolysis activity of Ni.

Diffusion and adsorption of olefins play a key role in hydroconversion. However, knowledge of the diffusion of olefins in zeolites is relatively limited, as modelling and experiments of this process are challenging. This challenging aspect rises from the fact that not only the physical interactions of the olefins and zeolite walls need to be taken into account, but also chemical interactions of the double bond with the zeolite protons are relevant. Further research endeavors could focus on the development of diffusion models for olefins in zeolites. Another research topic of interest is pore-mouth catalysis. In additional experiments it would be interesting to see if branching at selective positions occurs which could be indicative for pore-mouth or key lock adsorption and how this is affected by the location of metal nanoparticles. This would give more information on the way the olefins adsorb onto the zeolite crystals. Furthermore, blocking of zeolite pores by nanoparticles might be an interesting topic for further studies as this impacts the diffusion of reactants and intermediates. Studies could be performed to determine the uptake of certain molecules by virgin zeolite crystals as compared to zeolite crystals with metal particles.

This thesis shows that fundamental knowledge and innovations in well-established processes are relevant to modern chemistry. The research described in this thesis is directly relevant for the production of fuels and chemicals from amongst others municipal waste via indirect liquefaction. Moreover, current work on conversion of plastic waste could benefit from the knowledge obtained on hydroconversion including suppression of hydrogenolysis. The rational placement of metal nanoparticles at the nanoscale can be applied to other technologies, allowing for optimum utilization of scarce materials. These innovations are relevant to both the energy and the materials transitions.

Chapter 6b

Nederlandse samenvatting voor een breder publiek

In de afgelopen jaren heb ik regelmatig de vraag gekregen: “Waar doe je nou eigenlijk onderzoek naar?” Meestal zei ik zoiets als: “Ik doe onderzoek naar katalysatoren voor de productie van duurzame brandstoffen.” Toch bleef het een lastige vraag om te beantwoorden, want je weet niet altijd hoe veel chemische kennis de vraagsteller heeft. Daarnaast doe je tijdens een promotietraject vaak onderzoek naar een heel specifiek deelgebied. Ik was daarom zelf niet altijd tevreden met dat antwoord. In dit hoofdstuk ga ik daarom uitgebreider in op bovenstaande vraag.

Wat is een brandstof en hoe worden brandstoffen gemaakt?

Mensen gebruiken dagelijks energie. Energie is nodig voor het koelen en verwarmen van onze gebouwen, vervoeren van mensen en goederen en voor de productie van voedsel en andere producten. Een heel groot deel (momenteel circa 82 %) van deze energie is door het gebruik van fossiele brandstoffen. Brandstoffen bevatten energie; bij verbranding komt energie – in de vorm van warmte of mechanische energie – vrij. Warmte kan dan weer gebruikt worden voor bijvoorbeeld het verwarmen van gebouwen en de mechanische energie voor het opwekken van elektriciteit of het aandrijven van een motor.

Voor het maken van benzine, diesel en kerosine (vliegtuigbrandstof) moet aardolie worden bewerkt. Dit gebeurt in een olieraffinaderij. In de raffinaderij wordt de olie eerst gedestilleerd. Destilleren is een proces waarbij de individuele componenten van de olie van elkaar gescheiden worden, meestal op basis van de temperatuur waarbij deze componenten koken. De lichtste componenten, propaan en butaan, koken bij de laagste temperatuur, zijn onder normale omstandigheden al gasvormig en kunnen makkelijk van de rest gescheiden worden. Deze lichte fractie is geschikt voor ‘Liquefied Petroleum Gas’, beter bekend als LPG. Grotere en zwaardere moleculen hebben hogere temperaturen nodig om te koken en van de rest van het mengsel gescheiden te worden. Achtereenvolgens, op volgorde van toenemend kookpunt, volgen dan de fracties die geschikt zijn voor benzine, kerosine, diesel, stookolie en een vast residu dat bijvoorbeeld voor asfalt kan worden gebruikt.

Alle vloeibare fracties worden verder behandeld. Daarbij worden ongewenste elementen zoals stikstof (N) en zwavel (S) – de veroorzakers van de beruchte zure regen – verwijderd via een behandeling met waterstof (‘hydrotreating’). De fractie die gebruikt wordt voor benzineproductie ondergaat daarna ‘reforming’ om ervoor te zorgen dat het mengsel de juiste eigenschappen krijgt. De zwaardere fracties ondergaan de processen van hydroconversie en/of katalytisch kraken (‘fluid catalytic cracking’, FCC) om diesel en kerosine en respectievelijk benzine te maken.

Aardolie, aardgas en steenkool bevatten koolstofverbindingen die miljoenen jaren geleden door de fotosynthese in planten zijn gemaakt. De brandstoffen die daaruit gemaakt worden, hebben de bijnaam ‘fossiele brandstoffen’. Bij de verbranding van deze koolstofverbindingen komt koolstofdioxide (CO_2) vrij. Als wij deze fossiele brandstoffen niet zouden gebruiken, zouden de grondstoffen in de grond blijven en zouden ze niet bijdragen aan de CO_2-uitstoot. Nu we deze grondstoffen wel gebruiken, speelt deze extra CO_2 een belangrijke rol bij het versterkte broeikaseffect met klimaatverandering tot gevolg.

We kunnen ook duurzame brandstoffen maken uit hernieuwbare grondstoffen. Er wordt veel onderzoek gedaan naar de productie van brandstoffen uit CO_2. Dit proces staat nog in de kinderschoenen en omdat het nu “alle hens aan dek” is met de energietransitie wordt brandstofproductie uit andere grondstoffen ook onderzocht.

Een andere grondstof die tegenwoordig onderzocht wordt voor de productie van kerosine is vast afval uit huishoudens. In dit afval zitten de elementen die nodig zijn voor een brandstof: koolstof- en waterstof. Wanneer het afval vergast wordt, komen deze elementen voor in de moleculen koolmonoxide (CO) en waterstof (H_2). In een reactie die bekendstaat als de Fischer-Tropsch-synthese kunnen CO en H_2 gecombineerd worden tot alkanen en alkenen. Dat zijn langere koolwaterstofmoleculen die de basis voor een brandstof kunnen vormen. Om de brandstof de juiste eigenschappen te geven en om ook de langste ketens te gebruiken als brandstof, moeten deze alkanen en alkenen nog hydroconversie ondergaan. De hele keten van het maken van brandstoffen uit afval, ofwel waste-to-liquids (WTL), is schematisch weergegeven in Figuur 6.1. De eerste commerciële WTL-fabriek is opgestart in december 2022, in Nevada, VS. Voor veel van de genoemde reacties in zowel de olieraffinaderij als de waste-to-liquids-fabriek zijn katalysatoren nodig.

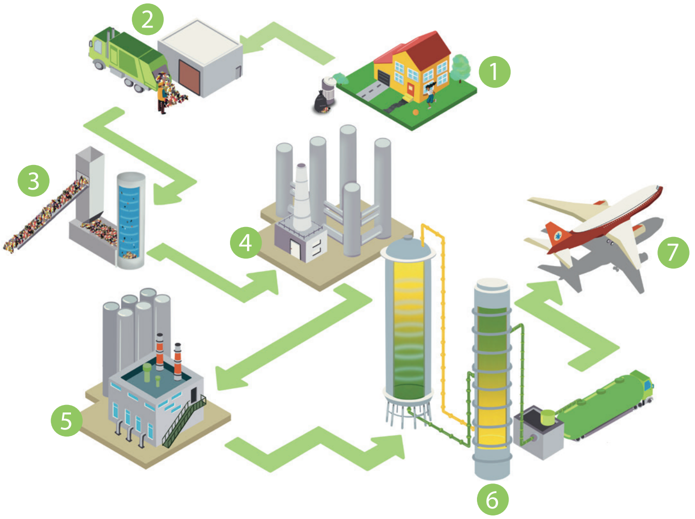

Figuur 6.1. Het WTL-proces in zeven stappen: 1) Afval wordt bij de huishoudens opgehaald; 2) Het huishoudelijk afval wordt verzameld op een speciale inzamelingsplek, bij voorkeur dichtbij de WTL-fabriek; 3) Het afval wordt vergast en er wordt een mengsel van koolmonoxide en waterstofgas verkregen; 4) Het koolmonoxide-waterstof-mengsel wordt gezuiverd en ongewenste stoffen worden eruit gehaald, daarnaast wordt de koolmonoxide-waterstof-verhouding nog aangepast voor de volgende stap; 5) Tijdens het Fischer-Tropschproces worden koolwaterstoffen gemaakt uit koolmonoxide en waterstof; 6) De koolwaterstoffen ondergaan hydroconversie om er kerosine en diesel van te maken; 7) De brandstof is klaar voor gebruik in o.a. vliegtuigen.

Wat is een katalysator?

Vaak wordt een katalysator beschreven als “iets dat een proces versnelt zonder daarbij zelf verbruikt te worden.” Dat is inderdaad een belangrijke eigenschap van een katalysator. We zeggen dan dat een katalysator actief is. Echter, er zijn nog twee belangrijke eigenschappen van een katalysator die we met die definitie over het hoofd zien: de selectiviteit en de stabiliteit. De selectiviteit betreft in hoeverre de katalysator het gewenste product maakt of alleen de gewenste moleculen omzet. De stabiliteit geeft aan of de katalysator het proces over langere tijd kan blijven versnellen en daarbij het gewenste product blijft maken. In de scheikunde is een katalysator meestal een eiwit, een moleculair complex of een vaste stof. Er wordt daarom een indeling gemaakt in drie verschillende deelgebieden: biokatalyse, homogene katalyse en heterogene katalyse.

De biokatalyse is gebaseerd op de katalytische werking van eiwitten. Eiwitten zijn grote moleculen die in organismen voorkomen. Katalytische eiwitten worden enzymen genoemd. Enzymen zijn heel goed in het omzetten van specifieke moleculen in andere, specifieke producten en staan daarom bekend als erg selectieve katalysatoren. Ze zijn letterlijk van levensbelang, want bijna elk chemisch proces in een levend wezen wordt gekatalyseerd door enzymen. In de homogene katalyse worden katalysatoren bestudeerd die zich in dezelfde fase bevinden als de stoffen die ze omzetten (ook wel reactanten genoemd). Meestal zijn zowel de katalysator als de reactanten in de vloeistoffase, ze zijn dus beide vloeibaar of opgelost in een oplosmiddel bij de reactietemperatuur. Homogene katalysatoren kunnen zo simpel zijn als protonen (H^+, een positief geladen waterstofion), maar kunnen ook complexe structuren hebben met metaalatomen die gestabiliseerd worden door zogenaamde liganden.

Het werk dat beschreven staat in dit proefschrift is uitgevoerd met heterogene katalysatoren. Een heterogene katalysator bevindt zich in een andere toestand dan de reactanten. Meestal is de heterogene katalysator een vaste stof, terwijl de reactanten zich in de gasfase of vloeistoffase bevinden onder de gebruikte reactiecondities. In de heterogene katalyse worden vaak metaaldeeltjes toegepast als katalysator. Deze metaaldeeltjes bevinden zich dan meestal op een dragermateriaal. Dat is om ervoor te zorgen dat je kleine deeltjes kunt maken en om te voorkomen dat de metaaldeeltjes samenklonteren en daardoor groter worden. Voor de meeste reacties is het namelijk wenselijk om de metaaldeeltjes zo klein mogelijk te hebben, zodat zoveel mogelijk van de atomen aan de buitenkant van het deeltje zitten. Dit wordt geïllustreerd aan de hand van het aantal zijvlakken van kubussen in Figuur 6.2. Alleen de atomen aan de buitenkant van het deeltje zijn actief. Het is daarom gunstig om nanodeeltjes te gebruiken. Bovendien hebben nanodeeltjes andere eigenschappen dan een groter blok metaal. Nanodeeltjes zijn een paar nanometer, ofwel een paar keer een miljardste van een meter groot. Ter vergelijking: een mensenhaar is ongeveer 80.000 tot 100.000 nanometer dik. Naast nanodeeltjes zijn er ook andere stoffen die een actieve katalysator kunnen zijn waaronder zeolieten.

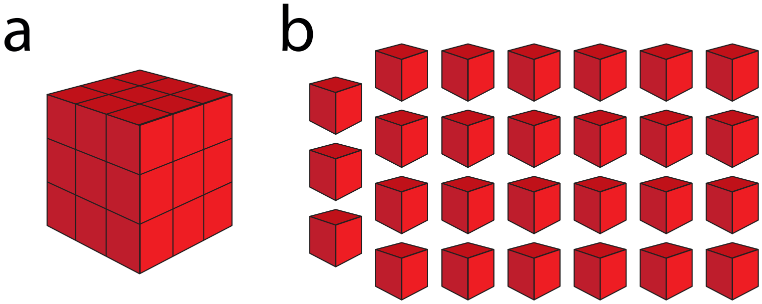

Figuur 6.2. Het oppervlak van een groot deeltje ten opzichte van het totale oppervlak van hetzelfde volume aan kleine deeltjes. a) Een grote kubus bestaande uit 3 x 3 x 3 = 27 kleine kubussen. Aan alle 6 zijvlakken van de grote kubus zijn in totaal 9 zijvlakken van de kleine kubussen aan de buitenkant: 6 x 9 = 54 kleine zijvlakken. b) De 27 kleine kubussen die in de grote kubus geplaatst kunnen worden, hebben elk 6 zijvlakken die aan de buitenkant zijn: 27 x 6 = 162 kleine zijvlakken. Het buitenoppervlak van de grote kubus is dus kleiner dan het totale buitenoppervlak van de kleine kubussen.

Wat is een zeoliet?

Zeolieten vormen een groep veelvoorkomende mineralen in de aardkorst. Het zijn kristallen die voor het grootste gedeelte bestaan uit silica (SiO_2) en alumina (Al_2O_3). Ook andere elementen kunnen gebruikt worden om een zeoliet-achtig kristal te maken. In dat geval wordt gesproken van zeotypen. De structuur van zeolieten is opgebouwd uit tetraëders waarin een siliciumatoom of een aluminiumatoom is omringd door vier zuurstofatomen. Deze tetraëders kunnen gecombineerd worden tot verschillende secundaire bouwstenen zoals vier-, zes- of achtringen. Deze ringen kunnen uiteindelijk gecombineerd worden tot een raamwerk voor het zeolietkristal, zoals te zien in Figuur 6.3. Zeolieten kunnen ook in het laboratorium gemaakt worden. In totaal zijn er ongeveer 260 verschillende zeolietstructuren bekend.

Zeolietkristallen bevatten een stelsel van heel kleine gangen die met het blote oog niet te zien zijn. Deze gangen worden microporiën genoemd. Vaak zijn deze microporiën net groot genoeg om er een molecuul in te laten passen of doorheen te laten bewegen. De microporiën in ZSM-22 bijvoorbeeld, zoals afgebeeld in Figuur 6.3, hebben afmetingen van 0.57 bij 0.46 nm. Daarom worden zeolieten en zeotypes soms moleculaire zeven genoemd; omdat het gangenstelsel moleculaire dimensies heeft, kunnen ze gebruikt worden voor het scheiden van verschillende moleculen en voor katalyse.

De katalytische eigenschap wordt toegeschreven aan de zure plaatsen die in de microporiën kunnen zitten. Deze zure plaatsen ontstaan doordat de silicatetraëders en aluminatetraëders een verschillende lading hebben. Wanneer een aluminatetraëder op een plek van een silicatetraëder zit, krijgt het raamwerk van het zeoliet een negatieve lading. Een proton (positief waterstofion) kan deze lading compenseren. Protonen hebben bovendien de eigenschap dat ze zuur zijn. Zeolieten met daarin protonen voor ladingcompensatie zijn daarom vaste zuren. Deze eigenschap van zeolieten wordt gebruikt bij reacties die versneld worden door een zure katalysator. Voorbeelden daarvan zijn: kraken van zware producten uit aardolie, isomeriseren van brandstofmoleculen om nog efficiëntere brandstoffen te maken, en de omzetting van GFT- of plasticafval in bruikbare producten. Voor een deel van deze toepassingen worden zeolieten en zeotypes gecombineerd met metaaldeeltjes tot zogeheten bifunctionele katalysatoren. Het onderzoek dat beschreven staat in dit proefschrift is uitgevoerd met zulke bifunctionele katalysatoren, gebaseerd op zeotype SAPO-11 en zeolieten ZSM-22 en mordeniet (MOR).

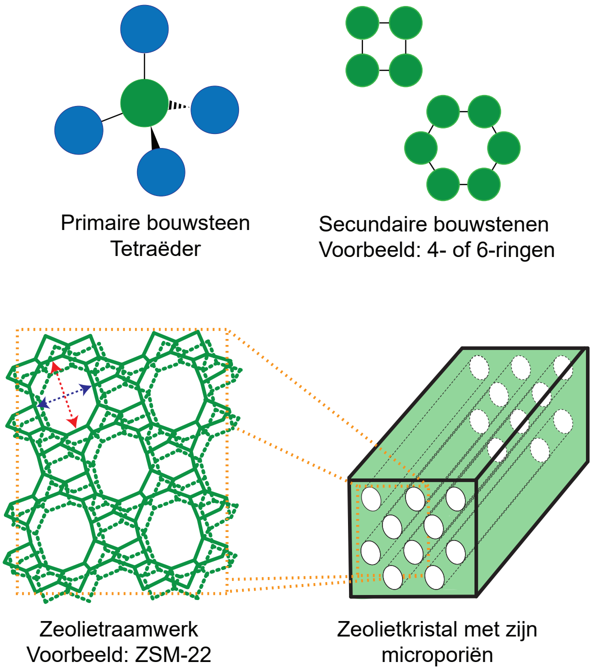

Figuur 6.3. Schematische weergave van een tetraëder met Si of Al als kern (groen) en zuurstofatomen (blauw); secundaire bouwstenen 4- of 6-ringen bestaande uit groene Si- en Al-atomen waarbij de zuurstofatomen niet worden getoond; het zeolietraamwerk van ZSM-22, met afmetingen van de poriën: een lange diameter van 0.57 nm (rood) en een korte diameter van 0.46 nm (blauw); en van een zeolietkristal met microporiën.

Wat is een bifunctionele katalysator en wat is de rol bij de productie van brandstoffen?

In een bifunctionele katalysator zitten twee verschillende katalytische functies die onder dezelfde reactie-omstandigheden actief zijn en samenwerken. Bifunctionele katalysatoren met metaaldeeltjes en zeolietkristallen worden veel toegepast in de productie van brandstoffen. Een belangrijke reactie in de brandstofproductie is, zoals eerder genoemd, hydroconversie. In dit proefschrift ligt de focus op bifunctionele katalysatoren voor hydroconversie.

In hydroconversiekatalysatoren worden de twee functies vervuld door metaal-, metaaloxide- of metaalsulfidedeeltjes enerzijds en een zure plaats anderzijds. Metaalsulfides worden met name toegepast wanneer aardolie dient als grondstof. Omdat de koolwaterstoffen uit de Fischer-Tropschsynthese ultraschoon zijn, kunnen hiervoor metaal- of metaaloxidedeeltjes toegepast worden. Vanaf nu zullen we deze hele groep samenvatten als metaaldeeltjes. Deze metaaldeeltjes kunnen een reactie katalyseren die bekendstaat as dehydrogenatie: een reactie waarbij een alkaan (een koolwaterstofketen) twee waterstofatomen verliest in de vorm van waterstofgas. Er ontstaat dan een molecuul met een dubbele binding en dus een alkeen. Waar alkanen eigenlijk moeilijk reageren met de zure plaatsen, doen alkenen dat wel. De zure plaatsen komen van protonen in een zeoliet. Wanneer deze reageren met het alkeen ontstaat een carbokation, een positief geladen koolwaterstofmolecuul. Dit molecuul kan zich herrangschikken en dat leidt tot vertakkingen in het molecuul. Wanneer het carbokation zijn lading weer afgeeft aan het zeoliet wordt een vertakt alkeen gevormd dat zich kan verplaatsen naar een metaaldeeltje. Dan vindt op het metaaldeeltje hydrogenatie plaats. Het vertakte alkeen reageert dan met waterstof, de dubbele binding verdwijnt en een vertakt alkaan wordt gevormd.

Benzine bestaat uit relatief kleine, vertakte alkanen. Daarnaast bestaan kerosine en diesel uit grotere, zwaardere moleculen en vertakkingen in deze moleculen voorkomen dat de brandstof vast wordt bij te lage temperaturen. Vooral op grote hoogtes zoals die van vliegtuigen wil je ervoor zorgen dat een brandstof nog goed blijft stromen. De reactie waarbij vertakkingen ontstaan wordt specifiek hydroisomerisatie genoemd. Bij hydroisomerisatie blijft het molecuulgewicht gelijk, maar krijgt het molecuul meer vertakkingen.

Hydroconversie kan echter ook doorgaan en met name wanneer een molecuul meerdere vertakkingen heeft, kan dat leiden tot hydrokraken. Hydrokraken is gunstig als de moleculen die omgezet moeten worden heel lang zijn. Hele zware koolwaterstofmoleculen zijn vaak in een vaste vorm, die ook wel was wordt genoemd. Deze was is niet toepasbaar als brandstof voor voertuigen en met hydrokraken worden ze op maat geknipt zodat ze de juiste grootte hebben voor brandstofmoleculen. Daarbij moet wel worden opgelet dat de katalysator niet te lang door blijft knippen, want dan ontstaan korte koolwaterstoffen (gassen) door overkraken. Het hydroconversieproces is samengevat in Figuur 6.4.

Het ontwerp van de katalysator zal invloed hebben op de activiteit en selectiviteit bij hydroconversie. Afhankelijk van verschillende factoren zal de katalysator meer hydrokraken of meer hydroisomeriseren. Voorbeelden van parameters die de selectiviteit beïnvloeden zijn: de zuurheid van het zeoliet, de grootte van de poriën in het zeoliet, de verhouding van het aantal metaaldeeltjes ten opzichte van het aantal zure plaatsen en het soort metaaldeeltje. Verder is gebleken dat ook de locatie van de metaaldeeltjes ten opzichte van de zure plaatsen belangrijk is. Al in de jaren ’50 werd hier onderzoek naar gedaan door Paul Weisz. Hij mengde een katalysator van Pt op silica met een silica-alumina vast zuur en varieerde de macroscopische korrelgrootte van beide katalysatoren om de afstand tussen de twee functies aan te passen. Daarnaast synthetiseerde hij een katalysator waarbij de Pt direct op de silica-alumina-katalysator was aangebracht. Hoe kleiner de korrelgrootte – en dus hoe kleiner de afstand tussen de twee functies – hoe hoger de *i*-heptaanopbrengst was. De hoogste *i*-heptaanopbrengst werd bereikt met de katalysator waarbij de Pt op de silica-alumina was aangebracht. Heel lang werd daarom gedacht dat de twee functies, metaaldeeltjes en zure plaatsen, zo dicht mogelijk bij elkaar moesten zijn.

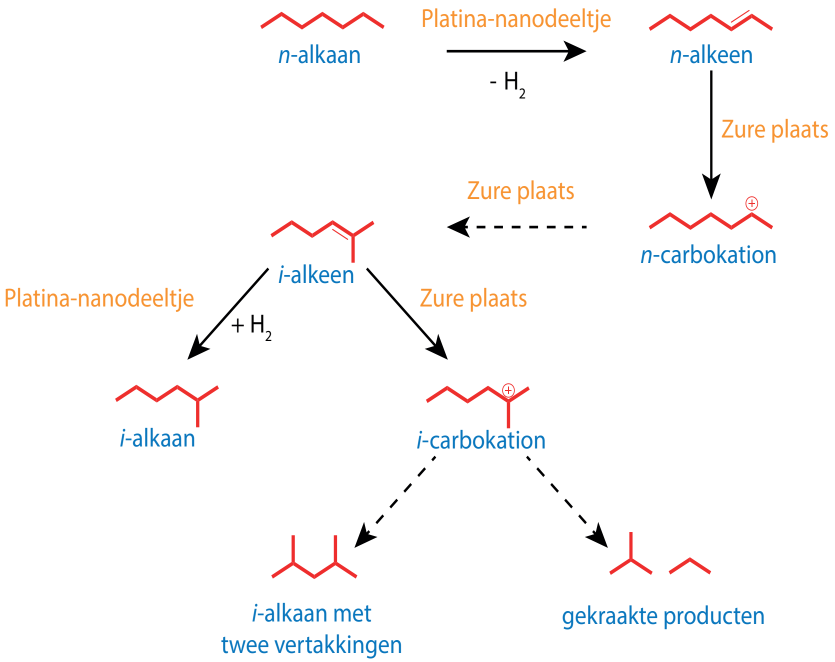

Figuur 6.4. Het hydroconversieproces aan de hand van de omzetting van *n*-heptaan. De koolwaterstofmoleculen zijn getekend in het rood. De blauwe tekst geeft de vorm aan waarin het molecuul zich begeeft. De katalytische functies zijn weergegeven in de oranje tekst en wanneer waterstof weggehaald wordt van de rode moleculen of eraan wordt toegevoegd staat dat weergegeven als – H_2 of + H_2. Een doorgetrokken pijl laat een directe reactie zien, de gestippelde pijl geeft een meerstapsreactie weer die uiteindelijk samengevat kan worden zoals het is getekend.

Uit eerder onderzoek in onze groep weten we dat het bij het gebruik van zeolieten als vaste zuren het beter kan zijn dat de metaaldeeltjes buiten de zeolietkristallen zijn, op een zogeheten bindermateriaal. Bindermateriaal wordt in de industrie gebruikt om een zeolietpoeder te binden tot een groter katalysatordeeltje, maar ook kunnen we het gebruiken als drager voor de metaaldeeltjes. Wanneer de metaaldeeltjes op het bindermateriaal geplaatst worden, is waargenomen dat de katalysator meer gaat hydroisomeriseren. Plaatsing van de metaaldeeltjes in het zeoliet leidt dan tot meer hydrokraken. Figuur 6.5 laat een schematische weergave van deze twee katalysatoren zien.

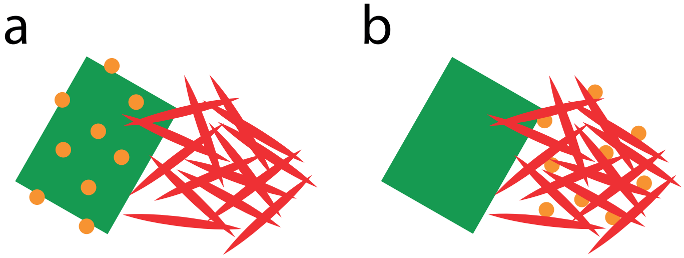

Figuur 6.5. Schematische weergaven van de verschillende locaties van Pt-deeltjes (oranje cirkels) in een bifunctionele katalysator, een zeolietkristal (groene vierhoeken) en alumina als bindermateriaal (rode naalden). a) Een katalysator met platinadeeltjes op en in het zeolietkristal en b) een katalysator met platinadeeltjes op het bindermateriaal. In de katalysatoren gebruikt in de eerste studies in onze groep waren de platinadeeltjes ongeveer 3 nm groot en was het zeolietkristal ongeveer 500 nm groot.

Wat staat er in dit proefschrift?

De zaken die hiervoor beschreven zijn, geven de achtergrond van het onderzoek dat in dit proefschrift is beschreven. Tijdens een promotietraject wordt meestal onderzoek gedaan naar een specifiek deelgebied. Mijn onderzoek heeft niet plaatsgevonden in een olieraffinaderij of bij een afvalverwerker, maar in een chemisch lab op de universiteit. Daarbij hebben wij ons vooral geconcentreerd op locatie-effecten in bifunctionele katalysatoren en gekeken hoe we die effecten kunnen gebruiken om zo min mogelijk van de metaalfunctie nodig te hebben. Naast een energietransitie moet er een materialentransitie plaatsvinden en daarbij hoort dat we zo min mogelijk zeldzame metalen willen gebruiken of dat we ze zelfs vervangen.

In **Hoofdstuk 1** wordt het onderzoek, net als eerder in dit hoofdstuk, in de bredere context geplaatst. In deze introductie gaan we daarnaast dieper in op de wetenschappelijke achtergronden van katalyse, zeolieten, bifunctionele katalysatoren, hydroconversie en locatie-effecten. Daarbij wordt ook de relevante wetenschappelijke literatuur aangehaald.

In **Hoofdstuk 2** staat beschreven hoe de hittebehandeling van een zeoliet of zeotype (vanaf nu samen zeoliet genoemd) met palladiumtetraamine-ionen de uiteindelijke locatie van de palladiumnanodeeltjes beïnvloedt. Hiervoor werden ZSM-22 en SAPO-11 gebruikt en werd palladium aangebracht via ionen-uitwisseling met palladiumtetraaminenitraat ($[Pd(NH_3)_4](NO_3)_2$) opgelost in water. Vervolgens ondergingen deze katalysatoren eerst een droogstap, waarna ze of een directe reductie (DR, directe behandeling met waterstofgas) of een calcinatie-reductie (CR, eerst een behandeling met zuurstofgas en daarna met waterstofgas) ondergingen. Deze Pd-ZSM-22 en Pd-SAPO-11 katalysatoren werden vervolgens gemengd met alumina als bindermateriaal. Ter vergelijking werden ook twee katalysatoren gemaakt met Pd op het alumina gemengd met lege ZSM-22- of SAPO-11-kristallen. De verschillen in locatie in zowel de katalysatorserie met ZSM-22 als in de serie met SAPO-11 werden onderzocht met transmissie-elektronenmicroscopie (TEM) en Röntgenfotoelektronenspectroscopie (XPS). Daarmee werd gevonden dat de meeste

Pd-nanodeeltjes zich aan de buitenkant bevonden wanneer de Pd aanwezig was op alumina, de DR-hittebehandeling ervoor had gezorgd dat er meer (maar niet alle) Pd-nanodeeltjes op de buitenkant van de zeolietkristallen terechtkwamen en dat de CR-hittebehandeling er juist voor had gezorgd dat de meeste Pd-nanodeeltjes in de zeolietkristallen aanwezig waren. Dit had ook gevolgen voor de katalyse, want hoe meer Pd-nanodeeltjes aan de buitenkant van het zeoliet aanwezig waren, hoe meer vertakte moleculen zoals *i*-heptaan en *i*-hexadecaan werden gevormd.

De minimale hoeveelheid platina (Pt) als functie van de locatie van het Pt-nanodeeltje is het hoofdonderwerp van **Hoofdstuk 3**. Voor dit onderzoek werden de zeolieten ZSM-22 en mordeniet (MOR) gebruikt. In de ZSM-22-serie werden Pt-beladingen van 0,005-0,5 gewichts-% aangebracht op de ZSM-22-kristallen of op alumina als bindermateriaal. In de MOR-serie werden katalysatoren gemaakt met een Pt-belading van 0,01-0,5 gewichts-% met Pt-nanodeeltjes in de MOR-kristallen of op het alumina. In de MOR-serie was het onafhankelijk van de Pt-belading altijd gunstig voor de selectiviteit naar *i*-heptaan als de Pt-nanodeeltjes op het bindermateriaal waren aangebracht. De ZSM-22 liet ook hogere *i*-heptaanselectiviteit zien als Pt-beladingen van 0,05 gewichts-% of hoger waren aangebracht op de alumina. Bij een gewichtsbelading van 0,01 gewichts-% was het echter gunstiger dat de Pt-nanodeeltjes op de ZSM-22-kristallen aanwezig waren. Deze katalysator was minstens net zo actief, selectief en stabiel als katalysatoren met hogere Pt-beladingen. Maar waarom presteerde de ZSM-22-katalysator met 0,01 gewichts-% Pt op alumina zo veel minder goed? Karakterisering met TEM liet zien dat de Pt-deeltjes op deze katalysator kleiner (0,7 nm tegenover 1,0 nm of groter op de zeoliet) waren. Daarnaast suggereerde verder onderzoek met XPS en Röntgenabsorptiespectroscopie (XAS) dat deze Pt-deeltjes zelfs na een behandeling met waterstof bij hoge temperatuur in een meer geoxideerde toestand waren. De Pt kwam voor als Pt-clusters (een paar atomen groot) of afzonderlijke atomen met een sterke interactie met het alumina. Dit werk laat zien dat de locatie van de Pt-nanodeeltjes een spectaculair effect kan hebben: het aanbrengen van 0,01 gewichts-% Pt op buitenkant van ZSM-22-kristallen resulteerde in een katalysator die minimaal 10-100 keer minder Pt bevat ten opzichte van de katalysatoren die gebruikt worden in de industrie.

Omdat de interactie van Pt met de alumina bij het gebruik van lage gewichtsbeladingen te sterk was, richt **Hoofdstuk 4** zich op het vervangen van alumina door silica. Silica staat bekend om het feit dat het chemisch meer inert is. De verwachting was dat dit zou resulteren in reductie van Pt-op-silica en dat deze bifunctionele katalysatoren daarom actiever zouden zijn dan de Pt-op-aluminakatalysatoren. Een serie Pt/SiO_2/ZSM-22 werd gesynthetiseerd met 0,005 tot 0,5 gewichts-% Pt op de silica of op de ZSM-22-kristallen. Karakterisering met XAS liet zien dat wanneer 0,01 gewichts-% Pt was aangebracht op de silica, de Pt inderdaad in een meer gereduceerde toestand aanwezig was. Dit leidde echter niet tot betere prestaties tijdens de hydroisomerisatie van *n*-heptaan; bij deze belading was het nog steeds beter om de Pt-nanodeeltjes aan de buitenkant van de ZSM-22-kristallen aan te brengen. Daarnaast werd de conversie van *n*-hexadecaan over de Pt/SiO_2/ZSM-22-serie vergeleken met die van de Pt/Al_2O_3/ZSM-22-serie. Bij de hydroconversie van *n*-hexadecaan bleek een minimale gewichtsbelading van 0,05 gewichts-%, het liefst aangebracht op het bindermateriaal (silica of alumina), wenselijk. Op deze locatie kunnen de grote hexadecaanmoleculen en tussenproducten makkelijker bij de metaalnanodeeltjes komen. Wanneer de Pt-nanodeeltjes op de silica aanwezig waren, werden minder nanodeeltjes gevonden met TEM en waren hogere gewichtsbeladingen nodig ten opzichte van de andere katalysatoren. Ondanks dat de Pt aanwezig was als metallisch Pt leidde het tot teleurstellende katalytische prestaties. Volgens deze resultaten is silica geen beter drager- en bindermateriaal in bifunctionele katalysatoren met lage Pt-gewichtsbeladingen.

Hoofdstuk 5 beschrijft een verkennend onderzoek naar locatie-effecten in bifunctionele katalysatoren waarin de edelmetalen vervangen zijn door nikkel(oxide). Ni(oxide) is een actieve dehydrogenatie/hydrogenatie-katalysator. Een groot nadeel van Ni(oxide) is echter de hydrogenolyse-activiteit. Bij de hydroconversie van alkanen is hydrogenolyse een ongewenste nevenreactie, waarbij het metaalnanodeeltje een willekeurige kraakreactie katalyseert. Er kunnen allerlei korte alkanen uit ontstaan en de producten die het duidelijkst wijzen op hydrogenolyse zijn methaan (1 koolstofatoom) en ethaan (2 koolstofatomen). Deze korte alkanen kunnen niet gebruikt worden voor benzine, diesel of kerosine. Voor dit onderzoek werd zeoliet ZSM-22 gebruikt. Verschillende katalysatoren werden gemaakt door Ni in verschillende chemische toestanden en op verschillende locaties aan te brengen: op silica, op/in ZSM-22-kristallen of in de vorm van een fysisch mengsel met nikkelphyllosilicaat. Alle Ni-katalysatoren lieten hydrogenolyse zien tijdens *n*-heptaan- en *n*-hexadecaanconversie. Interessant was dat de Ni/ZSM-22-katalysator (Ni aangebracht op/in ZSM-22-kristallen) hoge *i*-hexadecaanselectiviteit vertoonde, terwijl het de slechtste *i*-heptaanselectiviteit vertoonde. Onze hypothese is dat dit verschil veroorzaakt wordt door diffusielimitaties – een trage verplaatsing van de moleculen – van *n*-hexadecaan naar de Ni (oxide)-nanodeeltjes in de ZSM-22-kristallen. Daardoor zijn de Ni-nanodeeltjes minder actief voor het katalyseren van *n*-hexadecaanhydrogenolyse. De verhouding tussen de hydrogenolyse- en hydroisomerisatieselectiviteit is dus afhankelijk van de Ni(oxide)-locatie en het moleculair gewicht van de reactanten. Deze vinding is belangrijk voor zowel de hydroconversie van Fischer-Tropschproducten als voor het omzetten van plastic afval met veelvoorkomende metalen.

Samenvattend hebben wij onderzoek gedaan naar het effect van de locatie van metaalnanodeeltjes in bifunctionele katalysatoren. Daarbij hebben we gekeken naar een nieuwe methode om de locatie te beïnvloeden, manieren om de hoeveelheid benodigd edelmetaal te verminderen en ook naar de mogelijkheid om het edelmetaal te vervangen door nikkel. Hieruit zijn vier belangrijke bevindingen gekomen. Ten eerste kan de hittebehandeling tijdens de bereiding van de katalysator de uiteindelijke locatie van Pd-nanodeeltjes beïnvloeden. Ten tweede kan door het gericht plaatsen van Pt een katalysator gemaakt worden waar 10-100 keer minder Pt in zit, zonder dat dat ten koste gaat van de katalytische prestaties. Ten derde hebben we laten zien dat ondanks dat silica misschien een betere keuze lijkt als bindermateriaal, dit geen betere resultaten oplevert. Als laatste hebben we een stap in de richting gezet van edelmetaalvrije bifunctionele katalysatoren en daarbij gevonden dat de hydrogenolyse-activiteit ook afhankelijk is van de locatie en tevens van de reactanten.

List of abbreviations

A	Pre-exponential factor in Arrhenius equation
a.u.	Arbitrary units
BET	Brunauer-Emmett-Teller
C_m	Hydrocarbon molecule with m carbon atoms
CR	Calcination-Reduction
DHD/HD	Dehydrogenation/hydrogenation
DR	Direct Reduction
E_a	Apparent activation energy
EDX	Energy Dispersive X-ray Spectroscopy
Eq	Equation
EXAFS	Extended X-ray Absorption Fine Structure
FID	Flame Ionization Detector
FT	Fischer-Tropsch
FT-IR	Fourier-Transform Infrared Spectroscopy
GFT	Groente, Fruit en Tuin
HAADF-STEM	High-angle Annular Dark-Field Scanning Transmission Electron Microscopy
IA	Ion adsorption
i-C_m	Branched hydrocarbon molecule with m carbon atoms
ICP	Inductively Coupled Plasma
IE	Ion exchange
LCA	Life Cycle Assessment
LCF	Linear Combination Fitting
LPG	Liquefied Petroleum Gas
MOR	Mordenite
MSW	Municipal Solid Waste
n_A	Number of acid sites
n_M	Number of metal sites
n_{Pd}	Number of palladium sites
n_{Pt}	Number of platinum sites
NM	Noble metal
NP	Nanoparticle
n-C_m	Linear hydrocarbon molecule with m carbon atoms
PCP	Protonated Cyclopropane
SAC	Single Atom Catalyst
SAPO	Silicoaluminophosphate
SEM	Scanning Electron Microscopy
TCD	Thermal Conductivity Detector
TEM	Transmission Electron Microscopy
TPD	Temperature Programmed Desorption
TPR	Temperature Programmed Reduction

USD	American Dollar (US Dollar)
USY	Ultrastable Y-Zeolite
WTL	Waste-to-Liquids
XANES	X-ray Absorption Near-Edge Structure
XAS	X-ray Absorption Spectroscopy
XPS	X-ray Photoelectron Spectroscopy
XRD	X-ray Diffraction
XRF	X-ray Fluorescence
XTL	X-to-Liquids *or* Feed-to-Liquids
ZSM	Zeolite Socony Mobil

List of publications and presentations

Publications discussed in this thesis

Smulders, L.C.J.; Beeuwkes, A.J.; Cheng, K.; Meeldijk, J.D.; Xu, Z.; Tierney, G.F.; Doskocil, E.; Roberts, S.T.; Sunley, G.J.; de Jongh, P.E.; de Jong, K.P., Silica as support and binder in bifunctional catalysts with ultralow Pt loadings for the hydroconversion of *n*-alkanes, *Catalysis Today* **2024** (429), 114508.

Smulders, L.C.J.; van de Minkelis, J.H.; Meeldijk, J.D.; Tang, M.; Liutkova, A.; Cheng, K.; Roberts, S.T.; Sunley, G.J.; Hensen, E.J.M.; de Jongh, P.E.; de Jong, K.P., Steering the metal precursor location in Pd/zeotype catalysts and its implications for catalysis, *Chemistry* **2023**, (5), 348-364.

Cheng K.*; Smulders, L.C.J.*; van der Wal, L.I.; Oenema, J.; Meeldijk, J.D.; Visser, N.L.; Sunley, G.J.; Roberts, S.T.; Xu, Z.; Doskocil, E.; Yoshida, H.; Zheng, Y.; Zecevic, J.; de Jongh, P.E.; de Jong, K.P., Maximizing noble metal utilization in solid catalysts by control of nanoparticle location, *Science* **2022**, (377), 204-208.
*These authors contributed equally.

Other publications by the author

Keijzer, C.J.; Smulders, L.C.J.; Wezendonk, D.; de Rijk, J.W.; de Jongh P.E., Influence of Ag particle size and Ag : Al_2O_3 surface ratio in catalysts for the chloride-promoted ethylene epoxidation, *Catalysis Today* **2024**, (428), 114447.

Visser, N.L.; Verschoor J.C.; Smulders, L.C.J.; Mattarozzi, F.; Morgan, D.J.; Meeldijk, J.D.; van der Hoeven, J.E.S.; Stewart, J.A.; Vandegehuchte, B.D.; de Jongh, P.E., Influence of carbon support surface modification on the performance of nickel catalysts in carbon dioxide hydrogenation, *Catalysis Today* **2023**, (418), 114071.

Visser, N.L.; Daoura, O.; Plessow, P.N.; Smulders, L.C.J.; de Rijk, J.W.; Stewart, J.A.; Vandegehuchte, B.D.; Studt, F.; van der Hoeven, J.E.S.; de Jongh, P.E., Particle size effects of carbon supported nickel nanoparticles for high pressure CO2 methanation, *ChemCatChem* **2022**, (14).

van der Wal, L.I.; Oenema, J.; Smulders, L.C.J.; Samplonius, N.J.; Nandpersad, K.R.; Zecevic, J.; de Jong, K.P., Control and impact of metal loading heterogeneities at the nanoscale on the performance of Pt/Zeolite Y catalysts for alkane hydroconversion, *ACS Catal.* **2021**, (11), 3842-3855.

Vis, C.M.; Smulders, L.C.J.; Bruijnincx, P.C.A., Tandem catalysis with antagonistic catalysts compartmentalized in the dispersed and continuous phases of a Pickering emulsion, *ChemSusChem* **2019**, (12), 2176-2180.

Oral presentations

Advanced preparation of Metal-Acid Bifunctional catalysts to control metal nanoparticle location, *13th International Symposium on "Scientific Bases for the Preparation of Heterogeneous Catalysts" (PREPA13),* Louvain-la-Neuve, Belgium, July 2023 (keynote opening).

Optimizing noble metal utilization in Pt/zeolite bifunctional catalysts, *CHAINS*, Veldhoven, The Netherlands, September 2022.

Optimizing noble metal utilization in Pt/zeolite bifunctional catalysts, *International Zeolite Conference*, Valencia, Spain, July 2022.

Metal nanoparticle location effects in Pd/zeotype bifunctional catalysts for the hydroconversion of *n*-alkanes, *27th North American Meeting*, New York, USA, May 2022.

Metal nanoparticle location effects in Pd/zeotype bifunctional catalysts for the hydroconversion of *n*-alkanes, *Canadian Symposium on Catalysis*, Vancouver, Canada, May 2022.

Metal nanoparticle location effects in Pd/SAPO-11 bifunctional catalysts for the hydroconversion of *n*-alkanes, *The Netherlands' Catalysis and Chemistry Conference*, Noordwijkerhout, The Netherlands, May 2022.

Hydroisomerization of *n*-heptane over Pd/SAPO-11 catalysts: the impact of metal-acid proximity, *8th conference of the Federation of European Zeolite Associations,* online, June 2021.

Poster presentations

Effects of metal nanoparticle location in Pd/zeotype bifunctional catalysts for hydroconversion of *n*-alkanes, *CHAINS*, online, December 2021.

Hydroisomerization of *n*-heptane over Pt/SAPO molecular sieves: The impact of metal-acid proximity. *The Netherlands' Catalysis and Chemistry Conference*, Noordwijkerhout, The Netherlands, March 2020.

Acknowledgements | Dankwoord

Zo, daar zijn we dan. Dit is het stuk waarin ik eindelijk onder woorden kan brengen hoe dankbaar ik ben geweest voor de hulp, steun, inspiratie en gezelligheid die ik de afgelopen jaren genoten heb. Ook al heeft het soms als een moeilijk en eenzaam proces gevoeld, ik was nooit echt alleen, en dat heb ik aan jullie te danken. Jullie waren onderdeel van deze reis.

Allereerst wil ik uiteraard **Krijn** bedanken. Krijn, tijdens jouw colleges in de bachelor en de master raakte ik erg geïnteresseerd in de anorganische chemie en de katalyse. Jouw passie voor het vakgebied is onwijs inspirerend. Het was dan ook een hele eer dat ik mijn promotietraject mocht doen met jou als begeleider. Jij hebt mij de kans gegeven om te groeien in het vakgebied en je hield me scherp met kritische vragen. In deze tijd heb je me ook aangemoedigd en geholpen om af en toe naast de diepte ook de breedte op te zoeken, met als hoogtepunt de openingspresentatie bij PREPA. Dankjewel voor jouw geduld, passie en mentorschap.

Petra, ook jou wil ik graag bedanken voor alle hulp en steun tijdens mijn promotietraject. In het begin waren we allebei nog een beetje op zoek naar wat jouw rol precies kon zijn in deze tijd, maar ik denk dat we dat gaandeweg goed uitgevonden hebben: jij gaf wetenschappelijke input wanneer nodig, kwam met complimenten wanneer ik die nog harder nodig had en met jou regelde ik een aantal dagelijkse zaken toen Krijn met emeritaat was gegaan. Ik vind het ontzettend leuk dat je de samenwerking met BP op het gebied van bifunctionele katalysatoren voortzet en wens jullie heel veel succes met het vervolg.

I also really enjoyed the collaboration with BP. **Glenn**, thank you for sharing your knowledge to improve the level of the projects. You seem to be a walking encyclopedia of chemistry and your enthusiasm and passion are contagious. **Tegan**, I would like to thank you for your input and the help with the calculations regarding the experimental setup and statistics. Your engineering point of view was very helpful. **Eric** and **Andreas**, thank you for your questions and ideas regarding the project. You came up with additions which were not only useful but also helped me think out of the box sometimes. And of course **Zhuoran**, thank you for the XAS measurements, which ended up in two of the chapters. I know that the catalysts with ultralow Pt loadings were particularly challenging to measure, but you kept trying until we had a meaningful result. These results were definitely indispensable, so thank you for your perseverance!

The “bifunctional team” was very helpful, especially at the start of my PhD trajectory. Thank you **Justine** and **Jogchum** for showing me your tips and tricks regarding the synthesis and characterization of the catalysts. Daarnaast wil ik jou onwijs bedanken voor de hulp met de Flowrence, Jogchum. Je hebt me er zo goed als ging in korte tijd op ingewerkt tijdens de covidpandemie. Gelukkig was je ook na je vertrek in de groep beschikbaar voor hulp, zelfs vanuit Gent en Helsinki. **Lars**, dankjewel voor jouw fantastische TEM-skills, de gezellige meetochtenden en -middagen bij de Talos en ook de spelletjes buiten het werk om. **Min**, also thank you for helping me out with some of the TEM-measurements. **Nynke**, ik ben jou erg dankbaar voor de hulp bij de start van de PhD, maar misschien zelfs nog meer voor het feit dat jij mij destijds op deze positie gewezen hebt. Daarnaast is het erg leuk om als “buren” nog steeds contact te hebben. And of course **Kang**, thank you for all your help on all of the papers. I am very grateful that I could become part of the work that we published in Science and I am proud that our hard work got rewarded. During that time we were working from different sides of the world, allowing us to work basically 24/7 on that paper. Thinking about that collaboration still makes me smile.

Uiteraard wil ik ook graag mijn studenten bedanken voor al hun harde werk en toewijding. De samenwerking met studenten was voor mij echt de kers op de PhD-taart. **Jochem**, jij begon als masterstudent toen ik zelf pas net begonnen was aan mijn PhD. Je hebt heel hard gewerkt aan jouw thesis die uiteindelijk de basis vormde voor hoofdstuk 2 en een publicatie. Het was niet altijd even makkelijk om in covidtijd hieraan te werken, maar je bleef doorzetten en dat heeft geleid tot een super resultaat. Later kwam **Arvid** om een vraag die eigenlijk uit hoofdstuk 3 kwam rollen te beantwoorden. En dat is gelukt! Jouw resultaten vormden de basis voor hoofdstuk 4 en zijn ook gepubliceerd. Dankjewel voor jouw toewijding en nieuwsgierige houding waarmee je maar door bleef gaan met onderzoeken. **Sofie**, jij ging als eerste van mijn studenten aan de slag met mogelijke vervanging van de edelmetalen door nikkel tijdens jouw literatuurstudie. Ik heb erg veel van jou geleerd en ik heb zelf nog wat experimenten gedaan met jouw bevindingen. **Ilja** en **Sanne** hebben tijdens de bachelorprojecten verder gewerkt aan nikkel. De resultaten vormden de inspiratie voor hoofdstuk 5. Jullie zijn allemaal ontzettend gegroeid en met jullie werken was een feest, dankjulliewel!

I would also like to thank the other MCC staff members for their scientific input during the group meetings and at conferences, and for the small talks over a cup of coffee and sometimes even with some cake. Thank you **Jessi**, **Nong**, **Peter** and **Frank**!

Verder wil ik van MCC heel graag **Ilonka** en **Sylvia** bedanken. Bij jullie kon ik altijd binnenlopen met een urgente vraag of gewoon voor een praatje. Misschien liep ik jullie deur wel een beetje plat, maar het was ook wel erg fijn om af en toe mijn ei kwijt te kunnen. Jullie hebben precies door wat er speelt in de groep en staan voor iedereen klaar. Dankjulliewel voor jullie betrokkenheid, organisatieskills en hulp met eigenlijk alles van het begin van mijn PhD-traject tot het einde.

Een onderzoekslab kan niets zonder goede technici. Daarom wil ik graag **Ad**, **Dennie**, **Hans**, **Jan Willem**, **Remco** en **Ramon** bedanken. Ad, jouw inspanningen om het labwerk zo veilig mogelijk te houden heb ik ontzettend gewaardeerd. Dennie, dankjewel voor jouw hulp met de chemisorptie, TGA en de Flowrence. Daarnaast wil ik jou bedanken voor de gezellige fietstochten naar Leidsche Rijn. Hans, ik kijk met veel plezier terug op onze TEM-sessies. Met jouw positieve instelling ging het zelden over wat niet kan en vaak over wat we kunnen proberen. Een paar van de meest exotische experimenten zijn wellicht minder succesvol geweest, maar we hebben (al dan niet met moeite) katalysatoren met de laagste gewichtsbeladingen weten te karakteriseren. Jan Willem, bedankt voor de hulp met de gassen, het bestellen van de gascilinders en uiteraard ook de Flowrence. En Remco, ook jij bedankt voor de hulp met de Flowrence. Ik wil ook graag de technici van ICC bedanken voor de prettige samenwerking van zowel voor als na de splitsing: dankjulliewel **Jochem**, **Oscar**, **Joris**, **Pascal** en **Fouad**. En alle MCC- en ICC-technici bedankt voor de gezellige gesprekken tijdens koffiepauzes.

Additionally, I would like to express my gratitude to **Anna** and **Emiel** from the Eindhoven University of Technology. Thank you for the XPS measurements for chapter 2. It was a pity that I could not come to Eindhoven to help and to experience the experiments myself during the pandemic. Nevertheless, we managed to collaborate online and thanks to your quick response to questions and input on the manuscript we could improve the quality of that chapter (and the paper).

Tijdens mijn promotietijd bij MCC heb ik erg veel gehad aan mijn collega's. Het is superfijn om mensen om je heen te hebben die min of meer in hetzelfde schuitje zitten. Velen van jullie hebben mij geïnspireerd en gemotiveerd, waarvoor dank. **Oscar**, samen waren wij betrokken bij de BP-projecten en regelmatig moesten wij de BP-UU meetings regelen. Heel fijn dat we dat samen konden doen. Ik was ook altijd erg onder de indruk van jouw presentaties en achtergrondkennis en ik denk dat ik daar stiekem veel van heb geleerd. Later you joined our BP team too, **George**. Thank you for your help with the project and for taking over the supervision over the students when I was away. Your XAS input also made it to one of the chapters of this thesis, thank you very much for that! **Nienke**, wij vormden samen een goed DA-team en het was fijn om samen met jou Advanced Catalysis / AKC te geven. Je werkte ontzettend hard, maar maakte ook tijd om frustraties te delen en goede raad te geven. **Suzan**, jij was mijn buurvrouw tijdens bijna het gehele traject en we deelden heel veel. Dank voor de fijne gesprekken en voor de theezakjes als ik mijn eigen voorraad weer eens was vergeten aan te vullen. **Kris**, jouw positiviteit en enthousiasme lijken soms geen grenzen te kennen, ook al zit het soms tegen. Het was heerlijk om jou als buurman te hebben. **Carolien**, ik vond het leuk om na mijn masterproject onder jouw begeleiding ook nog even collega's en bureauburen te zijn geweest. Je bleef op afstand nog steeds betrokken met een regelmatig berichtje en met onze spelletjesmiddag en dat waardeer ik zeer. **Laura de K.**, ook jij bedankt voor de gezelligheid bij de bureaus en voor de paar spelletjesavonden. We moeten maar snel weer eens een spelletje inplannen! Over spelletjes gesproken: **Marta**, **Matt** en **Valerio**, thank you for the fun ROOT nights! Who knows, perhaps we will be playing also some other board games soon. **Claudia** en **Maaike**, bij jullie kon ik ook altijd terecht met goed nieuws of frustraties. Dankjulliewel voor de fijne gesprekken over politiek, huizenjacht, de PhD, etc. **Laura B.** and **Francesco**, thank you for the good times in the DDW and on the other side of the world. I think the conferences helped us to get to know each other better, and I am really thankful that we could share part of our PhD-journeys. **Yuang** you were the neighbor sitting across and I really enjoyed our small talks at our desks and the times we went to each other's places. Thank you for sharing your view on the world and talking about your travels. **Shuang**, thank you for the fun breaks at your desk every now and then. And thanks for the pomegranate and other snacks you shared with me. **Karan**, you only arrived in the last year of my PhD, but I really enjoyed the lunches and the outings: from eating herring at 10 in the morning to the Christmas Market in Maastricht. I hope we will do many more of these activities soon. Also a big thank you to all other colleagues who made my time at MCC unforgettable: **Daan**, **Giorgio**, **Henrik**, **Hidde**, **Jian**, **Jonas**, **Juliette**, **Just**, **Koen**, **Komal**, **Masoud**, **Qijun**, **Petra K.**, **Sergei**, **Théophile**, **Tom** and **Zixiong**.

En toen had ik **Johan** en **Savannah** nog niet genoemd. Johan, vanaf het begin van mijn promotietraject werd jij een goede vriend. Voor inzichten en inspiratie kon ik altijd bij jou terecht. De koffiepauzes om even weg te zijn van het DDW deden altijd veel goed. Jij kende de hoogte- en dieptepunten van een PhD als geen ander en gelukkig hebben we de bordspellen gevonden om ons daarvan af te leiden. Savannah, we were the last ‘students’ of the Krijn-lab and I am very grateful I could share that experience with you. You were always there to help me stop overthinking and to convince me to send my powerpoint slides or my manuscripts. We shared our craziest ideas in brainstorm sessions and also more serious stuff during coffee breaks. I am very happy that you, Savannah and Johan, want to be my paranymphs.

De (buitenlandse) conferenties vormden een paar van de hoogtepunten in mijn PhD-tijd en het allerleukste daaraan was dat ik die momenten kon delen met een aantal collega’s. Ik denk met veel vreugde terug aan de tijd van CSC in Vancouver, de NAM in New York en de IZC in Valencia en dat is dankzij jullie: **Caroline**, **Erik**, **Francesco**, **Laura B. Nienke**, **Oscar**, **Suzan**, **Romy** en **Yadi**! Ook heb ik erg genoten van PREPA in Louvain-la-Neuve met **Claudia**, **Kris** en **Nynke**!

Een aantal vrienden wil ik nog specifiek noemen voor hun steun. **Yoni** en **Bas**, ik heb onwijs genoten van de gezellige diners, zeildagen en Tivoli-concerten, hopelijk volgen er meer! Jullie kennen de PhD-struggles en het is fijn om daarover te kunnen praten met jullie of om het juist over hele andere zaken te hebben. **Jur** en **Mark**, tijdens onze PhD’s hebben we eigenlijk de eetclub voortgezet. Dit zijn stuk voor stuk avonden met een gouden randje. Inmiddels lukt het ons zelfs om het lekkere eten te combineren met een bordspel. **Veerle**, **Saydi** en **Patrick**, al vanaf het begin van de Scheikundestudie kan ik jullie goede vrienden noemen. We zien elkaar niet meer zo vaak als tijdens de studie, maar als we bij elkaar zijn is het als vanouds. Of we nou wel of niet uit een Escape Room ontsnappen, het is altijd gezellig. **Lisette** en **Stephanie**, het is ontzettend fijn dat wij al sinds (voor) de basisschool bevriend zijn en dat die vriendschap er nog steeds is. Jullie kennen mij door en door en dat heeft de afgelopen jaren echt geholpen! **Sanne** en **Richard**, met jullie is het altijd gezellig en niks is geforceerd. De Eftelingbezoeken en uiteraard de high beers en high wines moeten we er zeker in houden! **Marco**, fijn om een goede vriend te hebben om mee te lachen en ook serieuze, inhoudelijke gesprekken mee te kunnen voeren. Onze avonden waarbij tegenwoordig ook **Floor** steeds vaker aansluit zijn mij dierbaar, dankjulliewel! **Joanna**, **Carla**, **Jasper** and **Anton**, we met in Zurich 6 years (!) ago and we are still in touch. I really appreciate our phone calls, visits and other activities. Let’s try to keep organizing these things! **Simon**, **Paul**, **Sam**, **Jelle**, **Patrick** en **Veerle**, dankjulliewel voor de gezelligheid in vorm van Down the Rabbit Hole en spelletjesavonden. **Max**, **Jialun**, **Yord** en **Stijn**, dankjulliewel dat ik mij bij jullie mocht aansluiten. De samenkomsten en weekenden weg met jullie zijn altijd gezellig en heerlijk laagdrempelig. Het online gamen dat eigenlijk begon tijdens de covidtijd is nu nog steeds fantastisch. **Denise**, dankjewel voor jouw vriendschap en voor de Chinese les. Ik kijk uit naar de volgende keer dat je **Tom** weer meeneemt voor een potje Mariokart.

Ger en de andere trainers en medesporters van CrossFit Newstyle wil ik bedanken. Jullie hadden het vast niet door, maar de trainingen waren voor mij een goede afleiding.

Ik wil heel graag de tantes, ooms, neven en nichten bedanken die de afgelopen jaren met interesse en enthousiasme de ontwikkelingen rond mijn promotietijd hebben gevolgd. In het bijzonder wil ik tante **Petrie** en ome **Wil** bedanken: jullie hebben mij al (bijna) heel mijn leven aangemoedigd om vooral te doen wat ik leuk vind, om mijn eigen weg te bewandelen en me daarbij niet te veel aan te trekken van anderen. Ik ben ontzettend dankbaar voor jullie steun en natuurlijk ook voor de gezellige avonden met lekker eten en goede wijn.

Floris en **Anita**, dankjulliewel voor alle geïnteresseerde vragen, betrokkenheid en gezelligheid. Dankzij jullie voelt Arnhem inmiddels toch wel een beetje als een derde thuis. Dat is ook te danken aan jullie: **Susanna**, **Stijn**, **Diederik**, **Ellis**, **Daan** en **Nienke**. De gezellige avonden, weekenden weg en feestdagen met jullie hebben mij regelmatig opgeladen. De bijkomende, inhoudelijke discussies hielden mij scherp.

Meggy, **Marnix**, **Sanne** en **Matthijs** ook jullie bedankt voor de interesse, liefde en gezelligheid. Het is soms ontzettend jammer dat wij niet om de hoek wonen, maar naar het zuiden afreizen was dankzij jullie altijd fijn. Ik ben ontzettend dankbaar voor en trots op twee lieve zussen waarmee ik lief en leed kan delen. En ik vind het fijn dat Marnix en Matthijs erbij gekomen zijn.

Pap en mam, dankjulliewel voor alles. Het warme thuisfront dat jullie gecreëerd hebben is de basis geweest voor deze studieloopbaan. Deze stabiliteit, de wekelijkse telefoongesprekken en zo nu en dan opladen in Helmond (of in Zeeland) waren onmisbaar. Jullie adviezen, interesse en aanmoedigingen hebben er mede voor gezorgd dat dit proefschrift is afgerond.

Lieve **Elena**, de afgelopen jaren ben jij mijn rots in de branding geweest. Jij stond altijd voor me klaar en je hebt telkens met liefde en begrip naar mijn verhalen geluisterd. Alle hoogtepunten hebben we samen gevierd en je hebt me door alle dieptepunten heen gesleept. Daarnaast heb je fysiek bijgedragen aan dit proefschrift: de kaft en verschillende figuren in het proefschrift komen voort uit jouw creativiteit. Ik ben ontzettend gelukkig met jou en ik ben erg benieuwd naar wat de komende jaren ons gaan brengen. Ik hou van jou!

About the author

Luc Smulders was born on the 30th of December 1993 in Eindhoven, the Netherlands. During his secondary education (VWO) at the dr. Knippenbergcollege in Helmond he really enjoyed the Biology, Chemistry and Physics classes. This is when he was inspired to pursue a career in Natural Sciences. In 2012 he started to study Chemistry at Utrecht University. He obtained his bachelor's degree in 2016 after completing a thesis under supervision of prof. Andries Meijerink studying leaching of cadmium ions from CdSe-based quantum dots. Later that year Luc continued his studies at Utrecht University in the master's program Nanomaterials Science. During his master's he studied tandem catalytic conversion in Pickering emulsions under supervision of prof. Pieter Bruijnincx. Furthermore, he went to the ETH Zurich to conduct a project on organometallic fuel cells in the group of prof. Hansjörg Grützmacher, after which he obtained his master's degree in 2018.

In 2019, Luc started his PhD project in the Materials Chemistry & Catalysis group at Utrecht University, working with prof. Krijn P. de Jong and prof. Petra E. de Jongh, and in close collaboration with BP. The key focus of his project was on location effects in bifunctional catalysts for hydroconversion. The findings of his work were presented in peer-reviewed journals, at international and national scientific conferences and in this thesis. Additionally, he taught a practical course for bachelor students, tutorial classes for master students and he supervised multiple students with their research projects and/or literature reviews.

During his studies, Luc was an active member in several boards, committees and councils. This is where he learnt that he also has an affinity with policy and organization. Therefore, after the PhD, he decided to combine the passions for science and policy and joined the Dutch Institute of Public Health and the Environment (RIVM) where he works as radiation safety scientist. Luc spends his free time playing (board) games, listening to podcasts, doing a CrossFit training, and he loves skiing.